

**Australian Institute of Nuclear Science and Engineering**

**INIS-AU-0003**



AU9716139

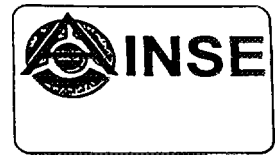
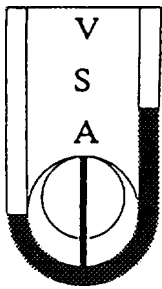
9th  
**Australian Conference  
on Nuclear Techniques  
of Analysis**

The University of Newcastle, NSW

27-29 NOVEMBER 1995

**PROCEEDINGS**

ISSN 1325-1694



**9TH AUSTRALIAN CONFERENCE**

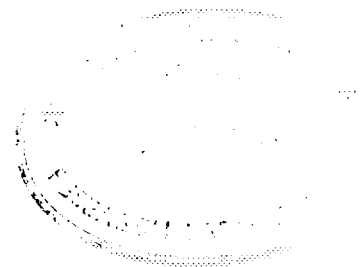
**ON**

**NUCLEAR TECHNIQUES OF ANALYSIS**

The University of Newcastle, NSW

27-29 November 1995

**PROCEEDINGS**



**Sponsored by**

**Australian Institute of Nuclear Science & Engineering  
Vacuum Society of Australia  
The University of Newcastle**

**LIST OF  
SPONSORS AND EXHIBITORS**

*Fisons Instruments Pty Ltd*

*Balzers Australia Pty Ltd*

*Javac Pty Ltd*

*John Morris Scientific Pty Ltd*

*Stanton Scientific*

*Varian Australia Pty Ltd*

*Ajax Chemicals*



# Legend

Aboriginal Education Centre - Wollotuka	AE	Great Hall	GH
Academic Office Block	AOB	Griffith Duncan Theatre	GDT
Advanced Technology Centre	ATC	Hunter Building	H
Animal House	AN	International House	IH
Architecture	A	Industry Development Centre (Hunter)	IDC
Architecture Drawing Studios	ADS	Language Centre	LC
Art	AT	Lecture Theatre :B	B1
Art Workshops	AW	Lecture Theatre :Basden	BA
Aviation	AV	Lecture Theatre :E	E
Behavioural Sciences Building	W	Library - Auchmuty	L
Biological Sciences	B	Library - Huxley	LH
Bowman Building	BB	Maintenance Workshop	MW
BSC Building	BSC	Mathematics	V
Central Garage	CG	McMullin Building	MC
Ceramics	CE	Medical Sciences Building	MS
Chancellery (Central Administration)	CH	Old Commonwealth Bank	OCB
Chaplaincy Centre	CC	Physics Building	P
Chemistry	C	Radio 2NUR FM	LC
Child Care Centre - Kintaiba	CCK	Richardson Wing	RW
Child Care Centre - Kooinda	CCB	Science Building	SB
Child Care Centre - Wonnyba	CCW	Sculpture Workshop	SW
Commonwealth Bank	CB	Security	GH
Computing and Information Sciences	CT	Services Building	SER
Design	D	Social Sciences Building	S/R
Drama Studio	DS	Special Education Centre	SE
Drama Theatre	DT	Sport and Recreation (portable)	SPT
Economics and Commerce	S/R	Sports Centre - Auchmuty	SC
Edwards Hall	EH	Sports Gymnasium - Hunter	GY
Engineering Administration	EA	Sports Pavilion	SP
Engineering Bulk Solids	EG	Staff House	SH
Engineering Chemical & Materials	EB	Stores	SER
Engineering Civil & Surveying	ED	Temporary Office Buildings	TB
Engineering Classrooms	EF	Tennis Courts	TC
Engineering Electrical & Computer	EE	The Station	ST
Engineering Mechanical	EC	TUNRA	AV
Engineering Science (DW George)	ES	TUNRA Annexe	TA
Evatt House	EV	University Union - Hunter	UH
Faith Centre	FC	University Union - Shortland	US
General Purpose Building	GP	Visual Arts/Media Studies	VA
Geology	G	Wetlands Pavilion	WP
Graduate Studios	GS		

# map

CALLAGHAN CAMPUS MAP

j a n u a r y 1 9 9 5

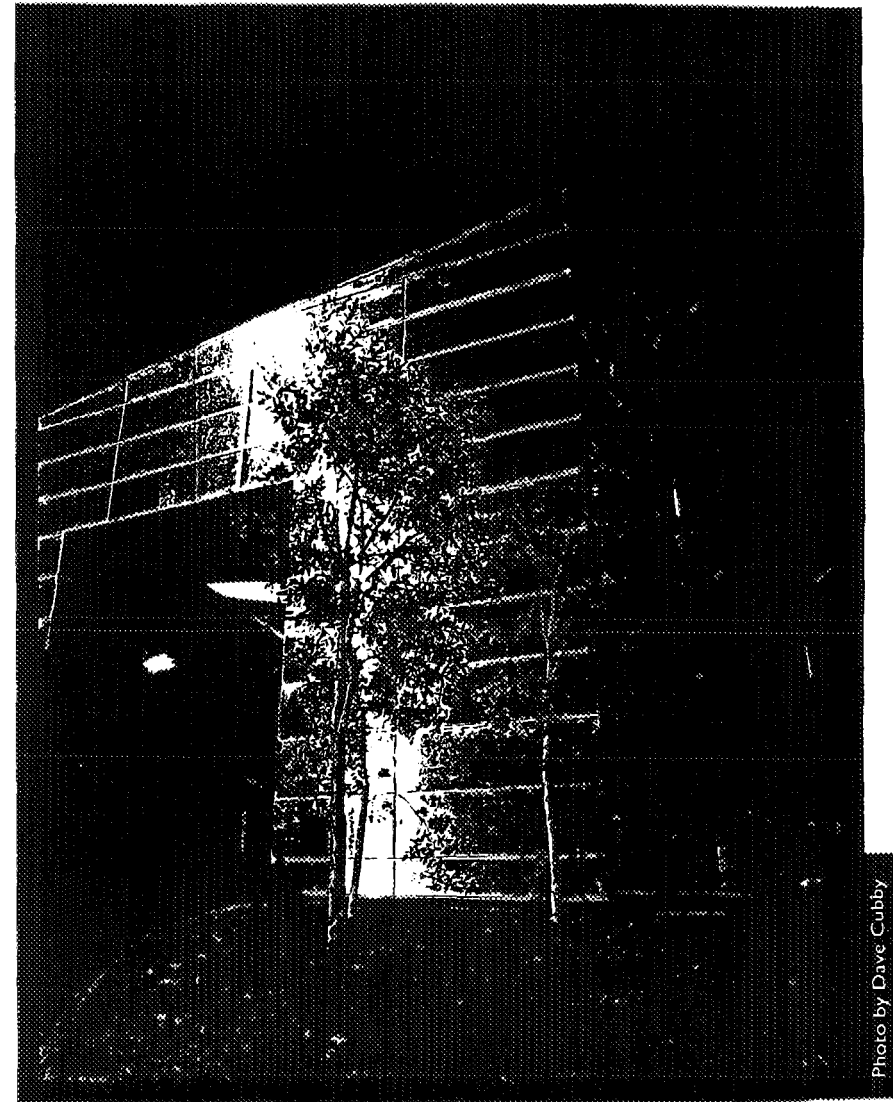


Photo by Dave Cubby



The UNIVERSITY of NEWCASTLE

AUSTRALIA

# **PROGRAM**

Monday 27 November	EO1		
09:00 -	REGISTRATION -	PHYSICS BUILDING	
10:10 - 10:30	MORNING TEA		
10:30 - 11:00	OFFICIAL OPENING	EO1	
11:00 - 11:40	OPENING PLENARY R. Watts P 1 Sputtering of Neutral Atoms from Zirconium		
	NTA EO1	Thin Films PG08	P105
11:40 - 12:00	H. Whitlow NTA 1 Development of Si-Based Detectors for Intermediate...	S. Russo TF 2 Modelling of Ion Beam Induced Heating in Thin Film Sl...	
12:00 - 12:20	P. Evans NTA 2 Characterisation of Metal Ion Implanted Fullerene Films	A. Durandent TF 3 Deposition of Silicon Dioxide Using Helicon Activated...	
12:20 - 01:30	LUNCH		
01:30 - 01:50	G. McOrist NTA 3 Trace Elements in Coloured Opals Using NAA	D. McKenzie TF 1 A New Configuration for Helicon Activated Reactive Evaporation	
01:50 - 02:10	S. Sie NTA 4 Proton Microprobe Study of Tin-Polymetallic Deposits		
02:10 - 02:30	I Plimer NTA 5 Ironstones of the Olary Block: Use of RNAA and INAA...	A. Perry TF 4 Fabrication of Silica Based Optical Waveguides using....	
02:30 - 02:50	S Reeves NTA 6 Platinum Group Elements and Gold: Analysis by RNAA....	R. Netterfield TF 5 Coating of Fabry Perot Etalons	
02:50 - 03:10	Poster Reviews	A. Bendavid TF 6 Synthesis of TiN Thin Films by Condensation of Ti from ....	
03:10 - 03:40	AFTERNOON TEA		
03:40 - 04:00	M. Cholewa NTA 7 Design of a Single Ion Facility and its Applications	R. Manory TF 7 Effects of Nitrogen Ion Implantation on Wear, .....	
04:00 - 04:20	C. Ryan NTA 8 Diamond Exploration and Mantle Structure Imaging...	S. Bhansali TF 8 Ion Implantation for Nucleation of Ni films....	
04:20 - 04:40	D. Jamieson NTA 9 NTA in Diamond Synthesis and Annealing	S. Askraba TF 9 New Technique for the Measurement of Stress....	
04:40 - 05:00	Poster Reviews	J. Singh TF 10 OPTO-Electronic Implications of Halogens In Amorphous Sl...	
05:00 - 06:30	POSTER SESSION -	HUNTER STUDENTS UNION	
06:30 - 08:00	BBQ -	HUNTER STUDENTS UNION	

TUESDAY 28 November	NTA EO1	Surface Science PG08	Cluster Science P105
08:30 - 08:50	Th R Niklaus P 2 Radiocarbon Dates to Access the Origin of the Man in the Ice		
08:50 - 09:10	L. Fifield NTA 10 Ultra-sensitive Detection of Plutonium by AMS	C. Lund SS 2 APECS Study of the 3d Transition Metal L23VV Auger Lines - Fe to Ga?	B. Pailthorpe CSMD 1
09:10 - 09:30	M. Hotchkis NTA 11 Precision and Reproducibility in AMS measurements	Z. Fang SS 3 Wave-Function Mapping by (e,2e) Spectroscopy	
09:30 - 09:50	J. Prescott NTA 12 NTA as a Component of Thermoluminescent Dating	I. Jamie SS 4 ...Liquid-Air Interface X-Ray Reflectometer	I. Snook CSMD 2 MD Simulation of Two Component Systems to Investigate....
09:50 - 10:10	L. Wielunski NTA 13 Multiple Scattering Contributions to Depth Resolutions and Low Energy	G. Watson SS 5 Reverse Imaging Mode by AFM Determination of Tip Shape	S. Russo CSMD 3 MD Investigation of the Dynamic Properties of Si
10:10 - 10:30	Z. Fang NTA 14 Study of Multiple Scattering Effects in Heavy Ion RBS	R. Nowak SS 6 Relaxation of High Internal Stresses in HfN Thin Films....	N. Marks CSMD 4 Microscopic Structure of Tetrahedral Amorphous Carbon
10:30 - 11:00		MORNING TEA	
11:00 - 11:20	R. Elliman NTA 15 Ion-Beam Synthesis of Ge(x)Si(1-x) Strained Layers...	G. Morris SS 23 FTO Films for Solar Cells	K. Stevenson CSMD 5 Experimental Total Differential Scattering Cross Sections....
11:20 - 11:40	J. Glasko NTA 16 Ion-Beam Induced Modification of Strain Levels of Pseudo....	D. Swingler SS 24 Characterisation of Metals by SIMS	E. Bieske CSMD 6 Evaluation of O and H Contamination on Si Surfaces...
11:40 - 12:00	C. Lachlan NTA 17 Ion Microprobe Analysis of Poly-X Si Photo-Voltaic Cells	R. Payling SS 25 Use of Differential GDOES Depth Profiles to Study....	T. McKay CSMD 7 Fragmentation of Rare Gas Dimers
12:00 - 12:20	K. Belay NTA 18 ....Non-Stoichiometry on... SPE of Amorphised GaAs		Y. Hsu CSMD 8 Pulse Valve Designs for Cluster Generation
12:20 - 01:30		LUNCH	
01:30 - 01:50	N. Dytlewski NTA 19 HI-TOF-ERDA of High Dose Metal Implanted Germanium	H. Brongersma SS 1 The Outermost Atomic Layer of Oxides	E. Felsobuki CSMD 9 Ab-initio Calculations on Small Argon Ion Clusters
01:50 - 02:10	K. Nugent NTA 20 Defects Formed During Ion Beam Modification of Diamond		D. Beck CSMD 10 Vibrational Frequency Shifts of a Water Monomer Embedded...
02:10 - 02:30	S. Bhansali NTA 21 Study of Annealing Effects of Pd Implanted Si	J. Yao SS 7 Studies of Ultrathin Pd Films in Cu(001)	J. Hughes CSMD 11 Variational Calculations of Rovibrational States of k2Na+
02:30 - 02:50	J. Wong-Leung NTA 22 Study of Au Trapped at Cavities	G. Cotterill SS 8 STM Study of the Initial Oxidation of Ni3Al(110)	M. Radny CSMD 12 Fluorine Chemisorption on the Si(111) 7x7 Surface - ....
02:50 - 03:10	K. Prince NTA 23 Dynamic SIMS: Applications to Materials and Environment...	F. Zhang SS 9 LEIS Measurement of Order in Alloy Surfaces	P. Smith CSMD 13 Chemisorption of Cl on the Si(111) 7x7 Surface - .....
03:10 - 03:40		AFTERNOON TEA	
03:40 - 05:00	Open Forum EO1 Future links between these groups Location and timing of next conference	Discussion NTA / VSA / AMRS	
05:00 - 06:00		VSA AGM	
08:00 - 09:00	CONFERENCE DINNER		SHORTLAND STUDENTS UNION

WEDNESDAY 29 November	NTA EO1	Surface Science PG08	Cluster Science P105
08:30 - 08:50	C. Tuniz P 3 Accelerator Mass Spectroscopy: State of the Art		
08:50 - 09:10	S. Sie NTA 24 Australia: Progress Report	P. Dastoor SS 10 Surface Morphology from Helium Specular Reciprocal...	S. Pickering CSMD 14 MD Simulations of Spinodal Decomposition in Three ....
09:10 - 09:30	J. Fallon NTA 25 Status of 8MV Tandem Accelerator, ANTARES	J. Singh SS 11 Simplified Data Acquisition of Surface NEXAFS for .....	A. McDonough CSMD 15 Implementation of the MD Method on a Parallel.....
09:30 - 09:50	D. Fink NTA 26 1129 Measurements at the ANTARES AMS Facility	J. O'Connor SS 12 Formation of Ni(100)-Al Surface Alloy	G. Williams CSMD 16 MD Simulation of Sputtering of Polycrystal Zr by 1.5keV Ar
09:50 - 10:10	G. Legge NTA 27 New 2-Stage Ion Microprobes and a Move to Higher Energy	Q.B. Lu SS 13 Negative Ion Spectra by Low Energy Li+ Scattering from...	B. O'Malley CSMD 17 Computer Simulation of the Structure and Interparticle...
10:10 - 10:30	A. Saint NTA 28 Mixed Beams for the Nuclear Microprobe	Y. Shen SS 14 Interaction of CO with Cu <sub>3</sub> Pt(111)	A. Dyson CSMD 18 Investigation of Diamond CVD Growth Processes on a Si...
10:30 - 11:00	MORNING TEA		
11:00 - 11:20	G.K. Muralidhar NTA 29 RBS Analysis of Magnetron Sputtered NdFeB Thin Film	N. Singh SS 15 Halocarbon Etching of Compound Semiconductors	
11:20 - 11:40	M. Kenny NTA 30 Evaluation of H and O Impurity Levels on Silicon..	M. Petracic SS 16 SIMS Depth Profiling at Elevated Temperatures	
11:40 - 12:00	M. Swain NTA 31 Influence of Implantation of Three Metallic Ions on .....	C. Kaalund SS 17 Electron Emission on Cleavage of Silicon	
12:00 - 12:20	P. Weiser NTA 32 Homo-Epitaxial Diamond Film Growth on Ion Implanted ....	P. Paterson SS 18 Electron Irradiation Induced Changes in Sapphire	
12:20 - 01:30	LUNCH		
01:30 - 01:50	T. Ophel NTA 33 RBS Using Silicon Beams	R. Clark SS 19 Semiconductor Nanofabrication & Microelectronics Facility	
01:50 - 02:10	M. von Bibra NTA 34 Waveguide Fabrication by MeV Ion Implantation	S. Myrha SS 20 Image Formation and Point Defect Analysis- STM of WTe <sub>2</sub>	
02:10 - 02:30	W. Stannard NTA 35 ERDA of Ferroelectric Films	D. Halfpenny SS 21 Laser Induced Removal of sub- Micron Particles from a....	
02:30 - 02:50	A. Bettiol NTA 36 IBIL Characterisations of CVD Diamond Films	B. Dinte SS 22 Image Artefacts in Non- Contact Mode AFM- Force.....	
02:50 - 03:10	AFTERNOON TEA		
03:10 - 03:40	C. Johnson NTA 37 Compaction of Fused Silica Resulting from Ion Implant...		
03:40 - 04:00	D. Cohen NTA 38 IBA for Elemental Finger- Printing of Fine Smoke....		
04:00 - 04:20	J. Gorman NTA 39 ...Rare Earth Containing Protective Oxide on Al		
04:20 - 04:40	CLOSING SESSION - EO1		

NTA / VSA '95 CONFERENCE - Session Chairs

27-29 NOVEMBER 1995

UNIVERSITY OF NEWCASTLE

Monday 27 November	NTA EO1	Thin Films PG08	
11:00 12:20	Bruce King	Phil Martin	
01:30 03:10	John Boldeman	Phil Martin	
03:40 05:00	Dave Cohen	Roger Netterfield	

TUESDAY 28 November	NTA EO1	Surface Science PG08	Cluster Science P105
08:30 10:30	Soey Sie	Paul Dastoor	Phil Smith
11:00 12:20	Mike Kenny	Nagindar Singh	Simon Biggs
01:30 03:10	Rob Elliman	John Furst	Marian Radny
03:40 05:00	John O'Connor		

WEDNESDAY 29 November	NTA EO1	Surface Science PG08	Cluster Science P105
08:30 10:30	David Jamieson	Peter Patterson	Ellak Von Nagy Felsobuki
11:00 12:20	Trevor Ophel	Yaogen Shen	
01:30 02:50	George Legge	Chris Lund	
03:10 04:40	Bruce King		

# **CONTENTS**

## CONTENTS

<b>Papers</b>	<b>Page</b>
Sputtering of Neutral Atoms from Zirconium R A WATTS	1
Development of Si-based Detectors for Intermediate Energy Heavy-Ion Physics at a Storage-Ring Accelerator H J WHITLOW, J JAWOROWSKI, M LEANDERSSON, M EL BOUANANI, B JACOBSSON, J ROMANSKI, L WESTERBERG, E J VAN VELDHUIZEN and THE CHICSI COLLABORATION	2
Trace Elements in Coloured Opals Using Neutron Activation Analysis G D McORIST and A SMALLWOOD	5
Proton Microprobe Study of Tin-Polymetallic Deposits S MURAO, S H SIE and G F SUTER	8
Ironstones of the Olary Block, South Australia: The Use of RNAA and INAA to Understand Their Genesis I R PLIMER, B G LOTTERMOSER, P M ASHLEY and D C LAWIE	11
The Platinum Group Elements and Gold: Analysis by Radiochemical and Instrumental Neutron Activation Analysis and Relevance to Geological Exploration and Related Problems S J REEVES and I R PLIMER	14
Design of a Single Ion Facility and its Applications M CHOLEWA, A SAINT and G J F LEGGE	17
Diamond Exploration and Mantle Structure Imaging Using PIXE Microanalysis C G RYAN, W L GRIFFIN and T T WIN	19
Nuclear Techniques of Analysis in Diamond Synthesis and Annealing D M JAMIESON, S PRAWER, P GONON, R WALKER, S DOOLEY, A BETTIOL and J PEARCE	22
Radiocarbon Dates to Access the Origin of the Ice Man TH R NIKLAUS, G BONANI and R PRINOTH-FORNWAGNER	25
Ultra-Sensitive Detection of Plutonium by Accelerator Mass Spectrometry L K FIFIELD, R G CRESSWELL, T R OPHEL, M DI TADA, J P DAY, A CLACHER and N D PRIEST	28

<b>Papers</b>	<b>Page</b>
Precision and Reproducibility in AMS Radiocarbon Measurements M A C HOTCHKIS, D FINK, Q HUA, G E JACOBSEN, E M LAWSON, A M SMITH and C TUNIZ	29
Nuclear Analysis Techniques as a Component of Thermoluminescence Dating J R PRESCOTT, J T HUTTON, M A HABERMEHL and J VAN MOORT	32
Multiple and Double Scattering Contributions to Depth Resolution and Low Energy Background in Hydrogen Elastic Recoil Detection L S WIELUNSKI	35
Study of Multiple Scattering Effects in Heavy Ion RBS Z FANG and D J O'CONNOR	38
Ion-Beam Synthesis of Ge <sub>x</sub> Si <sub>1-x</sub> Strained Layers for High-Speed Electronic Device Applications R G ELLIMAN, H JIANG, W C WONG and P KRINGHØJ	41
The Influence of Microscopic and Macroscopic Non-Stoichiometry on Interfacial Planarity During the Solid-Phase Epitaxial Growth of Amorphized GaAs K B BELAY, M C RIDGWAY and D J LLEWELLYN	44
Heavy Ion Time-of-Flight ERDA of High Dose Metal Implanted Germanium N DYTLEWSKI, P J EVANS, J T NOORMAN, L S WIELUNSKI and J BUNDER	47
Defects Formed During Ion Beam Modification of Diamond K W NUGENT, S PRAWER, S P DOOLEY and D N JAMIESON	50
Accelerator Mass Spectrometry: State of the Art C TUNIZ	53
AUSTRALIA: Progress Report S H SIE, T R NIKLAUS and G F SUTER	56
The Status of the Tandem Accelerator ANTARES J FALLON, J BOLDEMAN, D COHEN, C TUNIZ and P ELLIS	59
The Role of <sup>129</sup> I in the Environment and its Measurement at the ANTARES AMS Center D FINK, M HOTCHKIS, E M LAWSON, G E JACOBSEN, A M SMITH and C TUNIZ	62
New 2-Stage Ion Microprobes and a Move to Higher Energies G J F LEGGE, A DYMNIKOV, G MOLONEY, A SAINT and D COHEN	65

<b>Papers</b>	<b>Page</b>
Mixed Beams for the Nuclear Microprobe A SAINT, M B H BREESE and G J F LEGGE	68
Evaluation of Hydrogen and Oxygen Impurity Levels on Silicon Surfaces M J KENNY, L S WIELUNSKI, R P NETTERFIELD, P J MARTIN and A LEISTNER	71
Influence of Implantation of Three Metallic Ions on the Mechanical Properties of Two Polymers M V SWAIN, A J PERRY and J R TREGGIO	74
Homo-Epitaxial Diamond Film Growth on Ion Implanted Diamond Substrates P S WEISER, S PRAWER, K W NUGENT, A A BETTIOL, L I KOSTIDIS and D N JAMIESON	77
RBS using <sup>28</sup> Si Beams T R OPHEL and I V MITCHELL	80
Focussed MeV Ion Beam Implanted Waveguides M L VON BIBRA, A ROBERTS, K NUGENT and D N JAMIESON	83
Elastic Recoil Detection Analysis of Ferroelectric Films W B STANNARD, P N JOHNSTON, S R WALKER and I F BUBB	85
Ion Beam Induced Luminescence Characterisation of CVD Diamond Films A A BETTIOL, P GONON and D N JAMIESON	88
The Compaction of Fused Silica Resulting from Ion Implantation C M JOHNSON, M C RIDGWAY and P L LEECH	91
Ion Beam Analysis Techniques for the Elemental Fingerprinting of Fine Particle Smoke from Vegetation Burning in NSW D D COHEN	94
Nuclear Analysis of a Rare Earth Containing Protective Oxide on Aluminium J D GORMAN, A E HUGHES and P J K PATERSON	97
Trace Element Partitioning Between Aqueous Fluids and Silicate Melts Measured with a Proton Microprobe J ADAM, T H GREEN and S H SIE	101
Laser Annealing Effects of the Raman Laser on Nitrogen Implanted Glassy Carbon D BARBARA, S PRAWER and D N JAMIESON	104

<b>Papers</b>	<b>Page</b>
The Role of Oxygen in Quinternary Superconductors D R BECKMAN and D N JAMIESON	107
The Potential Use of Diamond Coated Tungsten Tips as a Field Ionisation Source A BROWN, S PRAWER, G J F LEGGE and L I KOSTIDIS	110
Trace Element Distribution in Geological Crystals J L DEN BESTEN, D N JAMIESON and P S WEISER	112
Transverse Microanalysis of High Energy Ion Implants S P DOOLEY, D N JAMIESON, K W NUGENT and S PRAWER	115
Electron Stimulated Desorption of Positive and Negative Oxygen Ions from $\text{YBa}_2\text{Cu}_3\text{O}_7$ Surfaces A HOFFMAN, S D MOSS, P J K PATERSON, D McCUBBERY and M PETRAVIC	118
Target Preparation at the ANTARES AMS Centre G E JACOBSEN, Q HUA, D FINK, M A C HOTCHKIS, E M LAWSON, A M SMITH and C TUNIZ	121
Lazer Tweezers: Spectroscopy of Optically Trapped Micron-Sized Particles K M KERR, M K LIVETT and K W NUGENT	124
Studies of Defects on Ion Irradiated Diamond P F LAI, S PRAWER, A E C SPARGO and L A BURSILL	127
Accuracy of Radiocarbon Analysis at ANTARES E M LAWSON, D FINK, M A C HOTCHKIS, Q HUA, G JACOBSEN, A M SMITH and C TUNIZ	130
The ANTARES Recoil Time-of-Flight Spectrometer J W MARTIN, D D COHEN, N DYTLEWSKI and G J RUSSELL	131
Structural Investigation of Two Carbon Nitride Solids Produced by Cathodic Arc Deposition and Nitrogen Implantation A R MERCHANT, D J McCULLOCH, D R McKENZIE, Y YIN and E G GERSTNER	136
A Study of the Distribution of Rare-Metals in Kuroko-Type Ore S MURAO, S H SIE and G F SUTER	139
Oxide Growth on Aluminium Alloys in the Presence of Ammonium Fluoborate J OLIVER, P PATERSON, T FLAVELL and G BIDDLE	142

<b>Papers</b>	<b>Page</b>
Radiation-Enhanced Thermal Processes During Implantation of Gold Into Copper N E PERRET, B V KING and P C DASTOOR	144
The Non-Destructive Analysis of Fluid Inclusions in Minerals Using the Proton Microprobe C G RYAN, C A HEINRICH, E VAN ACHTERBERGH, T P MERNAGH, C BALLHAUS and K ZAW	147
An Update in Proton Probe Tomography A SAKELLARIOU, J HOWARD, M CHOLEWA, A SAINT and G J F LEGGE	149
AMS of Heavy Radionuclides at ANTARES: Status and Plans A M SMITH, D FINK, M A C HOTCHKIS, E M LAWSON and C TUNIZ	152
Nanocrystalline Diamond in Carbon Implanted SiO <sub>2</sub> K A TSOI, S PRAWER, K W NUGENT, R J WALKER and P S WEISER	155
Multivariate Techniques of Analysis for ToF-E Recoil Spectrometry Data H J WHITLOW, M EL BOUANANI, L PERSSON, M HULT, P JONSSON, M ANDERSSON, M ÖSTLING, C ZARING, P N JOHNSTON, I F BUBB, S R WALKER, W B STANNARD, D D COHEN and N DYTLEWSKI	158
Application of <sup>14</sup> N( <sup>3</sup> He, <sup>4</sup> He) <sup>13</sup> N Nuclear Reaction to Nitrogen Profiling L S WIELUNSKI	161
Elastic Recoil Detection Analysis of Hydrogen in Polymers T R H WINZELL, I F BUBB, R SHORT, H J WHITLOW and P N JOHNSTON	164

**EXTENDED  
ABSTRACTS**



AU9716140

# Sputtering of Neutral Atoms from Zirconium

ROBERT O WATTS

School of Chemistry, The University of Melbourne, Parkville Victoria 3052

Angular distributions of neutral atoms sputtered from zirconium surfaces have been determined experimentally and by computer simulation. Sputtered atom distributions are measured using laser induced fluorescence following impact by a range of ion masses and energies. Results are presented for several different ion beam impact angles as a function of the Zr spin-orbit state. Computer simulations using  $\text{Ne}^+$  and  $\text{Ar}^+$  ions are based on molecular dynamics simulations. Sputtering mechanisms are shown to involve primarily and second layer atoms, and the importance of primary record mechanisms increases with ion mass.



AU9716141

# Development of Si-based detectors for intermediate energy heavy-ion physics at a storage-ring accelerator

H.J. WHITLOW\*, J. JAWOROWSKI\*, M. LEANDERSSON\*, M. EL BOUANANI\*, B. JAKOBSSON\*\*, J. ROMANSKI\*\*\*, L. WESTERBERG\*\*\*, E.J.VAN VELDHUIZEN\*\*\* AND THE CHICSI COLLABORATION.

\*Department of Nuclear Physics, Lund Institute of Technology, Sölvegatan 14, S-223 62 Lund, Sweden.

\*\*Division of Cosmic and Subatomic Physics, Lund University, Lund Institute of Technology, Sölvegatan 14, S-223 62 Lund, Sweden.

\*\*\*The Svedberg - Laboratory, Uppsala University, Box 531, S-751 21 Uppsala, Sweden.

## ABSTRACT

UHV compatible Si detectors are being developed by the CELSIUS Heavy Ion Collaboration (CHIC) for measuring the energy and identity of Intermediate Mass Fragments (IMF) with  $Z \approx 3 - 12$  and energies of  $0.7 - 10A$  MeV. Here we give an overview of the development of Si  $\Delta E$ -E detector telescopes and investigations on IMF identification based on the pulse shape from Si-detectors where the particles impinge on the rear-face of the detector.

## INTRODUCTION

The CELSIUS Heavy Ion Collaboration (CHIC) studies critical phenomena in nuclei at high compression. CHIC is constructing a Si-based detector array of  $\sim 600$  detector telescopes that will be used to detect Intermediate Mass Fragments (IMF) which have  $Z = 3 - 12$  as well as light particles (p, d,  $\alpha$ ) with energies of  $1 - 60A$  MeV, produced in the cluster gas jet target at the CELSIUS ion storage ring at The Svedberg Laboratory in Uppsala.

The requirements of CHIC are, low detection thresholds, large solid angle coverage with small dead areas and low-cost large scale production. Moreover, the ion storage ring environment requires ultra-high vacuum compatibility (Repeated cycling to  $\sim 200^\circ$  C and no outgassing). To satisfy these requirements the CHICSI collaboration have been actively developing suitable detector technologies. The findings from this work are not only of interest for fundamental nuclear physics but they open new possibilities for applied nuclear physics, including:

- Reduction of the Compton background in soft X-ray detection.
- Rugged detectors for cosmic and solar particle spectrometry from satellite and rocket payloads.
- Recoil Spectrometry (RS) using high energy ion beams with improved separation for heavy elements and vastly greater solid angles than for time of flight systems. (Essential for RS microprobe).
- Nuclear Reaction Analysis with simultaneous detection of many reaction products.

Together with SINTEF A/S in Oslo CHICSI has been developing Si  $\Delta E$ -detectors with thicknesses down to  $15\mu\text{m}$  and  $10 \times 10$  mm active area for production in quantities of 1000 or so.

The use of pulse shape analysis with Si detectors has long been established as a method of particle identification [3,4]. This technique is difficult because the pulses are short - a consequence of the fact that for junction side impingement the electron hole pairs are produced in the region where the field is greatest. Recently Pausch et al.[5-6] have demonstrated that rear-side impingement gives slower charge carrier collection and even low energy IMFs may be detected. We have investigated the dynamics of the charge carrier collection process for different ions both experimentally and theoretically.

## EXPERIMENTAL

The two different methods for identification of IMF and measurement of their energy were studied at the The Svedberg Laboratory in Uppsala.  $1 - 2$  pA of  $32A$  MeV  $^{14}\text{N}^{6+}$  ions from the Gustaf-Werner Cyclotron were directed at a  $^{124}\text{Sn}$  target. Data was collected using standard multi-parameter data acquisition systems.

The detectors developed by CHICSI together with SINTEF A/S are Si  $p^+ - i - n^+$  diodes formed on a thin Si membrane. The technique used for fabrication is essentially the same as described by Lavergne-Gosselin et al [1]. For testing purposes the detectors were mounted on a  $0.5$  mm copper carrier using a high-temperature curing silver epoxy [2] which is suitable for UHV applications.

The chip itself is fabricated from UHV compatible materials.

A critical parameter in  $\Delta E$  detectors is both the detector thickness and thickness variations. Tests during calibration with a  $^{226}\text{Ra}$  source using test detectors revealed the thickness of the detector used here to be  $15 \pm 0.7 \mu\text{m}$ . This is consistent with tests using the Lund nuclear microprobe in a Scanning Transmission Ion Microscopy (STIM) mode. Edge to edge and corner to corner thickness variations over the entire detector did not exceed  $\pm 1 \mu\text{m}$ . Furthermore mapping of the microscopic thickness over  $200 \times 200 \mu\text{m}$  regions at the centre and the corner of the detector showed the variations were less than  $200 \text{ nm p-p}$ . The Si E detector was  $380 \mu\text{m}$  thick. A veto detector was placed behind this to identify particles which passed right through the  $\Delta E$ -E telescope.

Large area ( $5 \times 5 \text{ cm}$ ) detectors from Micron and ( $600 \text{ mm}^2$ ) Inter technique were used for the pulse-shape discrimination studies. The energy signal was obtained using a standard amplifier chain. The pulse shape was characterised in terms of the first moment of the current distribution. This was measured by the time difference between a constant fraction trigger and the zero-crossing time of a bipolar output from a fast amplifier [6,9].

## RESULTS AND DISCUSSION

### $\Delta E$ -E detector telescope

Figure 1 shows the raw  $\Delta E$  vs.  $E$  data. IMF fragments from the multifragmentation reactions [7] have been produced with  $Z$  up to 12 easily identified. Seamster et al [8] have proposed an iterative procedure for identification of particles from their  $\Delta E$  and  $E$  signals that is based on determination of  $PI$  which for  $Z \leq 20$  is  $\approx Z$ :

$$PI = (0.5AZ^2)^{1/3} \quad (1)$$

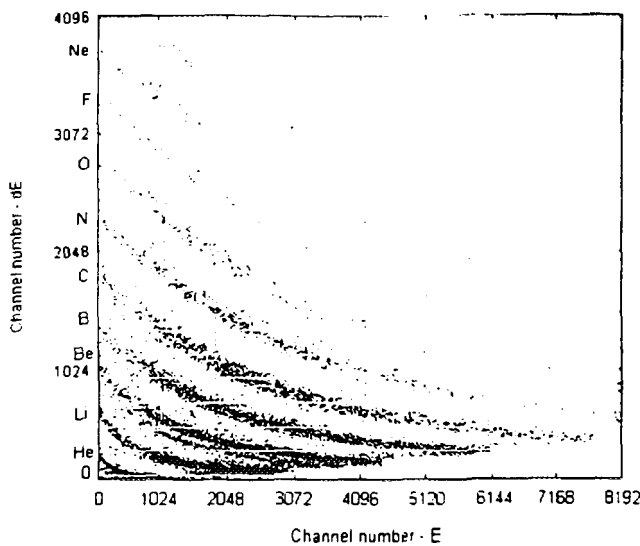


Fig. 1.  $\Delta E$  vs.  $E$  histogram for detector telescope with  $15 \mu\text{m}$  Si p-i-n  $\Delta E$  detector and  $380 \mu\text{m}$  Si E detector.  $\theta_{lab} = 30^\circ$

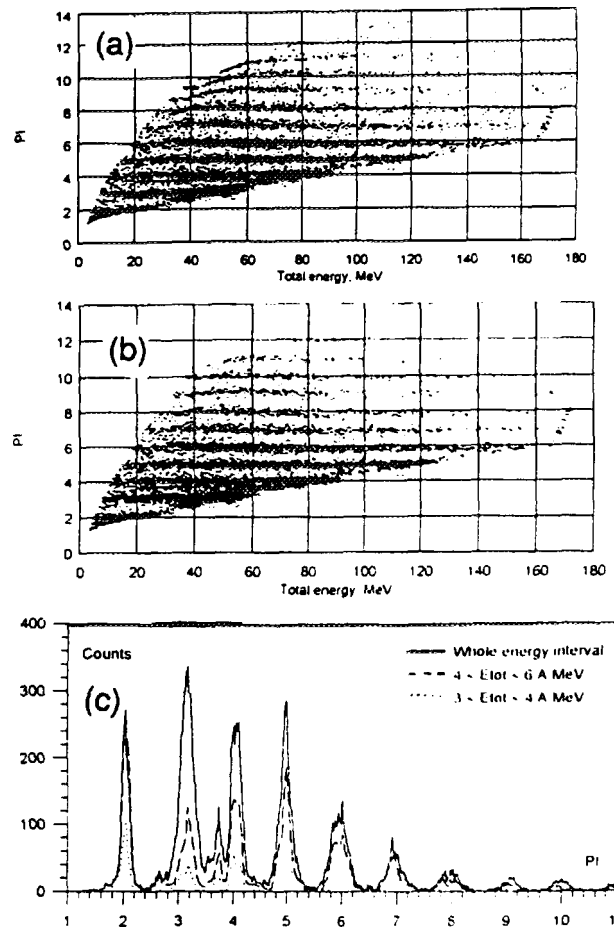


Fig. 2  $PI$  vs. total energy (a) effective charge correction for  $Z = 6$  (b) with  $Z$ -dependant effective charge correction (c) summation of (b) onto  $PI$  axis.

When transforming the  $\Delta E$  vs.  $E$  data to  $PI$  vs.  $E + \Delta E$  it was found the signals from the different elements did not lie along constant  $PI$  lines (Fig. 2a). The deviation could be associated with the uncertainty in the effective charge  $\gamma Z$  of the IMF in the  $\Delta E$  detector where:

$$\gamma = \left[ 1 - \exp \left( p_1 + p_2 \frac{E}{AZ^{4/3}} \right) \right] \quad (2)$$

The parameters  $p_1$  and  $p_2$ , which were taken as constants by Seamster et al [8], were found to be well described by a straight line dependence on  $Z$ . We subsequently modified the iteration procedure to use a look-up table for  $Z$ -dependant  $p_1$  and  $p_2$ , with  $Z = 6$  as a starting approximation. The results are shown in Figure 2 b and c. The width of the  $PI$  signals increases with increasing  $Z$  (Fig. 2 c), however it is clearly apparent that the combined resolution of the detector and algorithm is sufficient to identify the IMF's. Indeed  $^7\text{Be}$  and  $^9\text{Be}$  are clearly resolved. The  $Z$  dependence of  $p_1$  and  $p_2$ , in our semi-empirical approach suggest that  $\gamma$  the effective charge function eqn. (2) may be unrealistic. However, this conclusion should be regarded as tentative because it is based on measurements of  $\Delta E$  which is only indirectly a measurement of the energy deposited in electronic

processes due to plasma and charge carrier collection effects. Moreover, the assumed straight line energy dependence of stopping in the  $\Delta E$  detector and non-linearities in the E detector may also play a part.

### Pulse form identification

Figure 3 shows the first moment of the current signal vs. energy, obtained using one of the Micron detectors. The results show that separation is easily achieved for high energy IMF's, right up to the limit set by punch-through. However isotopic resolution was not achieved. At low energies there is a well-defined low energy smearing that represents the cut-off. This cut-off corresponds to an energy of  $\sim 2A$  MeV for all for IMFs. Evidently the

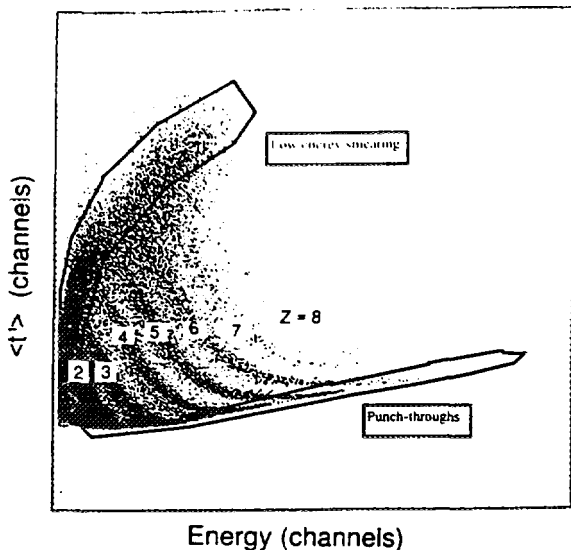


Fig. 3 Experimental measurement of first moment of time distribution vs. energy.  $\theta_{lab} = 20^\circ$

separation between the different elements is good except near the low energy smearing. The effect of reverse bias voltage was investigated on the resolving power. Best separation was observed at the voltage for full depletion (where the depletion layer edge just reaches the  $n^+$  layer of the  $p^+i-n^+$  structure) or small (10%) over-bias. We also compared separation using the rise-time and first moments to characterise the pulse shape[9]. The separation achieved was similar and no difference in the energy range or low-energy threshold was observed. However, rise-time measurements are more sensitive to noise than determination of the zero-crossing time of a bipolar-shaped signal.

To elucidate the interplay between the underlying processes we have undertaken a numerical simulation study of the pulse shape discrimination technique for both front and rear-side particle impingement. Fig 4. a and b show the first moment of the current distribution for junction and rear-side particle impingement which is in good agreement with our experimental observations. Although we could reproduce most of the features of our experimental data in the simulations, we could not

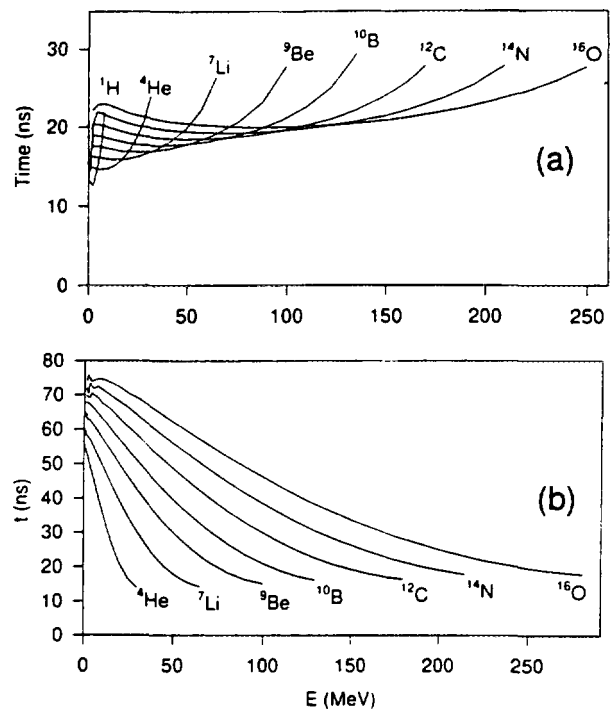


Fig. 4 Simulated first moment of the current distribution vs. energy for 500  $\mu\text{m}$  detector with 100 V reverse bias (70 V depletion voltage) (a) front side impingement (b) rear side impingement.

reproduce the smearing for rear-side impingement, that gives rise to the low energy threshold. This deviation might be associated with variations in the field because of point to point variations in the S resistivity or invalidity of some of the assumptions in the simulation such as effective-charge scaled proton stopping powers, a column shaped plasma and that the plasma is so dilute that it does not disturb the surrounding electric field.

### ACKNOWLEDGEMENTS

We are grateful to the Knut and Alice Wallenberg Stiftelse, Kungl. Fysiografiska Sällskapet and Wenner-Gren Foundation for financial support. We are also grateful to G. Pausch, G. Prete and the EURO GAM group for participation in the studies of pulse shape discrimination.

### REFERENCES

1. L. Lavergne-Gosselin, et al. Nucl. Instrum. Methods. A276(1989)210.
2. Epo-Tek H20E, Epoxy Technology inc. 14 Fortune Drive Billerica Ma 01821-3972, USA.
3. C.A.J. Ammerlan, R.F. Rumphorst and L.A. Ch. Kcl. Instrum. Methods 22(1963)189.
4. J.B.A. England., G.M. Field and T.R. Ophel, Nucl. Instrum. and Methods A280(1989)291.
5. G. Pausch, W. Bohne and D. Hilsher, Nucl. Instrum. and Methods A377(1994)573.
6. G. Pausch, W. Bohne and D. Hilsher, H.G. Ortlep and D. Polster Nucl. Instrum. and Methods A349(1994)281.
7. V. Avdeichikov, A. Bogdanov, O. Lozhkin, M. Zubkov, K. Nybo, E. Ølberg, T.F. Thorsteinsen, J. Bondorf, K. Sneppen, M. Berg, L. Carlen, R. Elmer, R. Ghetti, B. Jakobsson, B. Norén, M. Guttormsen, G. Løvholden, J. Nyberg, and L. Westberg, Physica Scripta, 50(1994)624-627.
8. A.G. Seamster, E.E.L. Green, and R.G. Kortling, Nucl. Instrum. and Methods 145(1977)583.
9. Annual report, Laboratori Nazionali di Legnaro, 1995.



# Trace Elements In Coloured Opals Using Neutron Activation Analysis

G.D. McORIST\*, A. SMALLWOOD\*\*

\* ANSTO Environmental Science Program, Lucas Heights Research Laboratories, PMB 1, Menai, NSW

\*\* Lecturer, Gemmological Association of Australia, 24 Wentworth Ave, Sydney, NSW

## SUMMARY

Neutron activation analysis (NAA) is a technique particularly suited to analysing opals since it is non-destructive and the silica matrix of opals is not prone to significant activation. It was used to determine the concentration of trace elements in 50 samples of orange, yellow, green, blue and pink opals as well as 18 samples of colourless opals taken from a number of recognised fields in Australia, Peru, Mexico and USA. The results were then evaluated to determine if a relationship existed between trace element content and opal colour.

The mean concentration of most of the elements found in orange, yellow and colourless opals were similar with few exceptions. This indicated that, for these samples, colour is not related to the trace elements present. However, the trace element profile of the green, pink and blue opals was found to be significantly different with each colour having a much higher concentration of certain trace elements when compared with all other opals analysed.

## INTRODUCTION

Opal is generally recognised as a valuable gemstone which exhibits glorious displays of colours<sup>1</sup>. This quality is also described as "play of colour" and opals with this unique characteristic are known as precious opals. A large amount of research into precious opals<sup>1-3</sup> has explained how this mineral exhibits sparkling colour across the entire visible spectrum from violet to deep red<sup>2</sup>.

In contrast, very few studies have been carried out on opals which do not display a play of colour. These are called common opals and comprise various colours which include black, white, grey, orange, yellow, green, blue and pink. The analysis common opals from South Bulgaria<sup>4</sup>, Brazil<sup>5</sup> and Tanzania<sup>6</sup> have provided a limited amount of physical and trace element data. Recently, neutron activation analysis (NAA) was used to analyse 42 samples of white, black and grey Australian common opals to characterise their trace element content<sup>7</sup>.

Common opals without any base colour (colourless as distinct from white) do exist and can be obtained from a number of different locations. Terms such as hyalite and crystal have also been used to describe these transparent to translucent variety of opals.

The purpose of this work is to use NAA to analyse a variety of orange, yellow, green, blue, pink and colourless common opals from a number of different locations around the world in order to characterise their trace element content and determine the relationship between trace element content and opal colour.

## EXPERIMENTAL

### Opal Preparation

Australian samples were obtained from their source by one of the authors following rough separation by normal mining methods. The remaining samples were obtained from reputable gemstone merchants. Each sample was cut from surrounding material and packed into polythene irradiation containers as previously described<sup>7</sup>.

### Sample Irradiation

Multielemental standards were prepared by accurately weighing about 100 mg of NBS F1633A fly ash and C1632a coal into pre-cleaned polythene containers.

Samples and standards were irradiated, counted and processed as previously described<sup>7</sup>.

## RESULTS AND DISCUSSION

A total of 50 coloured and 18 colourless opals were analysed using NAA. The number of orange, yellow, green, blue and pink coloured opals were 14, 27, 3, 3 and 3, respectively. The results for the analysis of these samples are summarised in Tables 1 and 2.

### Orange, Yellow and Colourless Opals

The mean concentration of most elements found in orange opals were similar, in most cases, to those in yellow and colourless opals (Table 1). The range of concentration values for these same elements was also surprisingly similar considering their greatly differing source locations. The few exceptions included Sc, Ti, V, Fe, Co and Th. The results for Sc, V, Co and Th were within a factor of 10 for both mean and range values.

### Green, Blue and Pink Opals

The trace element profile of the green, pink and blue opals was found to be significantly different from that of the orange, yellow and colourless opals. Tables 2 shows that the concentration of some trace elements in opals of one particular colour were found to be higher than results for the same element in either of the other two colours.

Green opals are significantly higher in alkali metals (Na, K, Rb and Cs), Co and W than either blue or pink opals. The concentration of As in green opals, though similar to pink levels, is higher than in all other opals analysed. However, when compared with most other opals, green opals are almost completely deficient in all rare earth elements.

Blue opals have a noticeably higher concentration of Mg, Zn and U when compared with green and pink opals. In contrast, however, blue opals are significantly lower in Al than almost all other opals analysed. Only colourless hyalite from Mexico has a similar Al concentration. Apart from relatively small amounts of V, Mn, Co, Ba and some rare earths, all other trace elements were below detection limits.

Pink opals are significantly higher in Al, V and Mn than all other opals analysed. As previously mentioned, these opals also share high levels of As with green opals. Most of the remaining trace element results were similar to the other opals analysed.

In contrast to the results for orange, yellow and colourless opals, the trace element profile of green, blue and pink opals exhibits great variations in the concentration of a number of elements. Each of these opals is significantly higher in specific trace elements when compared with all other opals analysed.

### Comparison with other data

The analysis of coloured opals from Bulgaria<sup>4</sup> and Brazil<sup>5</sup> yielded data for 16 and 8 trace elements, respectively. However, only results for elements common to both studies and were compared. The majority of data for similarly coloured opals from Bulgaria agreed well with our results with the exception of V. This was significantly higher for most Bulgarian samples. For Brazilian opals, only the results for the blue samples were compared. Here, trace element concentrations were higher than our study except for Ba data.

## CONCLUSIONS

This investigation used neutron activation analysis to determine the trace element profile of 50 samples of orange, yellow, honey, green, blue and pink opals and 18 samples of colourless opals from a number of recognised fields in Australia, Peru, Mexico and USA. The mean concentration of most of the elements found in orange, yellow and colourless opals were similar with few exceptions. This indicated that, for these samples, colour is not related to the trace elements present.

However, the trace element profile of the green, pink and blue opals was found to be significantly different from that of the orange, yellow and colourless opals analysed. In these cases, each opal has a much higher concentration of certain trace elements when compared with all other opals analysed.

\*

The authors are grateful for the assistance of Y.J. FARRAR for extensive computerised data reduction.

#### REFERENCES

1. J.V. SANDERS, *Nature*, Dec, (1964) 1151.
2. P.J. DARRAGH, A.J. GASKIN, J.V. SANDERS, *Scientific American*, 234 (1976) 84.
3. R.K. ILLER, *The Chemistry of Silica*, Wiley-Interscience, New York, 1979, 398.
4. R.I. KOSTOV, I.M. POJAREVSKI, *Dokl. Bolg. Akad. Nauk.*, 41 (1988) 63.
5. F. BARTOLI, R.D. BITTENCOURT, M. DOIRISSE, R. MEYER, R. PHILIPP, J.C. SAMAMA, *Eur. J. Mineral.*, 2 (1990) 611.
6. J.I. KOIVULA, C.W. FRYER, *Gems Gemol*, Winter (1984) 226.
7. G.D. McORIST, A. SMALLWOOD, J.J. FARDY, *J. Radioanal. Nucl. Chem., Articles*, 185 (1994) 293.

# Proton Microprobe Study of Tin-Polymetallic Deposits

S. MURAO<sup>1</sup>, S.H. SIE<sup>2</sup> and G.F. SUTER<sup>2</sup>

<sup>1</sup>Geological Survey of Japan, 1-1-3 Higashi, Tsukuba, 305, Japan

<sup>2</sup>CSIRO Division of Exploration and Mining, P.O.Box 136, North Ryde, NSW  
2113, Australia

## SUMMARY

Tin-polymetallic vein type deposits are a complex mixture of cassiterite and sulfides and they are the main source of technologically important rare metals such as indium and bismuth. Constituent minerals are usually fine-grained having wide range of chemical composition and often the elements of interest occur as trace elements not amenable to electron microprobe analysis. PIXE with a proton microprobe can be an effective tool to study such deposits by delineating the distribution of trace elements among carrier minerals. Two representative indium-bearing deposits of tin-polymetallic type, Tosham of India (Cu-In-Bi-Sn-W-Ag), and Mount Pleasant of Canada (Zn-Cu-In-Bi-Sn-W), were studied to delineate the distribution of medical/high-tech rare metals and to examine the effectiveness of the proton probe analysis of such ore. One of the results of the study indicated that indium and bismuth are present in chalcopyrite in the deposits. In addition to these important rare metals, zinc, copper, arsenic, antimony, selenium, and tin are common in chalcopyrite and pyrite. Arsenopyrite contains nickel, copper, zinc, silver, tin, antimony and bismuth. In chalcopyrite and pyrite, zinc, arsenic, indium, bismuth and lead are richer in Mount Pleasant ore, but silver is higher at Tosham. Also thallium and gold were found only in Tosham pyrite. The Tosham deposit is related to S-type granite, while Mount Pleasant to A-type. It appears that petrographic character of the source magma is one of the factors to determine the trace element distribution in tin-polymetallic deposit.

## 1. INTRODUCTION

Tin-polymetallic deposits in which cassiterite (SnO<sub>2</sub>) and sulfides occur together in crustified veins or in massive ore bodies were once called xenothermal type due to their complex structure of ore bodies and ore textures. The ore usually exhibits telescoping or dumpling character where small mineral grains of various kinds coexist in a small region. In most of the cases worldwide, this type of deposit is found in a volcano-plutonic complex, especially between volcanic rocks and plutonic batholith. Such occurrence mode of the ore implies strong magmatic contribution to the mineralizing fluid. Thus it is an interesting research target to identify magmatic elements in a magma-hydrothermal system. From economic point of view, this type of deposit is important as carrier of medical/high-tech rare metals, especially of indium and bismuth (1).

In spite of such importance, there is paucity of published geochemical research of tin-polymetallic deposit because of the difficulty in detecting trace elements in each mineral grain with sufficient sensitivity. It is essential to determine the distribution of trace elements in each mineral grain to study tin-polymetallic ore. But, usually, trace elements are not amenable to electron microprobe analysis and the grain size is very small in this deposit type. PIXE with a proton microprobe could be an effective tool to solve this problem through the low detection limit and the ability to treat small area of the target. We have thus performed proton microprobe study on two representative deposits of tin-polymetallic character, Tosham of India, and Mount Pleasant of Canada, to elucidate the occurrence mode of medical/high-tech metals in the ore and to examine the effectiveness of proton probe analysis on this type of deposit.

## 2. DEPOSIT GEOLOGY AND MINERALOGY

The Tosham deposit is situated at 120 km WNW of Delhi, India. The mineralized area is composed of metasediments, granitoid and rhyolite of Precambrian age. The rhyolite occupies the central area with long axis of NNE-SSW direction, surrounded by the granite on the western and southwestern flanks, and by metasediments along the southern, eastern, northeastern, and northwestern margins. The granitoid is of S-type character, associated with aplite and pegmatite, and is cut by the rhyolite dyke. Mineralization is observed as stringers and dissemination along the granite-rhyolite and rhyolite-metasediment contacts, especially in the former. It is also observed as stringer or veinlet within granite and rhyolite bodies. The major ore minerals are chalcopyrite, pyrite and marcasite. The

chalcopyrite coexists with pyrrhotite, biotite, small amount of sphalerite and Cu-Zn-Fe-In-Sn-S minerals, while pyrite and marcasite are in contact with calcite. Under the ore microscope, chalcopyrite sometimes contains small inclusions of sphalerite but usually its surface seems to be homogenous.

The Mount Pleasant deposit is situated in Charlotte County, New Brunswick, Canada. The mineralized area is a part of the caldera structure, and is composed of feldspar porphyry, quartz-feldspar porphyry, sedimentary breccia and A-type granites (2). The ore deposits are porphyry-type tungsten-molybdenum deposits and vein-type or replacement bodies of tin-polymetallic character that are related to the A-type granites. The tungsten-molybdenum mineralization is earlier than tin-polymetallic mineralization. Major constituent minerals of the tin-polymetallic ore at Mount Pleasant are sphalerite, arsenopyrite, pyrite, chalcopyrite, stannite and cassiterite. They exhibit dumpling and no time relationship can be speculated among the minerals genesis. Usually chalcopyrite and sphalerite are closely associated with each other, contacting with mutual boundary. Chalcopyrite often includes sphalerite stars, and sphalerite has chalcopyrite microinclusions with diameter ranging from less than 1  $\mu\text{m}$  to a few tens  $\mu\text{m}$ . Stannite is a few tens  $\mu\text{m}$  in diameter and is found in sphalerite.

### 3. PROTON PROBE STUDY AND RESULT

We selected chalcopyrite, pyrite and arsenopyrite for the study because these minerals often contain trace elements. We did not analyse sphalerite and stannite because trace elements in these minerals are amenable to electron microprobe analysis (3). During the analysis, we carefully avoided the grains which contains microinclusions, e. g., sphalerite stars in chalcopyrite.

The measurements were carried out using the proton microprobe at CSIRO (4,5). Samples were analysed with microbeams of 3 MeV protons, focused to between 10 - 30  $\mu\text{m}$  spatial resolution. The X-rays were detected in an energy dispersive Si(Li) detector at 135° with respect to the beam direction through Al or Be filters. The filters were chosen to optimize the detection sensitivity for trace elements: 300  $\mu\text{m}$  Al for chalcopyrite and pyrite; 300 or 400  $\mu\text{m}$  Al for arsenopyrite.

Figure 1 shows a typical X-ray spectrum of a Bi-bearing arsenopyrite from Mount Pleasant deposit, and figure 2 shows a spectrum of Ag and Sn bearing pyrite from Tosham. The X-ray spectra were deconvoluted for peak areas and converted to concentration using the CSIRO Geo-PIXE software (6). Data were collected for a minimum of 3  $\mu\text{C}$  beam charge, giving detection limit (MDL) for most elements ( $Z>26$ ) at 3 - 50 ppm. The MDL values are defined at 99 % confidence limit.

The proton microprobe at CSIRO was effective for detecting trace elements in the specimens. Especially indium and silver peaks were easily identified in the spectrum of sulfides. In chalcopyrite zinc is high up to 8690 ppm for Tosham and 8280 ppm for Mount Pleasant. The mineral also contains arsenic, antimony, selenium, silver, tin, lead and bismuth. In pyrite nickel was found at Tosham up to 2.4% but was not detected at Mount Pleasant.

Thallium, rubidium and strontium were detected only in Tosham, while indium was noticed only in Mount Pleasant specimens. The other elements in pyrite are copper, zinc, arsenic, selenium, silver, tin, antimony, bismuth, and lead. Bismuth is included by pyrite up to 8360 ppm. Arsenopyrite of Mount Pleasant contains nickel, copper, zinc, silver, tin, antimony, bismuth, and molybdenum. The bismuth concentration is high, up to 1310 ppm.

### 4. DISCUSSION

The data presented above indicate that Tosham ore is enriched in silver, gold and thallium compared to Mount Pleasant, while that of Mount Pleasant is richer in zinc, copper, arsenic, indium, tin, lead and bismuth than Tosham: Mount Pleasant seems to be better rare metal deposit.

Trace element concentration in a deposit is controlled by various factors including source character, host lithology, alteration, water/rock ratio and mineral assemblage. The deposits in this study are both embedded by shallow acidic intrusions and host lithology of the mineralized areas are not complex: Tosham area is mostly covered by S-type igneous rocks, and Mount Pleasant district is occupied by A-type intrusions. In spite of the absence of geochemical data to base a discussion on trace element partitioning, it appears that source character of magma is one of the most important factors to determine the distribution of rare metals: A-type magma is suitable for indium and bismuth accumulation, while S-type is necessary to concentrate silver and possibly gold.

Usually trace elements are not amenable to electron microprobe in tin-polymetallic ore. But the present study demonstrates that the proton microprobe can solve this problem and thus it is an essential tool for the study of complex tin-polymetallic deposits.

### REFERENCES

- (1) Murao, S., Furuno, M., and Uchida, A. C (1991). *Mining Geol*, 41, 1 - 13.

- (2) Taylor, R. P., Sinclair, W. D., and Lutes, G. (1985) Geochemical and isotopic characterization of granites related to W - Sn - Mo mineralization in the Mount Pleasant area, New Brunswick, in *Granite - related Deposits: Geology, Petrogenesis and Tectonic Setting*, Extended Abstracts pp 265 - 273 (CIM: Halifax).
- (3) Murao, S. and Furuno, M. (1990), *Mining Geol.*, 40, 35 - 42.
- (4) Sie, S. H., Ryan, C. G., Cousens, D. R. and Griffin, W. L. (1989), *Nucl. Instr. Method*, B40/41, 690 - 697.
- (5) Sie, S. H., Ryan, C. G., and Suter, G. F. (1991), *Scanning Microscopy*, 5, 977 - 987.
- (6) Ryan, C. G., Cousens, D. R., Sie, S. H., Griffin, W. L., Suter, G. F. and Clayton, E. (1990) *Nucl. Instr. method*, B47, 55 - 71.

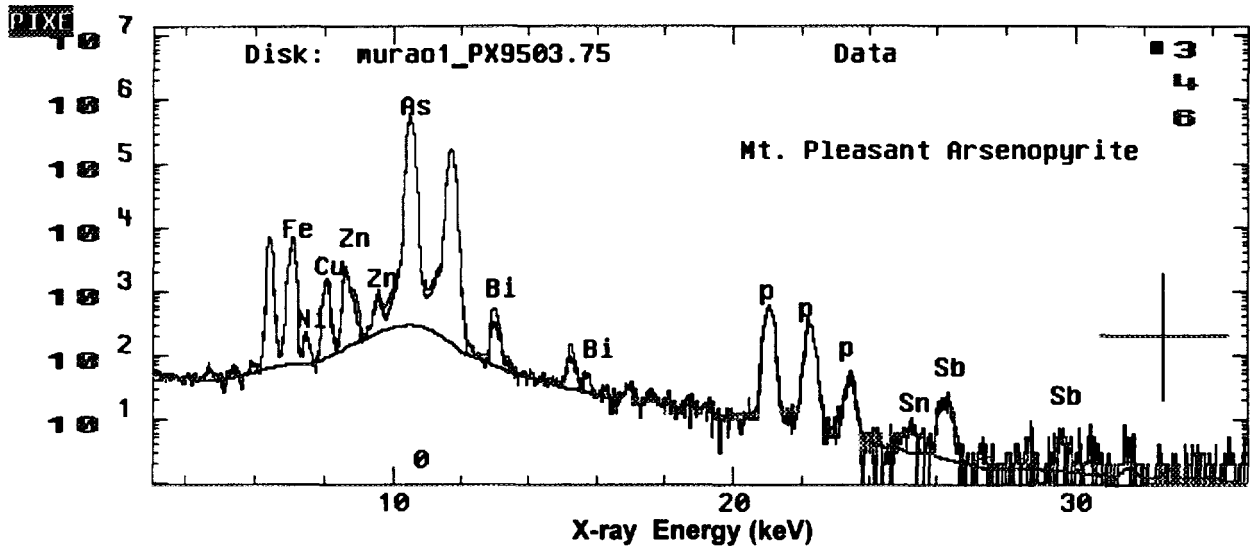


Fig.1. A typical X-ray spectrum including computer fit to the data of arsenopyrite from Mt. Pleasant deposit, showing the presence of Bi. Peaks labeled p are the pile-up peaks.

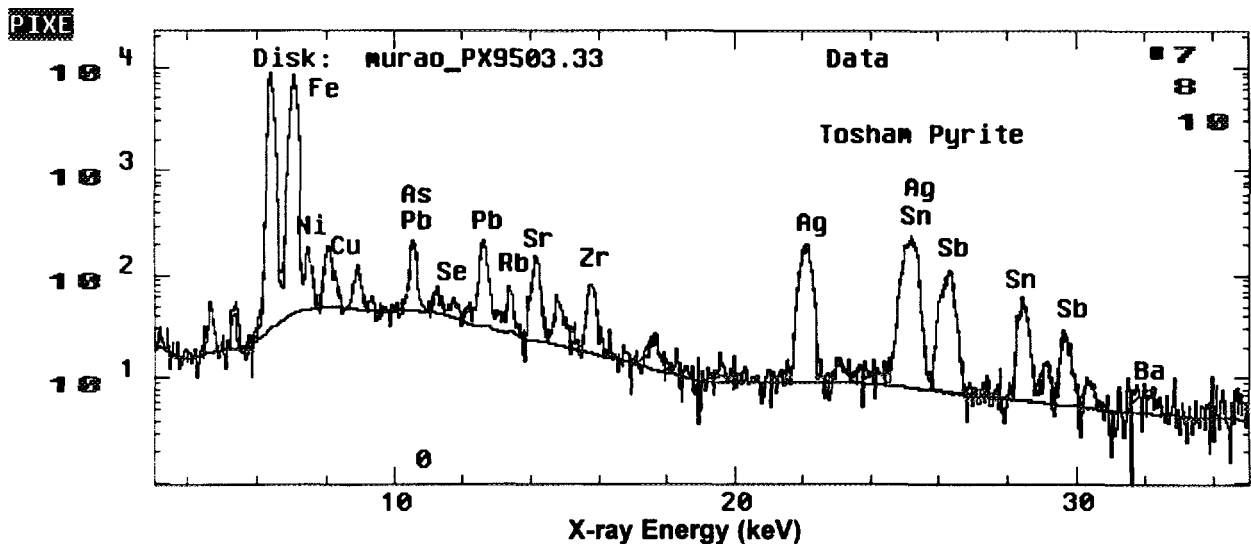


Fig.2. A typical spectrum of pyrite from the Tosham deposit showing the presence of Ag and Sn.



AU9716144

# **Ironstones of the Olary Block, South Australia: The use of RNAA and INAA to understand their genesis.**

**Ian R. Plimer (School of Earth Sciences, The University of Melbourne, Parkville, Victoria, 3052), Bernd G. Lottermoser, Paul M. Ashley and Dave C. Lawie (Department of Geology and Geophysics, The University of New England, NSW, 2351).**

## **INTRODUCTION**

### **Broken Hill Block**

The Early Proterozoic Willyama Supergroup in the Broken Hill Block is host to the huge Broken Hill Pb-Zn-Ag ore deposit and numerous occurrences of other types of mineralisation. The Broken Hill deposit formed during a period of crustal extension at 1700 Ma associated with rapid sedimentation, the influx of mantle-derived mafic melts and lower crustal melting. The circulation of seawater in the fractured rift sediments, volcanics and intrusives was driven by cooling of granite plutons and resulted in leaching of metals from crustal rocks, the leaching of continental evaporites, fluid reduction, fluid heating and focussed fluid exhalation. Sudden changes to fluid P-T-X resulted in rapid submarine sulphide precipitation in the deepest part of the rift {Parr and Plimer (1)}. Facies changes from sulphides in the deepest part of the rift to stratigraphically-equivalent exhalites reflects fluid mixing, oxidation and temperature changes. Such changes are reflected in the geochemistry of the proximal and distal exhalites {Lottermoser (2), (3)}.

### **Olary Block**

The adjacent Olary Block of South Australia contains Willyama Supergroup rocks stratigraphically equivalent to those in the Broken Hill Block. No massive sulphide deposits are known from the Olary Block despite the presence of numerous ironstones of submarine hydrothermal origin. This study reports RNAA and INAA analyses to document the geochemistry of ironstones as a mechanism of locating the locus of 1700 Ma plumbing conduits and the economic centres of mineralising systems.

## **GEOLOGY**

### **Metamorphism and deformation**

The Olary Block comprises upper greenschist to lower amphibolite low P-high T metamorphic facies Early Proterozoic metasediments and igneous rocks {Clarke et al. (4)} deposited at 1700 Ma {Cook et al. (5)}. Pre-regional metamorphic intrusions of leucocratic A-type granite at 1700 Ma formed andalusite-rich aureoles in metasediments. The Willyama Supergroup was intruded by I-type granodiorites at 1630 Ma, which may have initiated low P-high T metamorphism, and underwent coeval metamorphism and deformation (M1-D1 and M2-D2) at 1600 Ma (Olarian Orogeny). A number of S-type granitoids and associated rare metal-bearing pegmatites derived from the partial melting of composite

gneisses crystallised at 1590 Ma and a retrograde metamorphic event (D3) has been dated by Ar-Ar methods at 1530 Ma. Ar-Ar dates of 1100-1200 Ma (Grenvillian Orogeny) and 850 Ma (opening of Adelaide Geosyncline) are associated with brittle deformation. The Willyama Supergroup was unconformably overlain by the Adelaidean sequence of pelite, psammite, carbonate and diamictite and the Delamerian Orogeny (460-500 Ma) resulted in greenschist facies metamorphism, multiphase folding of the Adelaidean, faulting and shearing of the Willyama-Adelaidean unconformity and reactivation of retrograde shear zones.

### **Lithology**

Five major lithological units are recognised in the Willyama Supergroup. The total thickness of the Supergroup is unknown, basement is not exposed and unconformities have not been recognised.

The basal Composite Gneiss of psammopelitic composition grades via migmatite into banded, migmatitic and massive granitoids.

The Quartzofeldspathic Suite is dominated by quartzofeldspathic rocks, most of which comprise massive to laminated albite-quartz rocks. The Quartzofeldspathic Suite contains disseminated magnetite and a diversity of iron formations comprising quartz-magnetite +/- hematite, baryte, chalcopyrite. Iron formations are laminated, massive, brecciated and replaced. Some iron formations are enriched in Cu and Au.

The quartzofeldspathic rocks grade via calc-albitites into the Calc-silicate Suite. The calc-silicate rocks contain calc-silicate pseudomorphs after carbonate and gypsum and the presence of hypersaline fluid inclusions suggests evaporite mineral formation during deposition and early diagenesis. The influence of evaporite-derived brines and local hot spring exhalation have greatly modified the felsic metasediments.

The Bimba Suite is a thin heterogeneous discontinuous unit comprising calc-silicates, carbonates and psammopelitic and pelitic schist. Sulphides are ubiquitous as are surficial gossans and lags enriched in Cu, Pb, Zn, Co, As, Ag, Au, Mn, Ba, W, Mo, Bi and U {Lawie and Ashley (6)} The Bimba Suite formed in a shallow water lacustrine/sabkha/marine environment into which were episodic hot spring exhalations.

The Pelite Suite is widely distributed and comprises pelitic and psammopelitic schist, a distinct graphitic facies, calc-silicate ellipsoids and rare tourmalinite, FeMn garnet-quartz rocks and laminated manganiferous banded iron formation. The presence of common graded bedding, sediment composition, lamination and the thickness of the unit suggest deposition of a turbiditic sequence in a deepening marine or lacustrine environment.

### **Mineralisation styles**

In contrast to the Broken Hill Block, mineral occurrences in the Olary Block are dominated by Cu and U with the only significant deposit being the Radium Hill U(-REE) mine exploited from 1954-1961. Minor feldspar has been produced from pegmatite and baryte production from iron formations.

Ashley et al. (7) have recognised stratiform iron formations (with minor to trace Cu and Au) in the Quartzofeldspathic Suite, FeCuZnPbCoAs minerals in the Bimba Suite, and small banded iron formations and Mn silicates in the Calc-silicate and Pelite Suites. Stratabound Fe, Cu, Zn, Co, W, U and F occurrences are common in the Quartzofeldspathic, Calc-silicate and Bimba Suites. U, Th and REE veins, breccias and stockworks derive from 1590 Ma granites as do pegmatite-hosted feldspar, beryl, U, Th, REE, Nb, phosphates and muscovite. Structurally- and lithologically-controlled epigenetic veins and replacements occur in iron formations, calc-silicate rocks and albitites (Fe) and associated with D3 retrogression and Delamerian events (FeCuAu, FeZnCuPb, U-REE, CuAu, Au). Regolith-

related gossans, supergene-enriched Cu(CoAu) deposits and surficial ironstones formed during Tertiary to Recent weathering.

## **IRONSTONE GEOCHEMISTRY**

RNAA, INAA and electron microprobe analyses of ironstones and baryte from ironstones indicates a composition unlike metamorphic, vein-type, intrusive-hydrothermal, sedimentary and karstic barytes. In contrast, the iron formations and baryte from the Olary Block are geochemically similar to modern and ancient submarine hydrothermal precipitates. Geochemical analyses of iron formations and baryte generally show low Mn, Pb, Zn, As and Sb concentrations and elevated Au and Cu values. Major (Al, Si) and trace (REE, Th, U, PGEs) element data show that the ironstones and baryte rocks are of hydrothermal origin and that mixing occurred between oxidised (and possibly hypersaline) surficial waters and a hydrothermal fluid similar to that from modern sites of submarine exhalation. Such geochemical similarities imply rapid burial in the volcano-sedimentary pile or sub-seafloor replacement. The REE patterns in the iron formations demonstrate a range from low temperature reduced hydrothermal precipitates, seawater and oxidised hydrothermal precipitates. Geochemical signatures are due to precipitation from hydrothermal fluids of lower temperature with further influence by prolonged exposure to the overlying water column and subaqueous oxidation.

## **CONCLUSIONS**

RNAA and INAA analyses can be used to;

1. Delineate the focus of an ore-forming plumbing system, and
2. Assess whether a mineralising system is likely to contain economic metals.

## **REFERENCES**

1. Parr, J. and Plimer, I. R., (1995): Models for Broken Hill-type lead-zinc-silver deposits. In: Mineral deposit modelling; eds. Kirkham, R. V., Sinclair, W. D., Thorpe, R. I. and Duke, J. M.; Geol. Assoc. Canada Special Paper 40, 253-288.
2. Lottermoser, B. G. (1989): Rare earth element study of exhalites within the Willyama Supergroup, Broken Hill Block, Australia. *Mineralium Deposita* 24, 92-99.
3. Lottermoser, B. G. (1991): Trace element composition of exhalites associated with the Broken Hill sulfide deposit, Australia. *Economic Geology* 86, 870-877.
4. Clarke, G. W., Burg, J. P. and Wilson, C. J. L. (1986): Stratigraphic and structural constraints of the Proterozoic tectonic history of the Olary Block, South Australia. *Precambrian Research* 34, 107-137.
5. Cook, N. D. J., Fanning, C. M. and Ashley, P. M. (1994): New geochronological results from the Willyama Supergroup, Olary Block, South Australia. In: Australian Research on Ore Genesis Symposium, Adelaide. Australian Mineral Foundation.
6. Lawie, D. C. and Ashley, P. M. (1994): Reconnaissance geochemical sampling of ferruginous regolith in the Olary Block, South Australia. In: Australian Research in Ore Genesis Symposium, Adelaide. Australian Mineral Foundation.
7. Ashley, P. M., Cook, N. D. J., Lottermoser, B. G. and Plimer, I. R. (1994): Notes on geology and field guide book to excursion stops in the Olary Block, Geological Survey of South Australia Report Book 94/8, 37pp.



# **The Platinum Group Elements and Gold: Analysis by Radiochemical and Instrumental Neutron Activation Analysis and Relevance to Geological Exploration and Related Problems**

**Shane J. Reeves and Ian R. Plimer**

**University of Melbourne, School of Earth Sciences, Parkville, Melbourne, Australia, 3052**

## **INTRODUCTION**

This paper presents an overview of research conducted with the support of the Australian Institute of Nuclear Science and Engineering, at the University of Melbourne, School of Earth Sciences, Radiochemical Neutron Activation Laboratory. The primary objective of this research is to realise the high potential of the platinum group elements (PGE) and gold to the solution of petrogenetic problems, the study of magma generation and magmatic processes in mafic/ultramafic rock suites, as tracers in hydrothermal ore formation, the documentation of these elements in a broad range of geological settings and non-geological environments, their application in exploration and so on.

The PGEs (Os, Ru, Ir, Pt, Pd and Rh) are among the least abundant of all elements on earth with unique properties such as high melting points, high electrical and thermal conductivity, high density, strength and toughness as alloys. They exhibit both siderophile and chalcophile characteristics and are valuable tools in providing information about magmatic processes, in particular S-saturation, as well as crystal fractionation trends. Barnes et al. (1) showed that the PGEs, when chondrite normalized, are fractionated in order of decreasing melting point, which decreases in the order Os, Ir, Ru, Rh, Pt, Pd and Au. Two distinct groups of PGEs are discerned; the IPGEs (Ru, Os, Ir) and the PPGEs (Pt, Pd, Rh, Au) on the basis of their behaviour during fractionation processes. Using chondrite normalized PGE patterns it is possible to distinguish between sulphides that segregated from primitive magmas, such as komatiites, and sulphides which segregated from more fractionated magmas, such as tholeiites {Barnes et al. (2)}. It is critical to the understanding of these processes to be able to analyse key elements, such as the PGE and gold, in the parts per billion to parts per trillion range. Neutron Activation Analysis affords us this ability.

## **ANALYTICAL METHODS FOR PGES AND AU**

Platinum group elements and Au were determined by radiochemical neutron activation analysis using a modified NiS fire-assay preconcentration technique, adapted from procedures first used by Robert & van Wyk (3). Detection limits are generally 0.005-0.01 ppb (Au & Ir), 0.1-0.2 ppb (Pd & Pt), and 0.1-0.5 ppb for Ru.

## **BRIEF OUTLINE OF SIGNIFICANT PROJECTS AND RESULTS**

### **The PGE geochemistry of the Bucknalla Layered Complex, Central Queensland.**

The Bucknalla Complex is a small (10 km<sup>2</sup>) layered, tholeiitic, mafic-ultramafic intrusion located 50 km southwest of Rockhampton that was emplaced into a regional continental margin accretionary environment in the Late Permian and hosts minor Cu-Pd-Au-Pt mineralization. Background PPGE (Pd & Pt), Au, S and Cu values for the intrusion are high while IPGE (Ir & Ru) are low. A total of 116 analyses gave the range; Pd, 0.3-254 ppb; Pt, 0.3-137 ppb; Au, 0.1-74 ppb; Ir, <0.01-0.51 ppb; Ru, 0.1-2.4 ppb; S, 23-1000 ppm and Cu, 4-1000 ppm. A significant feature of the data is the systematic decoupling of Pd from Pt-Au-S-Se-Cu throughout the analysed stratigraphy, as in the Munni Munni and Great Dyke intrusions {Barnes (4)}. Major Cu-S-Se peaks generally occur just below whole rock Mg# ( $Mg^{2+}/Mg^{2+} + Fe^{2+}$ ) maxima and the precious metal tenor of the sulphides is generally highest between regions of Mg# maxima {Reeves and Keays (5)}.

### **Investigations of the platinum group elements, gold, silver and other metals in Melbourne sewerage sludges.**

Sewerage sludges from sewerage treatment plants have the ability to concentrate heavy metals, organic pollutants, gold and precious metals {Lottermoser and Morteani (6)}. This concentration likely occurs due to microbiological activity, reactions with organic matter, decreases in the ligand concentration and adsorption onto sulphides and organic material. The economic potential of this resource is yet to be exploited. The extraction of these metals could also result in reduced pollutant loads facilitating the use of sludges as fertilizer. This work documents the distribution of gold, silver and other metals throughout time in the Werribee Sewerage Sludges of Melbourne, which are more than 90 years old and provide a fascinating new insight into the history of Melbourne.

### **Experimentally Determined Sulphide/Silicate Melt Partition Coefficients for Ir and Pd.**

It is generally assumed that sulfide exerts a primary control on PGE geochemistry in mafic and ultramafic rocks. Observations of PGE abundance and distribution in these systems, however, do not reveal behaviour consistent with a single set of partition coefficients (Ds) for the metals between immiscible sulfide and silicate liquids. Also, the two distinct subgroups of the PGE, the IPGE (Ir, Ru and Os) and the PPGE (Pt and Pd) are clearly capable of fractionating from each other. This work was initiated in order to test whether Ds are constant over the compositional range in which the sulfides and silicates coexist.  $D_{Pd}$  was determined to fall within the range  $1.2 \times 10^4$  to  $7.8 \times 10^4$  {Peach et al. (7)}. However,  $D_{Ir}$  ranges from  $2.5 \times 10^4$  to  $152 \times 10^4$ . A striking aspect of this latter data is that they fall into two groups. Experiments in which the starting material was of synthetic silicate composition yielded highly variable results while those in which natural MORB glasses were used yielded consistent results. In all other respects the experiments were identical. This intriguing result may be due to the presence, in the natural MORB glasses, of some minor or trace component which complexes with Ir in such a way as to enhance its solubility in silicate relative to sulfide. The best value for  $D_{Ir}$  is  $3.5 \times 10^4$  and for  $D_{Pd}$   $3.4 \times 10^4$ .

### **Provenance Studies of Archaeological Artifacts Using PGEs and Au.**

The copper metal used to produce Bronze Age artifacts was often derived from the smelting of the copper minerals malachite, azurite and chalcopyrite. It is theoretically possible, therefore, to determine the provenance of the ore used to produce a particular artifact by the systematic study of the elemental and isotopic composition of the artifact. These provenance studies of Archaeological artifacts have historically suffered due to the inability to non-destructively analyse

for key elements in the parts per trillion to parts per billion range {Gale and Stos-Gale, (8)}. As the corrosion rind of these artifacts is of little value and easily accessible, it was hoped that the heavy, noble and precious metal and rare earth elemental distribution patterns and isotopic composition of these rinds could be used to study the artifacts rather than destructively analysing the piece itself. We, here, present preliminary data on this project.

#### **Spherules in Archaean Greenstone Terrane, W.A.; evidence of a meteoritic rain .**

In this project we have documented the distribution of the PGEs and Au above, below and within the spherule beds of the Archaean Wittenoom Formation, Western Australia, which have been suggested to represent droplets of silicate melt (microtektites) generated and dispersed by a major bolide impact. As with similar work we conducted on the Lake Acraman Ejecta Horizon in the Flinders Ranges {Wallace et al. (9)}, iridium clearly defines an anomaly consistent with the involvement of meteoritic material.

#### **ACKNOWLEDGEMENTS**

This work was funded by Australian Institute of Nuclear Science and Engineering grants to IRP (1993, 1994 and 1995). Significant sections of this work were contributed to by Malcolm Wallace, Wilhelm Snoek and Bernd Lottermoser (University of Melbourne), Cheryl Peach and Ed Mathez (American Museum of Natural History), David Lambert and Louise Frick (Monash University) and Reid Keays (Laurentian University).

#### **REFERENCES**

1. Barnes, S. J., Naldrett, A. J., and Gorton, M. P. (1985). The origin of the fractionation of platinum-group elements in terrestrial magmas. *Chemical Geology*, v. 53, pp. 303-323.
2. Barnes, S.- J., Boyd, R., Korneliussen, A., Nilsson, L.-P., Often, M., Pedersen, R. B., and Robins, B. (1988). The use of mantle normalisation and metal ratios in discriminating between the effects of partial melting, crystal fractionation and sulphide segregation on platinum-group elements, gold, nickel and copper: Examples from Norway. In *Geo-Platinum 87'*. Prichard, H. M., Potts, P. J., Bowles, J. F. W., and Cribb, S. J., (eds.). Elsevier, London, pp. 113-143.
3. Robert, R. V. D. & van Wyk, E (1975). The effects of various matrix elements on the efficiency of the fire assay procedure using NiS as the collector. Johannesburg National Institute of Metallurgy Report 1705.
4. Barnes, S. J. (1993). Partitioning of platinum-group elements and gold between silicate and sulphide magmas in the Munni Munni Complex, Western Australia. *Geochimica et Cosmochimica Acta*, 57, 1277-1290.
5. Reeves, S. J., and Keays, R. R. (1995). The platinum-group element geochemistry of the Bucknalla Layered Complex, central Queensland. *Australian Journal of Earth Sciences*, 42, 187-201.
6. Lottermoser, B. G., and Morteani, G. (1993). Sewage sludges: toxic substances, fertilisers or secondary metal resources. *Episodes*, vol. 16, nos. 1 & 2, 329-333.
7. Peach, C. L., Mathez, E. A., Keays, R. R., and Reeves, S. J. (1994). Experimentally determined sulfide melt-silicate melt partition coefficients for iridium and palladium. *Chemical Geology* 117, 361-377.
8. Gale, N. H., and Stos-Gale, Z. A. (1992). Lead isotope studies in the Aegean (The British Academy Project). *Proceedings of the British Academy*, 77, 63-108.
9. Wallace, M. W., Gostin, V. A., and Keays, R. R. (1990). Acraman impact ejecta and host shales: Evidence for low-temperature mobilization of iridium and other platinoids: *Geology*, v. 18, p. 132-135.



# Design of a Single Ion Facility and its Applications

M. Cholewa, A. Saint, G. J. F. Legge  
School of Physics, MARC, The University of Melbourne,  
Parkville, Vic 3052, Australia

In Recent years a number of groups in Europe, U.S.A. and Japan have started to develop, or to plan, installations for microbeam irradiation of cells to enable them to study certain radiobiological processes in ways that are inaccessible with conventional broadfield exposures. The field is at a point where MARC with its wide experience in low current and high resolution microbeams can make a valuable contribution. While most systems actually in operation are using collimated beams with resolution of a few microns, we are proposing construction of a facility with submicron (down to 300nm) resolution.

The stimulus for the current development of microbeams for radiobiology comes from two main areas of interest. The first is that while it has long been established that the nucleus of the cell is the most sensitive region for the majority of radiation effects, a number of studies, some very recent, indicate that with very short-range radiations the nucleus is not uniformly sensitive. Consequently, the cell does not respond in simple accordance with the total energy deposited in its nucleus. These effects, as well as being of mechanistic interest, are of practical concern for targeted radiotherapy employing short-range emitters and for boron neutron capture therapy (BNCT). They are also important in relation to risk assessment of environmental and occupational exposures to radiations involving short-range particles, such as with radon and its daughters and with neutrons.

The second area of interest also relates to radiation risk assessment. At low doses generally applying in radiological protection, individual cells only rarely experience traversals by an ionizing particle, the time intervals between the tracks typically ranging from weeks to many years, depending on the dose rate and the type of radiation. The biological effects of exactly one particle per cell are largely unknown because they cannot be simulated in the laboratory using conventional broad-field exposures due to the random distribution of tracks. Microbeam techniques can overcome this limitation by delivering exactly one (or more) counted particle per cell nucleus. It then becomes possible to set up *in vitro* models which relate much more closely to the protection level exposures that occur *in vivo*.

The use of micro-irradiation techniques in radiobiology is not new; however, the current techniques take advantage of recent developments in particle delivery, focussing detection, image processing, cell recognition and computer control. These developments have generally come from other fields, for example microbeam elemental analysis techniques and single-event upset testing of semiconductor devices. Also in radiation biology there have been important advances in developments of individual cell assays, which allow a wide range of endpoints to be studied with good accuracy at low doses. Many of the studies that are planned involve following the responses of individual cells after a programmed exposure to charged-particle traversals. This program we are planning to develop in collaboration with the Peter McCallum Cancer Institute and the Genetics Department at the University of Melbourne. Several groups from overseas already expressed interest in participating in this program.

To probe the radiation sensitivity of a single cell and/or its constituents with a submicron resolution several developments are needed. Figure 1 shows a schematic diagram of a system proposed by MARC. Essential details of the system are being discussed with local and overseas partners and the final shape of the system will depend strongly on the generosity of Australian government and other funding agencies.

The essential parameters of the system can be summarised as follows:

1. A focussed beam of ions of 300nm or less at the cell.
2. A reliable (close to 100%) single ion detection.
3. A fast beam switch to prevent second hits.

4. A target holder adapted for the irradiation of wet cells.

5 A fully automated system for cell recognition and single hits.

Each of these factors is an interesting challenge by its own and the combination of all of them in a single project makes the task even more exciting

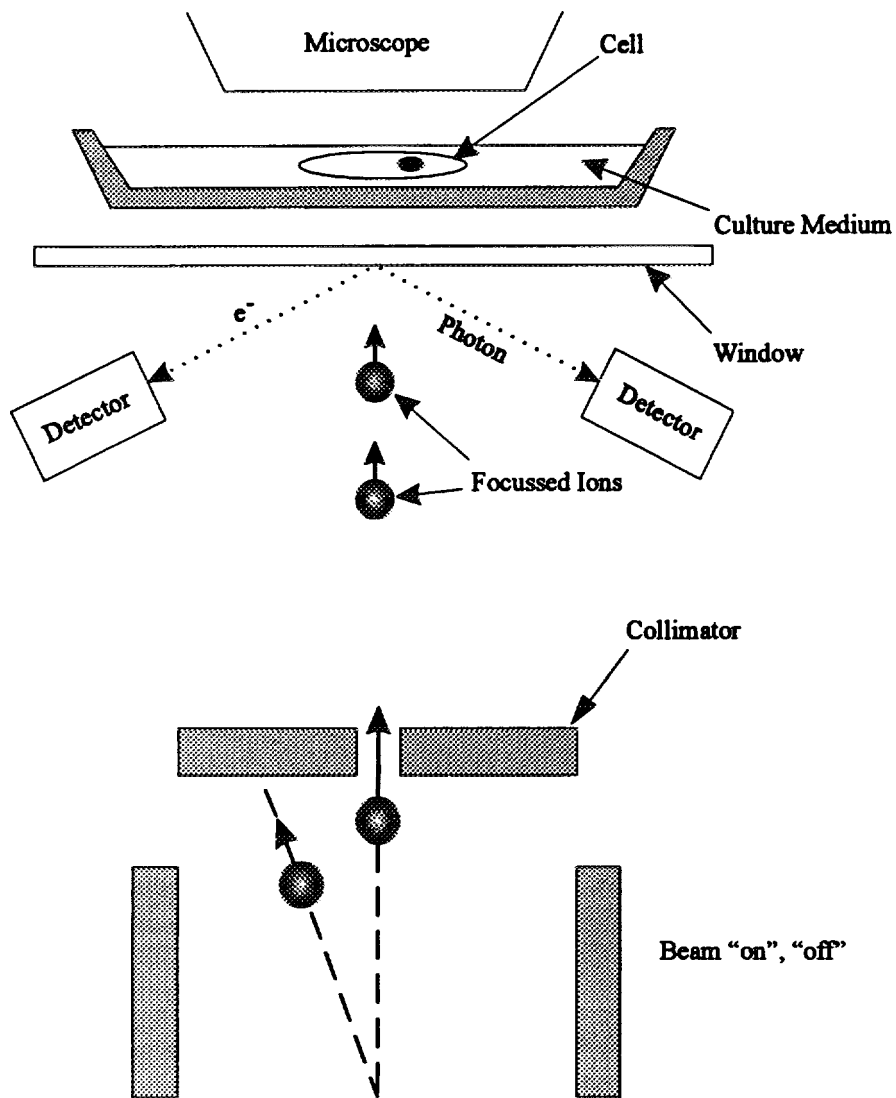


Figure 1 Schematic view of a single ion irradiation facility proposed for MARC



# Diamond Exploration and Mantle Structure Imaging using PIXE Microanalysis

C.G. RYAN, W.L. GRIFFIN and T.T. WIN

CSIRO Exploration and Mining, PO Box 136, North Ryde NSW 2113, Australia.

Geochemical methods of diamond exploration rely on recognizing indicator minerals that formed in the earth's upper mantle, within the diamond stability field, and were entrained in rapidly rising volatile-rich magmas and emplaced in or on the crust. Diamond is only stable at high pressure. Therefore, diamond exploration commonly targets prospects containing high pressure minerals, such as low-Ca, high-Cr ("G10") garnets and high-Cr chromites, similar to inclusions in diamonds. However, this procedure can be ambiguous; some barren pipes contain abundant "G10" garnets, while such garnets are extremely rare in the Argyle pipe, the world's largest diamond producer. Similarly, high-Cr chromites are shed by a wide variety of barren rock types.

PIXE microanalysis of trace elements in indicator minerals helps to remove the ambiguities by pinning down the source temperature (T), pressure (P) and local (paleo)geotherm (P-T relation), which permits the rich store of trace element information in these minerals, reflecting rock chemistry and metasomatic processes, to be placed in a stratigraphic context.

## PIXE MICROANALYSIS METHOD

Trace element analyses are obtained using PIXE and the CSIRO proton microprobe (typical beam spot size ~20-30  $\mu\text{m}$ , current 15-25 nA and live charge 3  $\mu\text{C}$ ); major element compositions are obtained by EMP analysis. X-rays are detected using a 30 mm<sup>2</sup> Si(Li) detector, and typically, a 200  $\mu\text{m}$  Al absorber is used to attenuate major element X-rays. Data are reduced using the GeoPIXE standardless quantitative method of Ryan *et al.* [1], which includes secondary-fluorescence contributions and can treat layered structures [2]. Comparisons with established geostandards samples have demonstrated that the method is accurate to better than 5% for major and 10% for trace elements. Minimum detection limits typically range down to ~2 ppm for a 4 minute analysis.

## TRACE ELEMENT THERMOMETERS

The partitioning of Ni between Cr-pyrope garnet and olivine was found by Griffin *et al.* [3] to be strongly temperature dependent, but insensitive to garnet composition ( $X_{\text{gnt}}$ ) and pressure (P). Moreover, the Ni content of mantle olivine is essentially constant (2900±360 ppm). This allows the construction of a single-mineral geothermometer ( $T_{\text{Ni}}$ ), based on Ni in Cr-pyrope garnets, and the assumption of coexisting olivine of uniform Ni content [3,4]. A similar effect enables Zn in chromites to be used to estimate temperature ( $T_{\text{zn}}$ ) [5,4].

## A GARNET ESTIMATE OF PRESSURE

The geobarometer of Nickel [6] is based on the P dependence of Cr solubility in coexisting garnet and orthopyroxene (opx). Ryan *et al.* [4] used this barometer and  $X_{\text{opx}}$ , constrained from experimental work and empirical relations for  $\text{Cr}_{\text{opx}}$  deduced from garnet+chromite-bearing xenoliths (chromite buffers Cr), to yield an iterative scheme for the estimation of pressure ( $P_{\text{Cr}}$ ) from garnet composition with the assumption of coexisting chromite [4].

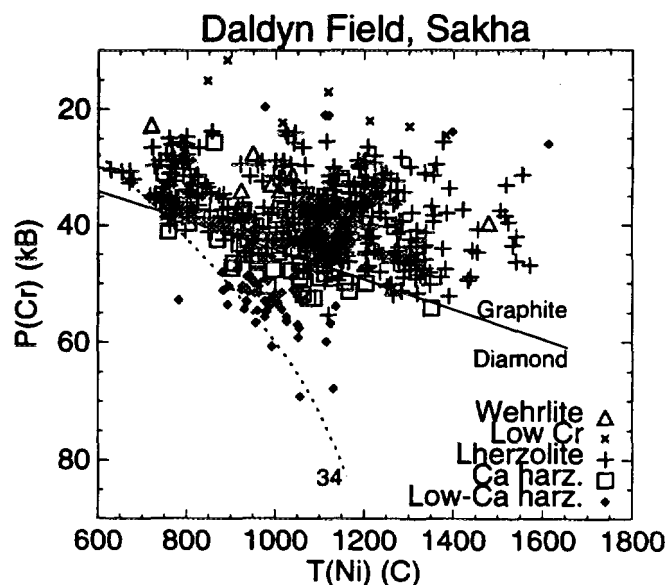


Fig. 1  $P_{\text{Cr}}, T_{\text{Ni}}$  diagram for garnets from the Daldyn kimberlite field, Siberia. Curves indicate the diamond-graphite phase boundary (solid line; [7]) and conductive geotherms (dotted curve, labelled in surface heat-flow units of  $\text{mW}/\text{m}^2$ ; [8]). The locus of maximum  $P_{\text{Cr}}$  at a given  $T_{\text{Ni}}$  defines the Garnet Geotherm, consistent with a 34  $\text{mW}/\text{m}^2$  conductive model. Symbols show approximate rock type inferred from Ca,Cr.

## THE GARNET GEOTHERM

Assuming Cr-saturation, and garnets sampled along the conduit of an erupting magma,  $P_{Cr}, T_{Ni}$  determined for a garnet suite maps out the local geotherm at the time of eruption. If only a subset of the garnets originated from Cr-saturated rocks, the geotherm will be defined by the locus of maximum  $P_{Cr}$  at each  $T_{Ni}$  (e.g. Fig. 1); we refer to this locus as the *Garnet Geotherm*. At the base of the lithosphere, strong interaction with asthenospheric melts produces a rapid rise in temperature relative to pressure. This effect is seen in xenolith geotherms; the same  $dP/dT$  slope is assumed to extrapolate the Garnet Geotherm.

## BASE OF LITHOSPHERE

Garnet chemistry reflects exposure of the upper mantle to metasomatism by infiltrating melts and fluids. The signature of asthenospheric melts is increased Ti, Ga, Y and Zr, as observed in overgrowth rims on garnets from high temperature sheared lherzolite xenoliths [9]. Pervasive infiltration of melts is evident in Tanzanian garnets (Fig. 2). The initial depleted rocks, indicated by low garnet Y ( $Y < 10$  ppm), show a high temperature cut-off which marks the effective base of the lithosphere; above this temperature most rocks acquire an asthenospheric composition.

## DIAMOND EXPLORATION

The geotherm determines the range of temperatures that fall within the diamond stability field. This defines a "Diamond Window", ranging from the diamond-graphite transition temperature down to temperatures at the base of the lithosphere [10]; garnets recording these temperatures may have coexisted with diamond.

Fig. 3 shows  $T_{Ni}$  histograms from three South African kimberlites, together with the Garnet Geotherms estimated for Group I and II kimberlites in the Kaapvaal craton. Garnet concentrates from high diamond-grade pipes show histograms of  $T_{Ni}$  with large proportions within the Diamond Window, indicative of strong sampling of mantle within the diamond stability field (Fig. 3b). Low grade pipes show poor sampling within the Diamond Window, and abundant melt-affected high-T garnets (Fig. 3c). The Zero pipe (Fig. 3d) is barren because its geotherm does not cross into the diamond stability field (see Fig. 3a).

The diamond grade of kimberlites is inversely correlated with the median Zr content of concentrate garnets within the Diamond Window. Evidently, the metasomatic processes which introduce Zr are detrimental to diamond survival. Combining this observation with the  $T_{Ni}$  Diamond Window proportion and the Ca-Cr score of Gurney *et al.* [11], yields an empirical estimator  $\Gamma$  that correlates well with the diamond grade of a pipe.  $\Gamma$  provides a ready means of recognizing low grade and barren prospects. Early rejection of barren pipes focuses exploration on better prospects and obviates the need for costly bulk

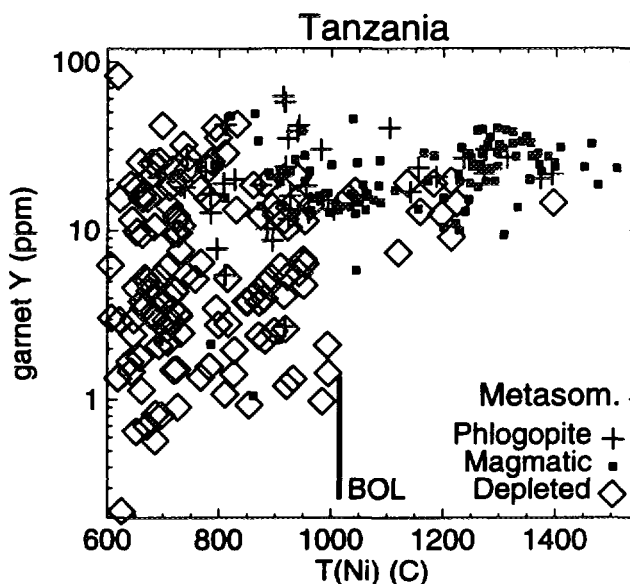


Fig. 2 Y plotted against  $T_{Ni}$ , for garnets from Tanzanian kimberlites. The symbols show asthenospheric-melt-effected garnets ("Magmatic";  $TiO_2 > 0.3$  wt%) and phlogopite-metasomatized garnets ("Phlogopite";  $Zr > 40$  ppm at low Ti) overprinting depleted rocks ("Depleted").

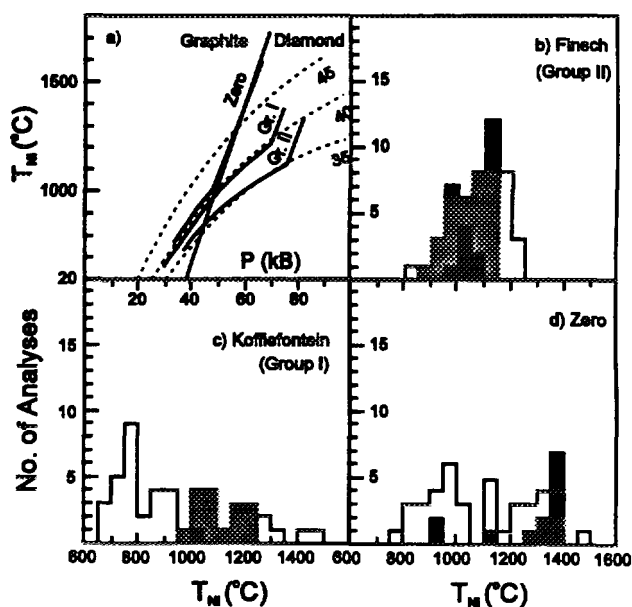


Fig. 3 a) Garnet Geotherms determined for the Zero pipe and Group I and II kimberlites on the Kaapvaal craton, South Africa (solid curves). The geotherms follow a conductive behaviour to the base of the lithosphere (1000, 1100 and 1150 °C, respectively). b-d)  $T_{Ni}$  histograms for garnet concentrate from the Finsch (b), Koffiefontein (c) and Zero (d) kimberlite pipes. Shaded area: the Diamond Window. Black area shows "G10" garnets.

testing. Prospects showing  $\Gamma$  greater than 50 are very prospective and deserve further sampling and analysis.

## MAPPING LITHOSPHERE STRATIGRAPHY

The pressure of any Cr-pyrope garnet in a suite can be found by projecting  $T_{Ni}$  onto the Garnet Geotherm. Pressure can then be related to depth to provide a depth ordinate for each garnet, a scale on which to map lithosphere stratigraphy using the composition of each garnet as a probe. The results for garnets from Group II kimberlites in the Kaapvaal craton are given in Fig. 4. They reveal a cool Garnet Geotherm (34 mW/m<sup>2</sup>; similar to Fig. 1) and a thick lithosphere extending to ~200 km (Fig. 4); depleted harzburgitic rocks (solid diamond symbols, and generally low Y and Ga) are abundant over a wide depth range. In contrast, the generally younger Group I kimberlites (not shown) show a higher geotherm, a thinner lithosphere (~170 km) and a lower proportion of depleted rocks. These data illustrate the evolution of the lithosphere beneath the Kaapvaal craton over the interval ~150-70 Ma, with progressive infiltration of asthenospheric melts and metasomatism of the lithosphere, and an accompanying rise in the mantle geotherm.

## CONCLUSIONS

The quantitative trace element analysis capabilities of microPIXE, applied to concentrate garnets and chromites from kimberlites and other volcanic rocks, provide unique tools for diamond exploration, and are in routine use at the CSIRO. Combined with the development of single mineral thermometers and barometers, these data provide a unique window on the structure, lithology and metasomatic processes in the lithosphere. Applied to the analysis of garnets from spatially distributed kimberlites, these techniques provide a method of building 3D maps of the lithosphere. With the added knowledge of the age of each intrusion, they permit the construction of 4D maps of the lithosphere in specific regions, charting the evolution of compositional and thermal variations in both space and time.

## References

- [ 1 ] C.G. Ryan, D.R. Cousens, S.H. Sie, W.L. Griffin, G.F. Suter and E. Clayton, *Nucl. Instr. and Meth. B* 47 (1990) 55-71.
- [ 2 ] D.R. Cousens, C.G. Ryan, S.H. Sie, and W.L. Griffin, *Proceedings of 5th Australian Conf. on Nuclear Techniques of Analysis*, Lucas Heights, ISSN 0811-9422 (1987) 58-60.
- [ 3 ] W.L. Griffin, D.R. Cousens, C.G. Ryan, S.H. Sie and G.F. Suter, *Contrib. Mineral. Petrol.* 103 (1989) 199-202.
- [ 4 ] C.G. Ryan, W.L. Griffin and N.J. Pearson, "Garnet Geotherms: Derivation of P-T data from Cr-pyrope garnets", submitted to *J. Geophys. Research*.
- [ 5 ] W.L. Griffin, C.G. Ryan, J.J. Gurney, N.V. Sobolev and T.T. Win, in *Diamond: Characterization, Genesis and Exploration*, eds. H.O.A. Meyer and O.H. Leonardos, *CPRM Spec. Pub.* 1B/93 (1994) 366-377.
- [ 6 ] K.G. Nickel, *Geol. Soc. Australia Spec. Pub.* 14 (1989) 901-912.
- [ 7 ] C.S. Kennedy and G.C. Kennedy, *J. Geophys. Res.* 81 (1976) 2467-2470.
- [ 8 ] H.N. Pollack and D.S. Chapman, *Tectonophysics* 38 (1977) 279-296.
- [ 9 ] D. Smith, W.L. Griffin, C.G. Ryan, D.R. Cousens, S.H. Sie and G.F. Suter, *Contrib. Mineral. Petrol.* 107 (1991) 60-79.
- [ 10 ] W.L. Griffin and C.G. Ryan, "Trace Elements and Indicator Minerals: Area Selection and Target Evaluation in Diamond Exploration", in *Diamond Exploration: Into the 21st Century*, ed. W.L. Griffin, *J. Geochem. Explor. Spec. Vol.* 53 (1995) 311-337.
- [ 11 ] J.J. Gurney and P. Zweistra, in *Diamond Exploration: Into the 21st Century*, ed. W.L. Griffin, *J. Geochem. Explor. Spec. Vol.* 53 (1995) 293-310.

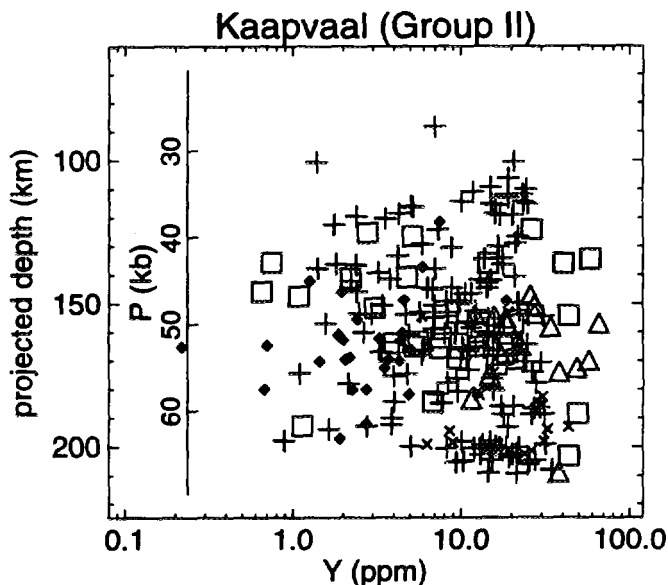


Fig. 4 Stratigraphic section through the Kaapvaal craton showing Y concentration, using the projected depth of garnets and the inferred base of the lithosphere. Symbols show rock type as in Fig. 1. The lithosphere extends to ~200 km.



# Nuclear Techniques of Analysis in Diamond Synthesis and Annealing

DAVID N. JAMIESON, STEVEN PRAWER, PATRICE GONON, RUSSELL WALKER, SEAN DOOLEY, ANDREW BETTIOL AND JON PEARCE

School of Physics, MARC, University of Melbourne, Parkville, 3052, AUSTRALIA

## INTRODUCTION

Nuclear techniques of analysis have played an important role in the study of synthetic and laser annealed diamond in Melbourne. These measurements have mainly used ion beam analysis with a focused MeV ion beam in a nuclear microprobe system. A variety of techniques have been employed. One of the most important is nuclear elastic scattering, sometimes called non-Rutherford scattering, which has been used to accurately characterise diamond films for thickness and composition. This is possible by the use of a data-base of measured scattering cross sections. Recently, this work has been extended and nuclear elastic scattering cross sections for both natural boron isotopes have been measured. For radiation damaged diamond, a focused laser annealing scheme has been developed which produces near complete regrowth of MeV P implanted diamonds. In the laser annealed regions, proton induced x-ray emission has been used to show that 50 % of the P atoms occupy lattice sites. This opens the way to produce n-type diamond for microelectronic device applications. All these analytical applications utilise a focused MeV microbeam which is ideally suited for diamond analysis. This presentation reviews these applications, as well as the technology of nuclear techniques of analysis for diamond with a focused beam.

## ION BEAM INDUCED DAMAGE IN DIAMOND

Ion beam irradiation of diamond introduces damage that can cause degradation of the quality of the crystal. This can be a problem for both ion beam analysis techniques and ion beam modification processes aimed at the production of diamond with useful properties. In Melbourne, analysis of diamond is typically done with a focused ion beam which can result in both lattice damage and considerable swelling of the diamond itself. In the case of measurements of the crystal quality,  $\chi_{\min}$ , the swelling of the crystal results in significant dechanneling of the analysis beam and the consequent degradation of the measurement unless precautions are taken (1). Since the tilted crystal planes at the edge of the irradiated region extend over about 10 mm in size, it is simply necessary to ensure that the tilted region lies outside of the region of interest. Within the irradiated region, away from the tilted edges, the crystal quality in the surface region is essentially unaffected by the analysis beam irradiation. This is shown by the results in figure 1 which show the  $\chi_{\min}$  measured as a function of dose in a diamond crystal. The critical dose,  $D_s$ , is where the tilting of the crystal planes begins to exceed the channeling critical angle for the measurement. Further measurements

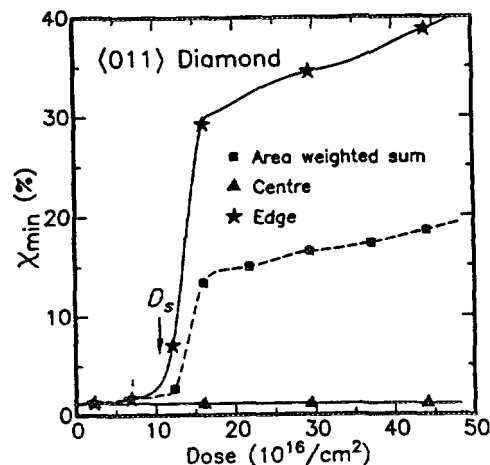


Figure 1: Build-up of damage in 1.4 MeV He<sup>+</sup> ion irradiated diamond.

on other materials reveals a similar behaviour (2). More detailed analysis of the damage produced by the ion beam irradiation of diamond is presently being carried out (3,4).

### ION IMPLANTATION AND LASER ANNEALING OF DIAMOND

Diamond is a potentially excellent material for microelectronic applications. With a wide band gap (5 eV) it is potentially insensitive to thermal noise and with excellent thermal conductivity it can operate at high temperatures. However a barrier to the fabrication of useful devices is the difficulty of making n-type diamond semiconductor material. Over the past few years in Melbourne, a scheme has been devised that has the potential to produce n-type diamond. Nuclear techniques of analysis have been essential for probing the extent of regrowth of the implantation-induced damage in the diamond crystal lattice and the lattice location of the dopant atoms in the annealed diamond crystal.

Our previous work has shown that focused laser annealing could partially regrow the damage produced by deeply buried 2.8 MeV C<sup>+</sup> implantation ( $R_p \pm \Delta R_p = 1.48 \pm 0.06 \mu\text{m}$ ) to a dose of  $3 \times 10^{15} \text{ C}^+/\text{cm}^2$  (5,6). In that early study, Channeling Contrast Microscopy (CCM) was used to probe the lattice regrowth following laser annealing from a single pulse. That work has now been extended to two new systems: P and As implantation. An example of the result of laser annealing of the As implanted diamond is shown in figure 2. In this figure, the laser pulse was of highly non-uniform intensity distribution. However several typical phenomena are visible. High laser intensities have resulted in the formation of a buried graphitic spot (labeled "laser burned" in figure 2). Intermediate laser intensities have resulted in laser annealing of the diamond, as seen by the bleaching of the dark damaged diamond.

In the case of P implantation, a new laser annealing scheme has been devised that uses multiple laser pulses of increasing energy to more fully anneal the diamond. This is shown by the histogram in figure 3 which shows the

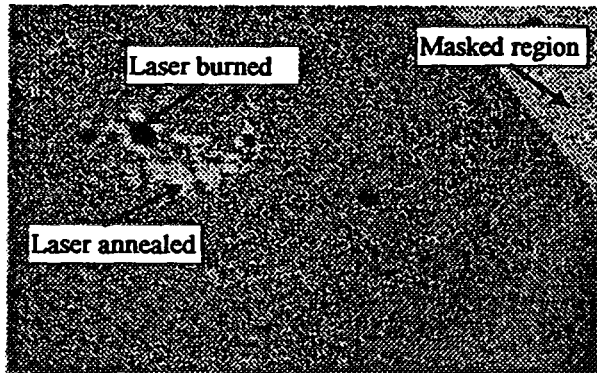


Figure 2: Laser annealed As implanted diamond showing an area of  $40 \times 20 \mu\text{m}^2$ .

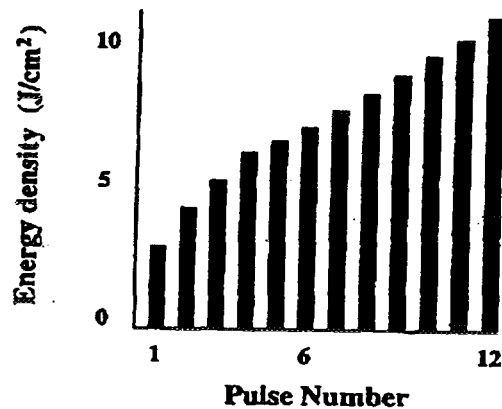
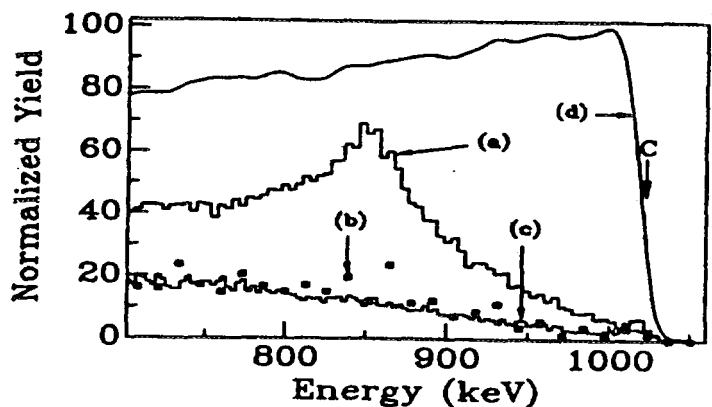


Figure 3: Multiple pulse laser annealing scheme for P implanted diamond.

increasing laser power required to more fully anneal the diamond (7). In this case a diamond implanted with 4.0 MeV P<sup>+</sup> to a dose of  $1 \times 10^{15} \text{ P}^+/\text{cm}^2$ . It is important to note that a single laser pulse of the intensity corresponding to pulse number 12 in this scheme on an as-implanted diamond will result in ablation of the diamond surface down to the end of range of the original implant. The effectiveness of the multiple pulse annealing scheme is clearly shown in figure 4 which shows results from CCM analysis of a multiple pulse annealed diamond.

Figure 4: (right) CCM analysis of a P implanted and laser annealed diamond showing backscattering spectra from several regions of interest: (a) As-implanted diamond, (b): multiple pulse laser annealed spot, (c): unimplanted diamond for comparison and (d): a randomly oriented diamond. All data from the  $\langle 110 \rangle$  axis using a 1.4 MeV H<sup>+</sup> microbeam and a detector at a scattering angle of 150°.



The backscattering spectrum cannot provide information about the lattice site of the implanted atoms owing to their very low concentration at the end of range. Instead it is possible to use the Proton Induced X-ray Emission (PIXE) signal. However this is challenging, since the yield of x-rays is very low as the P concentration at the end of range is about 18ppm. It is necessary to use a highly optimised system including a large area x-ray detector (80 mm<sup>2</sup>) in close geometry (~15mm). Figure 5 shows the PIXE channeling data from the P implanted diamond. The yield of P x-rays from the laser annealed regions of the diamond is about 50% of the yield from P in regions where the P is randomly sited in the lattice. This suggests partial substitution of P on the diamond lattice and electrical measurements are now in progress to determine the electrical activity of the substituted atoms.

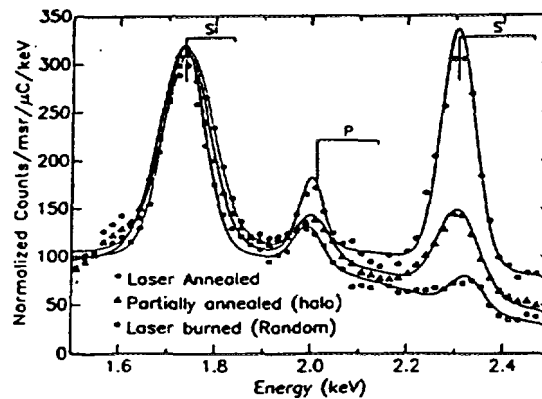


Figure 5: PIXE channeling data on P implanted diamond.

### NUCLEAR ELASTIC CROSS SECTIONS

In the examples of ion beam analysis of diamond presented here, advantage has been taken of the enhancement in the back scattering cross section that occurs as a result of the breakdown in the Rutherford scattering law owing to the projectile coming within range of the strong nuclear force. Measurement of these cross sections to produce a data base allows simulated spectra to be fitted to experimental data (8). An example of this is shown in reference (9) of these proceedings where the thickness of synthetic polycrystalline diamond films have been measured by 3 MeV H<sup>+</sup> backscattering. In addition, the ion induced luminescence has been studied and significant differences between films grown under different growth conditions have been observed. Recently this work has been extended to the measurement of the elastic scattering cross sections for both natural isotopes of boron. This may allow measurement of boron concentrations in thin diamond films. Such films can be made self supporting allowing the boron and carbon signals to be resolved in the backscattering spectrum. Preliminary data showing the yield from <sup>10</sup>B and <sup>11</sup>B in a thin natural boron film as a function of energy are shown in figure 6.

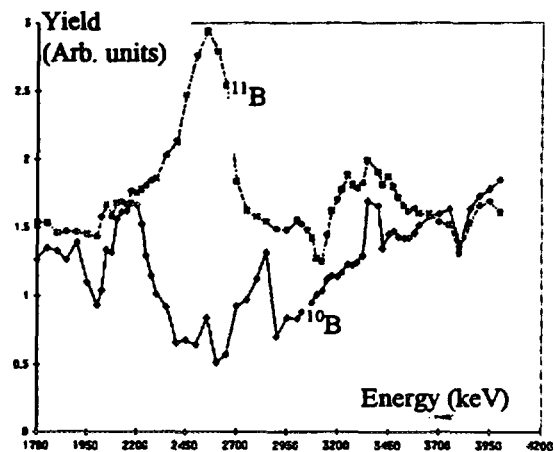


Figure 6: Yield at 170° from natural boron for H<sup>+</sup> irradiation.

This work has been supported by grants from the Australian research Council.

### REFERENCES

- (1) S.P. Dooley, D.N. Jamieson and S. Praver, Nucl. Instr. Meth. B77 (1993) 484.
- (2) S.P. Dooley and D.N. Jamieson, Nucl. Instr. Meth. B66 (1992) 369.
- (3) D.N. Jamieson, S. Praver, K.W. Nugent and S.P. Dooley, presented at IBMM95, ANU, Canberra, February 1995, to appear in Nucl. Instr. Meth. (NIB2967). (1995).
- (4) S.P. Dooley, D.N. Jamieson, K.W. Nugent and S. Praver, these proceedings.
- (5) S. Praver, D.N. Jamieson and R. Kalish, Phys. Rev. Lett. 69 (1992) 2991.
- (6) D.N. Jamieson, S. Praver, S.P. Dooley and R. Kalish, Nucl. Instr. Meth. B77 (1993) 457.
- (7) M.G. Allen, S. Praver, D.N. Jamieson and R. Kalish, Appl. Phys. Lett 63 (1993) 2062.
- (8) R. Amirikas, D.N. Jamieson and S.P. Dooley, Nucl. Instr. Meth. B77 (1992) 110.
- (9) A.A. Bettiol, P. Gonon and D.N. Jamieson, these proceedings.

# Radiocarbon Dates to Access the Origin of the Ice Man

TH. R. NIKLAUS<sup>1,2</sup>, G. BONANI<sup>1</sup> AND R. PRINOTH-FORNWAGNER<sup>3</sup>

<sup>1</sup> Institute of Particle Physics, ETH Zurich, CH-8093 Hnggerberg, Switzerland

<sup>2</sup> Now at CSIRO Exploration and Mining, PO Box 136, North Ryde, NSW, 2113, Australia

<sup>3</sup> Institut fr Ur- und Frhgeschichte, Universitt Innsbruck, A-6020 Innsbruck, Austria

## Summery

To determine the origin of the Ice Man from the Hauslabjoch using radiocarbon dating method, different samples from the Late and Final Neolithic in Northern Italy were radiocarbon dated at the AMS Facility in Zurich, Switzerland. Due to these radiocarbon dates the chronological classification of the burial site Remedello (Province of Brescia) which is of great interest in attempting to classify the man from the Hauslabjoch can be discussed. The main goal is the cultural and chronological classification of the Ice Man with the help of new and old radiocarbon dates.

## 1. Introduction

Radiocarbon dating has been a well established dating method since 50 years. At the beginning, the potential application range was limited by the rather large amount of carbon required for dating due to the method was based on counting the decay rate of a sample. Accelerator mass spectrometry (AMS) enables to count single atoms in a sample and therefore allows to reduce the sample size from typically a few grams to as small as 50µg, which is essential in archaeological applications [1].

In September 1991, a mummified corpse was found in a small rock depression at the Hauslabjoch, which is located in the tztal Alps (part of Similaun Massiv), South-Tyrol, Italy [2]. To determine the absolute age of the Ice Man and his origin, different samples were radiocarbon dated with AMS [3,4]. In addition, the dataset is completed by all available radiocarbon dates of Late and Final Neolithic cultures in the Northern and Southern Alps. The resulting time ranges for the Ice and the Late and Final Neolithic are then compared which allows a possible assignment to the cultural origin of the Ice Man.

## 2. Dating of the Ice Man

The Ice Man from the Hauslabjoch was radiocarbon dated by nine independent different radiocarbon dates of bone and tissue specimens (20-30 milligrams) from the body found on the glacier and of samples of grass from the Ice Man's clothing. The bone and tissue specimens were independently radiocarbon dated in Zurich, Switzerland and in Oxford, Great Britain. Grass from the man's straw cape and from his left shoe were radiocarbon dated in Uppsala, Sweden and Paris, France. Other loose blades of grass, which were found on the samples of the human remains, were radiocarbon dated in Zurich and grass samples from the 1992 excavation in Oxford [3].

Table 1 shows the measured conventional radiocarbon ages for the various samples of the different laboratories. The laboratory number and the laboratory, which has measured the sample, together with the material of the sample are also listed in table 1. In addition, the  $\delta^{13}\text{C}$  values, if available, are shown in per mil. From all conventional radiocarbon ages the weighted average was calculated (table 1). The  $\chi^2$  is equal to 1.25 and indicates, that the average can be used to determine the age of the Ice Man: the conventional radiocarbon is  $4546 \pm 17$  years BP. The transformation of the conventional radiocarbon date into a calendar age can be achieved by calibrating the conventional radiocarbon age using the computer program CalibETH [5]. The calibration was performed using the radiocarbon calibration curve from Stuiver and Pearson [6]. The result is also given in table 1. Multiple calendar age intervals for the respective  $2\sigma$  confidence range may result from the calibration procedure due to fluctuations in  $^{14}\text{C}$  concentration in the atmosphere. For each interval the probability of finding the true age in the respective time interval is also given.

Figure 1 illustrates the details of the calibration procedure. The upper part shows the relevant part of the calibration curve between 3050 cal BC and 3400 cal BC. The three horizontal solid lines represent the conventional  $^{14}\text{C}$  age with the  $1\sigma$  standard deviation. The dashed line indicates the  $1\sigma$  error band of the calibration curve. The calibration curve has a so-called plateau between 3340 cal BC and 3100 cal BC, corresponding to a range in the conventional  $^{14}\text{C}$  age of 4550 y BP to 4460 y BP. Therefore the age determination of the Ice Man can not be improved by reducing the error as long the measured age lies in this plateau [7,8]. The lower part of figure 1 shows the probability density function resulting from the calibration of the conventional radiocarbon age for the Ice Man ( $4546 \pm 17$  y BP). The probability density is displayed as a histogram with a bar width of five years. The bar height is calculated by integrating the probability density along the bar width. Therefore the bar height corresponds to the probability of finding the true age in the corresponding time interval. The  $1\sigma$  confidence ranges are calculated by integrating the probability density function to a level of 68% [7,8] and are marked by filled areas. The true age of the Ice Man lies somewhere between the boundaries

Lab. No.	Material	<sup>14</sup> C age [BP]	δ <sup>13</sup> C [‰]	Lab
OxA-**1	tissue	4500±30	-20.6±0.5	Oxford
OxA-**2	bone	4580±30	-23.1±0.5	Oxford
ETH-8345	tissue	4555±35	-23.9±0.6	Zurich
ETH-8342	bone	4560±65	-27.9±1.0	Zurich
ETH-8345-3	grass	4535±60	-25.4±0.9	Zurich
Ua-2373	grass	4612±51	-26.0	Uppsala
Ua-2374	grass	4343±100	-24.5	Uppsala
GifA91402/13	grass	4452±148		Paris
GX-18504AMS	grass	4555±48	-25.5	Oxford
Weighted average		4546±17	Chi-square = 1.25	
Calibrated age ranges of weighted average (2σ confidence range)		3352 - 3300 cal BC	31.1 %	
		3235 - 3175 cal BC	35.5 %	
		3166 - 3108 cal BC	33.4 %	

Table 1. Radiocarbon dating results of the Ice Man.

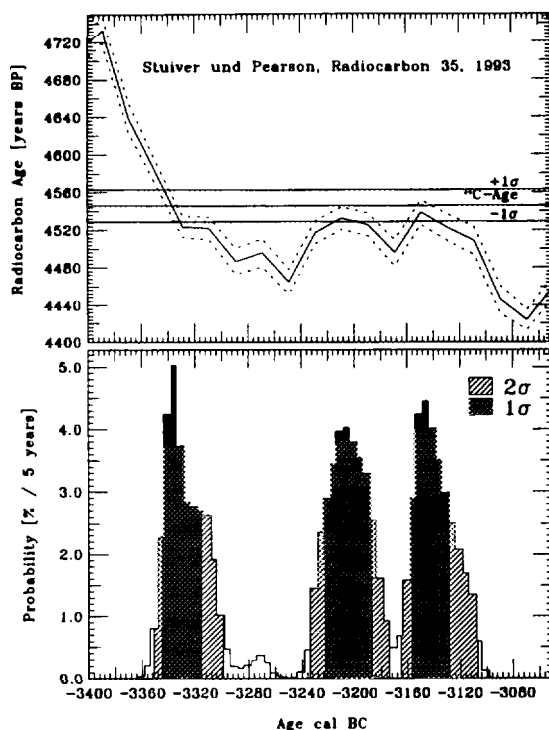


Fig. 1: Calibration of the conventional <sup>14</sup>C age of the Ice Man, including part of the calibration curve and the resulting probability density function.

show the 2 sigma confidence range.

### The Cultural Classification of the Man in the Ice

The cultural classification is obtained on the basis of typological studies (of the copper axe and of the flint dagger, of studies of artefact materials (of the flint and of the wood of a composite arrow) and on the basis of radiocarbon chronological studies.

The axe of the Ice Man, made of pure copper with small traces of As (0.22%) and Ag (0.09%) is characterised by a body of trapezoidal form with straight side and with a blade that is ca. double as wide as the butt and having flanges slightly raised through hammering. In the whole Alpine region, most founded copper axes display typological characteristics which differ from those of the Ice Man's axe. The typological studies show, that the Ice Man's copper axe has no satisfying correspondence north of the Alps. The best correlation to the Ice Man's axe come from Northern Italy, where we know of ca. 50 axes which are placed chronologically before the Early Bronze Age. Due to the form of the body, the Ice Man's axe can best be compared to axe of grave 102 of Remedello Sotto (Brescia), which belongs to the earlier period of the necropolis (Remedello I) [4].

It is at the present time difficult to establish a definitive typological comparison for the flint dagger, because its base is partly splintered. North of the Alps, the Alheim culture offers the most justifiable parallel to the flint daggers with groove hafting. Such daggers made of northern Italian flint may be found in southern Germany as import articles. In

of this intervals with a probability of 68%. But, with a probability of 32% the true age can also be outside these intervals, but not too far away. Expanding the error band from 1σ to 2σ the probability to find the true age in this 2σ confidence range (hatched areas) increases to 95%. The probability of finding the true age outside this 2σ confidence range is only 5% and has to be inside the blank area. To determine the age of the Ice Man the 2σ interval is the most reliable information and therefore also the most convenient one. The 2σ confidence range consists of three single time intervals of similar size (40-60 years). All three intervals have more or less the same probability (31%-36%) of finding the true age in the corresponding time window. The effect of the plateau in the calibration curve discussed above is responsible for the fact that the calendar age uncertainty could not be reduced, although the standard deviation of the conventional radiocarbon age was reduced to 17 years.

### Neolithic Cultures around the Alps

The radiocarbon dates of the Ice Man fall all into the second half of the fourth millennium. To determine the duration of a culture, all available conventional <sup>14</sup>C ages of such a culture are calibrated individually. The resulting probability density functions of the individual samples are summed together and normalized to 1. The obtained distribution is also a probability density function and can be used to discuss the duration of a culture by calculating the cumulative probability distribution and the corresponding 2σ interquartile range (95%) or interquartile range (floruit, 50%) [9]. The probability of finding the true age is: within the floruit 50%, below the floruit 25%, and above the floruit is 25%. The duration of the Northern Alps cultures is calculated by the method discussed above and already by discussed elsewhere [3]. For the Southern Alps cultures only a few radiocarbon dates were available. Therefore, different samples from the Late and Final Neolithic in Northern Italy were radiocarbon dated at the AMS Facility in Zurich, Switzerland. The result of these measurements are published elsewhere [5,6]. Figure 2 shows a comparison of the resulting time periods of the Late and Final Neolithic cultures of the Alpine region with the lifetime of the Ice Man. This lifetime is delineated by the two vertical lines. In the upper part of the graph, the cultures of the Northern Alps are shown: in the lower part, those of the Southern Alps. The solid bars depict the floruit and the hatched bars

summary, we note a clear typological correspondence with the Remedello culture: for the axe, with grave 102; for the flint dagger, with grave 97 [4].

The six flint instruments which the Man in the Ice carried are made of a grey hornstone found only in the Alps. Its fine grain and the presence of silicified molluscs in these instruments are characteristics which clearly indicate an origin in northern Italy's flint deposits. A flint mine discovered in Ceredo (Province of Verona) may have provided - judging on the basis of characteristic microfossiles - the raw material for the manufacturing of four of the above-mentioned instruments carried by the Man in the Ice. The raw material of the instruments is, in any case, of subalpine origin. As concerns the kinds of wood used in the Ice Man's equipment, one arrow presents a possible indication of southern origin. The arrow foreshaft is made of cornel wood. Should future studies reveal this wood to be *Cornus sanguinea*, further evidence of a subalpine origin would be offered, because south of the Alps, *Cornus sanguinea* is found in the nearby Vinschgau whereas to the north it is found in the geographically more distant Vorarlberg and probably in the even more distant Zillertal [4].

Prior studies have shown that to the north of the Alps we find Late and Final Neolithic civilisations as the Altheim and Cham cultures, which developed in the same area, though at a different time, and the Horgen culture [3]. These civilisations fit in well with the time period of the Ice Man's lifetime between 3350 and 3100 cal BC. The cultures used copper and produced flint tools which are comparable to those of the Man in the Ice. To the south of the Alps, there may have been a relationship between the Ice Man and phase I (B) of St. Martin de Corleans or the Grotticelle Sepolcrali group (fig. 2) which are in the vicinity of the site where the Ice Man was found. In addition, the radiocarbon dates of the older phase of the burial site of Remedello are in line with the radiocarbon datings of the Ice Man. The striking similarities between grave 102 of Remedello and the corresponding equipment of the Man in the Ice thus point towards relations between Hauslabjoch and Remedello.

### Conclusions

Some graves of the Grotticelle Sepolcrali group as well as the site at Tolereit (Province of Bolzano) are contemporary to the Ice Man. The excitement, however, lies in evaluating the radiocarbon dates from ten graves on the necropolis of "Remedello Sotto" (Province of Brescia), which defines the Remedello culture. The duration of the Remedello culture together with the typological support the hypothesis that the Man in the Ice had a direct or indirect connection with the Early Remedello culture.

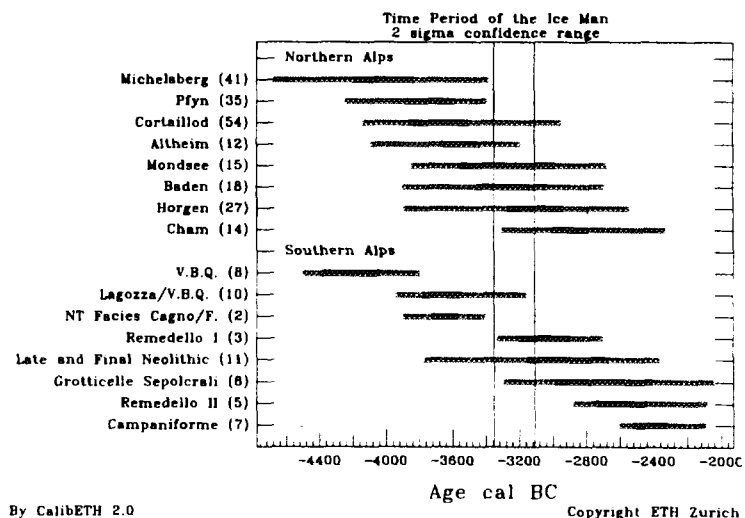
### Acknowledgment

We also thank Keller, S. Ivy and I. Hajdas for the sample preparation. We also thank R. C. de Marinis from Milan and A. Pedrotti from Trento for the information of Late and Final Neolithic cultures south of the Alps in Italy and providing corresponding radiocarbon results.

### References

- [1] Wölfli W., (1987), Nucl. Instr. and Meth. B29, 1-13.
- [2] Bonani G., Ivy S., Niklaus Th.R., Suter M., Housley R.H., Bronk C.R., van Klinken G.J. and Hedges R.E.M., (1992), Der Mann Im Eis, Veröffentlichungen der Universität Innsbruck 187, 389-409
- [3] Prinoth-Fornwagner R. and Niklaus Th.R., (1994), Nucl. Instr. and Meth. B92, 282-290.
- [4] Niklaus Th. R., Bonani G., De Marinis R., Pedrotti A., Prinoth-Fornwagner R. and Dal Ri L., (to be published), New Radiocarbon Dates to Access the Cultural and Chronological Characterisation of the Man in the Ice.
- [5] Niklaus Th.R., Bonani G., Simonius M., Suter M. and Wölfli W., (1992), Radiocarbon 34, 483-492.
- [6] Stuiver M. and Pearson G.W., (1993), Radiocarbon 35(1), 1-33.
- [7] Niklaus Th.R., (1993), Ph.D. thesis ETH-Nr. 10065.
- [8] Niklaus Th.R., Bonani G., Suter M. and Wölfli W., (1994), Nucl. Instr. and Meth. B92, 194-200.
- [9] Aitchison T.C., Ottaway B.S. and Scott E.M., (1991), PACT 29-II.6, 95-104.

Fig. 2: Comparison the time periods of Late and Final Neolithic Cultures of the Alpine region with the lifetime of the Ice Man. In the upper part, the cultures of the Northern Alps, and in the lower part, the cultures of the Southern Alps are shown. The solid bars depict the floruit and the hatched bars show the 2 sigma confidence range. The two vertical dashed lines mark the lifetime of the Ice Man





AU9716150

# Ultra-Sensitive Detection of Plutonium by Accelerator Mass Spectrometry

L.K.FIFIELD<sup>1</sup>, R.G.CRESSWELL<sup>1</sup>, T.R.OPHEL<sup>1</sup>, M. DI TADA<sup>1</sup>, J.P.DAY<sup>2</sup>, A.CLACHER<sup>2</sup> and N.D.PRIEST<sup>3</sup>

<sup>1</sup> Department of Nuclear Physics, RSPHYSSE, Australian National University

<sup>2</sup> Chemistry Department, University of Manchester, UK

<sup>3</sup> AEA Technology, Harwell, UK

Anthropogenic plutonium has been introduced into the environment over the past 50 years as a result of nuclear weapons testing, of reactor accidents, and of the discharge of nuclear fuel wastes from re-processing plants. While all isotopes of plutonium with mass numbers ranging from 238-242 and 244 have been released, under most circumstances the isotopes 239 and 240 are the most important. These isotopes decay with the emission of alpha-particles, and are toxic if they enter the body.

Based on the analysis of limited autopsy tissues it has been estimated that the average plutonium body burden of the UK population is a little less than 100mBq or  $10^{11}$  atoms. More extensive surveys of the population, in particular in at-risk groups, has not been possible because the normal monitoring technique - urine sampling - cannot presently be undertaken at the predicted levels of plutonium output. Best estimates suggest that about 5-10 mBq is excreted in the urine each day and this is much below the the practical detection limit of current analytical methods, of which the most commonly used is alpha-spectrometry with a detection limit of 100 mBq or  $10^8$  atoms. It follows that a detailed examination of plutonium contamination of the population requires a more sensitive assay method. Accelerator Mass Spectrometry (AMS) is a candidate method and the present work was undertaken to explore its limits of sensitivity.

On the basis of the measurements performed to date, a sensitivity of  $10^6$  atoms is achievable with AMS for each of the plutonium isotopes. Not only does this open the way to the sort of study outlined above, but it also makes possible other novel applications, of which two examples are given below.

1. The ratio of  $^{240}\text{Pu}$  to  $^{239}\text{Pu}$  is a sensitive indicator of the source of the plutonium. Reactors geared to nuclear weapons production use very short burn times to minimise the production of  $^{240}\text{Pu}$ , whereas commercial power reactors utilise much longer burn times and may produce up to 30%  $^{240}\text{Pu}$ . Alpha-spectrometry is unable to discriminate between the two isotopes. With AMS the measurement of this ratio is straightforward.

2. Much remains to be learnt about the biochemistry of plutonium in humans. The ultra-sensitive atom counting capability of AMS will make it possible to use the very long-lived  $^{244}\text{Pu}$  ( $8 \times 10^7$  a) in human volunteer studies without any significant increase in radiation body burden.

This paper will describe the AMS technique as applied to plutonium using the ANU's 14UD accelerator, will present the results obtained to date, and will discuss the prospects for the future.



# Precision and Reproducibility in AMS Radiocarbon Measurements

M.A.C. HOTCHKIS, D. FINK, Q. HUA, G.E. JACOBSEN, E.M. LAWSON,  
A.M. SMITH AND C. TUNIZ

Australian Nuclear Science and Technology Organisation  
Private Mail Bag 1, Menai, NSW 2234, Australia

## SUMMARY

Accelerator Mass Spectrometry (AMS) is a technique by which rare radioisotopes such as  $^{14}\text{C}$  can be measured at environmental levels with high efficiency. Instead of detecting radioactivity, which is very weak for long-lived environmental radioisotopes, atoms are counted directly. The sample is placed in an ion source, from which a negative ion beam of the atoms of interest is extracted, mass analysed, and injected into a tandem accelerator. After stripping to positive charge states in the accelerator HV terminal, the ions are further accelerated, analysed with magnetic and electrostatic devices and counted in a detector. An isotopic ratio is derived from the number of radioisotope atoms counted in a given time and the beam current of a stable isotope of the same element, measured after the accelerator. For radiocarbon,  $^{14}\text{C}/^{13}\text{C}$  ratios are usually measured, and the ratio of an unknown sample is compared to that of a standard. The achievable precision for such ratio measurements is limited primarily by  $^{14}\text{C}$  counting statistics and also by a variety of factors related to accelerator and ion source stability.

At the ANTARES AMS facility (1,2) at Lucas Heights Research Laboratories we are currently able to measure  $^{14}\text{C}$  with 0.5% precision. In the two years since becoming operational, more than 1000  $^{14}\text{C}$  samples have been measured. Recent improvements in precision for  $^{14}\text{C}$  have been achieved with the commissioning of a 59 sample ion source. The measurement system, from sample changing to data acquisition, is under common computer control. These developments have allowed a new regime of automated multi-sample processing which has impacted both on the system throughput and the measurement precision. We have developed data evaluation methods at ANTARES which cross-check the self-consistency of the statistical analysis of our data. Rigorous data evaluation is invaluable in assessing the true reproducibility of the measurement system and aids in the identification of physical problems with the system.

## $^{14}\text{C}$ MEASUREMENTS

For precise ratio measurements, it is necessary to switch rapidly between counting  $^{14}\text{C}$  and measurement of the  $^{13}\text{C}$  beam current, on a timescale shorter than ion source current fluctuations. For this purpose, the accelerator injection magnet has an insulated vacuum chamber, so that the beam energy can be modulated electrostatically to allow fast switching between rare and stable isotopes (2). A sequencer provides the pulse cycle and gating signals for the detector

electronics and current integrators. The cycle is normally 5 Hz, with  $^{13}\text{C}$  injected for 1% of the time (i.e. 2 ms  $^{13}\text{C}$ , 198 ms  $^{14}\text{C}$ ). The  $^{13}\text{C}$  beam transmitted through the accelerator is measured in an off-axis Faraday cup on the  $90^\circ$  analysing magnet.

A typical measurement sequence consists of several sets of three unknowns, each bracketed by measurements of standards. Each individual 'run' is 300s long, or 500s for older samples and blanks. For high precision samples, the sequence is repeated three times, providing three independent measurements of each sample. With typical beam currents of 500 nA  $^{13}\text{C}^{4+}$ , this provides 20,000  $^{14}\text{C}$  counts per run (for a modern sample), and 0.4% overall counting statistics per sample. During each run, the  $^{14}\text{C}/^{13}\text{C}$  isotopic ratio is at intervals corresponding to approximately 2500 events. Hence a run provides about 10 separate ratio values, one every 30 seconds, with 2% statistical error per value. For old samples and blanks, the ratios are calculated less frequently and with poorer statistics.

## DATA ANALYSIS

The data analysis consists of a series of steps, as follows: (1) any runs where there were known problems with the system, e.g. Wien filter discharge, are eliminated; (2) the ratios for each run are analysed and weighted average ratios calculated, weighted according to the  $^{14}\text{C}$  count; (3) the ratio values for the standards measured before and after each set of unknown runs are averaged and this number is used to normalise the intervening ratios and derive the percent modern carbon (pMC) value for each run on an unknown sample, with appropriate combining of uncertainties from the unknown and standard; (4) results for each run are then sorted into tables and the weighted mean pMC is determined for all multiple measurements on the same sample.

During this process there are two opportunities to examine the statistical qualities of the data. The short-term stability of the system (over periods of minutes) can be checked by examining the constancy of the individual ratio measurements within a run. Outliers beyond the spread of ratios expected by statistical fluctuations may indicate short-

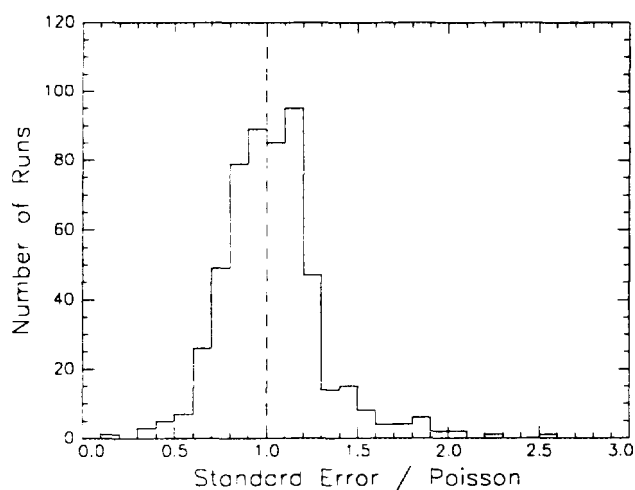


Figure 1. Histogram of the ratio of the standard error in the mean ( $\sigma/\sqrt{n}$ ) to the Poisson error ( $\sqrt{N_{14}}/N_{14}$ ).

term instability. If the source of the instability can be identified, the data can be rejected. However, small instabilities may be disguised by the statistical fluctuations, so it is useful to test the data by comparing the standard error in the mean ( $\sigma/\sqrt{n}$ , where  $\sigma$  is the standard deviation of a set of  $n$  ratios) to the statistical (Poisson) error in the total number of  $^{14}\text{C}$  counts ( $\sqrt{N_{14}}/N_{14}$ ) (see Fig. 1). If there are no contributions to the standard error other than the Poisson error, then the two are equal and their ratio unity. In practice, there is a significant spread in values, due to the small number of ratios in each run (5 to 15). The mean value is 1.033 for the data in Fig. 1, indicating no significant non-Poisson contributions to the errors in the ratios. In the further analysis of the data, the uncertainty is taken to be the larger of ( $\sigma/\sqrt{n}$ ) and the Poisson error, i.e. we adopt the 'conservative' error rule discussed by Currie (3).

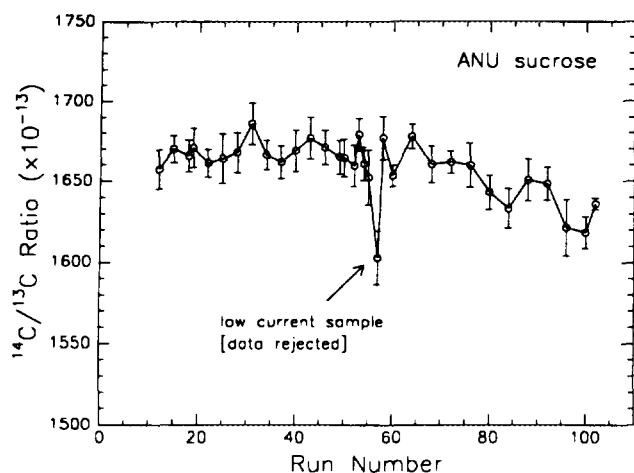


Figure 2. Measured  $^{14}\text{C}/^{13}\text{C}$  ratios for the ANU sucrose standard over a two day period. Unknown samples were measured between standard measurements.

The long-term stability of the system (over periods of hours or days) can be evaluated by examining the constancy of the standards measurements. These are shown over a 24 hour period in Fig. 2. The figure shows good performance for most of the period, except for one standard sample which did not give adequate current output. After Run 70 the standard ratio declines gradually; this was found to be due to a slow drift in beam energy, which we believe was caused by a drift in the GVM. Because we use GVM terminal stabilisation, a drift in the GVM drags the terminal voltage with it. Occasional checking by centring the beam through the analysing magnet slits is required to correct this. In the near future, this process will be done automatically at intervals by centring the  $^{13}\text{C}$  in the off-axis cup.

The system reproducibility is tested by examining the repeat measurements of unknowns. As outlined above, each sample is usually measured three times and normalised to its neighbouring standard ratios to derive the final pMC result. These repeat measurements are analysed by calculating the weighted mean and, for each run, the relative deviation  $(x_i - \mu) / \sigma_i$ , where  $\mu$  is the mean and  $x_i$  are the pMC values with uncertainties  $\sigma_i$ . The relative deviations for all repeated sample measurements are shown in Fig. 3 as a histogram. If the individual uncertainties are truly representative of the system reproducibility, the histogram should have a standard deviation of 1.00. Our value of 1.18 demonstrates that our uncertainties underestimate our reproducibility by a small amount, and that a source of random error other than from counting statistics and standardisation is present. Further analysis of this body of data, which spanned three months, indicates that certain running periods were less satisfactory than others, due, we believe, to changes in the behaviour of the terminal voltage stability. Splitting the data into separate running periods (usually about three days each) shows that some periods gave values close to 1.0, while others were worse. Such data evaluation is useful in identifying problem areas which can be worked on to improve measurement reproducibility.

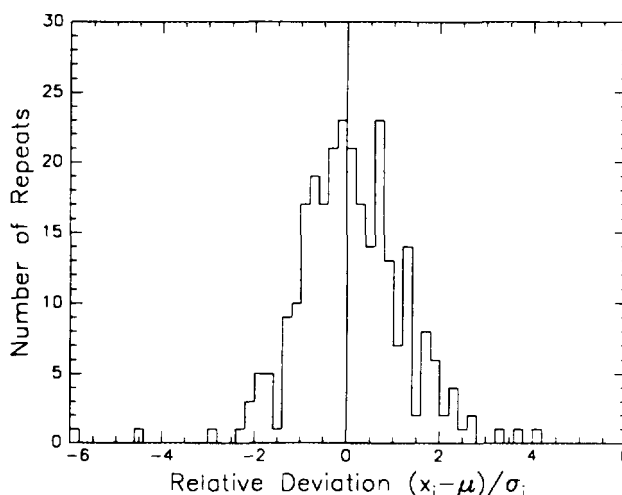


Figure 3. Relative deviations  $(x_i - \mu) / \sigma_i$  for a set of repeated sample measurements over a three month period.

## REFERENCES

- (1) C. Tuniz et al., in: Proc. 15th Int. Radiocarbon Conf., Glasgow, 1994, to be published in Radiocarbon.
- (2) A.M. Smith et al., Nucl. Instr. and Meth. B92 (1994) 122.
- (3) L.A. Currie, Nucl. Instr. and Meth. B92 (1994) 188.



## Nuclear analysis techniques as a component of thermoluminescence dating

J.R. PRESCOTT, J.T. HUTTON, M.A. HABERMEHL<sup>1</sup>, J. VAN MOORT<sup>2</sup>

Physics Department, University of Adelaide, SA 5005

<sup>1</sup> Australian Geological Survey Organisation, Canberra, ACT 2601

<sup>2</sup> Geology Department, University of Tasmania, Hobart, TAS 7001

### INTRODUCTION

In luminescence dating, an age is found by first measuring dose accumulated since the event being dated, then dividing by the annual dose rate. Analyses of minor and trace elements performed by nuclear techniques have long formed an essential component of dating. We report here results from some Australian sites to illustrate the application of nuclear techniques of analysis in this context. In particular, a variety of methods for finding dose rates are compared, an example of a site where radioactive disequilibrium is significant is given and a brief summary is given of a problem which was not resolved by nuclear techniques.

### METHODOLOGY

#### Thermoluminescence (TL) Dating

In luminescence dating, see e.g. Aitken (1) the time is found since a mineral sample was last exposed to heat or solar ultraviolet radiation, either of which sets the TL "clock" to zero. Suppose the sample is then covered over by natural causes and shielded from subsequent exposure to light. The mineral, e.g., dune quartz, now receives a radiation dose from low levels of natural radioactivity in the environment (K, U, Th) and from cosmic rays. A portion of the dose energy is stored in the crystal as trapped charge, which grows continuously with time. Heating the quartz releases this energy as TL light, which is thus a measure of the time since the material was last reset. This time can be expressed by the "Age Equation":

$$\text{Age} = (\text{TL of sample}) / (\text{TL per unit dose}) \times (\text{dose rate})$$

In this equation, the "TL of sample" and the "TL per unit dose" are measured in the laboratory on quartz from the sample; and the "dose rate" (in Gy ka<sup>-1</sup>) is found by measurements in the field and/or the laboratory

#### Measurement and comparison of dose rates

A number of methods for finding the dose rates are available. All contain some element of nuclear techniques.

In situ scintillometry, e.g., Hutton and Prescott (2) uses a sodium iodide scintillation crystal, calibrated for K, U and Th, in the auger hole from which the sample for dating is taken. It gives a completely self-contained measure of dose rate.

Thick source alpha particle counting (TSAC) gives the contribution to the dose rate from U and Th combined, together with an estimate of the U and Th concentrations separately. In fact, the dose rate to the sample is determined by the total alpha count and is almost independent of the U/Th ratio. Combined with measurement of K by XRS, TSAC gives an almost independent measure of the dose rate.

X-ray fluorescence spectrometry is used to find K and, with limited precision, U and Th also. Where all three are measured, this is also a fully independent analysis.

Finally, U and Th can be found using neutron activation analysis (NAA) for Th and delayed neutron activation (DNA) for U. Combined with K, it gives an further quasi-independent dose rate.

Table 1 shows comparisons of dose rates from the Cooloola site in Queensland. Dose rates have been calculated from Nambi and Aitken (3) and the contribution of cosmic rays from Prescott and Hutton (4) The agreement among the different methods in table 1 is excellent.

#### Radioactive disequilibrium

For a radioactive chain in equilibrium, all members of the chain show the same number of disintegrations per second. Comparison of DNA and scintillometry may give an indication of disequilibrium, since DNA measures the parent U-238 (via U-235) while scintillometry measures Bi-214, a late member of the decay chain. High resolution alpha or gamma counting may then confirm it.

Hutton and Prescott (5) have shown that there is little or no evidence of disequilibrium in aeolian dune systems. Table 2 show selected data from the spring mounds which occur along the southwestern margin of the Great Artesian Basin. They are built from evaporation of calcium carbonate solution carried up by artesian groundwater; in addition, aeolian debris is added to the dune as it grows. Several periods of activity are evident on geological grounds, the earliest of which is probably older than 1 Ma; many springs are still active. In such a watery environment, radioactive disequilibrium is not unexpected. The table shows two examples from "young" springs (Blanche Cup BC1 and Bubbler BB1, both 10-20 ka), and two from "old" springs (Elizabeth Springs ES1 and Kewson Hill KH1, both older than 500 ka).

The data for the thorium system are consistent with equilibrium--which is expected since the lifetimes of all the daughters are short with respect to likely geochemical transport times. For BC1 and BB1, disequilibrium is clearly established in the uranium chain because the parent uranium is insufficient to support its daughters. The data from BC1 and BB1 strongly suggest an open system where Ra-226 is being carried up with the water and being incorporated into the mound with its daughters. The old mounds, ES1 and KH1, are heavily indurated and the system has long been closed, so that equilibrium has been reestablished.

#### Thermoluminescence properties of quartz

As part of the study of the physics of TL, we have made an extensive study of the TL emission spectrum as a function of temperature. Some samples, of which SK11 and CA9 of table 1 are examples, emit strongly in the red. In an attempt to identify the luminescence centres responsible, we did PIXE/PIGME and NAA analyses on 39 elements for 11 samples. Unfortunately, there seems to be no correlation between spectral features and element concentrations. It was a good try!

#### ACKNOWLEDGMENTS

The late John Hutton was associated with all of the work described here. It is regretted that he did not see it completed. Special thanks to T. Wall, A. Murray and H. Heijnis for specialist measurements. The work was supported by AINSE, ARC and AGSO.

REFERENCES

- 1 Aitken, MJ (1985) *Thermoluminescence Dating*, Academic Press
- 2 Hutton, JT & Prescott, JR (1992). Field and laboratory measurements of low-level thorium, uranium and potassium. *Nucl Tracks and Radiat Meas*, 20, 367-370
- 3 Nambi, KSV and Aitken, MJ (1986). Annual dose conversion factors for TL and ESR dating. *Archaeometry*, 28, 202-205.
- 4 Prescott, JR and Hutton, JT (1994). Cosmic Ray contributions to dose rates for luminescence and ESR dating: large depths and long-term time variations. *Radiat Meas* 23, 497-500.
- 5 Hutton, JT and Prescott, JR (1989). Low level U and Th in Australian dune systems *Proc, Sixth Australian Conference on Nuclear Techniques of Analysis*. AINSE, Sydney. 184-186.

Table 1 Dose rates ( $Gy\ ka^{-1}$ ) for sampling sites at Cooloolo Queensland  
Cosmic ray contributions are included.

site	age ka	scintillation	alpha/XRS	DNA/NAA/XRS	XRS
CA2	0.92+0.19	1.45+0.05	1.36+0.13	1.52+0.09	1.66+0.11
CA5	0.52+0.14	#1.69+0.08	2.66+0.14	2.59+0.15	-
CA7	44.0+0.4	0.317+0.021	0.319+0.033	-	-
* SK11	110+9	-	0.526+0.10	-	0.58+0.13
* SK11W	119+11	0.502+0.026	-	0.581+.07	-
CA9	480+100	0.277+0.021	0.296+0.025	-	-

\* stratigraphically equivalent neighbouring sites

# This value is believed to be lower than the others because the instrument is sampling a large volume round the sample which contains lower activity.

Table 2 Analyses for Mound Springs expressed as  $Bq\ kg^{-1}$

Uranium series

	DNA U-238	high resolution					scint Bi-214	TSAC U equiv
		gamma U-238	alpha U-238	alpha U-234	alpha Th-230	gamma Ra-226		
BC1	6.9	2+4	6.3	0.6	9.1	39.5	53	37.1
BB1	9.1	9+6	7.7	7.9	11	59.9	91	39.7
ES1	1.7	-	5.6	3.0	2.1	-	2.7	1.8
KH1	7.8	-	9.1	10.9	12	-	5.6	10.1

Thorium series

	high resolution					scint Tl-208
	alpha Th-232	gamma Ra-228	alpha Th-228	gamma Th-228	TSAC Po-216	
BC1	12	18.1	15	17.3	11.1	13.0
BB1	14	18.0	14	18.4	12.5	16.5
ES1	6.2	-	5.8	-	4.5	4.9
KH1	1.7	-	3	-	0.7	0.8

The errors on the scintillation numbers are about 5%,

The DNA error is about 7%;

The TSAC total alpha count is better than 3% but the split between U and Th depends on the statistics of the pairs count which is mostly about 20% for these samples;

The high-resolution gamma counts are better than 3%, except U-238.



# Multiple and Double Scattering Contributions to Depth Resolution and Low Energy Background in Hydrogen Elastic Recoil Detection.

L. S. Wielunski, Division of Applied Physics, CSIRO, Lindfield, NSW 2070, Australia.

## Abstract

The sensitivity of hydrogen elastic recoil detection ( ERD ) is usually limited by the low energy background in the ERD spectrum. A number of 4.5 MeV He<sup>++</sup> hydrogen ERD spectra from different hydrogen implanted samples are compared. The samples are chosen with different atomic numbers from low Z carbon to high Z tungsten carbide to observe the effects of multiple scattering and double scattering within the sample material. The experimental depth resolution and levels of the low energy background in ERD spectra are compared with theoretical predictions from multiple and double scattering.

## 1. Introduction

Hydrogen elastic recoil detection ( ERD ) is the most frequently used method for hydrogen depth profiling in thin films and surfaces [1-3]. The materials studied vary from hydrocarbons to heavy metal ( gold, platinum or tungsten ) thin films.

The sensitivity of hydrogen detection and the depth resolution are functions of sample composition and experimental parameters [4-6]. It has been shown that very high sensitivity ( below 1 ppm ) can be obtained in UHV systems for samples containing less than 1 ppm atomic hydrogen and without hydrogen on the surface [4].

This work presents experimental results of hydrogen detection in different materials and shows how low energy background and depth resolution depend on the atomic number of the sample material and the amount of hydrogen present in the sample. The effect of multiple and double scattering is estimated and compared with results.

## 2. Experimental

Samples of glassy carbon, silicon, germanium and tungsten carbide were ion implanted with 50 keV hydrogen ions to a dose of  $3.7 \times 10^{17} \text{cm}^{-2}$ . The hydrogen detection ( ERD ) used a 4.5 MeV He<sup>++</sup> ion beam from a tandem accelerator. The silicon surface barrier detector was placed at scattering angles of 24, 30 and 36°. A 24 µm mylar absorber foil was used in front of the detector to absorb scattered He ions. The samples were mounted on a goniometer and rotated to the position where glancing angles of both the He incident beam and the detected H recoils are equal (12°,12° or 15°,15° or 18°,18°). The ERD spectra were recorded using 512 channels with energy conversion of about 3.8 keV per channel using standard ion beam analysis system ( HYPRA ).

Fig 1. shows ERD spectra collected from glassy carbon and tungsten carbide samples for a 24° scattering angle (12°,12°). Similar data for Si and Ge samples are shown on Fig. 2. These results can be described as consisting of (i) a surface hydrogen peak of different intensity but the same energy width, (ii) a nearly Gaussian implanted hydrogen peak and (iii) a continuous almost constant low energy background. The energy width of the ion implanted hydrogen peak varies substantially from small values in the case of glassy carbon sample ( Z=6 ) to large values in the case of tungsten carbide sample ( Z=74 for W ). In a similar way, low energy background is very low in the case of low Z and increases with Z to the highest value in tungsten carbide.

Figs 3 and 4 show similar spectra collected in the case of 30° scattering angle ( 15°,15° ). In this case similar structure is observed with the peak positions shifted towards lower energy as expected from kinematic calculations. Fig 5 shows spectra collected from germanium and tungsten carbide samples for a 36° scattering angle.

## 3. Results and discussion

The results shown on Figs 1-5 can be compared with implantation profiles generated by computer simulation program TRIM-90 [7]. Table 1 compares the ratios of peak width (FWHM) to ion range obtained from our ERD results with the same ratios from TRIM-90 computer simulations. It is clear that the experimental ERD results are much broader than the calculated TRIM-90 results. The detector resolution, detector acceptance angle and beam spot size effects are small and are not able to explain the substantial differences shown in table 1. Effects of the energy straggling of the He beam before the hydrogen recoil process and the energy straggling of hydrogen ions after recoil have been estimated to be no more than 30 keV total ( FWHM at the detector ) and vary by no more than 30% in the materials compared in this work [8]. These energy stragglings are too small to explain a substantial part of the differences shown in table 1.

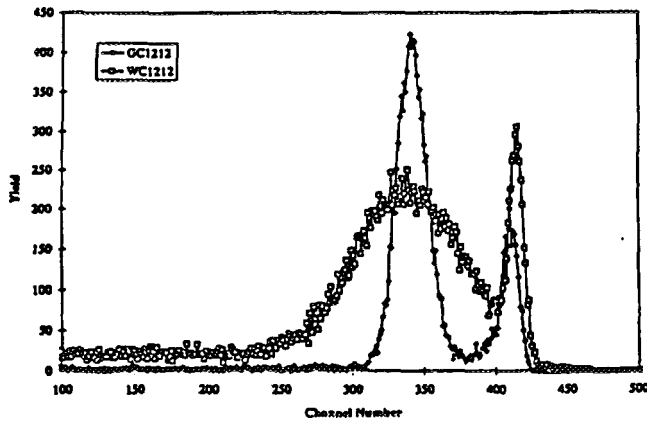


Fig 1. ERD spectra from hydrogen implanted glassy carbon ( GC ) and tungsten carbide ( WC ) samples in  $24^\circ$  scattering angle geometry (  $12^\circ, 12^\circ$  ).

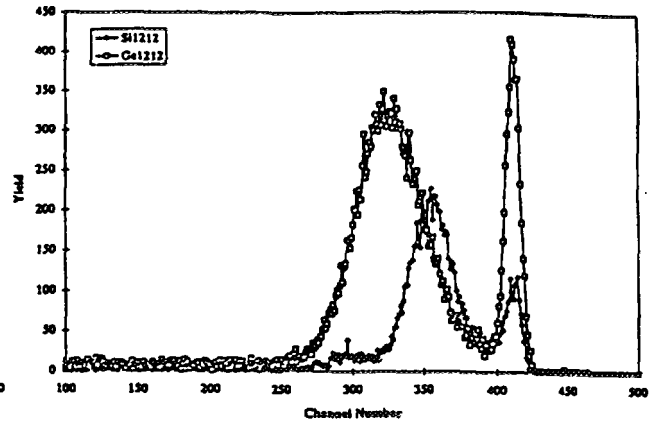


Fig 2. ERD spectra from hydrogen implanted silicon and germanium samples in  $24^\circ$  scattering angle geometry (  $12^\circ, 12^\circ$  ).

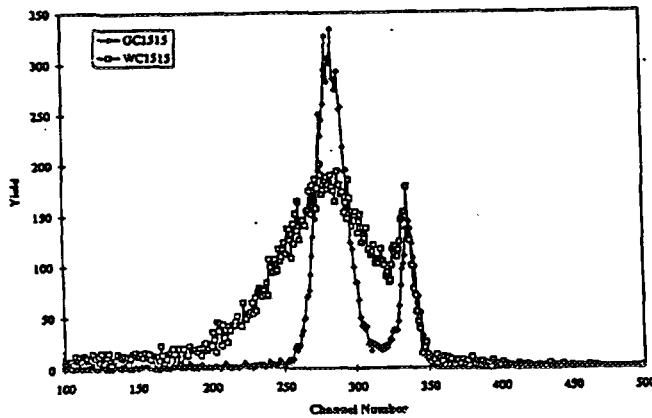


Fig 3. ERD spectra from hydrogen implanted glassy carbon ( GC ) and tungsten carbide ( WC ) samples in  $30^\circ$  scattering angle geometry (  $15^\circ, 15^\circ$  ).

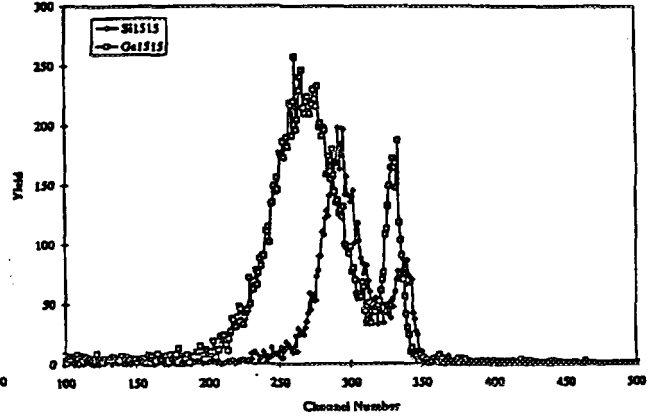


Fig 4. ERD spectra from hydrogen implanted silicon and germanium samples in  $30^\circ$  scattering angle geometry (  $15^\circ, 15^\circ$  ).

Fig 5. ERD spectra from hydrogen implanted germanium and tungsten carbide samples in  $36^\circ$  scattering angle geometry (  $18^\circ, 18^\circ$  ).

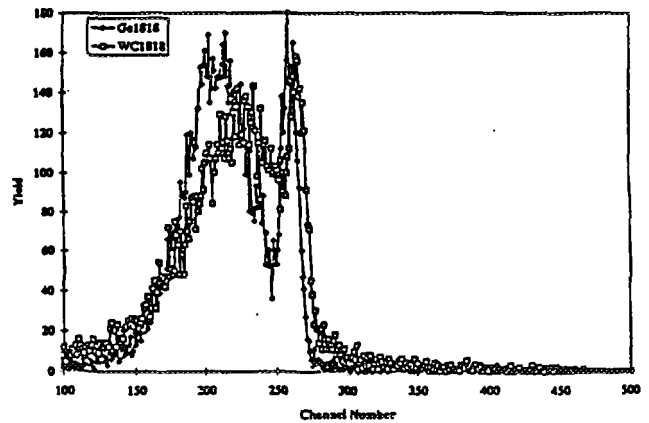


Table 1.

Comparison of FWHM hydrogen implanted profile peak width from ERD experiment and TRIM simulation ( in fractions of hydrogen ion projected range ).

Scattering angle [°]	Carbon	Silicon	Germanium	Tungsten Carbide
24	0.34	0.56	0.67	1.23
30	0.42	0.58	0.87	1.38
36	----	----	1.08	1.60
TRIM	0.10	0.24	0.42	0.55

The average angle of multiple scattering in the sample material is strongly dependent on the atomic number (Z)

and may, in the case of the ERD analysis, substantially contribute to the final depth resolution due to very strong recoil energy angular dependence ( $-\cos^2$ ). The FWHM of multiple scattering angular distributions was estimated using the method of Sigmund and Winterbon [9,10]. In the carbon sample, the total width ( FWHM ) of the angular distribution for He and H ions for  $30^\circ$  scattering angle (  $15^\circ, 15^\circ$  ) is about  $0.93^\circ$  ; however in tungsten carbide, the total width is about  $3.31^\circ$ . Similar results were obtained using the TRIM-90 program in transmission mode with angular directions of transmitted ions recorded and final distributions analysed [7]. Equivalent TRIM-90 results were  $0.92^\circ$  for carbon and  $3.25^\circ$  for tungsten carbide. These multiple scattering angular widths are equivalent according to ERD kinematic calculations to energy widths of about 41 keV in carbon and 149 keV in tungsten carbide or 11 and 39 channels respectively on Fig 3.

The total theoretically estimated implanted hydrogen peak width in the case of  $30^\circ$  scattering in carbon material, including ion implantation projected range straggling, ERD He and H energy straggling, detector and experimental system resolution and multiple scattering effect in carbon is about 17 channels (64 keV). The same quantity for tungsten carbide material is about 51 channels (190 keV). The carbon result agrees well with the experimental data shown on Fig 3 (FWHM=19 channels); however in the tungsten carbide case the experimental width ( about 78 channels ) is about 50% wider than theoretical predictions.

In all shown ERD spectra, the sensitivity is limited by a continuous almost constant background level in the low energy region well below the implanted hydrogen peak. This background level is well visible in samples with high atomic number Z, see tungsten carbide spectra on Figs 1 and 3 or germanium spectra on Figs 2 and 4. Table 2 shows these background levels measured as a function of sample and scattering angle used in this work. The total hydrogen counts are also shown. The background level increases with atomic number of the sample material Z, decreases with increasing ERD scattering angle and is almost proportional to the total hydrogen counts.

It is suggested from this data that this background is mostly generated by double scattering which includes He or H small angle scattering on a heavy sample atom ( strong Z dependence ) and hydrogen forward recoil scattering.

The secondary scattering background can be theoretically estimated using Rutherford scattering cross-sections for the half of the nominal ERD angle and involved material stopping powers. This simple calculation shows that for the case of  $24^\circ$  ERD in tungsten carbide the secondary scattering background in the 500 keV region ( 134 channels ) is estimated to be about 7% of the total of the hydrogen peak area. This very simple estimate agree reasonably with experimental background levels shown in table 2 and on Fig. 1.

**Table 2.**

Comparison of averaged low energy background ( backg ) in counts per channel and total hydrogen counts ( H count ) in spectra shown on Figs 1-5.

Scattering angle [°]	Carbon		Silicon		Germanium		Tungsten Carbide	
	backg	H count	backg	H count	backg	H count	backg	H count
24	2.14	14374	2.87	10692	8.30	25558	20.85	25367
30	1.48	10079	1.86	7582	4.30	15716	10.00	16551
36	----	----	----	----	2.80	11868	5.73	12294

#### 4. Conclusions

Multiple scattering of He and H ions in the sample material is a major factor limiting the depth resolution of hydrogen detection using ERD at depths around 400 nm or more. This effect shows a very strong Z dependence and in heavy materials the depth resolution is very low. The sensitivity of hydrogen detection is limited by low energy background, mostly generated by double scattering in the sample material. This background level is proportional to the amount of hydrogen present in the sample surface layer and increases with the Z of the sample material. The relative level of this background is reduced with increasing ERD scattering angle.

#### References

- [1] L. S. Wielunski, R. E. Benenson and W.A. Lanford, Nucl. Instr. and Meth. in Phys. Res. 218 (1983) 120.
- [2] A. Turos and O. Meyer, Nucl. Instr. and Meth. in Phys. Res. B 4 (1984) 92.
- [3] J. E. E. Baglin, A. J. Kellock, V. R. Deline, M. A. Crockett and A. H. Shih, Nucl. Instr. and Meth. in Phys. Res. B 64 (1992) 469.
- [4] L. Wielunski, R. Benenson, K. Horn and W. A. Lanford, Nucl. Instr. and Meth. in Phys. Res. B 15 (1986) 469.
- [5] E. Szilagyi, F. Paszti, V. Quillet and F. Abel, Nucl. Instr. and Meth. in Phys. Res. B 85 (1994) 63.
- [6] E. Szilagyi and F. Paszti, Nucl. Instr. and Meth. in Phys. Res. B 85 (1994) 616.
- [7] J. P. Biersack, Nucl. Instr. and Meth. in Phys. Res. B 27 (1987) 21.
- [8] W. K. Chu and J. F. Ziegler in: Ion Beam Handbook for Materials Analysis, eds J. W. Mayer and E Rimini ( Academic Press, Inc. New York 1977 ) p. 8.
- [9] Ion Beams for Materials Analysis, eds J. R. Bird and J. S. Williams ( Academic Press, Sydney 1989 ) p. 620.
- [10] P. Sigmund and K. B. Winterbon, Nucl. Instr. and Meth. 119 (1974) 541.



# Study of Multiple Scattering Effects in Heavy Ion RBS

Z. Fang<sup>†</sup> and D.J. O'Connor

Department of Physics, The University of Newcastle, NSW 2308, Australia

## Abstract

Multiple scattering effect is normally neglected in conventional RBS analysis. The backscattered particle yield normally agrees well with the theory based on the single scattering model. However, when heavy incident ions are used such as in HIRBS, or the incident ion energy is reduced, multiple scattering effect starts to play a role in the analysis. In this paper, we present the experimental data of 6MeV C ions backscattered from a Au target. In measured time of flight spectrum, a small step in front of the Au high energy edge is observed. The high energy edge of the step is about 3.4ns ahead of the Au signal which corresponds to an energy ~300keV higher than the 135° single scattering energy. This value coincides with the double scattering energy of C ion undergoes two consecutive 67.5° scattering.

Efforts have been given to investigate the origin of the high energy step observed. This leads to an Monte Carlo simulation aimed to reproduce the experimental spectrum on computer. As a large angle scattering event is a rare event, two consecutive large angle scattering is extremely hard to reproduce in a random simulation process. Obviously faster algorithms and a better physical model are necessary for a successful simulation.

## 1. INTRODUCTION

Multiple scattering effect is generally overlooked in conventional RBS analysis. The calculated spectrum using single scattering model and unscreened Coulomb interaction (Doolittle (1)) agrees satisfactorily with the experiment. However as the energy of the incident ions is reduced, the measured spectra show significant differences with the calculation (Weber et al (2-4)). In the forward recoil measurement using 2.9MeV He<sup>++</sup> impinged on SiH<sub>x</sub> films (Replinger et al (5)), the forward scattered H spectrum exhibits a low energy tail which can not be explained by the single scattering theory. The plural and multiple scattering effect as well as the electronic screening in the interaction potential need to be considered.

Qualitatively, the behaviour of plural and multiple scattering is quite well understood. In low energy ion scattering, the double scattering peak is clearly observed and can be used to indicate a certain surface structure (Shen et al (6)). Although it was proposed more than twenty years ago (Verhey et al (7)) that computer simulation could be used to generate spectrum with double scattering effect included to compare with the measurement, a well established method taking advantage of the double scattering effect is still under development.

The plural and multiple scattering theory on small angle elastic scattering of charged particles is relatively well established (e.g. Wentzel (8), Bielajew (9)). The theory provides the probability for a particle scattering into a polar angle  $\theta$  after a total flight path length  $l$ . The small angle approximation in formalizing the equations has ruled out its application in large angle backscattering analysis. However, the theory does indicate that a wide-angle scattering comes predominantly from a single event rather than many small-angle events. This has shed some light on the simulation of the backscattering process, with plural and multiple scattering effects included. An paper by Smit (10) presented an interesting way to consider the plural and multiple scattering contribution to RBS yield. Although the

---

<sup>†</sup> Current address: ESM center, The Flinders University of South Australia, Adelaide, SA 5001.

validity of the model is limited to light ion and heavy target, to  $\sim 180^\circ$  scattering angle, and to the high energy part of the spectra, it indicates that ion trajectories with different numbers of collisions contribute to the total scattering yield in a way similar to the double scattering process. Therefore the double scattering process is explicitly considered as an essential contribution. As Smit's major purpose in (10) is to obtain a factor to correct the single scattering spectrum, the double scattering contribution in the energy range higher than the single scattering energy is neglected.

Monte Carlo computer simulation has been claimed by Biersack et al (11-13) to be the only way to obtain more realistic results. The modified TRIM program (Biersack et al (11, 14)), has been optimised to calculate RBS spectra in a more efficient way. The result, obtained in a reasonable computing time, agrees well with the experimental data. However, no efforts has been made to study the double scattering process which leads to backscattered particles with energies higher than the single scattering energy.

## 2. EXPERIMENT

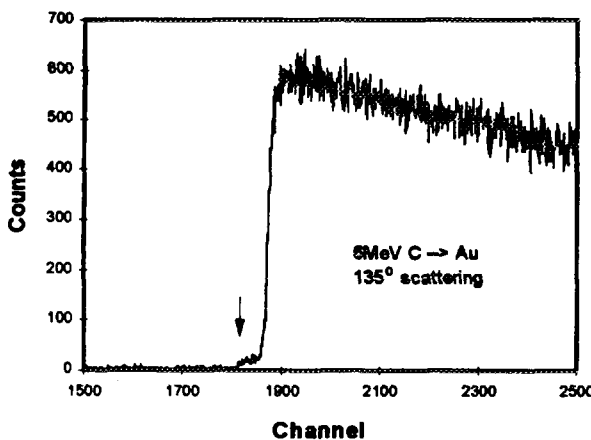


Fig. 1 The TOF spectrum of 6MeV C ions scattered into  $135^\circ$  from a thick Au (100) sample. The channel width is 60ps.

High energy C ions generated from the 14UD accelerator (ANU, Canberra) were used as the incident beam for HIRBS analysis. The scattered particles were collected by a time of flight (TOF) detector aligned in a  $135^\circ$  angle to the incident beam. The beam is perpendicular to the sample surface hence the exit angle is  $45^\circ$ . The TOF detector has a solid angle  $0.4\text{mstr}$  and a flight path length 1m (Fang (15)). In the measured random spectrum of 6MeV C scattered from Au (100) sample, a small step in the high energy part of the spectrum is observed (indicated in fig. 1 by an arrow). A direct measurement from the spectrum reveals that the step extends out of the Au leading edge for about  $3.4 \pm 0.1\text{ns}$ . Such a phenomenon was observed as well in C scattering into  $90^\circ$  from Au, but not in other C-Si or C-GaAs measurements.

## 3. DISCUSSION

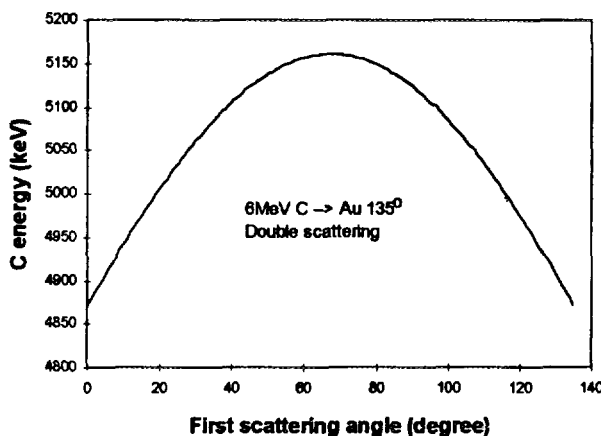


Fig.2 C ion energy as a function of the first scattering angle. The double scattering energy equals to the single scattering energy if the first scattering angle is  $0^\circ$  or  $135^\circ$ .

A carbon ion scattered from a Au atom with  $135^\circ$  scattering angle has an energy  $k_{135}E_0$ , where  $k$  is the kinematic factor. For  $E_0=6\text{MeV}$ , the single scattering energy is 4.872MeV. As indicated in fig.2, a C ion undergoes two  $67.5^\circ$  scattering will have an energy  $(k_{67.5})^2 E_0$ , which is 5.161MeV. Over the 1m flight path length, the 5.161MeV C has a flight time 3.2ns shorter than the 4.872MeV C, which agrees well with the observation. Therefore we assume the small step in fig.1 is caused by double scattering effect.

To quantitatively explain the spectrum shown in fig. 1, one needs to introduce a model to calculate the shape of the small step to facilitate comparison with the experiment. Such a task involves a

quantitative estimation on the population of the double scattering events. As indicated in Smit's paper, double scattering events are even popular than the single scattering events. However, it should be noticed that the mean flight path length between two large angle scattering events is quite large (11) and the particle will, on average, lose a significant amount of energy before the second scattering event. The double scattering contribution is then mainly on the low energy part of the spectrum and C ion leaving the sample with an energy higher than the single scattering energy becomes a rare event.

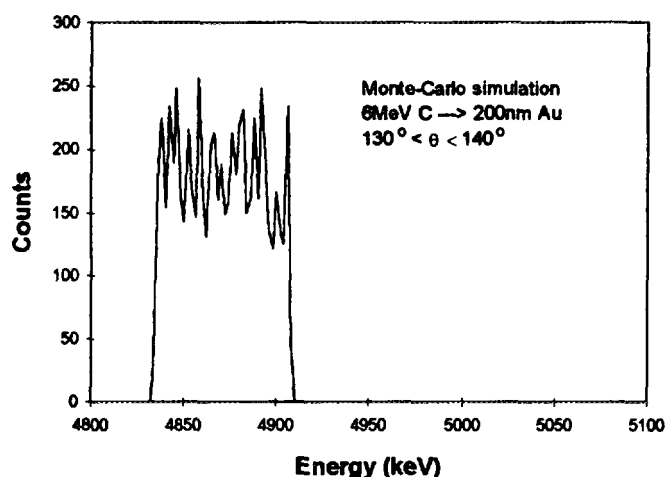


Fig. 3 The simulated HIRBS spectrum of 6MeV C scattering into  $130^\circ - 140^\circ$  from a  $2000\text{\AA}$  Au (100) film.

A Monte Carlo simulation has been carried out to account for the small step observed in fig.1. The physical model used in the simulation is similar to the one described in (11). Since the simulation is concentrated on the high energy part of the spectrum, C ions with energies lower than a certain value will not be followed. A crystal target Au (100) was used to give a more realistic simulation. A fast algorithm for scattering angle under the ZBL universal potential is used and the stopping power is calculated from an empirical formula given by Rauhala (16). Unfortunately, as shown in fig.3, the simulation has not found a particle scattering into  $130^\circ - 140^\circ$  with an energy higher than the single scattering energy. As pointed earlier, two consecutive

large angle scattering is a rare event, improvement in the simulation efficiency is necessary to catch such events. Also a better method to generate a large amount of random numbers without repetition is required in this Monte Carlo simulation.

#### ACKNOWLEDGMENT

The authors would like to thank Professor J.A. Davies and Dr. H.J. Whitlow for their valuable suggestions.

#### REFERENCES:

- [1] L.R. Doolittle, (1985) Nucl. Instr. and Meth. B9, p344.
- [2] A. Weber, H. Mommsen, W. Sarter and A. Weller, (1982) Nucl. Instr. and Meth. Vol.198, p527
- [3] A. Weber, and H. Mommsen, (1984) Nucl. Instr. and Meth. B4, p79
- [4] A. Weber, Q. Fazly and H. Mommsen, (1983) Nucl. Instr. and Meth. Vol.204, p559
- [5] F. Reppinger, J.P. Stoquert and P. Siffert, (1993) Nucl. Instr. and Meth. B80/81, p24
- [6] Y.G. Shen, D.J. O'Connor, K. Wandelt and R.J. MacDonald, (1995) Surface science 328(1-2), p21
- [7] L.K. Verhey and A.L. Boers, (1973) Atomic Collisions in Solids, eds. S. Datz, B.R. Appleton and C.D. Moak, Plenum Press, New York, p583
- [8] G. Wentzel, (1922) Ann. Phys. 69, p335
- [9] A.F. Bielajew, (1994) Nucl. Instr. and Meth. B86, p257
- [10] Z. Smit, (1993) Physical Review A 48(3), p2070
- [11] J.P. Biersack, E. Steinbauer and P. Bauer, (1991) Nucl. Instr. and Meth. B61, p77
- [12] P. Bauer, E. Steinbauer and J.P. Biersack (1992) Nucl. Instr. and Meth. B64, p711
- [13] E. Steinbauer, P. Bauer and J.P. Biersack, (1990) Nucl. Instr. and Meth. B45, p171
- [14] J.P. Biersack and L.G. Haggmark, (1980) Nucl. Instr. and Meth. Vol.174, p257
- [15] Z. Fang, (1994) PhD thesis: Time of Flight Detector and Its Application in High Energy Heavy Ion Scattering.
- [16] E. Rauhala, in: Proc. High Energy and Heavy Ion Beams in Materials Analysis, Albuquerque, eds. J.R. Tesmer, C.J. Maggiore, M. Nastasi, J.C. Barbour and J.W. Mayer (Materials Research Society, Pittsburgh, PA), p61



# Ion-Beam Synthesis of $\text{Ge}_x\text{Si}_{1-x}$ Strained Layers for High-Speed Electronic Device Applications

**R.G. ELLIMAN, H. JIANG, W.C. WONG AND P. KRINGHØJ**  
Electronic Materials Engineering Department,  
R.S.Phys.S.E., Australian National University, Canberra, ACT 0200.

## SUMMARY

It is shown that  $\text{Ge}_x\text{Si}_{1-x}$  strained layers can be fabricated by Ge implantation and solid-phase epitaxy and that the use of these layers can improve the performance of electronic devices. Several materials science issues are addressed, including the effect of Ge on solid-phase-epitaxy, the effect of oxidation on the implanted Ge distribution, and the effect of Ge on the oxidation rate of Si. The process is demonstrated for metal-oxide-semiconductor field-effect-transistors (MOSFETs).

## INTRODUCTION

GeSi/Si strained-layer heterostructures have great potential for high-speed electronic and optoelectronic device applications [Bean (1)]. For example, GeSi-MOSFETs are expected to operate faster than Si devices due to the higher carrier mobility in GeSi alloys. To date research on the use of GeSi layers has concentrated on GeSi/Si heterostructures grown by either molecular-beam-epitaxy (MBE) or chemical-vapour-deposition (CVD) [Nayak (2)]. However, simple GeSi/Si strained-layer heterostructures can also be fabricated by Ge ion-implantation and solid-phase epitaxial-growth (SPEG) [Paine et al (3), Elliman et al (4), Elliman and Wong (5)]. Although this process is less flexible than MBE or CVD, it does offer a simple, inexpensive alternative for the fabrication of simple device structures such as MOSFETs [Jiang and Elliman (6)]. This paper examines some of the materials-science issues associated with ion-beam synthesised GeSi/Si strained layer heterostructures and demonstrates the potential of this approach for MOSFET fabrication.

## EXPERIMENTAL

Experiments were designed around two device structures: surface-channel MOSFETs, where the GeSi channel region was formed by segregating implanted Ge during oxidation, Fig. 1a, and buried-channel devices, where the GeSi channel was formed at a depth greater than the oxide thickness, Fig. 1b. Surface-channel structures were formed by 30 keV Ge ( $R_p=22\text{nm}$ ) implants at doses of  $0.5 - 4.0 \times 10^{16} \text{ Ge.cm}^{-2}$ , followed by the growth of a 100 nm thick oxide (100 min. at  $1000^\circ\text{C}$ ). Buried-channel structures were formed by 90 keV Ge ions ( $R_p=60\text{nm}$ ) implanted to doses of  $1.0 - 6.0 \times 10^{16} \text{ Ge.cm}^{-2}$ , followed by the growth of a 50 nm oxide (35 min. at  $1000^\circ\text{C}$ ). The processing steps employed to make MOSFETs are summarised in Fig. 2. Bulk samples were characterised using Rutherford backscattering spectrometry and channelling (RBS-C), double crystal x-ray diffraction (DCXRD), and transmission electron microscopy (TEM).

## RESULTS AND DISCUSSION

### a) Solid-Phase Epitaxy of Ge Implanted Si

The effect of Ge on SPEG can be understood from RBS-C measurements. Fig. 3 shows the channelled yield in the implanted layer (90 keV Ge) after SPEG at  $600^\circ\text{C}$  as a function of Ge dose. The sudden increase in yield for Ge doses above  $3.5 \times 10^{16} \text{ Ge.cm}^{-2}$  is indicative of strain relaxation. This suggests that fully strained GeSi/Si heterostructures can only be produced for doses less than this critical value and that strain relief occurs during SPEG for doses greater than this value. TEM and DCXRD analysis, combined with similar studies at higher implant energy (800 keV Ge) [Elliman and Wong (4), Elliman et al (5)], confirm this interpretation and show that strain relaxation occurs via strain induced roughening of the crystalline-amorphous interface. A high density of threading dislocations was observed in samples implanted above the critical dose. Such defects are expected to have a deleterious effect on the electrical properties of the GeSi alloy. MOSFETs with Ge doses greater than the critical dose are therefore expected to be inferior to those implanted at doses lower than the critical dose.

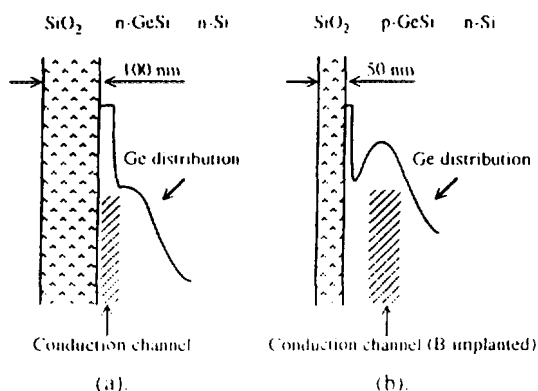


**Figure 1.** SiO<sub>2</sub>/GeSi/Si structures for a) surface-channel p-MOSFETs and b) buried-channel MOSFETs.

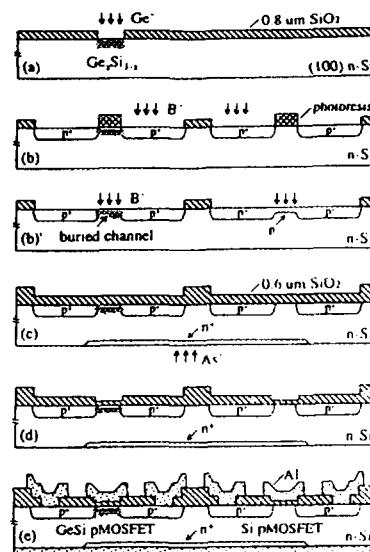
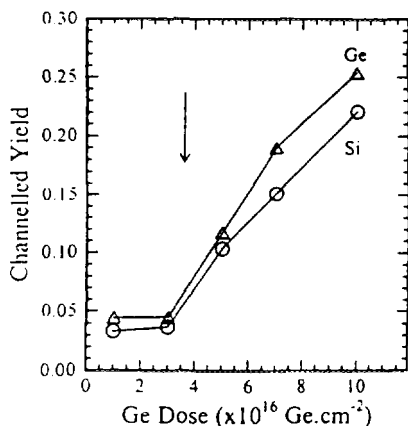


**Figure 2.** Device fabrication. a) Ge implantation for channel region, b) source/drain doping, b') B-doping for buried-channel devices only, c) SiO<sub>2</sub> deposition and backside doping, d) gate opening and oxide growth, and e) opening of contact windows and metallisation.

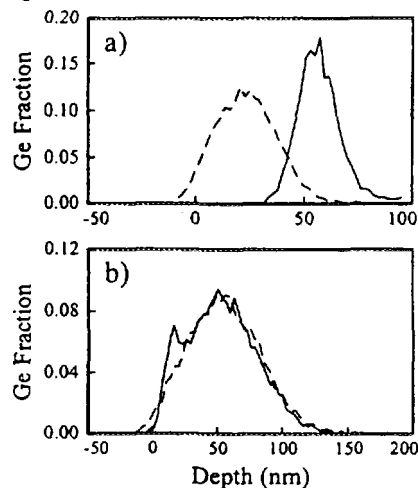
### b) Ge Redistribution during Oxidation of Ge Implanted Si

Fig. 4 shows Ge distributions, before and after oxide growth. For surface-channel structures, Fig. 4a, where the thickness of Si consumed during oxidation is greater than the projected range of the Ge, complete redistribution of the Ge is observed and the Ge concentration at the oxide-semiconductor interface exceeds that of the as-implanted Ge. (The depth resolution of the measurement is 11 nm, suggesting that the Ge concentration is even higher than the 17% shown). For buried-channel structures, Fig. 4b, where the thickness of Si consumed, 15 nm, is much less than the projected range of the Ge, only limited near-surface segregation is observed and no diffusive broadening of the profile is evident.

TEM analysis after oxidation revealed the presence of end-of-range loops. These dislocations form at the original amorphous-crystalline interface produced by Ge implantation, and grow during oxidation. They are mainly concentrated in the region beneath the GeSi alloy layer and are not expected to have a significant effect on device performance.



**Figure 3.** Channelled RBS yields as a function of Ge dose for 90 keV implants. The arrow indicates the maximum dose for fully strained SPEG [Paine et al (3)].



**Figure 4.** Ge profiles before (dashed) and after (solid) oxide growth. a) 30 keV,  $1.7 \times 10^{16} \text{ Ge.cm}^{-2}$ ,  $t_{\text{ox}} = 100 \text{ nm}$ , and b) 90 keV,  $3.1 \times 10^{16} \text{ Ge.cm}^{-2}$ ,  $t_{\text{ox}} = 50 \text{ nm}$ .

### c) The Effect of Ge on the Oxidation Rate of Si

Transconductance measurements were used to evaluate the performance of MOSFETs and to estimate the hole mobility in the GeSi channel region of these devices. The transconductance,  $g_d$ , of the MOSFET is given by:

$$g_d = e\mu_p WC_{\text{ox}}(V_G - V_T)/L \quad (1)$$

where  $e$  is the electronic charge,  $\mu_p$  is the hole mobility,  $W$  is the channel width,  $V_G$  is the gate voltage,  $V_T$  is the threshold voltage,  $L$  is the gate length, and  $C_{ox}$  is the capacitance of the gate oxide, given by:  $\epsilon_{ox}/t_{ox}$ , where  $\epsilon_{ox}$  is the permittivity ( $\sim 0.34 \times 10^{-12}$  F/cm) and  $t_{ox}$  the thickness of the oxide. Since the transconductance is directly proportional to the hole mobility and inversely proportional to the gate oxide thickness, determination of the oxide thickness is essential for an accurate estimate of the hole mobility.

Fig. 5 shows the normalised gate oxide thickness as a function of implant dose, as measured by RBS-C. The results clearly show that implanted Ge enhances the oxidation rate for surface channel structures, where the Ge concentration at the oxide-semiconductor interface is high. No change in oxide thickness was observed for buried-channel structures.

#### d) Device Performance

Transconductance measurements were made on a range of MOSFETs with different geometries [Jiang and Elliman (6)]. These were used to determine the hole mobility in the GeSi channel region of MOSFETs according to equation 1. Fig. 6 shows the mobility as a function of Ge dose for surface- and buried-channel devices. The results are corrected for variations in the gate oxide thickness and show a maximum mobility enhancement of 37% for surface-channel devices implanted with a dose of  $1.7 \times 10^{16}$  Ge.cm<sup>-2</sup>. The decrease in mobility for the highest implant doses is a consequence of strain relief during SPEG. The Ge dose is above the critical value.

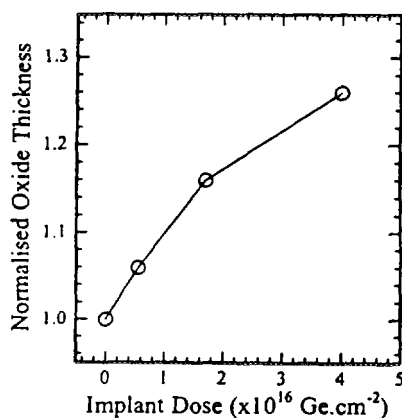


Figure 5. Gate oxide thickness as a function of Ge implant dose for surface-channel structures.

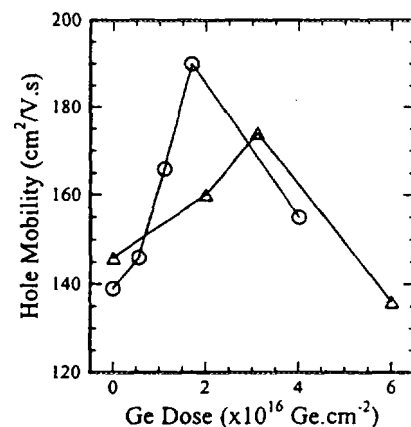


Figure 6. Hole mobility versus Ge dose for surface-channel (circles) and buried-channel (triangles) devices.

## CONCLUSIONS

This study demonstrated the feasibility of ion-beam synthesised GeSi alloy layers for the fabrication of high speed electronic devices and highlighted the importance of materials science studies in understanding the processing and its limitations. It was shown that: i) fully strained GeSi/Si heterostructures can be fabricated by Ge implantation and solid-phase epitaxial-crystallisation provided the Ge dose is below a critical value., ii) the segregation of Ge during the oxidation of GeSi alloy layers can be used to synthesise thin, high concentration alloy layers, iii) that the presence of high Ge concentration at the SiO<sub>2</sub>/Si interface enhances the oxidation rate of Si, and iv) ion-beam-synthesised GeSi alloy layers can be employed to improve the performance of integrated electronic devices, such as MOSFETs.

## REFERENCES

1. Bean, J.C., (1992). 'Silicon-Based Semiconductor Heterostructures: Column IV Bandgap Engineering', *Proceeding of the IEEE*, **80**, 571-587.
2. Nayak, D.K., Woo, J.C.S., Wang G.K., and MacWilliam K.P. (1991), 'Enhancement-Mode Quantum-Well Ge<sub>x</sub>Si<sub>1-x</sub> PMOS', *IEEE Electron Dev. Lett.*, **12**, 154-156.
3. Paine, D.C., Howard, D.J., and Stoffel, N.G., (1991), 'Strain Relief in Compositionally Graded Si<sub>1-x</sub>Ge<sub>x</sub> Formed by High Dose Ion Implantation', *J. Electron. Mat.*, **20**, 735-746.
4. Elliman, R.G., and Wong, W.C., (1993), 'The Fabrication of Epitaxial Ge<sub>x</sub>Si<sub>1-x</sub> Layers by Ion Implantation', *Nucl. Instr. Meth.* **B80/81**, 768-772.
5. Elliman R.G., Wong W.C. and Kringhoj, P., (1994), 'Solid-Phase Epitaxial Crystallisation of Ge<sub>x</sub>Si<sub>1-x</sub> Alloy Layers', *Mat. Res. Soc. Symp. Proc.* **321**, 375-385.
6. Jiang, H. and Elliman, R.G., (1996). 'Electrical Properties of GeSi Surface- and Buried-Channel P-MOSFETs Fabricated by Ge Implantation', *IEEE Trans. Electron. Dev.*, (In Press).



# The Influence of Microscopic and Macroscopic Non-Stoichiometry on Interfacial Planarity during the Solid-Phase Epitaxial Growth of Amorphized GaAs

K.B.Belay<sup>a</sup>, M.C.Ridgway<sup>a</sup> and D.J.Llewellyn<sup>a,b</sup>

<sup>a</sup> Department of Electronic Materials Engineering, Research School of Physical Sciences and Engineering, Australian National University, Canberra, Australia

<sup>b</sup> Electron Microscopy Unit, Australian National University, Canberra, Australia

## ABSTRACT

The influence of microscopic and macroscopic non-stoichiometry on the Solid-Phase Epitaxial Growth of GaAs has been studied. Ion implantation has been employed to produce microscopic non-stoichiometry via Ga and As implants and macroscopic non-stoichiometry via Ga or As implants. In-situ Time Resolved Reflectivity and Transmission Electron Microscopy and ex-situ Rutherford Backscattering Spectroscopy and Channeling have been used to investigate the regrowth of amorphized GaAs layers. As non-stoichiometry shifts from microscopic to macroscopic the interface loses its planar nature and subsequently gets rougher.

## INTRODUCTION

Owing to its potential applications in electronic and optoelectronic device fabrication, a number of research groups have devoted their work to the effects of irradiation-induced damage and subsequent annealing on the semi insulating properties of GaAs. Low-temperature Solid-Phase Epitaxial Growth (SPEG) of irradiation-induced amorphous layers of GaAs has been demonstrated (1-7). SPEG is a thermally-activated process. It is the reordering of the amorphous layer on the underlying crystal structure in an epitaxial manner. In GaAs, the layer immediate to the substrate is single crystalline bordered by a thick and highly defective layer. The effect of microscopic and macroscopic non-stoichiometry on interfacial non-planarity is the subject of this report.

Amorphous layers with microscopic and macroscopic non-stoichiometry were considered. Macroscopic and microscopic non-stoichiometry can be formed by implanting As and / or Ga into GaAs where the amount of disorder for a given dose, is approximately the same for all ion species. In macroscopic non-stoichiometry the one-to-one ratio of the constituent atoms is not maintained where as in microscopic non-stoichiometry the excess of either of the constituent atoms is localized. Their effect on the crystalline / amorphous (c/a)-interface morphology during the regrowth process has been studied using in-situ Time Resolved Reflectivity (TRR) and Cross-Sectional Transmission Electron Microscopy (XTEM) and ex-situ Rutherford Backscattering Spectroscopy and Channeling (RBS/C), Belay et al (3). At present we shall concentrate on the TRR analysis.

## EXPERIMENTAL

To form amorphous layers of the desired thickness and stoichiometric imbalance, semi-insulating (100) GaAs substrates were implanted at -196°C with <sup>75</sup>As<sup>+</sup> ions and / or <sup>69</sup>Ga<sup>+</sup> ions at an energy of 200keV and 190keV, respectively, to fluences in the range 3e14 - 3e15 /cm<sup>2</sup>, Belay et al (4).

A schematic diagram of the TRR technique is depicted in Fig. 1. A 3x3 mm<sup>2</sup>, as-implanted sample of GaAs is placed on a hot stage kept at a temperature of 260°C in air. In - situ TRR was used to monitor the regrowth process. Light is reflected from the sample surface and the c/a-interface. When the c/a-interface proceeds towards the surface the intensity of the reflected light oscillates due to constructive or destructive interference related to the position of the interface, A or B in the figure. The magnitude of the TRR signal (reflectivity) is indicative of the interface structure, Licoppe et al (5). The decrease in the intensity of the signal indicates that the structure of the interface is transforming

from planar to non-planar. Based on this concept we will show how the morphology of the c/a -interface deteriorates as the non-stoichiometry shifts from microscopic to macroscopic for a given initial amorphous layer width.

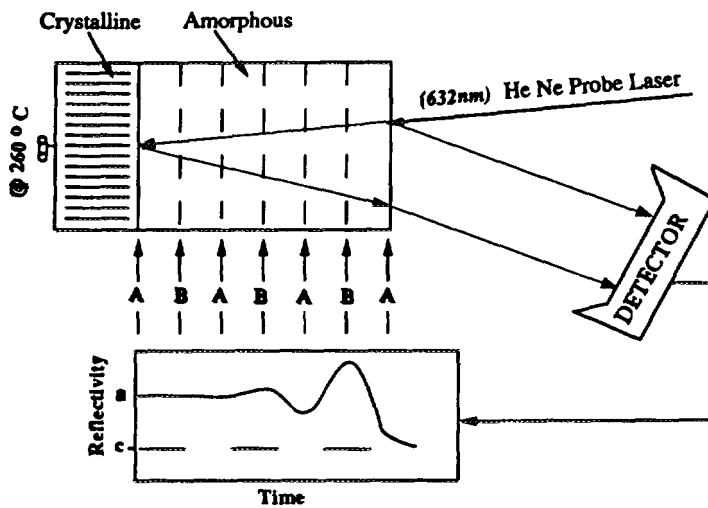


Fig.1 Schematic of the TRR technique used in this study.

## RESULTS AND DISCUSSION

Fig. 2 shows the TRR spectra as a function of fluence for (a) Ga and As, (b) Ga and (c) As implants. Cross correlating the figures is invalid given differences in gain. However, the figures are internally consistent. In all cases, during the first ~ 300 sec of annealing time, the attenuation of the modulation amplitude increases with time. This is characteristic of the roughening evolution of the c/a - interface during regrowth, Licoppe et al (6).

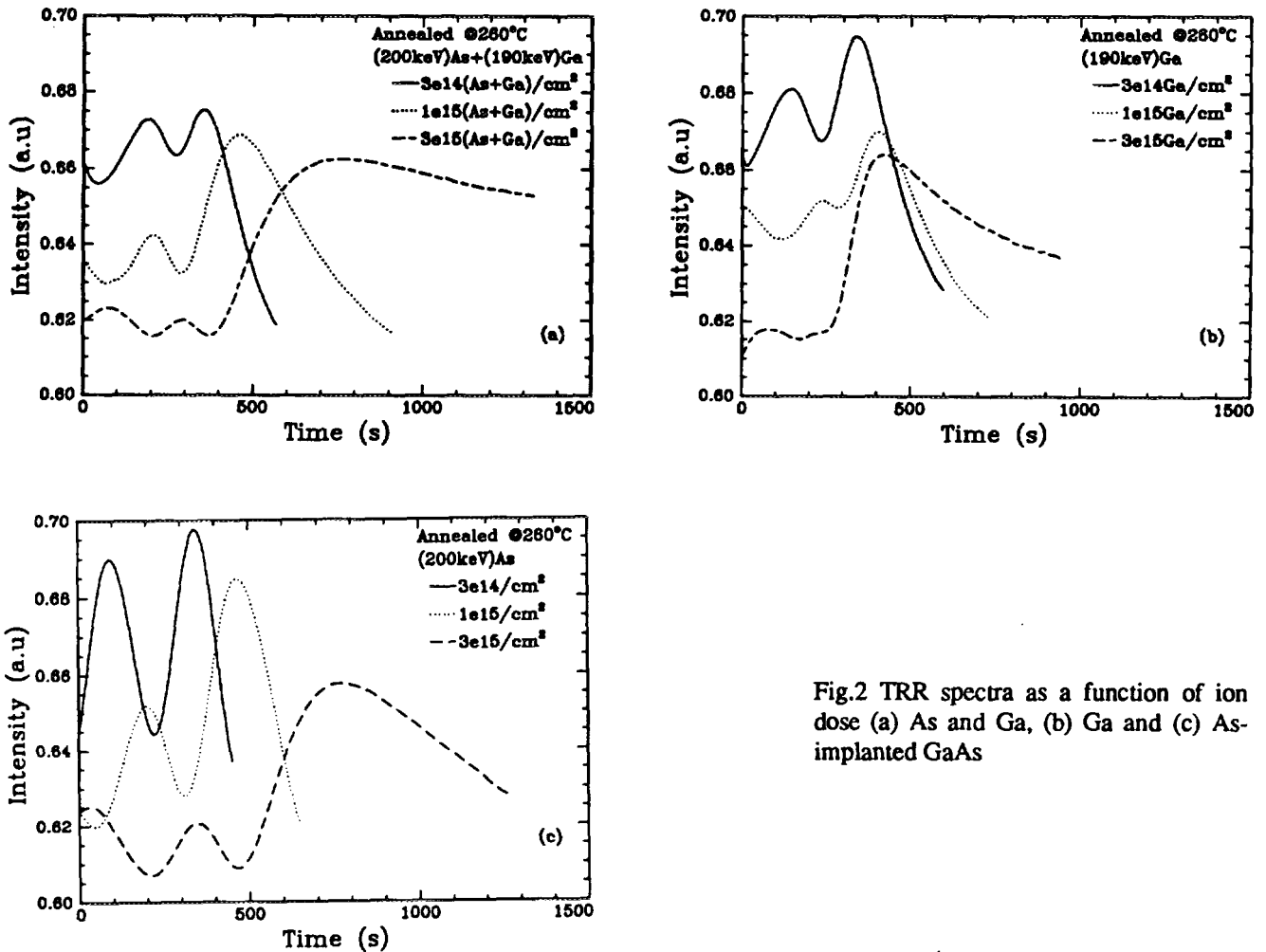


Fig.2 TRR spectra as a function of ion dose (a) As and Ga, (b) Ga and (c) As-implanted GaAs

In Fig. 3, the ratio of the amplitude of the first oscillation, for the low dose, and the corresponding oscillation, for the higher doses, as a function of initial amorphous depth is shown. It indicates that the roughening rate of the interface is greater in the Ga or As-implanted layer than in the Ga-and-As implanted layer. From the same figure it is evident that the effect of Ga-rich non-stoichiometry has a greater influence than the As-rich case which is in good agreement with XTEM analysis, Belay et al (7). This is potentially due to the presence of molten Ga precipitates which may favour rapid regrowth.

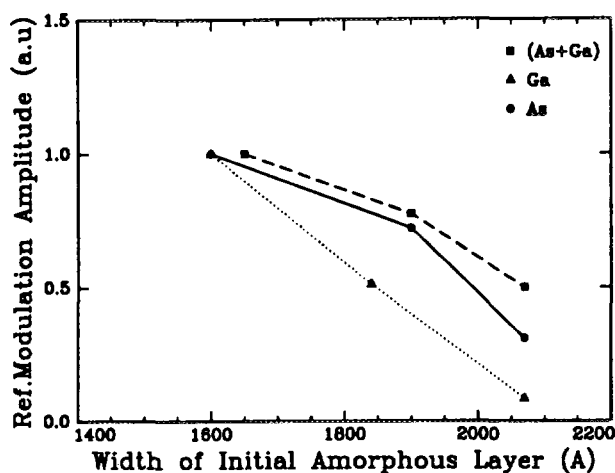


Fig.3 Amplitude oscillation of the reflectivity signal as a function of amorphous layer width prior to recrystallization

## CONCLUSION

Macroscopic non-stoichiometry significantly affects the morphology of the *c/a*-interface during the SPEG of amorphous GaAs layers. Macroscopic Ga-rich non-stoichiometry has greater effect than that of excess As.

## REFERENCES

- (1) Christel L.A. and Gibbons J.F. (1981), Stoichiometric disturbances in ion implanted compound semiconductors, *J. Appl. Phys.* **52**(8), 5050-5055.
- (2) Kaminska M., Weber E.R. and Jagadish C., (1994), Defects in non-stoichiometric III-V Compounds, Proceedings of 8<sup>th</sup> Conference on Semi-insulating III-V Materials, June 6-10, 327-334.
- (3) Belay K.B., Llewellyn D.J. and Ridgway M.C., to be published.
- (4) Belay K.B., Llewellyn D.J. and Ridgway M.C., (1995), The influence of implantation-induced non-stoichiometry on solid-phase epitaxial growth of amorphized GaAs, and the references there in, (IBMM'95), in press.
- (5) Licoppe C., Nissim Y.I., Meriadec C. and Krauz P., (1986), Interface structure evolution and impurity effects during solid-phase epitaxial growth in GaAs, *J. Appl. Phys.* **60**(4) 1352-1358.
- (6) Licoppe C., Nissim Y.I., Krauz P. and Henoc P., (1986), Solid phase epitaxial regrowth of ion-implanted InP, *Appl. Phys. Lett.* **49**(6), 316-318.
- (7) Belay K.B., Llewellyn D.J. and Ridgway M.C., (1995), Low-temperature solid-phase epitaxial growth of amorphized, non-stoichiometric GaAs, (MRS SPRING'95), in press.

# Heavy Ion Time-of-Flight ERDA of High Dose Metal Implanted Germanium

N. DYTLEWSKI<sup>1</sup>, P.J. EVANS<sup>1</sup>, J.T. NOORMAN<sup>1</sup>, L.S. WIELUNSKI<sup>2</sup> and J. BUNDER<sup>3</sup>

<sup>1</sup>Australian Nuclear Science and Technology Organisation, PMB 1, Menai NSW 2234

<sup>2</sup>CSIRO Division of Applied Physics, Lindfield, NSW

<sup>3</sup>Physics Dept., University of Wollongong, Wollongong, NSW

## INTRODUCTION

In silicon microelectronic technologies, the use of transition metal-silicides for contacts and interconnects has been the subject of much study. These metal silicides can be formed by depositing a metal layer on a Si substrate, followed by thermal annealing at a few hundred degrees Celsius. Of particular interest are  $\text{CoSi}_2$  and  $\text{TiSi}_2$ , both of which have good thermal stability and low resistivity. These metal-silicides, amongst others, can also be formed directly by ion implantation techniques [1]. With the emerging development of GaAs and  $\text{Si}_x\text{Ge}_{1-x}$  based microelectronic devices, the use of metal-germanides for thermodynamically stable metallisation contacts is being considered [2-7]. Low resistivity metal-germanides such as  $\text{CoGe}_2$ ,  $\text{TiGe}_2$  and  $\text{Cu}_3\text{Ge}$  have been produced by thermal annealing, but to our knowledge, there have been no reported attempts to produce metal-germanides directly by metal ion implantation.

Although germanium has the same crystal structure and similar chemical properties to silicon, the metal-germanides can have different thermodynamic properties as compared to their corresponding silicides. For example,  $\text{Cu}_3\text{Ge}$  is stable in air up to at least  $600^\circ\text{C}$  [2], whereas  $\text{Cu}_3\text{Si}$  is catalytically oxidised in air at room temperature resulting in the formation of a layer of  $\text{SiO}_2$  according to the reaction  $\text{Cu}_3\text{Si} + \text{O}_2 \rightarrow \text{SiO}_2 + 3\text{Cu}$  [8]. Furthermore, the oxidation characteristics of Ge have been seen to be significantly different from Si [9]. The application of RBS analysis for metal-silicide studies is adequate, as the light Si substrate permits oxygen uptake to be observed, as well as providing sufficient mass and depth resolution to profile the reacted transition metal species. This is not always the case for metal-germanides, unless very thin layer samples are prepared on light substrates. The reaction of Ti with Ge by thermal annealing a deposited bilayer has been observed to start near  $450^\circ\text{C}$ , with the formation of a compound identified by X-ray diffraction as  $\text{Ti}_6\text{Ge}_5$  [4]. The reaction in a Cu+Ge bilayer has been observed to start near  $200^\circ\text{C}$ , with  $\text{Cu}_3\text{Ge}$  being formed [2,10]. The necessary conditions to form a layer of metal-germanide by ion implantation are unknown, and may not even be possible, as the diffusion constants and solubilities of the implanted species in Ge are uncertain, as well as ion beam sputtering effects being more significant for implantation into Ge, as compared with Si. Hence the implanted doses could be sputter limited. The formation of  $\text{Cu}_3\text{Ge}$  by ion implantation is unlikely, due to the high atomic fraction of Cu required.

With the thick Ge substrates used in ion implantation, RBS can have difficulty in resolving the mass-depth ambiguities when analysing materials composed of mixtures of elements with nearly equal masses. Additional, and complimentary techniques are thus required. This paper reports the use of heavy ion time-of-flight ERDA, and conventional RBS in the analysis of Ge(100) implanted with high dose Ti and Cu ions from a MEVVA ion source [11]. Heavy ion ToF ERDA has been used to resolve, and profile the implanted transition metal species, and also to study any oxygen incorporation into the sample resulting from the implantation, or subsequential reactions with air or moisture. This work is part of a study on high dose metal ion implantation of medium atomic weight semiconductor materials.

## EXPERIMENTAL

Wafers of (100) n-type Ge were implanted at normal incidence with ions from a metal vapour vacuum arc (MEVVA) ion implanter, operating with an extraction voltage of 40 kV. In a MEVVA ion source, the ion beam contains a mixture of charge states, with the average charge state being 2.1 for Ti and 2.0 for Cu [12]. Incident ion doses for all samples were determined from calibration plots which correlated the retained dose obtained from RBS analysis with the integrated charge collected on the target holder. The latter neglects the contribution of secondary electron emission as no electron suppression was applied to the target holder. However, numerous measurements over a wide range of implant conditions have found the relationship between collected charge and retained dose to be approximately linear providing sputtering is negligible. Thus, the dose ranges employed for the above calibrations were restricted to values which fulfilled the latter condition. For higher doses, the incident dose was determined by extrapolation, for which the maximum uncertainty was estimated to be  $\pm 10\%$ .

Implantations were made at ambient temperature,  $200^\circ\text{C}$  and  $300^\circ\text{C}$ , and for Ti, an additional implant at  $370^\circ\text{C}$ . In experiments at elevated temperatures, a strip of cut Ge(100) wafer was clamped to a heated sample holder which incorporated a thermocouple. The MEVVA ion source, being a high current pulsed implanter causes some beam induced heating of the sample surface. The attached thermocouple cannot measure these pulsed excursions in the surface temperature, however from previous calculations done in this laboratory, the surface temperature could rise to approx.  $100^\circ\text{C}$  above that of the bulk substrate. Implanted samples were left to cool to near ambient temperature before

removal from the vacuum chamber. RBS measurements were made using a 2.0 MeV  $^4\text{He}$  ion beam with a backscatter detector at  $160^\circ$ . Samples were mounted in a computerised goniometer which can automatically adjust the sample orientation to select either a randomly rotated or channelled spectrum. Heavy ion ToF ERDA measurements were made on the ANTARES Tandem Accelerator using a 76 MeV iodine beam, with recoiled particles being detected at  $45^\circ$  using a time-of-flight plus total energy spectrometer [13].

## RESULTS

### A. Cu-Ge reaction

It is difficult to obtain a reliable estimate of the depth distribution of Cu implanted into Ge using RBS, as the backscatter energies from these two elements are nearly the same. Heavy ion ToF ERDA can provide sufficient mass separation to resolve these two elements as is shown in fig.1 for the  $300^\circ\text{C}$  implant. In this figure, five separate mass tracks are observed, corresponding to O, Al, Cu, Ge and some scattered I. The short length (depth) of the observed aluminium arises from co-implantation of sputter deposited material, from aluminium clamps holding the germanium sample in the target holder. The inset spectrum is an expanded view of the recoil spectrum from approximately the first  $1000\text{\AA}$  below the Ge surface, and shows that the Cu recoils can be separated from the Ge. By extracting the Cu recoils from the recorded data set, and subdividing and plotting the event density as a function of recoil energy, a histogram depicting the event yield (concentration) is obtained as shown in fig. 2.

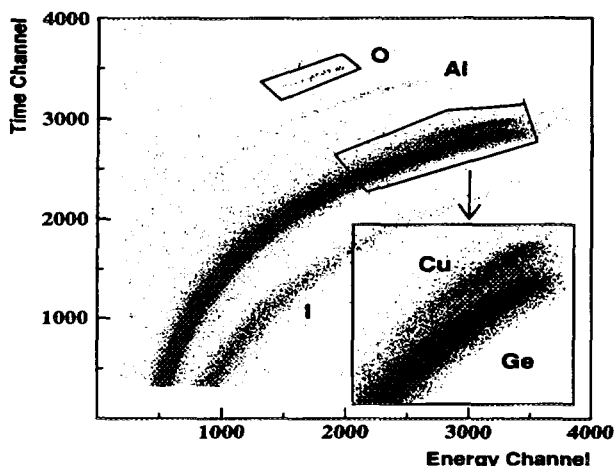


Fig.1 ToF ERDA spectrum of Cu implanted Ge at  $300^\circ\text{C}$ . The inset is a magnified view of the near surface region showing the Cu resolved from the Ge. The small amount of co-implanted oxygen is indicated.

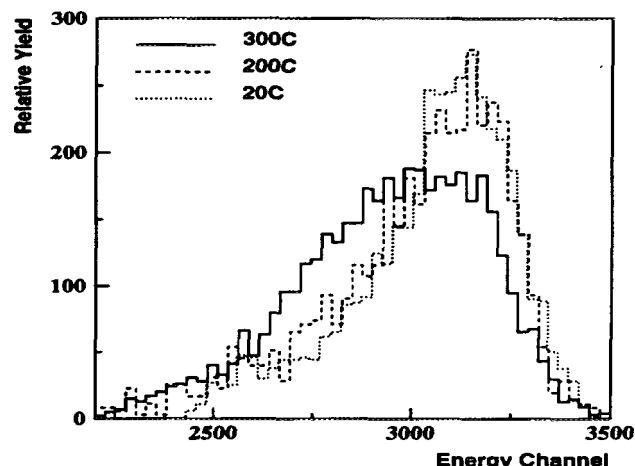


Fig. 2 Recoil yield profiles of Cu implanted into Ge at  $20^\circ\text{C}$ ,  $200^\circ\text{C}$  and  $300^\circ\text{C}$ . All histograms have been normalised to the same integrated area.

Fig. 2 shows a comparison between the implanted copper profiles obtained with different germanium substrate temperatures. The applied incident ion dose from the MEVVA implanter was  $3 \times 10^{17}$  atoms/cm<sup>2</sup>. It is seen that at  $20^\circ\text{C}$  and  $200^\circ\text{C}$ , there is essentially no difference in the copper profiles, but a change has occurred at  $300^\circ\text{C}$ , with the copper redistributing to a greater depth. This is consistent with the reaction temperature in a Cu+Ge bilayer [2,10]. The prepared samples were left in air for approximately 4 weeks before measurement, in order to allow time for any reaction with oxygen or water vapour that may occur. In thermal annealing reactions using thin deposited bilayers, the reacted product is in a crystalline form. With ion implantation however, the implanted region is highly damaged, and so may provide a more rapid diffusion, or alternate reaction pathway to effects not observed with conventional thermal annealing. As seen in fig. 1, there has been essentially no reaction as indicated by the small oxygen recoil yield. This recoil yield is consistent that previously observed by us in other work, and is due to a combination of direct co-implanted oxygen from the MEVVA ion source, and ballistically implanted oxygen. The extent of the oxygen profile is consistent with that calculated by TRIM-90.

### B. Ti-Ge reaction

Fig. 3 shows the randomly rotated RBS spectrum of Ge(100) implanted with Ti, at a substrate temperature of  $370^\circ\text{C}$ , and clearly shows a step at the germanium surface resulting from the titanium admixture. An incident Ti ion dose of  $5 \times 10^{17}$  atoms/cm<sup>2</sup> was applied. The shape of this RBS spectra can be described approximately by a RUMP simulation, using a homogeneous surface layer of approximate average composition  $\text{GeTi}_{0.8}$ . The layer thickness increases with increasing implantation temperature. This simulation is illustrated in fig. 4 for the  $370^\circ\text{C}$  implant, where the contributions to the backscatter yield from the implanted Ti, and Ge from the surface layer and bulk are shown. A surface layer of thickness  $1000\text{\AA}$  has been used.

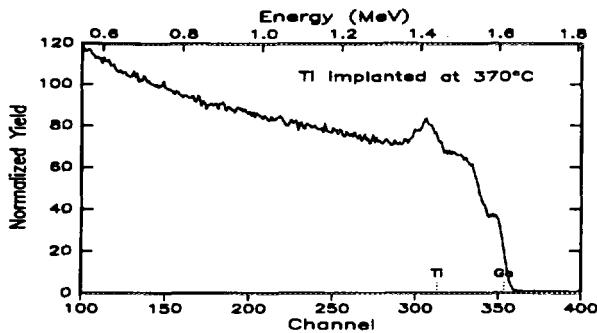


Fig. 3 Randomly rotated RBS spectrum of Ti implanted into Ge at 370°C, with an incident dose of  $5 \times 10^{17}$  atoms/cm<sup>2</sup>.

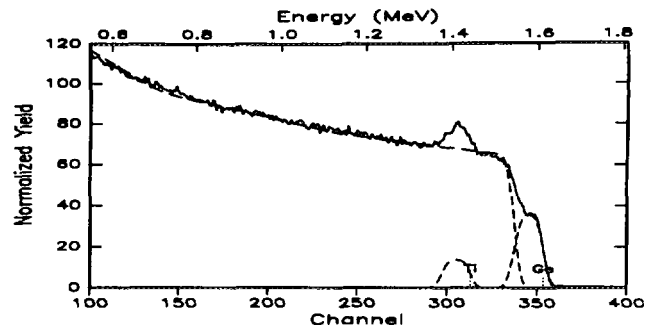


Fig. 4 Simulation of the RBS spectrum showing the separate contributions from Ti and Ge in the implanted layer and the bulk. Best stoichiometry fit is GeTi<sub>0.8</sub>.

Heavy ion ToF measurements were also made on these titanium implanted samples, with the raw data plot for the 370°C sample shown in fig. 5. The inset spectrum is the oxygen yield profile of the boxed region of interest, and shows some co-implanted oxygen as well as a much larger surface peak. This surface peak, which is absent in the copper implantations, is likely due to the uptake of some oxygen by the titanium, as titanium has a high affinity to form TiO<sub>2</sub>. Relative concentration profiles for titanium have been obtained in an analogous way to that for copper, with the results shown in fig. 6. It is seen that the profile centroid moves to lower recoil energies (greater depth) as the implant temperature increases, as well as a broadening of the distribution.

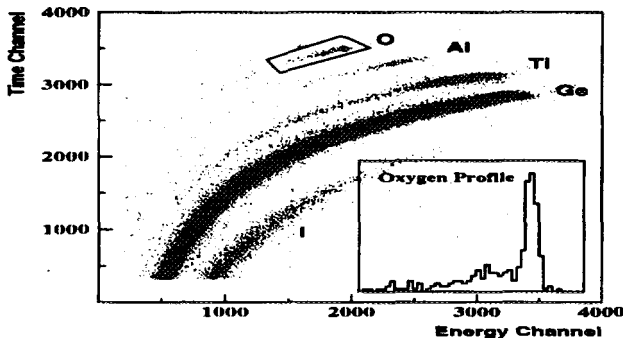


Fig. 5 ToF ERDA spectrum of Ti implanted into Ge. The inset spectrum is the oxygen recoil yield profile contained in the boxed region of interest.

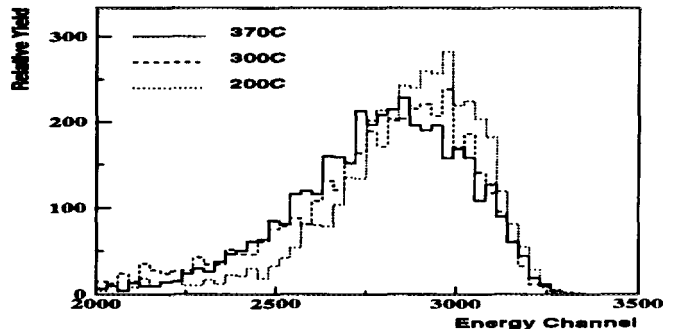


Fig. 6 Recoil yield profiles for Ti implanted into Ge at 200°C, 300°C and 370°C. All histograms have been normalised to the same integrated area.

## DISCUSSION

Heavy ion ToF ERDA has been demonstrated to provide information on the depth distribution of implanted transition metal ions in thick germanium substrates. A change in the implantation profile for copper is observed at temperatures consistent with that using thermal annealing. Implantation of titanium shows that as the substrate temperature increases, so does the thickness of the implanted surface layer, with an average stoichiometry of approximately GeTi<sub>0.8</sub>. Work is in progress to upgrade the MEVVA heater assembly to study implantation effects in the region 450°C to 500°C, where the Ti+Ge reaction has been observed to occur in thermally annealed bilayers.

## REFERENCES

- [1] S. Mantl, Nucl. Inst. Meth. B80 (1993) 895.
- [2] L. Krusin-Elbaum and M.O. Aboelfotoh, Appl. Phys. Lett. 58 (1991) 1341.
- [3] Jian Li, Q.Z. Hong and J.W. Mayer, J. Appl. Phys. 66 (1989) 3600.
- [4] O. Thomas, S. Delage, F.M. d'Heurle and G. Scillia, Appl. Phys. Lett. (1989) 228.
- [5] S.P. Ashburn, M.C. Öztürk, G. Harris and D.M. Maher, J. Appl. Phys. 74 (1993) 4455.
- [6] T.K. Marais, E. Taylor, M. Ndwande, B. Spoelstra and R. Pretorius, Nucl. Inst. Meth. B85 (1994) 183.
- [7] E.D. Marshall, C.S. Wu, C.S. Pai, D.M. Scott and S.S. Lau, Mater. Res. Soc. Symp. Proc. 47 (1985) 161.
- [8] J.M.E. Harper, A. Charai, L. Stolt, F.M. d'Heurle and P.M. Fryer, Appl. Phys. Lett. 56 (1990) 2519.
- [9] K. Prabhakaran and T. Ogino, Surf. Sci. 325 (1995) 263.
- [10] S. Q. Hong, C. M. Comrie, S. W. Russell and J. W. Mayer, J. Appl. Phys. 70 (1991) 3655.
- [11] I.G. Brown, J.E. Galvin, B.F. Gavin and R.A. MacGill, Rev. Sci. Instrum. 57 (1986) 1069.
- [12] I.G. Brown and X. Godechot, IEEE Trans. Plasma Sci. vol. 19 (1991) 713.
- [13] J.W. Martin, D.D. Cohen, N. Dytlewski, D.B. Garton, H.J. Whitlow and G.J. Russell, Nucl. Inst. Meth. B94 (1994) 277.

# Defects Formed During Ion Beam Modification Of Diamond

\*NUGENT K.W., PRAWER S., DOOLEY S.P. and JAMIESON, D.N.  
 Micro Analytical Research Centre, School of Physics  
 University of Melbourne, Parkville VIC 3052

The doping of diamond for semiconductor use by ion implantation causes new problems compared with the well known cases of Si and GaAs. These problems are related to the strongly directional nature of carbon-carbon bonding and to the formation of C=C bonds. This results in the formation of a large variety of specific comparatively stable defects being formed upon ion implantation. The presence of the double bonded defects is expected to have a large influence on the electrical properties of the resultant material. Also as a consequence of these attributes of carbon, there is the problem of the metastability of diamond and the ease of graphite formation during implantation or annealing.

Raman spectroscopy was found to be sensitive to the presence of these specific defects and also to the overall level of damage produced in the sample when diamond was implanted with doses in the range of  $10^{16}$ - $10^{18}$  ions/cm<sup>2</sup> H or He with energies greater than 1 MeV. The main series of experiments discussed herein used  $1 \times 10^{16}$ - $3 \times 10^{17}$  ions/cm<sup>2</sup> of 3.5 MeV He<sup>+</sup>.

Use of a geometry, shown in Figure 1, in which ions were implanted into the edge of a diamond slab allowed the damage to be measured as a function of distance along the ion track by both Channeling Contrast Microscopy (CCM)<sup>1</sup> and Raman spectroscopy.

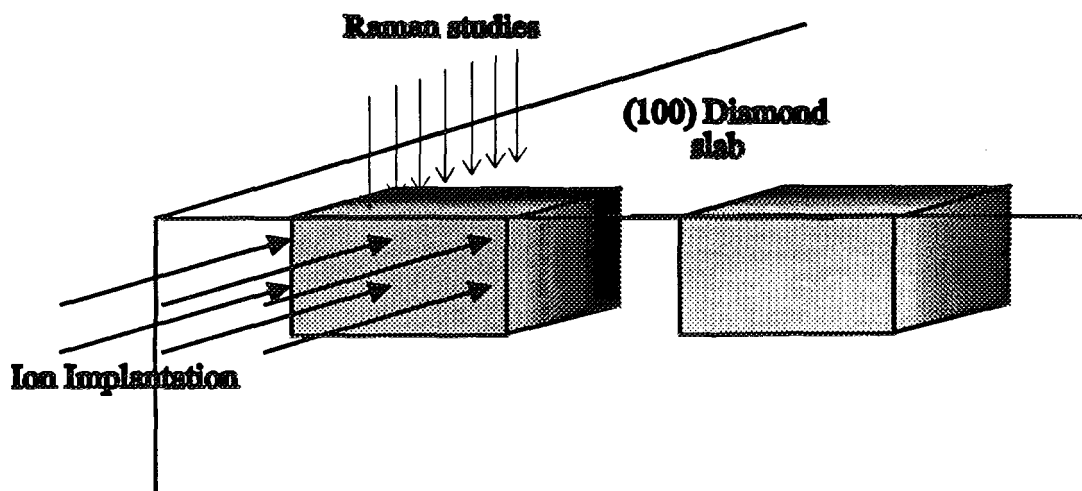


Figure 1. The geometry used for Raman (and CCM) studies relative to the original ion implantation.

Comparison of the data taken at the same distance along the ion track for the range of ion doses used showed that the shift in the diamond line position from that of virgin diamond was linear with ion dose. The shift in the diamond line to lower energy with increased dose is consistent with measurements of diamond under externally applied stress in that a shift to lower energy is observed for tensile stress, and the presence of defects in the lattice produces a tensile strain, evidenced by the swelling of the implanted region. The diamond line position was therefore confirmed to be a sensitive experimental measurement of damage. The shift in the diamond line as a function of distance along the ion path for a given dose was then compared with TRIM predictions. The comparison showed that TRIM overestimates the damage in the region approaching end of range, possibly due to the effects of dynamic annealing.

The specific defects mentioned above are characterised by a number of sharp peaks in the range  $1350\text{-}1700\text{ cm}^{-1}$ , the most important being those at  $\sim 1490\text{ cm}^{-1}$  and  $\sim 1630\text{ cm}^{-1}$ , as shown in Figure 2. The sharpness of the peaks indicates that only a limited number of specific defects are produced, rather than a range of related defects. The peaks have been further shown to be Raman rather than luminescence peaks by looking at the dependence of the spectrum on the exciting wavelength. These defects are produced when diamond is implanted with a range of ions, including H, He, C, P and As. As the same defect peaks are observed for a variety of ions, including C and He, the defects must contain only carbon atoms. The positions of the peaks in the Raman spectrum, at higher energy than the diamond peak, lead to the assignment of these peaks as arising from double bonded defects. Comparison of the dose dependence and annealing behaviour of the defect peaks showed that two main defects are formed, and these are respectively assigned as due to interstitial C atoms (giving rise to the  $1630\text{ cm}^{-1}$  peak) and to an ordered array of vacancies (most of the other peaks). Temperatures of up to  $1000^\circ\text{C}$  are required to anneal these defects.

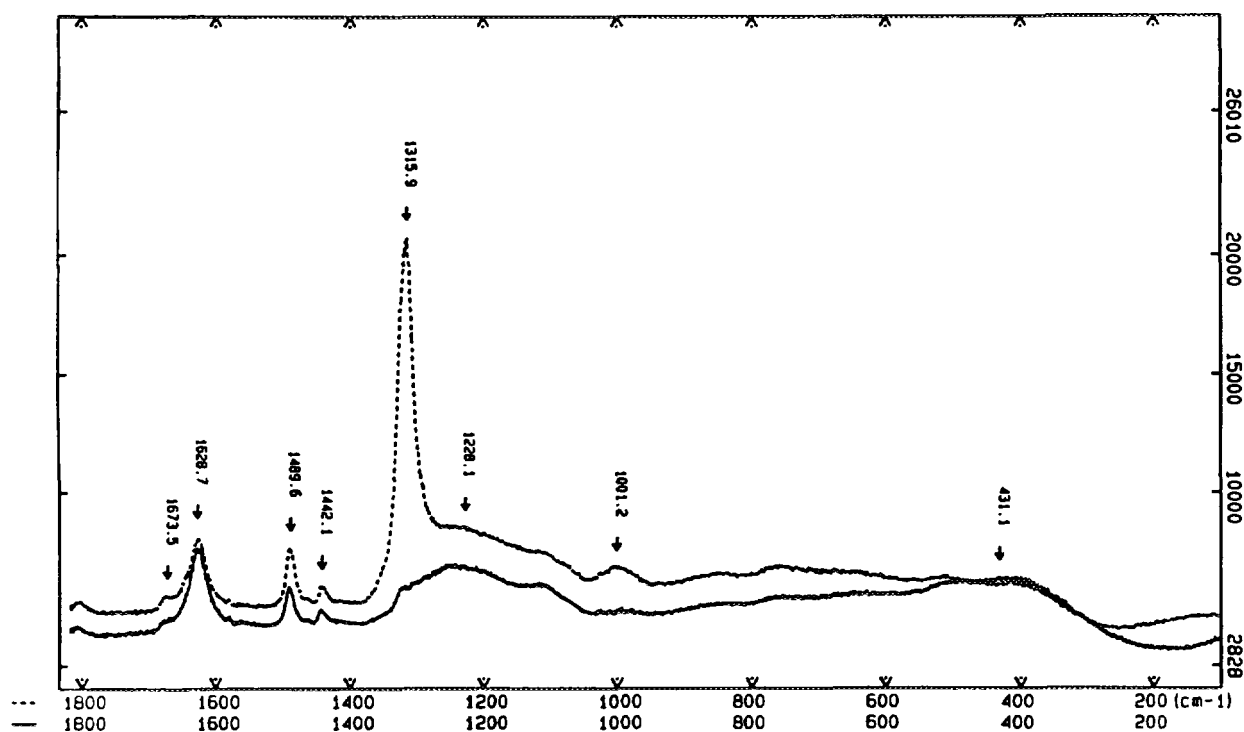


Figure 2. The Raman spectra for parallel and perpendicular polarisations of aligned (100) diamond implanted with  $1 \times 10^{17}$  ions/cm<sup>2</sup> 3.5 MeV He. The spectra were recorded near the beginning of the ion track. The perpendicular spectrum includes a strong diamond peak at  $1317\text{ cm}^{-1}$ . For unimplanted diamond this peak is observed at  $1332\text{ cm}^{-1}$ .

A further point of interest in the Raman spectrum is the presence of the broad peak to the low energy side of the diamond line. This is assigned as due to the presence of diamond like carbon (DLC, "amorphous diamond"), although it is very unlike the spectrum of chemically produced DLC, which is dominated by resonance enhanced peaks from  $sp^2$  clusters.

#### REFERENCES

1. Dooley, S.P, Jamieson, D.N, Nugent, K. W. and Prawer, S. "Transverse Microanalysis of High Energy Ion Implants" AINSE 1995



# Accelerator Mass Spectrometry: State of the Art

CLAUDIO TUNIZ

Australian Nuclear Science and Technology Organisation  
Private Mail Bag 1, Menai, NSW 2234, Australia

## SUMMARY

Accelerator Mass Spectrometry (AMS) is the analytical technique of choice for the detection of long-lived radionuclides which cannot be practically analysed with decay counting or conventional mass spectrometry. The main use of AMS has been in the analysis of radiocarbon and other cosmogenic radionuclides for archaeological, geological and environmental applications. In addition, AMS has been recently applied in biomedicine to study exposure of human tissues to chemicals and biomolecules at attomole levels. There is also a world-wide effort to analyse rare nuclides of heavier masses, such as long-lived actinides, with important applications in safeguards and nuclear waste disposal. The use of AMS is limited by the expensive accelerator technology required and there are several attempts to develop smaller and cheaper AMS spectrometers.

## INTRODUCTION

In AMS, the intrinsic analytical properties of ion accelerators are exploited to perform ultra-sensitive isotopic analyses. In particular, high energies allow molecular fragmentation and identification of nuclear mass and charge in an ion detector. The high selectivity achieved for the isotope of interest makes possible measurements of isotopic ratios some four or five orders of magnitude smaller than is possible with conventional mass spectrometry (MS). In particular, AMS allows an isotopic sensitivity of one part in  $10^{15}$  for  $^{14}\text{C}$  (5.73 ka),  $^{10}\text{Be}$  (1.6 Ma),  $^{26}\text{Al}$  (720 ka),  $^{36}\text{Cl}$  (301 ka),  $^{41}\text{Ca}$  (104 ka),  $^{129}\text{I}$  (16 Ma) and other long-lived radionuclides occurring in nature at ultra-trace levels. The sensitivity of AMS is unaffected by the half-life of the isotope being measured, since the atoms not the radiations that result from their decay, are counted directly. Hence, the efficiency of AMS in the detection of long-lived radionuclides is  $10^6 - 10^9$  times higher than decay counting and the size of the sample required for analysis is reduced accordingly. For example,  $^{14}\text{C}$  has been analysed in samples containing as little as 20  $\mu\text{g}$  carbon. The precision of AMS measurements (0.2 - 2%) is adequate for a wide range of applications. AMS has demonstrated the capability to provide a precision of 0.2 - 0.3% for the radiocarbon analysis of 'recent' samples, comparable to decay counting. In general, AMS can achieve higher precision in the radiocarbon analysis of 'old' samples and has the potential to reach greater ages because of the low background (as an example, a date of  $55,100 \pm 2300$  a BP was recently obtained at ANTARES for a shell).

## CHOICE OF ACCELERATOR

Electrostatic tandem accelerators are the optimum choice for a variety of AMS applications. Small tandems (2 - 3 MV) have been specifically designed for  $^{14}\text{C}$  analysis, Purser (1). These relatively low energy accelerators can also be used to detect other long-lived radioisotopes, such as  $^{10}\text{Be}$ ,  $^{26}\text{Al}$  and  $^{129}\text{I}$  or stable isotopes. Larger tandem accelerators, originally developed for nuclear physics research, are used to analyse a variety of rare radionuclides, Tuniz et al. (2). In this case, higher energies allow an effective separation of isobaric interferences and radionuclides such as  $^{36}\text{Cl}$  and  $^{41}\text{Ca}$  can be detected in natural samples.

Other accelerators, e.g. cyclotrons, were used for early AMS attempts to measure long-lived cosmogenic radioisotopes. An AMS system based on a small cyclotron has been recently developed to detect  $^{14}\text{C}$  at natural abundances, but its practical use will require further developments to allow precise measurements of isotopic ratios, Mao- Chen et al. (3). Linacs with positive ion sources have been applied for the detection of long-lived radioisotopes of noble gases such as  $^{39}\text{Ar}$  and  $^{81-85}\text{Kr}$ , Kutschera (4).

## AMS WITH TANDEM ACCELERATORS

Negative ions are produced in a sputter ion source and, after energy and mass analysis, are injected into the tandem accelerator. High precision AMS measurements are carried out by either using simultaneous injection or rapid

sequential injection of the isotopes of interest. Simultaneous injection restricts the range of masses analysed and has been recently adopted in commercial accelerators dedicated to radiocarbon analysis. Sequential injection, achieved by modulating the ion energy, allows the development of more versatile systems, suitable for high precision analysis of a wide range of isotopes. After their injection, negative ions are attracted by the positive voltage at the terminal and thereby accelerated to energies of 2 - 15 MeV, at which point they pass through a gas or a carbon stripper foil and are stripped of some of their electrons. Multi-charged positive ions are then further accelerated by the same positive voltage on the terminal. The stripping process is used to intercept all the molecular interferences which are the main limitation for conventional mass spectrometry. After the acceleration stage, double focussing magnets, Wien filters, electrostatic analysers and gas-filled magnets provide the selectivity necessary to separate the radioisotope of interest. Finally, identification of the rare isotope is performed in the ion detector. Depending on the isotopes to be analysed, a variety of detectors are available for this final stage of the AMS spectrometer such as ionisation chambers and time-of-flight detectors. Energy, stopping power, range and velocity are measured to identify the isotopes of interest. New approaches based on selective laser induced ionisation and detection of ion induced x-rays are being attempted to separate isobaric interferences.

## AMS APPLICATIONS

Radionuclides are useful tracers and chronometers in many disciplines: geology, archaeology, astrophysics, biomedicine and materials science. Low-level decay counting techniques have been developed in the last 40-50 years to detect the concentration of cosmogenic, radiogenic and anthropogenic radionuclides in a variety of specimens. Radioactivity measurements for long-lived radionuclides, such as  $^{10}\text{Be}$ ,  $^{14}\text{C}$ , etc., are made difficult by low counting rates and in some cases the need for complicated radiochemistry procedures and efficient detectors of soft beta particles and low energy x-rays. AMS can measure these long-lived radionuclides in natural samples up to  $10^6$  times smaller than those required for conventional techniques, allowing novel applications in the aforementioned disciplines. Some examples are illustrated in the following.

### Palaeoenvironment

Tree rings, polar ice and other materials serve as archives of the environmental conditions in the past to study changes in the natural system. The high sensitivity of AMS makes possible radiocarbon measurements in individual tree rings and  $\text{CO}_2$  trapped in annual layers of ice (typically, only 10-20  $\mu\text{g}$  of carbon are available from 1 kg of ice).  $^{10}\text{Be}$  can be measured in one kg of ice (one ton of ice would be necessary with conventional techniques). The fossil record of these natural radioisotopes is useful to understand the variability of the environmental system and its response to solar and bio-geological forcing. For example,  $^{14}\text{C}$  and  $^{10}\text{Be}$ , cosmogenically produced in the atmosphere and deposited in permanent terrestrial reservoirs, vary in concentration in a way that correlates with the 11 year sunspot cycle and the sunspot-free period known as the Maunder Minimum (1650-1700 AD).

### Geophysics

$^{10}\text{Be}$ ,  $^{14}\text{C}$ ,  $^{26}\text{Al}$  and  $^{36}\text{Cl}$  are also produced in-situ in the shallow horizons of the Earth's crust via neutron and muon interactions. AMS detection of these radionuclides is possible in ten grams of rock exposed for as little as 10 ka. The analysis of these radionuclides have been used to study: erosion rates, exposure ages of surfaces, chronology of volcanic flows and movement of sand dunes.

### Oceanography

Measurements of  $^{14}\text{C}$  in seawater provides evidence of rates of movement and mixing of surface waters into the main body of the ocean. A major advantage of AMS is that 100 ml of seawater provides sufficient carbon for  $^{14}\text{C}$  measurements. A new generation of dedicated AMS facilities has been designed specifically for oceanographic studies particularly for high throughput, high precision measurements in programs such as WOCE (World Ocean Circulation Experiment)

### Archaeology

Radiocarbon dating has provided an absolute time scale of great importance for the study of human history during the last 40 ka and AMS has had a major impact on radiocarbon dating. For example,  $^{14}\text{C}$  measurements are now being made on sub-milligram masses of well defined chemical fractions isolated from ancient bones. The results have overthrown much of the evidence purported to document human entry into North America before 12 ka BP. The study of ancient agriculture can now proceed from the dating of single seeds rather than from the dating of grams of charcoal bearing an uncertain relation to the seeds. Similarly, ancient rock paintings can be dated from the carbon present in the pigments themselves rather than in material found nearby. Laser-induced combustion and AMS have been recently used to date single laminae in 2 mm thick rock surface accretions, a very useful method to study prehistoric paintings and engravings.

## Biomedicine

Biomedical applications of AMS include: dosimetry of toxins, carcinogens and mutagens at levels of  $10^{-18}$  mole; pharmacokinetic studies of  $^{14}\text{C}$ -labelled compounds with tracing through multiple organs and excreta as a function of dose and time;  $^{26}\text{Al}$  in studies of uptake, toxicity, excretion and possible links with conditions such as Alzheimer's disease;  $^{41}\text{Ca}$  in studies of bone resorption, uptake and deposition in heart tissue.

## Materials and Industrial Science

Radioactive tracers are widely used in industry. Pilot studies carried out with AMS have explored the behaviour of  $^{14}\text{C}$  labelled compounds during combustion. Stable-isotope AMS has also been tested for determining specific isotopes at ultra-trace levels in semiconductors and other materials. AMS promises to be yet another valuable tool in the development of advanced materials. The fabrication of today's most advanced integrated circuits involves a very complex technology. With shrinking device dimensions and thicknesses of insulating layers down to 10 nm, it has become imperative to control contamination at the level of  $10^{12}$  atoms/cm<sup>3</sup>.

## Nuclear safeguards and environmental monitoring

AMS is being proposed as the analytical technique of choice in the detection of radionuclides that can be used to trace specific nuclear activities: reactor operations and nuclear explosions ( $^{14}\text{C}$ ,  $^{36}\text{Cl}$ ,  $^{129}\text{I}$ ,  $^3\text{H}$ ), fuel reprocessing: ( $^{129}\text{I}$ , U-Pu) and Uranium enrichment (U isotopes).

## PROSPECTS

In almost two decades, AMS has made many major contributions to science and further progress can be expected in a number of different aspects:

i) *New radioisotopes.*  $^{32}\text{Si}$ ,  $^{44}\text{Ti}$ ,  $^{55}\text{Fe}$ ,  $^{59}\text{Ni}$ ,  $^{90}\text{Sr}$  and  $^{236}\text{U}$  have been detected by AMS but not yet used in applications; technical improvements should expand the useable range and other examples deriving from the potential analysis of more than 140 radioisotopes with half lives greater than one year are likely to arise.

ii) *Noble gas isotopes.* Linacs and cyclotrons with ECR positive ion sources are useful for detection of long-lived radioisotopes of noble gases, such as  $^{39}\text{Ar}$  and  $^{81,85}\text{Kr}$  but work is still in the demonstration stage.

iii) *Stable isotopes.* Stable isotopes of a number of elements have been determined by AMS at ultra-trace levels in geological samples, semiconductors and other materials. Exploitation is likely to expand significantly if new facilities based on ultra-clean ion sources and microprobe sputtering stages are successful for mapping trace isotopes with sensitivity at the ppt level and with micron resolution.

iv) *Actinides.* AMS detection of Th, U and Pu isotopes, difficult to detect by  $\alpha$ ,  $\beta$  or  $\gamma$  radioactivity measurements, will make possible new applications in environmental science and nuclear safeguards, Purser et al. (5).

## REFERENCES

- (1) Purser, K.H. (1994), A future AMS/chromatography instrument for biochemical and environmental measurements, Nucl. Instr. and Meth. in Phys. Res. B92, 201-206.
- (2) Tuniz, C., Fink, D., Hotchkis, M.A.C., Jacobsen, G.E., Lawson, E.M., Smith, A.M., Bird, J.R., Boldeman, J.W. (1994), The ANTARES AMS Centre at Lucas Heights Research Laboratories, Nucl. Instr. and Meth. in Phys. Res. B92, 22-26.
- (3) Mao-Bai Chen, De-Ming Li, Sen-Liu Xu, Guo-Sheng Chen, Li-Gong Shen, Ying-Ji Zhang, Xiang-Shun Lu, Wei-Yu Zhang, Yue-Xiang Zhang and Zong-Kun Zhong (1994), The successful SINR mini cyclotron AMS for  $^{14}\text{C}$  dating, Nucl. Instr. and Meth. in Phys. Res. B92, 213-216.
- (4) Kutschera, W., Paul, M., Ahmad, I., Antaya, T.A., Billquist, P.J., Glagola, B.G., Harkevics, R., Hellstrom, M., Morissey, D.J., Pardo, R.C., Rehm, K.E., Sherrill, B.M. and Steiner, M. (1994), Long-lived noble gas radionuclides, Nucl. Instr. and Meth. in Phys. Res. B92, 241-248.
- (5) Purser, K.H., Kilius, L.R., Litherland, A.E., Zhao, X. (1995), Detection of  $^{236}\text{U}$ : A possible 100-million year neutron flux integrator, Nucl. Instr. and Meth. in Phys. Res., in press.



# AUSTRALIS: PROGRESS REPORT

S.H. SIE, T.R. NIKLAUS AND G.F. SUTER

Heavy Ion Analytical Facility,

CSIRO Exploration and Mining, P.O. Box 136, North Ryde, NSW 2113, AUSTRALIA

## SUMMARY

The first stage of the development of AUSTRALIS, a microbeam AMS system at the HIAF laboratory at North Ryde, Sydney has been completed. The system is designed to enable in-situ microanalysis of geological samples for ultra-traces and for isotopic data for minerals exploration research. The negative ions for analysis are produced by sputtering with a microbeam of Cs<sup>+</sup> from a modified General Ionex model 834 HICONEX ion source. The source features a novel intermediate or 'screen' electrode to correct for the effect of the secondary ion extraction field on the trajectory of the primary beam, in order to bring the primary beam to the geometric centre. The high energy analysis system of AUSTRALIS features a pair of deflector systems to permit fast switching of isotopes without altering the magnet setting. The paper describes the initial tests' results showing good agreement with the design parameters.

## 1. INTRODUCTION

A microbeam AMS system suitable for in-situ microanalysis scale of ultra-traces and of isotopic ratios for geochronology is being developed at the HIAF (Heavy Ion Analytical Facility) laboratory at North Ryde, Sydney. Based on a 3 MV Tandron accelerator, the microbeam AMS system, known as AUSTRALIS (AMS for Ultra Sensitive TRAce eLement and Isotopic Studies), features a microbeam primary ion source and a high energy mass spectrometer capable of analysing actinides at >~2 MV terminal voltage.

## 2. AUSTRALIS

A general description of the AUSTRALIS system has been given elsewhere previously [1]. Special features that set it apart from most other AMS systems are the microbeam source, and the facility for fast isotope switching at the high energy side using deflector plates [1,2].

A diagram of the AUSTRALIS injector system is shown in figure 1. The sample chamber features two ports at + and -45° angle with respect to the secondary ion beam axis, allowing installation of two primary Cs beam sources, the proposed mass analysed primary beam system and the modified HICONEX source. The secondary negative ions sputtered from the sample at the center of the chamber are extracted at normal angle, and focused by an einzel lens at the first set of slits to form the object for a double focusing, 45° bend spherical electrostatic analyser (ESA) with a 30 cm mean radius and 3 cm gap. A second set of slits follows the Faraday cup, designed to reduce beam halo. The image of the ESA serves as the object of a high resolution, double focusing 90° magnet corrected to the second order, with a 30 cm mean radius and 2.5 cm gap, designed to operate with a demagnification of 2. The magnet beam box is insulated to permit application of the usual 'bouncing' technique. Since the secondary ions are produced by microbeams, the ESA and the magnet can be operated with narrow slit settings. At 0.5mm slit setting an energy resolution of 600 and a mass resolution of 1200 will be obtained with this injector system.

The main part of the high energy system of AUSTRALIS is the new larger Danfysik 90° double focusing magnet which is corrected to the second order. The nominal maximum beam product (mE/q<sup>2</sup>) of the magnet is 140 MeV.amu, but it can be operated up to 10% above specification. The pole tips are 130 cm in mean radius, 15 cm wide and separated by a 3.0 cm gap. At maximum excitation, the magnet will permit analysis of mass 230, 5+ ions at ~2.5 MV terminal voltage or 4+ at ~2 MV. Following the magnet the beam passes through two electrostatic analysers with 22.5° bend, separated by an electrostatic quadrupole doublet. The quadrupole is situated between the two ESA's to maintain the beam envelope below 25 mm, in order to keep the maximum voltages of the ESA below 50 kV and minimize hazardous background of high energy X-rays. The quadrupole focuses the beam into either a Faraday cup or an ion detector, which can be a proportional counter. A time-of-flight system will be implemented by installing a start detector at the entrance to the first ESA.

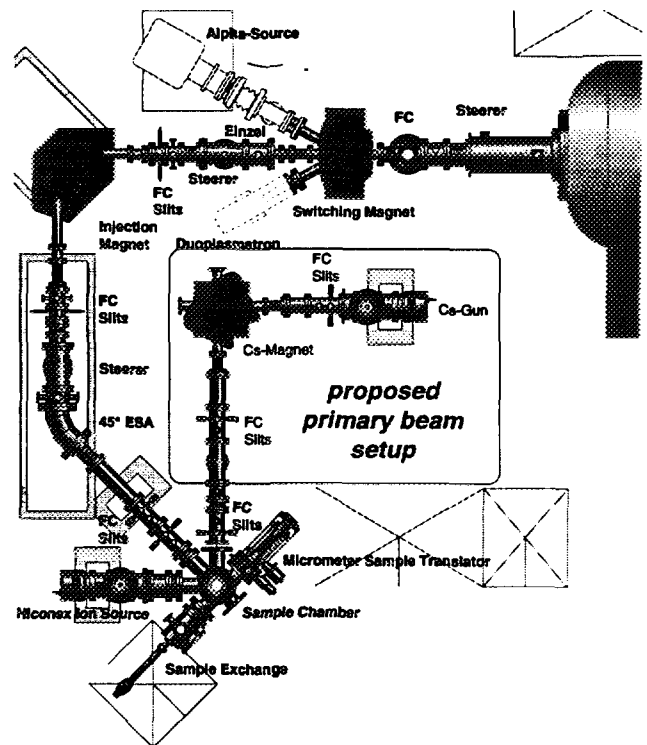


Fig. 1. Plan view of the AUSTRALIS injector system. The sample is mounted at the centre of the chamber on a 3 axis microstage.

Two sets of deflecting plates, 40 cm long with 4 cm gap, at the entrance and the exit ports of the magnet box comprise the high energy 'bouncer' system. Different isotopes are deflected by different amounts transversely in the orbit plane by the entrance plates and returned to the main axis by the exit deflectors by applying common voltages to both sets, without altering the magnetic field setting. Originally devised as an energy modulator [2], this technique adapts well as an isotope switcher. Preliminary tests with 3 MeV proton beam in the energy modulating mode indicate a flat transmission over energy range of up to 1.2% from the mean value, corresponding to similar range in mass difference when used as an isotope switcher. Figure 2 shows the plot of the deflector voltage vs. the accelerator terminal voltage for the proton beam test, and the calculated values as a function of  $D$ , the effective mean distance of the plates from the field boundary.

### 3. THE ION SOURCE

The ion source is designed to enable microanalysis of geological samples, where spatial information is crucial. In the AUSTRALIS sample chamber, a high magnification, direct sample viewing system is achieved by means of an zoom microscope with a 71 mm working distance, combined with a prism with a hole coaxial with the secondary beam axis at 25 mm distance from the sample. With a x10 ocular, a total maximum magnification of 70 is obtained. This is further magnified by the lens for CCD camera, approximately by a factor of 2 resulting in a one micron pixel resolution on the video monitor. The prism is located inside the extractor block and can be retracted out of the way and into a position shielded from the sputtered sample material, without affecting the secondary ion optics. This feature will help prolong the service time between prism replacements or cleaning, since it is expected that the reflecting surface would be coated with some material sputtered from the sample during viewing. The sample is mounted on a rugged, computer controlled 3 axis microstage, with 0.5  $\mu\text{m}$  step size. The target mounting is designed such that target exchange can be carried out conveniently through a vacuum lock.

An existing HICONEX is modified by replacing the secondary ion extraction electrode with a 'faraday cage' biased at the same Cs extraction voltage as applied to the magazine of cones, to extract the beam through the aperture of the cone, and transport it to another lens for focusing into a microbeam. The cage includes a condenser cylindrical einzel lens at the entry side which is designed to improve the optics of the beam transport. The original target 'cones' assembly is now a convenient set of collimators or object apertures for the microbeam production. The final focusing lens is a cylindrical einzel lens, with end elements at the cage potential. The focused Cs beam passes through an intermediate ('screen') electrode before accelerated to its final energy by the secondary ion extraction potential. Figure 3 shows the beam optics of the modified HICONEX source, computed with the program SIMION [3]. The first extraction einzel lens, together with the condenser lens control the first waist of the Cs beam, either to focus it at the object collimator for maximum beam through the collimator or to illuminate the collimator for a more uniform beam distribution at the target. For minimum spherically aberrated image, the focus can be adjusted such that the rays are parallel after the collimator.

The 'Screen' electrode electrode has two functions: first to screen the primary beam as much as possible from the secondary extraction field that will affect its trajectory, and second to correct the deviation caused by the field by tailoring the shape of the field to return the intersection point to the desired geometric center of the target. The optics of the secondary ion extraction region showing the effect of the screen is shown in figure 4. Because of cylindrical symmetry restrictions, the primary beam is simulated by a bundle of rays converging at the geometric centre. For clearer definition of the centre, two

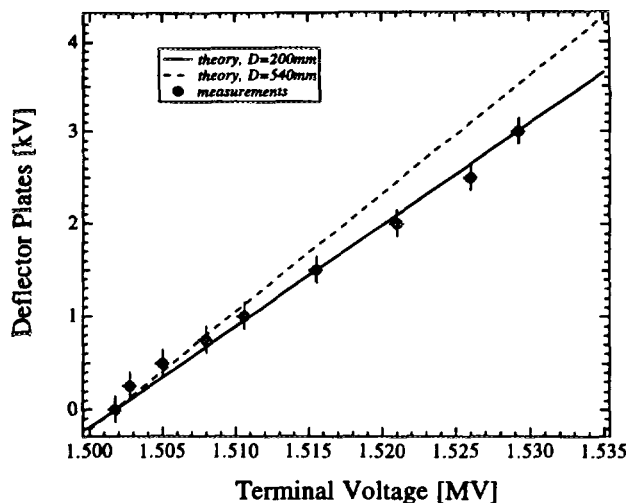


Fig. 2. The high energy bouncing system was tested using 3 MeV proton beam. The plot shows the deflector plate voltage against the proton beam energy represented by the terminal voltage, and the calculated values for various distance  $D$  representing the mean distance of the deflector plate to the magnetic field boundary.

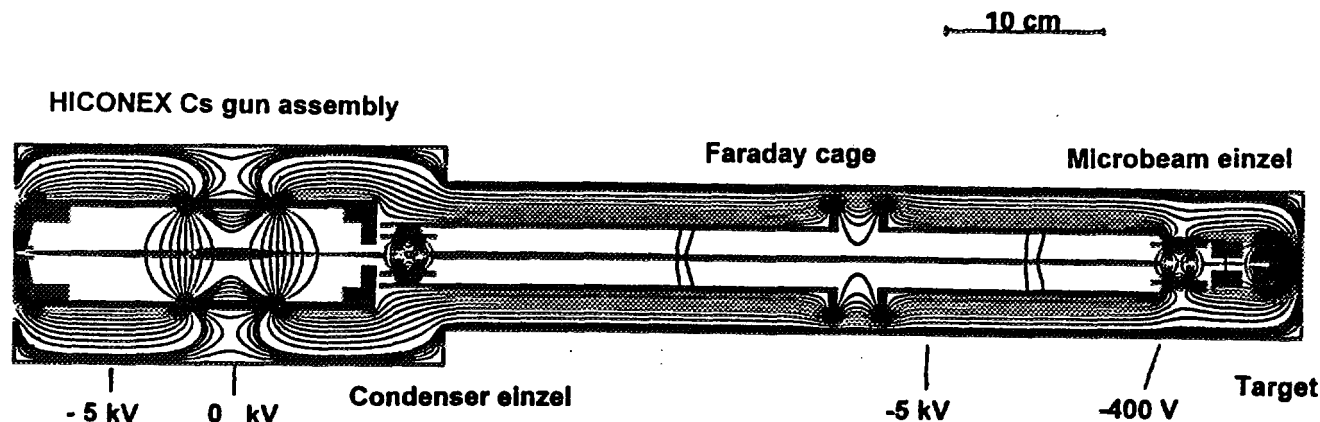


Fig. 3. The beam optics of the modified HICONEX source calculated using the code SIMION in cylindrical symmetry geometry.

symmetric bundles of primary rays are shown. When the screen is set at the same potential as the 'extractor block', the primary beam can be seen to deviate from the centre. The effect would be even larger if the screen were removed. By varying the screen voltage slightly, the spot can be returned to the centre. The displacement is approximately linear with the voltage difference between the screen and the extractor voltage and can therefore also be used to correct deviation caused by residual misalignment of the primary beam axis, provided that it is on the same plane as the secondary axis. Results of the tests show good agreement with the values derived with SIMION of  $\sim 400 \mu\text{m}$  displacement for a 200V change in the screen voltage for Cs beam extracted at 5 kV. The target bias was -10 kV, and the screen voltage was -5.4 kV, indicating the existence of some residual misalignment.

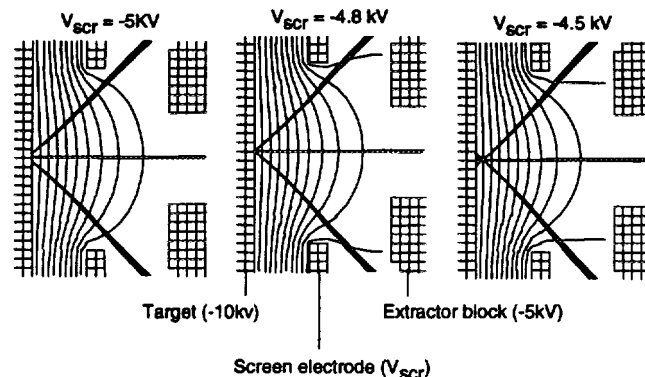


Fig. 4. Beam optics of the secondary ion extraction region calculated with SIMION 5 to show the effect of the screen electrode.

#### 4. THE MICROBEAM

The beam spot can be observed readily in real time on the video monitor, or directly through the microscope ocular, as erosion spots on a thin carbon layer vacuum deposited on a polished Au target, followed by sputtering of the Au itself. The best focus for uncollimated gun, i.e. when there is no cone in place corresponding to an aperture of 10 mm was  $300 \mu\text{m}$ . The spot is an ellipse with its long axis  $\sqrt{2}$  times the short axis, consistent with a cylindrical beam intercepting the target plane at  $45^\circ$  incidence. The short axis is taken to be the focus size. With the 2 mm aperture cone, the best focus obtainable was  $160 \mu\text{m}$ . However, a more uniform erosion spot but larger diameter ( $300 \mu\text{m}$ ) is obtained when the beam intensity is not optimised at the target. This corresponds to the 'Köhler's illumination' mode [4]. Under this condition, the Cs einzel is focused to produce a waist before the aperture and the beam envelope at the aperture is larger than its size. The waist coincides with the focal point of the condenser einzel, resulting in a parallel beam which is further focused by the final einzel lens. Hence spherical aberration effects are minimal and the beam spot scales geometrically with the aperture size. The smallest aperture tried so far is  $150 \mu\text{m}$ , resulting in a  $30 \mu\text{m}$  spot size.

The intensity of the primary beam can only be estimated from the measured secondary ion intensity measured either in the source or the injector magnet Faraday Cup. With the ioniser of the Cs gun at maximum setting and the Cs reservoir heated to  $220^\circ \text{C}$ , up to 1 nA of C was measured from the thin C coating at  $30 \mu\text{m}$  resolution. For graphite targets a  $\sim 6\%$  yield (12 keV Cs beam, 20 keV extraction) can be obtained [5]. Considering that in the present test the target is not graphite, and the Cs energy and secondary extraction energy are lower, this efficiency may represent only the upper limit. With this proviso we estimate that the intensity of the primary beam is at least 16 nA at this resolution, corresponding to  $\sim 2 \text{ mA/cm}^2$  beam density. The Cs gun type used here can generate  $\sim 60 \mu\text{A}$ , and without collimation it can be focused to  $\sim 500 \mu\text{m}$  corresponding to  $\sim 30 \text{ mA/cm}^2$  beam density. During this test however the gun was not run at maximum possible output, and it should be noted that the estimate of the microbeam density is a lower limit. Further test with graphitised target with known characteristic ion yield or direct measurement of the primary current will be attempted in the near future.

#### 5. CONCLUSION

The first stage of the AUSTRALIS development is completed and is currently undergoing tests. A number of key features of the system have been successfully tested. The optics of the microbeam system based on a modified HICONEX source behaves according to the model calculation. The source proves to be a versatile device for providing Cs beam spanning the sub-milli and micron range of spatial resolution at maximum possible delivered intensity. The 'screen' electrode in the secondary ion extraction region behaves as predicted and presents a convenient technique for correcting the effect of the secondary ion extraction field on the primary beam, giving a high degree of decoupling of the primary and secondary ion optics. The same electrode can be employed to correct for residual geometric misalignment of the lens axes. A test of the high energy bouncing system shows good agreement with the calculation permitting application of fast bouncing techniques to improve the precision in isotopic ratio measurements not possible by the inevitably slow switching of magnetic fields.

#### ACKNOWLEDGEMENTS

We thank the University of North Texas and the ISOTRACE groups for fruitful discussions during the planning of AUSTRALIS, and Prof. Georges Amsel and Dr. D'Artemare for their cooperation in the design of the high energy bouncing system. We thank Peter Nicolay for the engineering design of the extraction region and the viewing optical system. Technical assistance of Gary Cripps, Tim Young, Ernie Alejandrino, Charles Dawson and Colin O'Keefe are gratefully acknowledged. Dennis Wulff and his team manufactured the ESA and the extraction optics.

#### REFERENCES

1. Sie, S.H. and Suter G.F., [1994], Nucl. Instr. Meth. B92, 221
2. Amsel G., D'Artemare E. and Girard E., [1983], Nucl. Instr. Meth. 205, 5
3. Dahl D.A. and Delmore J.E., [1988], SIMION User's Manual, EGG-CS-7233 Rev. 2, April 1988 and ext. DOS version
4. Liebl H., [1983], Vacuum 33, 525
5. Middleton A., [1989], "A Negative Ion Cookbook", University of Pennsylvania, unpublished.



# The Status of the Tandem Accelerator ANTARES

JOHN FALLON, JOHN BOLDEMAN, DAVID COHEN, CLAUDIO TUNIZ and PETER ELLIS  
Australian Nuclear Science and Technology Organisation.  
Private Mailbag 1, Menai, NSW, 2234

## INTRODUCTION

The ANTARES facility at the Lucas Heights Research Laboratories has now operated for 4 years. A research program in Accelerator Mass Spectrometry, Ion Beam Analysis and small scale radioisotope production has been pursued. During the same period, the accelerator has been significantly upgraded from the configuration which existed at Rutgers University, NJ, USA, before shipment to Australia in 1989. Both the experimental program and the engineering developments are discussed further.

## ANTARES EXPERIMENTAL PROGRAM

### Accelerator Mass Spectrometry

Accelerator Mass Spectrometry (AMS) uses 75 % of the ANTARES beamtime. Measurements of the rare isotopes  $^{14}\text{C}$ ,  $^{36}\text{Cl}$ ,  $^{26}\text{Al}$ ,  $^{10}\text{Be}$  and  $^{129}\text{I}$  are being carried out and refinements to improve precision, particularly in the case of  $^{14}\text{C}$ , form the major part of the ongoing development program. Two beamlines have been constructed for use in AMS: the first is used almost exclusively for the measurement of  $^{14}\text{C}$  and features an ExB filter to separate the interfering isotopes, and a Bragg curve spectroscopy detector for ion identification; the second beamline, comprising a  $22^\circ$  electrostatic analyser and a time-of-flight detector is used in the analysis of  $^{129}\text{I}$  and  $^{36}\text{Cl}$ .

In performing an AMS measurement, a milligram size sample is placed in the multi sample ion source and injected into the accelerator at an injection energy up to 100 keV. As beam transmission can unavoidably change with time, it is essential that any changes do not degrade the measured isotopic ratio. A fast isotope cycling system is used with the isotopic ratio being measured several times a second thus overcoming any effects of transmission variation. Beam from the ion source is mass analysed by the  $90^\circ$  injection magnet and, as such a large magnet cannot change flux at the required rate for fast cycling, the magnetic rigidity of the different isotopes is changed by modulating the injection energy. Once accelerated to high energies, the isotopes are separated with the abundant isotope being measured in a Faraday cup after the  $90^\circ$  analyser magnet and the rare isotope measured in the final AMS beamline detector.

### Ion Beam Applications

A dedicated beamline is used for a variety of ion beam analysis techniques which include heavy ion forward recoil and heavy ion backscatter using surface barrier detectors; a heavy ion time-of-flight detector employing thin carbon foil, micro channel plate start/stop timing, is also available. These techniques allow sub micron elemental profiles to be made from hydrogen right through to heavier ions. Limitations to the terminal voltage at times and thus the ion beam energy, have hampered mass resolution, particularly when investigating forward recoil of Ga and As used in integrated circuits. Targets are mounted in a large vacuum chamber with XYZ goniometer positioning.

### Radioisotope Production

Small quantities of two isotopes,  $^{45}\text{Sc}$  from the  $^{45}\text{Ti}(p,n)^{45}\text{Sc}$  reaction, and  $^{18}\text{F}$  from the  $^{18}\text{O}(p,n)^{18}\text{F}$  reaction, have been produced at ANTARES. These isotopes have been used in biomedical research at Lucas Heights and supplement larger scale production by a cyclotron at the National Medical Cyclotron Facility, Camperdown. As the ANTARES facility was not set up with heavy radiation shielding in place, special administrative procedures are necessary to ensure personnel safety when producing these isotopes.

## **ENGINEERING DEVELOPMENTS**

### **The High Voltage Generator**

Although still maintaining a rubberised charging belt, terminal voltage stability has been improved with the addition of a new terminal voltage stabiliser and power supply. With the replacement of the column resistors that set the voltage gradient down the length of the accelerating tubes, a stability figure of 0.02 % is now achievable at 6 MV. Improved beam transmission and better electron suppression have been realised with the installation of a Dowlish spirally inclined field accelerating tube at the entrance to the accelerator. Limitations have been placed on the maximum terminal voltage, firstly by the poor column resistors which are now upgraded with spark gap protected, co-axially shielded resistors and secondly, by the lack of SF<sub>6</sub> insulating gas in the pressure vessel. Designed to operate with ~600 kPa of insulating gas, only ~400 kPa has been possible due to gas loss from various parts of the gas handling system over the years. An almost full inventory of gas is now available and conditioning for higher terminal voltages is about to begin.

In the ANTARES tandem accelerator until now, ion stripping has been achieved by the use of very thin carbon foils. These foils suffer from thickening and/or breakage with continual beam strike, both of which seriously affect beam transmission and as only a limited number are available on a cassette, tank entry is necessary to replace them. A gas stripping system incorporating a gas recirculating turbo molecular pump is installed and presently being tested. Stripper gas pressure is sent via fibre optic link to the operating console outside the pressure vessel.

### **Ion Sources**

Following successful installation of the HVEE Model 846 Ion Source onto the 90° injection magnet toward the end of 1994, the single sample, General Ionex Model 860 caesium sputter source mounted on a 75 kV injection platform, has been relocated to inject through a 30° injection angle into a low energy beamline that passes straight through the 90° magnet. The optical properties of both injection lines ensure a focus is formed at the same point prior to final injection into the accelerator. The 60 sample, Model 846 ion source used primarily in the AMS program, had to be extensively re-worked in almost every facet of operation prior to installation but over the past 12 months has performed fairly reliably as a high throughput, high intensity source.

An alpha ion source is presently on order and will be delivered late 1995. It will be mounted on the adjacent side to the single sample source at an angle of 45°.

### **Accelerator Control**

Graphical control from a DEC 5000 station of most beamline components such as Faraday cups, gate valves, magnets, power supplies is now possible as is the control of the terminal voltage. Interfacing of the remaining components to the VME based system is proceeding using primarily, 4-20 mA loops, or opto-isolated RS232 links. Beam currents can be read locally or sent to the computer as a digitised signal, whilst beam quality is monitored by rotating wire beam profile monitors. Terminal voltage correction is achieved during AMS measurements using a split Faraday cup to measure the off-axis, high-mass component of the beam. Upgraded power supplies for the large magnets have also been installed.

### **FUTURE PLANS**

There is an immediate need for terminal voltages up to 8MV and conditioning will shortly commence to achieve this voltage. Further Dowlish tubes are planned for installation with all but the last tube now on site. Interfacing of the remaining components such that full computer control can be implemented will also help facilitate long experimental runs with little or no operator intervention.

A new beamline with the possibility of several end configurations is planned for general purpose use. The Alphasource Ion Source from NEC will be installed in the early part of 1996, whilst development and installation of an actinide AMS facility is planned for 1996. Preliminary design of a microprobe beamline using a unique four focussing quadrupole system to focus the beam spot size down to 10 um has been carried out and implementation is proposed over the next two years.

### **CONCLUSION**

The ANTARES facility has successfully operated a research program over the past few years and has established itself as the national centre for radiocarbon dating in quaternary research and global climate change. AMS measurement techniques of several long lived isotopes are being developed for environmental, industrial and biomedical applications.

Surface analysis techniques using high energy, heavy ions, are being pursued and with the accelerator upgrading program, will become more viable for studies in material science and other industrial applications.

ANTARES is available to the entire Australian scientific community and can be accessed through ANSTO or in the case of university researchers, through AINSE.

#### **ACKNOWLEDGMENTS**

The author wishes to acknowledge the efforts of many people, from many disciplines and too numerous to mention individually, who have contributed to the successful development of ANTARES as a world class national facility.



# The Role of $^{129}\text{I}$ in the Environment and its Measurement at the ANTARES AMS Center

D FINK, MAC HOTCHKIS, EM LAWSON, GE JACOBSEN,  
AM SMITH and C TUNIZ

Australian Nuclear Science and Technology Organization, PMB 1 Menai, NSW, 2234

## SUMMARY

Anthropogenic production of several radionuclides during the nuclear era has resulted in a dramatic enhancement in their ambient concentrations relative to cosmogenic values for geophysical systems which are in exchange with the atmosphere and oceans. These environmental pulses have been archived in sediments and polar ice caps where for example profiles of  $^{90}\text{Sr}$  and  $^{135}\text{Cs}$  have been measured to establish global transport rates and deposition budgets for bomb-test products.  $^{129}\text{I}$ , half-life 16 Ma, is another nuclear fission product that is and has been periodically released into the atmosphere, but unlike the shorter lived  $^{90}\text{Sr}$  and  $^{135}\text{Cs}$ , had not found widespread utilization because previous detection via neutron activation analysis ( $^{129}\text{I}(2n,\gamma)^{131}\text{I}$ ) was cumbersome and lacked the required sensitivity. AMS has resolved this problem for  $^{129}\text{I}$  measurements by reducing the required sample size, measurement time and atom-counting sensitivity to as little as  $10^6$  atoms that enable  $^{129}\text{I}/^{127}\text{I}$  isotopic ratios as low as  $2 \times 10^{-14}$  to be measured on milligram samples within an hour. As a result of this new detection capability, an ever-growing interest and awareness in the application of  $^{129}\text{I}$  as an environmental tracer, radiometric dating tool and monitor of operations of the nuclear industry has been generated. In response to these advances we have commenced  $^{129}\text{I}$  AMS measurements at ANTARES

## INTRODUCTION

Prior to nuclear testing, the two main mechanisms for  $^{129}\text{I}$  production were radiogenic - the spontaneous fission of  $^{238}\text{U}$  (99.3%) and neutron induced fission of  $^{235}\text{U}$  (0.7%) in the subsurface, - and cosmogenic - cosmic ray spallation of Xe in the atmosphere. These two modes shared on an equal basis supply of  $^{129}\text{I}$  to the global inventory of the hydrosphere. With an iodine ocean residence time of  $\sim 300$  ka being far shorter than the  $^{129}\text{I}$  16 Ma half-life and considerably longer than the turn-over time in the marine system, it can be safely assumed that iodine is well mixed. Analogously to the behaviour of  $^{14}\text{C}$  between the biosphere and atmosphere, reservoirs actively exchanging iodine arrive at an isotopic equilibrium - but once the  $^{129}\text{I}$  becomes detached from the main reservoir such as below the bioturbation depth in marine sediments or closed in evaporite deposits and oil field brines, exchange ceases and the decay clock begins. The 'initial' equilibrium ratio is difficult to determine but is estimated from recent (pre-bomb) ground-waters and sediments to be  $120 \times 10^{-14}$ . Given that the lowest AMS  $^{129}\text{I}/^{127}\text{I}$  measurement (blank) in an ancient (600 Ma) deep salt mine sample is  $4 \times 10^{-14}$ , dating of marine sediments, Fehn et al (1), evaporite and ore deposits, and oil brines, Fehn et al (2), can potentially reach  $\sim 80$  Ma. In U-rich ore bodies, where radiogenic  $^{129}\text{I}$  concentrations may be quite considerable, its use as an analog

tracer to study migration and distribution of fission products has been carried out, eg the Stripa Granite formation, Sweden, Fabryka-Martin et al (3).

However, with the advent of the nuclear era, an overwhelming proportion of the global inventory of  $^{129}\text{I}$  is anthropogenically produced via induced fission of  $^{235}\text{U}$  (yield of 0.74%) and  $^{239}\text{Pu}$  (1.5%) from nuclear power and reprocessing plant operations.  $^{129}\text{I}$  release from the Chernobyl incident in 1986, Paul et al (4), was recorded in rain in Germany and as far afield as Israel with concentrations of  $30 \times 10^9$  and  $2 \times 10^9$  atoms  $^{129}\text{I}/\text{litre}$ , respectively - a factor of  $\sim 300$  higher compared to rain collected in 1982. Ocean profiles in the Gulf of Mexico from surface to ocean bottom (1500 m) show values of  $^{129}\text{I}/^{127}\text{I}$  ranging from  $\sim 100 \times 10^{-12}$  (anthropogenic  $^{129}\text{I}$ ) to  $1 \times 10^{-12}$  respectively, Schink et al (5). The distribution of large quantities of effluent emissions from coastal nuclear fuel reprocessing plants at La Hague, France, and Sellafield, Great Britain, have been investigated using  $^{129}\text{I}$  tracing along the zone of the ocean plume, Yiou et al (6).  $^{129}\text{I}/^{127}\text{I}$  ratios in those ocean surface water samples and seaweeds in close proximity (tens of kms) to the plants show a  $10^4$ -fold increase. Rough estimates indicate that an astonishing 1.2 tons of  $^{129}\text{I}$  has been released into the environment from Sellafield and La Hague alone over the past 25 years.

Although the anthropogenic signal presents a serious complication to the use of cosmogenic  $^{129}\text{I}$  as a geologic and marine chronometer, the above studies clearly indicate the new roles of  $^{129}\text{I}$  to remotely monitor nuclear activity with respect to arms control and safeguard agreements, and as an oceanographic tracer.

#### **THE $^{129}\text{I}$ PROGRAM and AMS MEASUREMENTS at ANTARES**

A number of  $^{129}\text{I}$  projects, in conjunction with AINSE, (eg dating the secondary ore zone at Broken Hill, tracing and dating ground waters), the IAEA (distribution of  $^{129}\text{I}$  concentrations in the environs of a nuclear power plant using water, sediment and biological samples) and dealing with an AMS inter-laboratory calibration have been scheduled and are in progress. To deal with the rather diverse selection of sample materials which involve  $^{129}\text{I}$  studies at Ansto, comprehensive and efficient chemical procedures for pretreatment and reduction of raw samples into the desired form of  $\text{AgI}$  have been tested and established. Procedures for extraction of I from water, sediment, and biota are available.

Due to the absence of formation of negative ion beams of the isobar  $^{129}\text{Xe}$ , identification of  $^{129}\text{I}$  above residual background events is made relatively easier than that for some of the other AMS radioisotopes. In fact, this has allowed the use of even small tandem accelerators running at 3MV for  $^{129}\text{I}$  measurements, Kilius et al (7). The major complication arises from the ever-present background of  $^{127}\text{I}$  ions which through scattering and charge exchange manage to leak through the magnetic and electrostatic filtering elements prior to the detector.

Our measurements of  $^{129}\text{I}$  are being carried out at ANTARES using the  $55^0$  beam-line equipped with the high resolution  $22^0$ , 5m radius electrostatic deflector (ESA). A new time-of-flight (TOF) system has been installed comprising a multi-channel plate (MCP) start detector and a silicon barrier stop detector ( $300 \text{ mm}^2$ ), which also provides a total energy signal. The MCP operates at -3800V with a 19mm radius,  $20 \mu\text{g}/\text{cm}^2$  carbon foil positioned at  $45^0$  to the beam. The TOF path at present is 600 mm. Modifications are in progress to increase this to 1200mm and construct retractable MCP units with electrostatic mirror assemblies to enable a perpendicular foil orientation so as to minimize flight path straggling and improve the TOF transmission. We have achieved a TOF timing resolution (FWHM) of 500 psec, which is sufficient to completely resolve the  $^{129}\text{I}$  peak from the low background rate of  $^{127}\text{I}$ , which at equal rigidities, has a TOF difference from  $^{129}\text{I}$  of 1 nsec. The tandem is operated at 6.3 MV for the 11+ charge state to give final  $^{129}\text{I}^{11+}$  energies of 75 MeV. Particle

transmission varies from 1-3% depending on foil quality. The use of a gas stripper will considerably improve this. A 2-dimensional TOF vs E(Si) spectrum is used to give unambiguous identification of  $^{129}\text{I}$  events.

The beam line is tuned with an equal-rigidity  $^{127}\text{I}$  beam to a Farady cup assembly positioned after the ESA and in front of the MCP unit. The analyzing magnet off-axis cup was positioned to intercept the  $^{127}\text{I}^{11+}$  beam at the terminal voltage used for measuring the  $^{129}\text{I}^{11+}$  rate. The bouncer could not be used simultaneously with  $^{129}\text{I}$  measurement due to excessive rates in the E(Si) detector during isotope cycling and was effectively used as a beam chopper with AM cup insertions for each mass changeover as protection. A measurement sequence involved 300 sec for  $^{129}\text{I}$  (bouncer off) and 50 sec for  $^{127}\text{I}$  (bouncer on).

A series of measurements on different blanks and low level samples and standards has been carried out. Commercial AgI and chemically prepared AgI at ANSTO both give  $^{129}\text{I}/\text{I}$  ratios of  $20 \times 10^{-14}$ . Blanks supplied by M. Paul at the AMS lab at the Hebrew Univ Jerusalem, Israel and from M. Roberts at the AMS lab at Lawrence Livermore, USA have also been measured at ANSTO. These blanks are reported to have  $^{129}\text{I}/\text{I}$  ratios of  $4 \times 10^{-14}$ . Our result of  $20 \times 10^{-14}$  for these samples, equivalent to that for the chemistry blank processed at ANSTO, indicates that the potential of on-site  $^{129}\text{I}$  contamination from HIFAR operations into our chemistry preparation system is negligible and the source of our  $^{129}\text{I}$  events is most likely the result of  $^{127}\text{I}$  misidentification, ion-source cross talk and/or random coincident events from other lower mass background ions. Further tests are planned to improve our sensitivity into the  $10^{-14}$  range.

S. Vogt at PRIME lab, Purdue University, USA, has kindly donated a complete set of  $^{129}\text{I}$  standards with strengths ranging from 120 to  $62200 \times 10^{-14}$ . We have used a number of these standards to assess our reproducibility, accuracy and mechanism of ion-source cross-talk. Due to rapid stripper foil deterioration and unsteady  $\text{I}^-$  ion-source output which both lead to unacceptable variations in the measurement of the standard, our reproducibility is at present no better than 10%.

To date, we have successfully analyzed a suite of ~20 samples consisting of waters, sediments and biota collected for the IAEA project. Our results for the ocean waters range from 10 to  $300 \times 10^9$  atoms  $^{129}\text{I}/\text{litre}$  which is consistent with that measured by Yiou et al (6).

## REFERENCES

1. U. Fehn, G Holdren, D Elmore et al, *Geophys. Res. Lett*, 13 (1986) 137.
2. U Fehn, J Moran, R Teng et al, *Nucl Instr and Meth*, B92 (1994) 380.
3. J. Fabryka-Martin, S Davis, D Elmore et al, *Geochim. Cosmochim. Acta*, 53 (1989) 1817
4. M Paul, D Fink, G Hollos et al, *Nucl Instr and Meth*, B29 (1987) 341.
5. D.R Schink, P Santschi, O Corapcioglu et al, *Nucl Instr. and Meth*, B99 (1995) 524
6. F. Yiou, G Raisbeck, Z ZHou et al, *Nucl Instr. and Meth*, B92 (1994) 436.
7. L Kilius, N Baba, M Garwan et al, *Nucl Instr and Meth*, B52 (1990) 357.



# New 2-Stage Ion Microprobes and a Move to Higher Energies

G. J. F. LEGGE<sup>1</sup>, A. DYMNIKOV<sup>1,2</sup>, G. MOLONEY<sup>1</sup>, A. SAINT<sup>1</sup> AND D. COHEN<sup>2</sup>

1. School of Physics, MARC, the University of Melbourne

2. ANSTO, Lucas Heights

Recent moves in Ion Beam Microanalysis towards the use of a rapidly growing number of very high resolution, low current and single ion techniques has led to the need for high demagnification and greatly improved beam quality. There is also a move to apply Microbeams at higher energies and with heavier ions. This also puts demands on the focusing system and beam control. This paper describes the recent development of 2-stage lens systems to be applied here and overseas, both at very high resolution and at high energies with heavy ions. It looks at new IBA applications of such ion microprobes.

## INTRODUCTION

The spatial resolution achievable by an ion microprobe is determined by only a few factors and, by means of a figure, it can be readily seen that this resolution is practically defined by the beam brightness available from the accelerator and the beam current required at the focused spot. These two factors are related by the emittance. From this it can be readily seen what resolution is achievable at various beam currents or emittances and how major improvements in ion sources will affect resolution. It is also seen that changes in ion optics will have little effect on the above limits. However, there are very significant practical advantages in the 2-stage systems now under development and there are important applications which require the development of high energy ion microprobes.

## SINGLE STAGE ACCELERATOR-BASED MICROPROBES

An ion microprobe, as used in nondestructive ion beam microanalysis, is basically an ion source and lens, followed by an accelerator of some MeV energy which delivers beam to a microprobe beam line. This beam line consists of an object diaphragm (or slit), which acts like a source, an aperture diaphragm (or slit) and a microprobe lens, which forms an image of the object on the specimen. The two diaphragms together determine the emittance.

We reported on progress and future directions in ion microprobe development at an AINSE conference four years ago (1) and the arguments presented in that report still apply. In this paper, fig. 1 summarizes the situation. It shows the dependence of focused spot diameter on the half angle of convergence,  $\alpha$ , at the specimen. The three basic contributions arise from:

- (i) the chromatic aberration of the lens, which depends directly on the first power of  $\alpha$ ,
- (ii) the spherical aberration of the lens, which depends directly on the third power of  $\alpha$ , and
- (iii) the first order spot size, which depends inversely on the first power of  $\alpha$ .

In an electron microprobe equipped with a field emission source, as recently discussed by Crewe (2), there is effectively no first order spot size contribution, because the brightness is sufficient to provide the required beam current with extremely low values of source size and  $a$ ; but there is a diffraction limit, which depends inversely on the first power of  $\alpha$ . In an ion microprobe, there is effectively no diffraction limit, but the low brightness of presently used sources results in an equivalent dependence of the first order spot size.

The lines shown in fig. 1 represent typical values for modern ion microprobes. The third contribution is set by the emittance,  $\epsilon$ , and this, in turn, is set by the ratio of ion source brightness to required beam current. Therefore several lines are shown, the one labelled with highest emittance being that required for typical currents (100 pA) at 3 MeV with RF ion sources ( $5 \text{ A m}^{-2} \text{ rad}^{-2} \text{ eV}^{-1}$ ). It can be seen that the total effect of all three contributions is to limit resolution to a value in the vicinity of a micron. Effective resolution will depend on definition (FWHM or envelope) and it will not be a simple addition of all contributions in quadrature; however we are here only concerned with principles and orders of magnitude.

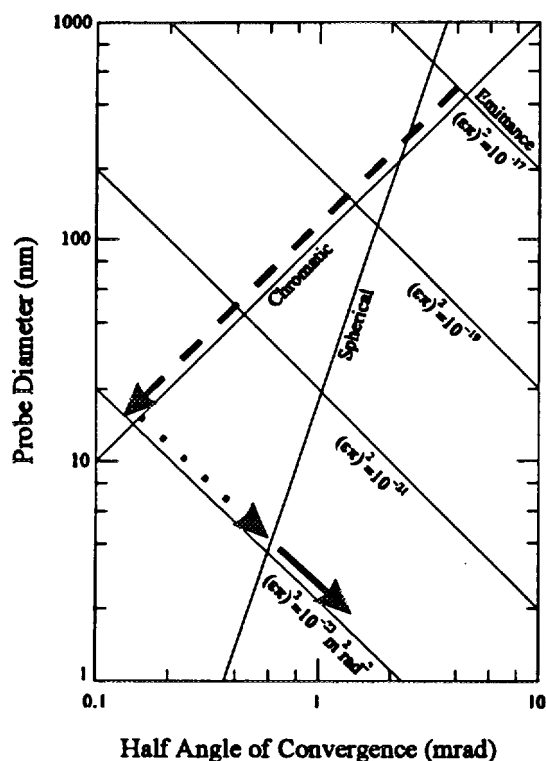


**Fig. 1** Contributions to the beam spot diameter in an ion microprobe and their dependence on the half angle of beam convergence at the focus. The contributions are typical for the present generation of ion microprobes. The emittance value to be used depends on the application. Typically, for an RF ion source of reduced brightness  $5 \text{ A m}^{-2} \text{ rad}^{-2} \text{ eV}^{-1}$ , and a beam energy of 3 MeV, the emittance is given by  $(\epsilon\pi)^2 = 10^{-17} \text{ m}^2 \text{ rad}^2$ .

We cannot expect to improve the aberration coefficients of microprobe lenses sufficiently to make orders of magnitude improvement in resolution, since the necessary strong correction lenses are likely to introduce parasitic aberrations. We have not considered parasitic aberrations, of which the commonest (sextupole) shows a second order dependence on  $a$ . Therefore we must decrease the emittance, as represented in fig. 1 by the dashed arrow. A wide variety of powerful analytical techniques utilizing single ions or beam currents less than a fA have thereby achieved resolutions down to 50 nm (3). A much brighter ion source, technically achievable with field ionization but a great challenge, will enable such resolution or better with analytical beams of 100 pA or more. Further improvements can be made by improving the energy stability of the accelerator, represented by the dotted arrow in fig. 1. Ultimately, resolution would be limited again by spherical aberrations and the solid arrow in fig. 1 represents the effect of correcting such aberrations.

### TWO STAGE MICROPROBES

By splitting the microprobe lens into two separated magnetic quadrupole doublets and thereby achieving two stages of focusing, several advantages accrue (4):

- (i) the demagnification factor is much greater - 150 in place of 20.
- (ii) the octupole lenses required to correct spherical aberrations are now weak and less likely to introduce significant parasitic aberrations.
- (iii) each optical plane has an intermediate focus or crossover where a slit may be installed.

Two stage microprobes and their advantages were discussed by Moloney and Legge (4) and Brazhnik et al. have also shown that they can be used to construct a short system (5). A system of standard length (9 m) and demagnification of 150 has now been constructed and tested at MARC. It is the basis for several new systems to be installed elsewhere, one of which will be a short (3m) system.

Higher demagnification, in itself, does not improve resolution, since emittance is unchanged; but the resolution is less affected by mechanical vibrations at the object and larger object diaphragms may be used, resulting in less scattering. Such scattering is a significant concern with single stage microprobes and considerable effort is expended in minimizing it. The system has a proportionately smaller aperture diaphragm (now comparable in size with the object); but scattering from diaphragm edges can be removed by placing an antiscattering slit at each of the two crossovers. These slits may be very narrow (10 - 100 micron) without intercepting, and hence scattering, any primary beam. The so-called Russian Quadruplet configuration, whose four quadrupole lenses together emulate an orthomorphic symmetrical lens, retains this property, even when physically separated into two doublets.





# Mixed Beams for the Nuclear Microprobe

A.Saint, M.B.H. Breese and G.J.F. Legge

School of Physics, MARC, The University of Melbourne, Parkville, 3052, Australia.

## 1 Introduction

Recently the Micro-Analytical Research Centre (MARC) has developed a technique to provide mixed beams of ions for a magnetically focussed nuclear microprobe [1]. Such a mixed beam is defined as two (or more) beams of different species ions that can quickly and easily be made to have the same magnetic rigidity  $R_m = (mE/q^2)$  and therefore be transported, focused and scanned the same in a magnetic nuclear microprobe. The production of mixed beams in an electrostatically focussed microprobe have already been demonstrated [2]. This paper will show how mixed beams can be produced on a single-ended accelerator. Indications of how to produce them on a tandem will also be given. Applications of these mixed beams in micro-lithography, STIM imaging and IBIC imaging will also be presented.

## 2 Production of Mixed Beams

There are two simple ways to produce mixed beams using a single-ended accelerator. These are called extracted and post-accelerator stripped (PAS) mixed beams.

An extracted mixed beam consists of two beam species whose magnetic rigidities are almost the same. In this case  $H_2^+$  and  $He^{2+}$  are extracted. The ion source is filled with a mixture of hydrogen and helium. These ions are extracted from the high voltage terminal simultaneously and accelerated. As they pass around the higher resolution analysing magnet they are separated and the accelerators slit stabilisation system can be used to change the energy of each ion beam so that they have identical  $R_m$  when they enter the microprobe beamline. This type of mixed beam is illustrated in figure 1.

The second method used to produce a mixed beam is the PAS (post acceleration stripping) method. This technique utilises a change in charge state of the ions as they pass through a thin carbon foil after they have been accelerated. If an  $He^+$  ion is accelerated from a terminal of voltage  $V$  (MV) it obtains an energy  $V$  (MeV). If this ion is then stripped to produce a  $He^{2+}$  ion it has a value of  $R_m$  close to that of a proton accelerated through the same potential. The ion source is again filled with a mixture of hydrogen and helium and  $H^+$  ion and  $He^+$  ions are alternately extracted from the terminal using a velocity selector installed in the high voltage terminal. After post acceleration stripping the accelerators analysing magnet and slit stabilisation system automatically adjust the beam energy so that each beam has the same  $R_m$  when present in the microprobe beamline. This type of mixed beam is illustrated in figure 2.

In both the above cases the mixed beams will be transported, focused and scanned to the same extent. In the case of the  $H_2^+ - He^{2+}$  mixed beam the two ion species

have approximately the same range in matter, but the  $He^{2+}$  ion has twice the energy of the  $H_2^+$  ion. This mixed beam should therefore be used when we wish to see the effect of different energy deposition in the specimen. This type of mixed beam has found applications in Ion Beam Induced Charge (IBIC) analysis [3]. The PAS mixed beam, however, produces the  $H^+$  and the  $He^{2+}$  with the same energy. The range of  $H^+$  is approximately 4 times that of  $He^{2+}$  at 1 MeV. This mixed beam should therefore be used when we wish to effect the specimen to different depths. This type of mixed beam may find applications in micro-lithography.

### 3 Results and Discussion

To test the spacial resolution of the mixed beams each of the above mixed beams was scanned over a section of 2000 mesh (12 micron period) copper grid. Scanning transmission ion microscopy (STIM) images were obtained for all 4 beams using a beam current of approximately 2000 ions per second. The 4 images obtained are shown in figure 3.

The resolution is approximately the same for each image and was estimated to be between 200 and 300 nm.

The technique and resolution of mixed beams for a magnetically focussed microprobe has been clearly demonstrated. Possible fields of application of such beams have also been indicated.

### 4 References

1. A.Saint, M.B.H. Breese and G.J.F. Legge (unpublished)
2. LeFevre, H.W., Connolly, R.C., Xi, D.P., Sieger, G.E., Overley, J.C. Nucl. Instr. Meth. B 10/11, 707-712, (1985).
3. Jour. Appl. Phys. 77(8), 3734, (1995).

### 5 Figure Captions

Figure 1 - Production of a Extracted Mixed Beam

Figure 2 - Production of a PAS Mixed Beam

Figure 3 - STIM scans of Mixed Beams a).Extracted alpha particles b). Extracted molecular hydrogen ions c).PAS proton beam d). PAS alpha particle beam

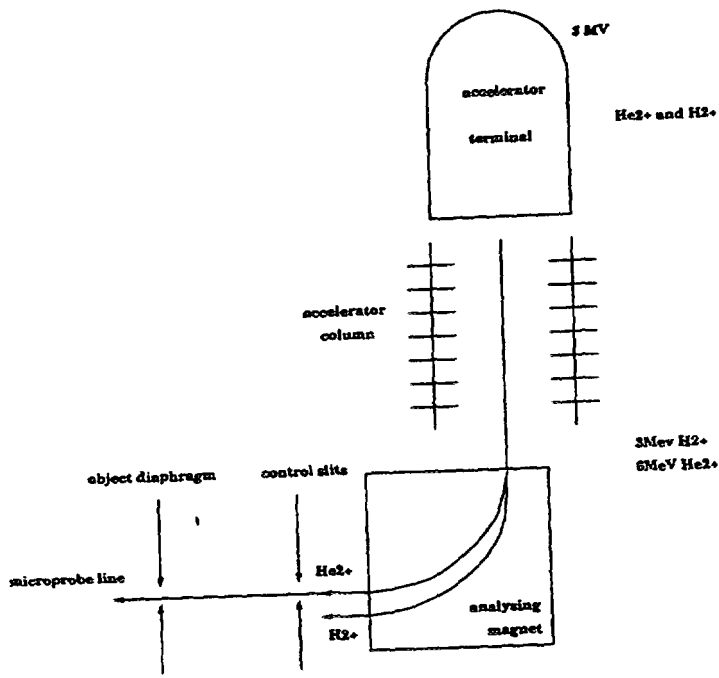


Figure 1

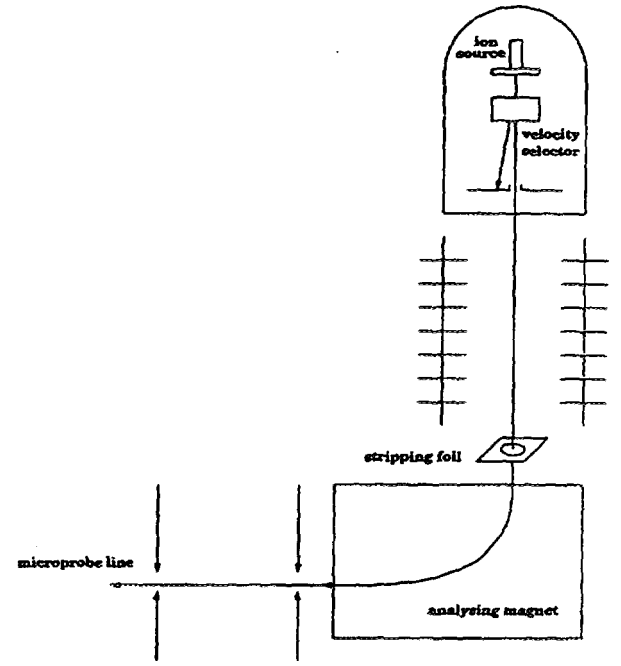
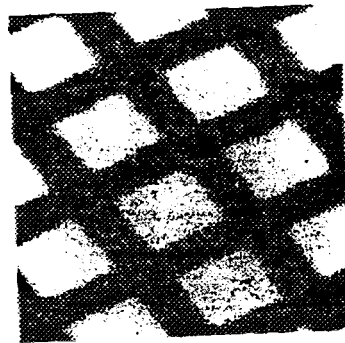
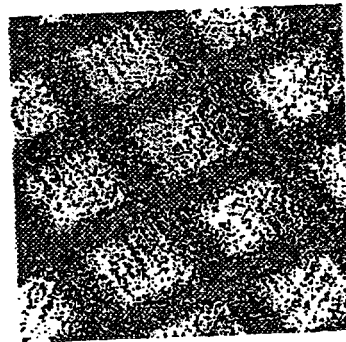


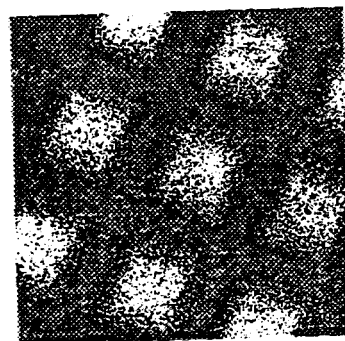
Figure 2



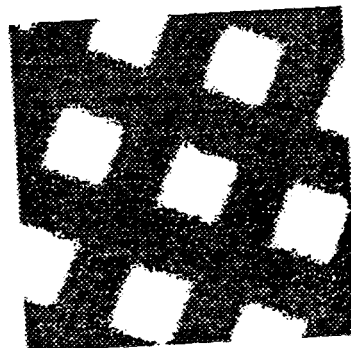
a).



b).



c).



d).

Figure 3



# Evaluation of Hydrogen and Oxygen Impurity Levels on Silicon Surfaces

M.J.KENNY, L.S.WIELUNSKI, R.P.NETTERFIELD, P.J.MARTIN and A.LEISTNER  
CSIRO Division of Applied Physics, PO Box 218 Lindfield, NSW, 2070, Australia

## 1 Introduction

Experimental work relating to the silicon mole as a possible definition of the kilogram requires amongst other things a knowledge of both the level of impurities present and their stability as a function of time. The ultimate requirement is for the mass to have an uncertainty of less than  $1 \times 10^{-8}$ <sup>(1)</sup>.

More than 90% of the high purity silicon which has been produced has been used in the semiconductor industry and effort has been directed to remove electrically active elements (eg. B, Al, P, As, Sb) and fast -diffusing metallic impurities such as Cu, Ni and Fe. On the other hand carbon fractions of up to 200 parts in  $10^9$  are acceptable<sup>(2)</sup>. Oxygen concentrations are typically 10 to 20 parts in  $10^9$  in crucible pulled Czochralski (CZ) grown silicon. In determining the Avogadro constant using a silicon crystal, the presence of carbon or oxygen in the bulk material at these concentrations would alter both the lattice parameter and density of the silicon.. Silicon grown by the FZ process offers the best prospect for pure Si. Irrespective of how pure the bulk material may be, the silicon surface may interact with the environment and in particular water and oxygen may be adsorbed onto the surface. The impurities may exist in any one of several forms:  $H_2O$ ,  $SiO_2$ ,  $SiO$ ,  $SiH$ ,  $SiOH$ .

A 1 kg silicon sphere has a diameter of 93.4 mm. If there is an unaccounted -for monolayer of water molecules on the surface, then these will weigh about 2.4  $\mu g$  and will produce a fractional error of  $2.4 \times 10^{-9}$ . Since the current limit of acceptability of mass uncertainty is  $10^{-8}$ <sup>(1)</sup> it is seen that just a few molecular layers of water could account for the maximum acceptable uncertainty. If there is a 1 nm oxide layer on the surface, this will account for a mass change of at least 10  $\mu g$  due to its different density.

This paper reports on surface analytical techniques used to quantify surface concentrations of impurities such as oxygen and hydrogen. The data must be considered as preliminary at this stage, but give some insight into the suitability of the techniques and a general idea of the significance of impurities at the monolayer level. These measurements have been carried out on a small number of silicon surfaces both semiconductor grade <111> crystalline material and silicon which has been used in sphere fabrication<sup>(3)</sup>.

## 2 Surface Analysis

Some surface analytical techniques are destructive, others are non-destructive. Ion Beam Analysis, SIMS, Auger and XPS require the sample to be in a vacuum, while Spectroscopic Ellipsometry and Raman Spectroscopy can be performed in air. Typically they are useful for analysis down to a depth of about a micron. In analysing surface contamination, it is important to consider whether the vacuum system adds or removes impurities.

In the present work, the following analytical techniques were used:(a) IBA: (Rutherford Backscattering and Elastic Recoil Detection), (b) SIMS (Time-of-Flight), (c) Spectroscopic Ellipsometry (d) X-ray Photoelectron Spectroscopy.

### 2.1 Ion Beam Analysis

Rutherford Backscattering and Channelling measurements were performed using a 2MeV helium beam from the HIAF accelerator<sup>(4)</sup> Samples used were <111> semiconductor grade wafers, both as received and after polishing and using a variety of simple surface cleaning treatments such as alcohol, detergent and vapour degreasing.

Figure 1 shows RBS and channelling data (2 MeV He<sup>+</sup>) for both semiconductor grade silicon and sphere material silicon. The two channelled (aligned) spectra are near identical, particularly in the surface region indicating that polishing does not result in any observable damage to the crystal structure. The ratio of counts in the channelled spectrum to those in the random alignment spectrum in the region of the surface peak is 0.025, which is indicative of good crystal quality in the <111> orientation. For the sphere material sample, there are no observed counts above the silicon edge, indicating that polishing does not introduce heavy impurities such as titanium.

The theoretical random orientation spectrum (indicated by the smooth line in Figure 1) includes a surface component of 2 nm of silicon oxide. (This appears as a small bump in the theoretical spectrum at 717 keV). For the semiconductor grade material, the experimental spectra, both random and channelled show no observable peak above the statistical noise in this region, but the sphere material shows a small bump in this region indicating that there may be a small amount of oxygen present. It can be concluded that an upper limit to the oxide thickness is 1.0 nm and that the more likely figure is less than this value

A piece of <111> semiconductor grade silicon was polished using the same technique as for sphere material. The grazing angle RBS channelled data showed clear evidence for about 1 nm of carbon on the polished material, whereas no significant carbon was on the as received sample. The carbon is presumed to be due to the pitch used in the polishing process.

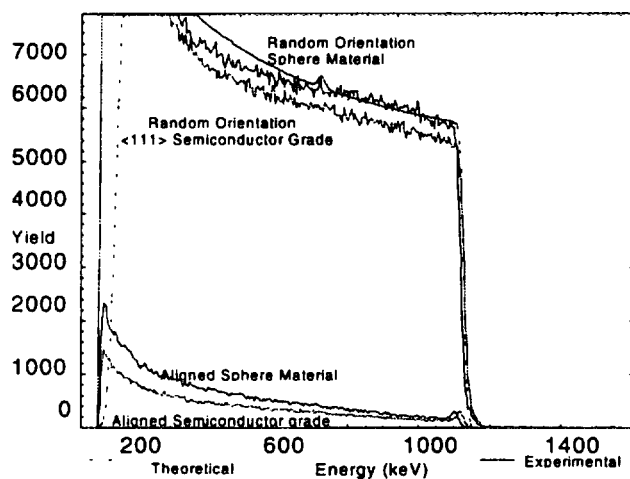


**Figure 1.** Rutherford Backscattering and Channelling Spectra for semiconductor grade and sphere fabrication silicon.

A 4.5 MeV helium beam was used to measure hydrogen concentration by elastic recoil. Whilst this showed the presence of a hydrogen concentration of about  $8 \times 10^{15}$  atoms  $\text{cm}^{-2}$ , there was evidence of hydrogen build up during irradiation, presumably from water molecules within the vacuum system. It was necessary to extrapolate to zero time. Assuming all the observed hydrogen was in the form of water, this corresponds to about one molecular layer on the surface.

## 2.2 Spectroscopic Ellipsometry

For very thin surfaces (~ 2 nm), spectroscopic ellipsometry does not provide direct information on the optical properties of the surface layer, however if it is assumed that the surface is a particular structure eg. SiO<sub>2</sub>, then the technique will accurately calculate the thickness of the layer.

Measurements to determine the thickness of surface oxide layer were made on a sample of silicon sphere material over a number of days showed that the initial thickness was 1.4 nm and this increased by about 25% after one day and then remained relatively stable thereafter.

These figures suggest that several atomic layers of oxygen are present on the surface and indicate that oxygen must be bonded to the silicon because on the basis of the hydrogen forward scattering data, water would only account for one oxygen monolayer.

### 2.3 SIMS Data

Time-of-flight SIMS measurements were made on semiconductor grade <111> silicon crystal. A small hydrogen peak was observed, but the oxygen peak intensity was nearly two orders of magnitude less than that of hydrogen and so the hydrogen is unlikely to be due to water and is more likely associated with hydrocarbons in the system. Similarly the oxide layer must be at or below the monolayer level.

### 2.4 X-ray Photoelectron Spectroscopy

Measurements were made for the Si 2p and O 1s lines from silicon sphere material, semiconductor <111> grade silicon, oxidised silicon wafer (1 $\mu$  thick oxide on Si) and polished fused silica (reference materials). The silicon samples were as received (no etching). The observed peak had an energy consistent with a surface layer of SiO rather than SiO<sub>2</sub>. The oxide layer thickness was calculated from the areas of the peaks in the Si 2p spectra and assuming a homogeneous film of SiO was present<sup>(5)</sup>, the layer thickness was estimated at 1.0 to 1.4 nm.

## 3 Discussion

For both the RBS / channelling data and SIMS data the oxide concentration on semiconductor grade silicon is too low to quantify. On the other hand, the ellipsometry data for sphere grade material shows about 1.6 nm of oxide on the surface, the XPS data shows 1.0 to 1.4 nm of oxide for both sphere and semiconductor material. The RBS data shows an oxide layer less than 1 nm thick on the sphere material.

Combination of this data suggests that up to 1.6 nm of oxygen is present on the surface in the form of SiO. The density of Si is 2.33 g cm<sup>-3</sup> and that of SiO is 2.13 g cm<sup>-3</sup>. If it is assumed that the outer 1 nm of a 47 mm diameter sphere is SiO, then the measured density will be lower than the expected density for pure silicon by about  $1 \times 10^{-8}$ . This would be at the limit of acceptability.

Hydrogen forward scattering shows that the hydrogen concentration is at the monolayer level in both the semiconductor grade and sphere fabrication material. However it is still necessary to establish the effects (positive or negative) on surface hydrogen concentration of placing the sample into a vacuum.

In fabricating a silicon sphere, polishing is an essential and long part of the process. There is risk that the crystal structure can be damaged in the surface region, thereby fractionally changing the number of atoms per unit cell and polishing lubricants can contaminate the surface. The RBS/ Channelling data show that there is no detectable damage to the surface. Some carbon contamination( 1 nm) is left behind on a polished sample.

## 4 Conclusion

In order to establish the extent of impurities on silicon surfaces a range of experimental techniques will need to be used. It is clear that hydrogen and oxygen impurities at monolayer concentrations can produce uncertainties in mass at the current level of tolerance ( $5 \times 10^{-8}$ ) and well above the desired tolerances for the future( $1 \times 10^{-8}$ ).

A range of experimental techniques has been used in the present work. The results have shown a spread in thickness of oxide layer, ranging from unmeasurable to 1.6 nm. Assuming the oxide layer is amorphous, then it will lead to a lower density value than that expected for pure silicon.

Measurements on hydrogen concentration have been performed in vacuum and it must be established whether the vacuum system increases or decreases water content on the surface.

These and other techniques must be developed and data taken for a range of silicon samples to finally establish whether the impurities can be kept to an acceptably low level.

## 5 References

- [1] T.J.Quinn, Metrologia 31(1994)275
- [2] W.Zulehner, Metrologia 31 (1994) 255
- [3] A.J.Leistner and W.J.Giardini, Metrologia 31 (1994) 231
- [4] S.H.Sie Nucl. Instr. and Meth. In Phys. Res B 10/11 (1985) 664
- [5] D.Wagner, NIST X-ray Photoelectron Spectroscopy Database. U.S.Dept. of Commerce, Gaithersburg, Maryland, USA. October 1989.



# **Influence of Implantation of Three Metallic Ions on the Mechanical Properties of Two Polymers**

M.V. Swain, A.J. Perry, and J.R. Treglio  
CSIRO, Division of Applied Physics, Lindfield NSW 2070, Australia,  
ISM Technologies, Inc, 9965 Carroll Canyon Rd., San Diego CA 92131 USA

## **Abstract:**

Ion implantation of poly ethylene terephthalate (PET) and polystyrene (PS) with various high energy metallic ions at 70 kV to dose of  $3 \times 10^{16}$  ions/cm<sup>2</sup> have been made. Measurements of the mechanical properties of the polymers before and after implantation have been made with an ultra micro-indentation system using both pointed and a small (2  $\mu$ m) radiused spherical tipped indenter. Significant differences have been observed between the Ti-B dual implanted surfaces and those of the Au and W implanted surfaces. For both the PET and PS the resistance to indenter penetration at very low loads was much greater for the Ti-B dual implanted surfaces. The estimated hardness and modulus versus depth of penetration for both indenters shows that the spherical indenter produces more consistent and less controversial values that are somewhat lower than the optimistic estimates from pointed indenters.

## **1. INTRODUCTION.**

Over the past decade there have been many reports of the influence of ion implantation on the properties of polymers [ 1-4 ]. The latter authors have made a systematic study and shown that the high energy implantation with virtually any species imparts improved surface wear properties to the polymer.

The observations to date have shown that the hardness, wear resistance and surface electrical conductivity all increase with ion implantation dose and energy. The general consensus [4,5] is that the mechanism responsible for the enhanced mechanical properties is that the high energy particles upon impact cause ionisation of the polymers resulting in the formation of free radicals that may readily cross-link the polymer chains. Rao et al [4] have recently suggested that the improvement is directly related to the linear energy transfer (LET) difference between the ionisation and displacement of the target atoms. Displacement of the target atoms or ions leads to polymer chain scission which it is argued as being detrimental to the mechanical properties as it essentially reduces the molecular weight of the polymer.

The main purpose of this study is to examine in more detail the mechanical properties of implanted materials. In particular pointed indentation response at very low loads shows a very elastic response compared with the very elastic-plastic behaviour of the unimplanted polymers. Also there has been little appreciation that the thickness of these modified layers is often sub micron and lies on a very compliant substrate which undoubtedly influences the force-displacement response of the indenter. The influence of the substrate on the measured properties will depend upon the ratio of the contact dimensions to the thickness of the modified layer and the ratio of the moduli of the substrate and layer [6]. The secondary aim is to compare the estimates of the measured properties using both pointed and spherical tipped indenters.

## **2. EXPERIMENTAL**

### **Indentation**

Indentation of the polymeric materials was conducted with a commercially available ultra-micro indentation system (UMIS-2000) at CSIRO. This system independently measures force and displacement during indentation in either a continuous loading and unloading procedure or (usually with spherical tipped indenters) a load partial unloading technique. The basis of the analysis with pointed and spherical indenters has been presented elsewhere [7,8].

### Materials.

Two polymeric materials were indented, a polystyrene (PS) and polyethylene terephthalate (PET). Plates of these materials were ~ 1 mm thick and 2 x 2 cm were cut from larger sheets.

### Ion Implantation

Implantations with various species were performed at ISM Technologies using a metal vapour vacuum arc (MEVVA) ion source [9]. The following species; W, Au, and a Ti-B dual composition were implanted with an accelerating voltage of 70 kV, although the ion source used delivers multi charged ions. Both polymers were implanted to doses of  $3 \times 10^{16}$  ions /  $\text{cm}^2$  at room temperature.

## 3. OBSERVATIONS.

Prior to implantation the polymeric materials were either transparent (PS) or white (PET), where as after implantation the colours were black {Ti-B dual} brown {W} or a brown with a golden hue {Au}.

Force-displacement curves for unimplanted and Ti-B implanted PS with a pointed indenter are shown in Figure 1. Another feature of the Ti-B dual implanted systems is the almost complete absence of any permanent deformation. The most indistinct behaviour was observed for the Au implanted PET which showed considerable scatter in the curves at low loads and often more than one inflection in the loading curve.

Load partial unload response of a 2  $\mu\text{m}$  radius spherical tipped indenter for both materials with and without Ti-B dual implantation showed similar response to that for the pointed indenter..

AFM observations revealed significant differences between the PET and PS material with more subtle differences between the implanted and unimplanted surfaces. PET has a granular surface structure with grain size in the 1 to 3  $\mu\text{m}$  range, whereas the PS shows striations in one direction indicative of an extruded or rolled material.

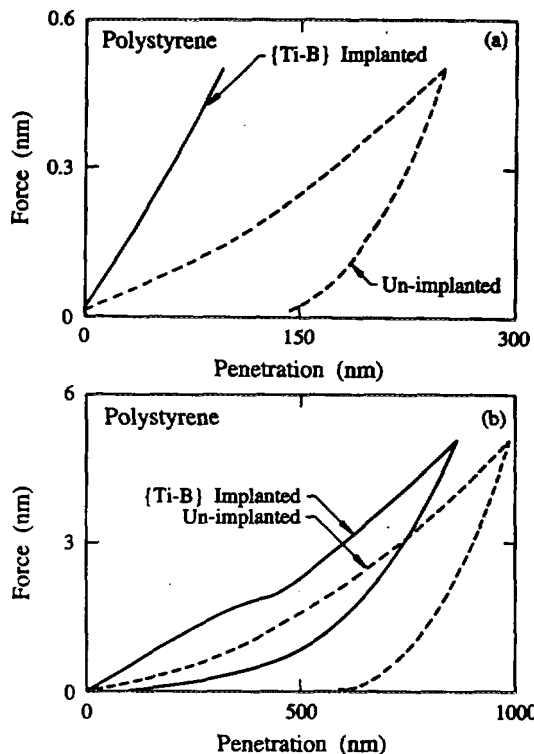


Figure 1. Continuous force-displacement observations using a UMIS-2000 with a Berkovich indenter pressed into; a) PS to 0.5 mN, b) PS to 5mN.

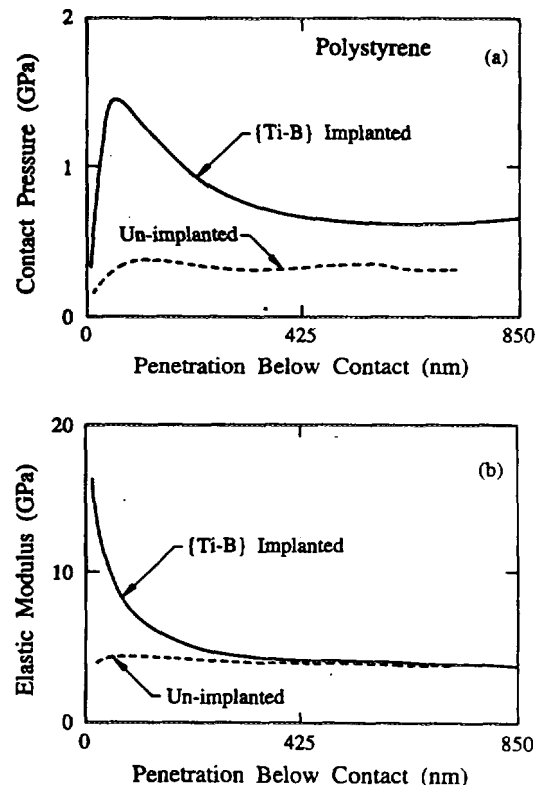


Figure 2. a) Contact pressure (Hardness) and, b) Elastic modulus versus depth for PS tested with the spherical indenter.

#### 4. RESULTS and DISCUSSION

The pointed indentation observations shown in Fig 1 maybe interpreted in terms of the approach outlined in [7,8]. The only reasonably reliable estimate of H and E from the data is for those curves which are continuous and even then only for the maximum value of load and displacement. Attempts to estimate the hardness at shallower depths of penetration relying upon extrapolating the unloading compliance from the maximum depth, although reasonable for homogenous bulk materials are highly unsatisfactory for stiff films on much softer substrates as is the present case. Another significant problem with the PET is the significant roughness on the scale of the lower load impressions.

Interpretation of the partial load and unload data shown in Figure 2 for PS with and without implantation with Ti-B. The contact pressure or hardness for the unimplanted PS in Figure 2 rises very steeply with penetration depth before reaching a maximum of ~ 0.3 GPa after 60 to 80 nm of penetration whereas for the implanted PS a maximum of ~ 1.4 GPa after 50 to 60 nm of penetration. The PET material implanted with with Ti-B also rises steeply and has a maximum of ~ 0.8 GPa at approximately 45 to 50 nm penetration at which point yield of the surface region occurs followed by rapid strain softening . At 50 nm depth of penetration the radius of contact is less than 300 nm and the maximum shear stress (assuming a homogenous material) would occur at less than 150 nm. Irrespective of the maximum load used with the load partial unload tests the maximum contact pressure never exceeded 0.8 GPa, a four fold increase in the hardness over that of the bulk PET. For the PS material the increase of the hardness for the implanted material is a little over four times that of the bulk material. In contrast to the contact pressure the elastic modulus determinations of the Ti-B implanted materials shows a monotonic decrease with depth of penetration, whereas that of the bulk PS material is virtually constant over the entire penetration range. Again in all instances the maximum modulus value was 16 GPa for implanted PS and 8 GPa for the implanted PET at depths of penetration of less than 10 nm. The modulus asymptotically approaches that of the substrate as anticipated from theoretical considerations of Gao [9].

#### 5. CONCLUSIONS.

Implantation with the Ti-B dual MEVVA beam is a very effective means of hardening and stiffening the very near surface region of two very common engineering polymers PET and PS. This surface hardening should impart significantly improved tribological properties whereby increasing the engineering applications of these polymers. Work is currently in progress to identify the hardening and stiffening mechanism responsible for these greatly improved properties.

#### References

1. S. Liu, Z. Liu, B. Zhai and Z. Wang, *Vacuum* 39 (1989) 271
2. K. Ueno, Y. Matsumoto, N. Nishimiya, M. Noshiro and M. Satou, *Nucl. Instru. & Methods in Phys Res.* B59/60 (1991) 1263 and 1276
3. G.R.Rao, E.H.Lee, R.Bhattacharya and A.W. McCormick, *J.Mater.Res.*, 10(1995) 190
4. S.J.Bull, A.R. McCabe and A. M. Jones, *Surface & Coating Tech.*, 64 (1994) 87-91
5. J.F.Ziegler, J.P. Biersack and U. Littmark, *The Stopping Range of Ions in Solids*, Pergamon, New York, 1985
6. J.S. Field and M. V. Swain, *J. Mater. Res.*, 8 (1993) 297
7. J.Mencik and M.V. Swain, *Materials Forum* 18 (1994) 277
8. H. Gao, C.H. Chiu and J. Lee, *Int. J.Sol. and Struct.*, 29(1992) 2471



# Homo-epitaxial diamond film growth on ion implanted diamond substrates.

PAUL S. WEISER, STEVEN PRAWER, KERRY W. NUGENT, ANDREW A. BETTIOL,  
LOUIE I. KOSTIDIS AND DAVID N. JAMIESON.

School of Physics, MARC, The University of Melbourne, Parkville, Victoria 3052, Australia.

## INTRODUCTION

The nucleation of CVD diamond is a complicated process, governed by many interrelated parameters. In the present work we attempt to elucidate the effect of strain on the growth of a homo-epitaxial CVD diamond. We have employed laterally confined high dose (MeV) Helium ion implantation to produce surface swelling of the substrate. The strain is enhanced by the lateral confinement of the implanted region to squares of  $100 \times 100 \mu\text{m}^2$ . After ion implantation, micro-Raman spectroscopy was employed to map the surface strain. The substrates were then inserted into a CVD reactor and a CVD diamond film was grown upon them. Since the strained regions were laterally confined, it was then possible to monitor the effect of strain on diamond nucleation. The substrates were also analysed using Rutherford Backscattering Spectroscopy (RBS), Proton induced X-ray Emission (PIXE) and Ion Beam induced Luminescence (IBIL).

## EXPERIMENT

The diamond substrates were  $3 \times 3 \text{ mm}^2$  (100) faces of natural diamonds from Argyle diamond mines. The substrates were inserted into the Micro-Analytical Research Centre's (MARC) Nuclear Microprobe and evacuated to a base pressure better than  $5 \times 10^{-6}$  Torr. The diamond substrates were implanted with 2 MeV He ions in the random orientation over an area of  $100 \times 100 \mu\text{m}^2$  with a dose of  $5.0 \times 10^{16}$  ions/cm<sup>2</sup>. (The ion range,  $R_p$ , and straggling,  $\Delta R_p$ , as predicted by TRIM90 [1], for randomly aligned 2 MeV He ions into diamond are  $3.46 \mu\text{m}$  and  $0.05 \mu\text{m}$  respectively.) Further information regarding the implantation technique can be found in ref. [2]. The implanted squares were analysed using a surface profilometer and micro-Raman spectroscopy.

The Raman measurements were taken using a Dilor XY confocal micro-Raman spectrometer employing the 514 nm line from an Ar ion laser with a  $\times 100$  objective and a confocal aperture of  $50 \mu\text{m}$ . The confocal optical arrangement is such that, even though diamond is transparent to the 514 nm light used in the Raman measurement, the sampling volume is restricted to a cylinder of diameter  $1 \mu\text{m}$  and depth  $2 \mu\text{m}$ . A depth scan is performed by varying the position of the focus of the laser using a piezoelectric driven objective. A shift in the Raman peak to higher energy is indicative of compressive strain, while a shift to lower energy is indicative of tensile strain [3].

After Raman analysis the samples were inserted into a hot-filament CVD deposition system. The CVD deposition conditions were: pressure 30 Torr; total flow 100 sccm; 1% CH<sub>4</sub>; deposition temperature 1000°C and deposition time 4 hours. The samples were then re-analysed using surface profilometry and micro-Raman Spectroscopy.

RBS, PIXE and IBIL spectra were then collected using the Nuclear Micro-probe. A  $20 \mu\text{m}$  beam spot was employed. IBIL spectroscopy enables a clear distinction between high quality natural diamond (blue peak) and CVD diamond films (green peak) [4]. By varying the analysing beam energy we obtain information from varying depths within the substrate. Firstly, 3 MeV H<sup>+</sup> ( $R_p + \Delta R_p = 47.6 + 0.76 \mu\text{m}$ ) was chosen to investigate the natural diamond substrate beneath the CVD diamond film. Secondly, a 1.4 MeV H<sup>+</sup> beam ( $R_p + \Delta R_p = 13.6 + 0.25 \mu\text{m}$ ) was employed, enabling a more selective analysis of the CVD diamond film ( $\sim 5 \mu\text{m}$ ) and the underlying natural diamond. Thirdly, a 2 MeV H<sub>2</sub><sup>+</sup> (molecular Hydrogen) beam ( $R_p + \Delta R_p = 7.98 + 0.16 \mu\text{m}$ ) was employed to investigate the CVD diamond film. (The molecular Hydrogen splits up on impact with the sample producing 1 MeV H<sup>+</sup> ions.)

## RESULTS AND DISCUSSION

Figure 1 shows the shift in the Raman diamond line position in steps of  $5 \mu\text{m}$  across a  $5.0 \times 10^{16}$  ions/cm<sup>2</sup> 2 MeV random He implant. The Raman diamond line position from the surface of the implant is shifted to lower energy by on average  $5.4 \text{ cm}^{-1}$  (FWHM,  $12 \text{ cm}^{-1}$ ) from its unstrained value of  $1331.3 \text{ cm}^{-1}$  (FWHM,  $3.2 \text{ cm}^{-1}$ ). The diamond line is broadened indicating that the strain in the cap is caused by defects in the cap, rather than by the end of range damage [5]. Recently, K.W. Nugent *et al* [6] have identified two new Raman peaks at  $1497$  and  $1630 \text{ cm}^{-1}$  associated with damage centres in diamond. Figure 1 plots the ratio of the  $1497 \text{ cm}^{-1}$  defect peak to that of the  $1332 \text{ cm}^{-1}$  diamond line across the surface of the implant. The presence of the  $1497 \text{ cm}^{-1}$  peak confirms that the strain is induced by defects in the cap layer itself.

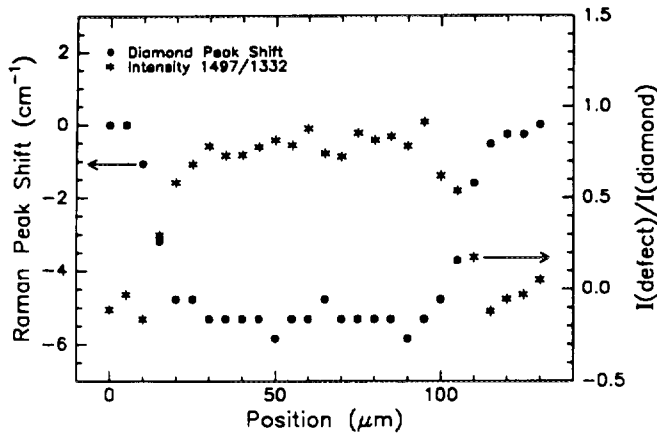


Figure 1. The Raman diamond peak position as a function of position across the implant. Also shown is the ratio of the intensity of the  $1497\text{ cm}^{-1}$  peak to that of the  $1332\text{ cm}^{-1}$  peak.

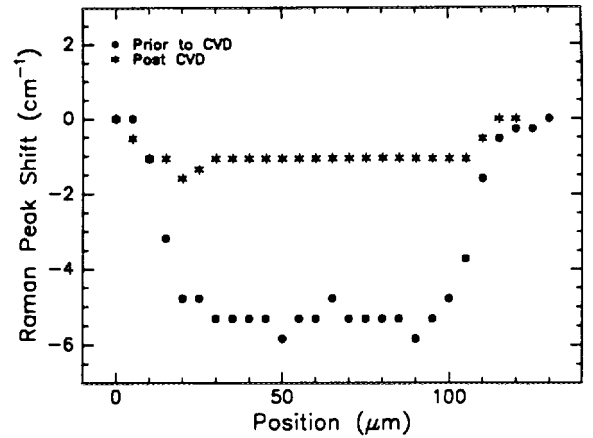


Figure 2. The Raman diamond peak position as a function of position across the implant post and prior to 4 hours of CVD diamond deposition.

After CVD, optical microscopy showed that a film has grown over the entire surface of the diamond substrate. Surface profilometry shows that the rate of diamond film growth on the implanted and unimplanted diamond substrate is the same. The deposited film was established as being homo-epitaxial, with respect to the substrate, by comparing polarised Raman azimuthal scans of the surface of the deposited diamond film and of the underlying diamond substrate at a depth greater than  $8\text{ }\mu\text{m}$  below the surface [see ref. 7 for details of this technique].

After CVD, the Raman spectra were once again performed across the surface of the implant. The shift in the diamond line across the implant is plotted in figure 2 (the shift across the implant prior to the CVD is also shown). The diamond line of the implant is still shifted to lower energy by, on average,  $1.1\text{ cm}^{-1}$ . There is no evidence of the  $1497$  and  $1630\text{ cm}^{-1}$  damage peaks. In addition, the FWHM of the diamond line is  $3.7\text{ cm}^{-1}$ . The absence of the damage peaks and the shift in the diamond line back towards its unstrained value could be due to either (i) the growth of an epitaxial film or alternatively (ii) to the annealing of the ion-induced damage which has been observed at these temperatures [6]. For this reason a depth scan of the Raman spectra in the implanted region was performed. Figure 3 shows the ratio of the intensity of the  $1497\text{ cm}^{-1}$  damage peak to the diamond line on the implant as a function of depth from the surface. The  $1497\text{ cm}^{-1}$  peak is absent for the first  $5\text{ }\mu\text{m}$  of the depth profile, but then its value rises and reaches a steady value about  $10\text{ }\mu\text{m}$  below the surface. There is no change in the diamond line position or FWHM throughout the depth profile. These results are consistent with an incompletely annealed implanted layer lying underneath a  $\sim 5\text{ }\mu\text{m}$  thick homo-epitaxial diamond film.

The Raman spectra of the film grown on the unimplanted diamond shows a large fluorescent background, which is not observed from the film grown on the implanted region. The inset to figure 3 is a depth profile performed on the film grown on the unimplanted diamond, showing the ratio of the fluorescent background intensity to that of the diamond. The large fluorescent background is present for the first  $\sim 5\text{ }\mu\text{m}$ , consistent with the thickness of the

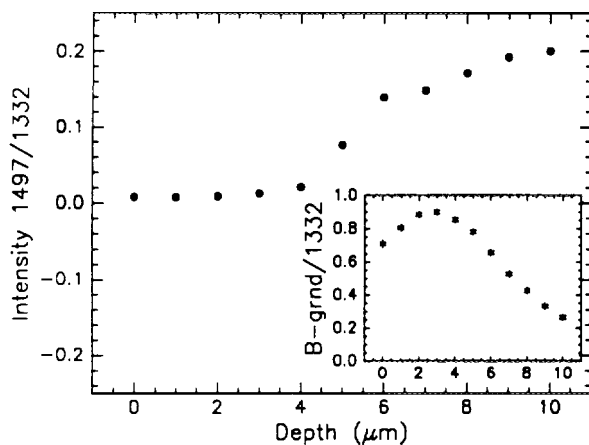


Figure 3. The ratio of the intensity of the  $1497\text{ cm}^{-1}$  damage peak to that of the diamond line (on the implant) as a function of depth after CVD deposition. The inset shows the ratio of the fluorescent background to the diamond peak intensity into the diamond grown on the unimplanted diamond.

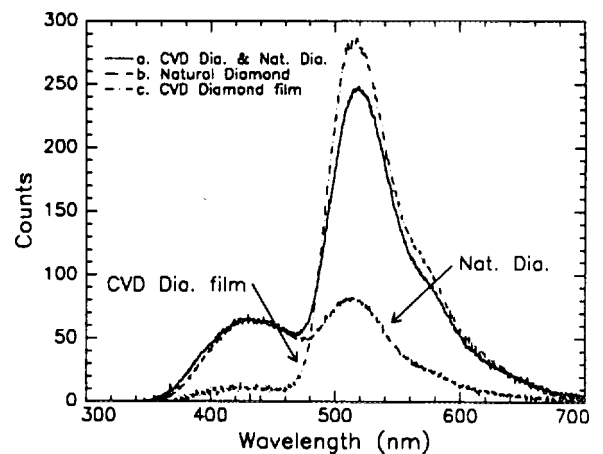


Figure 4.  $3\text{ MeV H}^+$  IBIL spectra from (a) the CVD diamond film and the underlying natural diamond substrate, (b) the uncoated natural diamond substrate and (c) the  $2\text{ MeV H}_2^+$  IBIL spectra of the CVD diamond film.

diamond film grown on the diamond substrate. In general, the fluorescent yield increases with defect density; however caution must be exercised since a high defect concentration can also act to quench fluorescence. Therefore all we can state at present is that the defect structure of the homo-epitaxial film grown on the implanted diamond is different to that grown on the unimplanted diamond. The presence of residual strain in the homo-epitaxial film grown on the implanted region as compared to the strain free film grown on the unimplanted diamond supports this assertion.

Figure 4 shows the 3 MeV  $H^+$  IBIL spectra of (a) the CVD diamond film and the underlying natural diamond substrate and (b) the uncoated natural diamond substrate. Figure 4(c) shows the 2 MeV  $H_2^+$  IBIL spectra of the CVD diamond film (figure 4(c) has been scaled to fit on the same graph as the 3 MeV  $H^+$  spectra). The IBIL results show that while the natural diamond substrate is an even mix of blue (425 nm, 2.9 eV) and green (515 nm, 2.4 eV) the spectra from the CVD diamond film is entirely green. (Note that only the ratio of the green to blue peak heights can be compared between the different beam energies.) The light emitted from the CVD film (2 MeV  $H_2^+$ ) above the implanted regions of the diamond substrate was too low in intensity to be detected by our Ocean Optics CCD array spectrometer. This is consistent with the very low luminescent yield observed in the Raman spectra. Visually the light emitted from the CVD diamond above the implant appears more blue (similar to that of the uncoated, unimplanted natural diamond) when compared to the light from the CVD diamond grown on the unimplanted portion of the diamond. Hence, since the homo-epitaxial diamond film is of low luminescent yield, it may indeed be transparent and the luminescence observed may be coming solely from the underlying natural diamond substrate.

The PIXE spectra obtained, using 1.4 MeV  $H^+$ , is shown in the inset to figure 5. This spectra shows that the only impurity within the first 13.6  $\mu\text{m}$  of the CVD diamond film/natural diamond interface is some W. The RBS spectra, obtained simultaneously from the same region of the sample, shows the expected C edge and surprisingly, a peak situated at 730 keV. Interestingly, there is no W present at the surface. When a RBS simulation is performed, taking into account the non-Rutherford C cross section at this energy, it is found that the peak at 730 keV is attributable to a layer of CVD diamond film containing 0.5% W buried 6.25  $\mu\text{m}$  below the surface of the CVD diamond. The thickness of this W containing layer is 5000  $\text{\AA}$ . The source of the W is undoubtedly from the W filament used in the CVD deposition process, with W being deposited over the entire surface of the diamond and covering both implanted and unimplanted portions of the substrate. The Raman fluorescence data, showing no fluorescence from the CVD film above the implanted natural diamond and fluorescence from the CVD above the unimplanted natural diamond, suggests that the W impurity is not responsible for the observed fluorescence

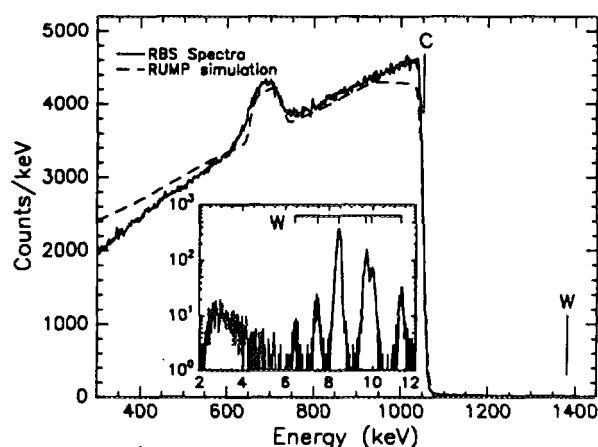


Figure 5. 1.4 MeV  $H^+$  RBS spectra of the CVD coated natural diamond substrate and RUMP simulation showing a 5000  $\text{\AA}$  layer containing 0.5 % W 6.25  $\mu\text{m}$  below the surface. The inset shows the PIXE spectra obtained.

## CONCLUSION

In order to investigate the effect of strain on the nucleation density of CVD deposited diamond we have employed high dose Helium ion implantation into diamond substrates, to produce surface swelling of the substrate. Raman spectroscopy revealed that the surfaces of the implanted regions are under tensile strain (up to 2.7 GPa). The growth rate of homo-epitaxial diamond is the same on the implanted and unimplanted regions of the diamond substrate. However, the CVD film grown on the implanted region shows slight residual tensile strain, but a reduced fluorescent yield as compared with the film grown on the unimplanted diamond substrate. The results show that defects and strain in the diamond substrate can influence the properties of homo-epitaxial diamond films.

## REFERENCES

1. TRIM90 - J.F. Ziegler and J.P. Biersack, *The Stopping and Ranges of Ions in Solids*, (Pergamon, New York, 1988).
2. S.P. Dooley and D.N. Jamieson, *Nuclear Instruments and Methods in Physics Research B66*, p369, (1992).
3. D.S. Knight and W.B. White, *J. Mater. Res.*, 4, p385, 1989.
4. A.A. Bettioli, D.N. Jamieson, S. Praver and M.G. Allen, *Nucl. Inst. and Meth. in Phys. Res. B* 85, p775, 1994.
5. D.N. Jamieson, S. Praver, K.W. Nugent and S.P. Dooley, *In Press*, *Nucl. Inst. and Meth. in Phys. Res. B*, 1995.
6. K.W. Nugent, S.P. Dooley, S. Praver and D.N. Jamieson, *In Preparation*.
7. P. John, D.K. Milne, P.G. Roberts, M.G. Jubber, M. Liehr and J.I.B. Wilson, *J. Mater. Res.*, 9(12), p3083, 1994



# RBS using $^{28}\text{Si}$ Beams

T.R. OPHEL

Department of Nuclear Physics, R.S.Phys.S.E.,  
Australian National University, Canberra 0200

I.V. MITCHELL

Physics Department, University of Western Ontario,  
London, Ontario N6A 3K7

## SUMMARY

Measurements of RBS using  $^{28}\text{Si}$  beams have been made to evaluate the enhancement of sensitivity that should obtain from kinematic suppression of silicon substrate scattering.

Two detection methods were tried. Aside from a surface barrier detector, a magnetic spectrometer, instrumented with a multi-electrode gas focal plane detector, was used to indicate the resolution attainable with low energy  $^{28}\text{Si}$  ions.

The results confirm that kinematically suppressed RBS does provide greatly improved sensitivity.

## INTRODUCTION

It has been established that the superior depth resolution, in principle possible with ions heavier than  $\alpha$ -particles, can be achieved with suitable detection techniques. For example, 4 and 6 MeV  $^{12}\text{C}$  and 10 and 18 MeV  $^{35}\text{Cl}$  measurements, using either or both a magnetic spectrometer and time of flight, have been made by Yang (1) and Fang (2).

Aside from depth resolution, the question of sensitivity arises. Sensitivity of typical RBS measurements is limited by pile-up beyond the substrate edge. The pile-up level can be significantly reduced, though not entirely eliminated, by electronic rejection techniques. With time of flight, the limit is determined by random events caused by x-rays produced at the target.

The present work sought to evaluate the simple technique of using heavy ions to suppress kinematically all substrate scattering. Clearly, with a  $^{28}\text{Si}$  beam,  $^{28}\text{Si}$  substrate scattering cannot be observed beyond  $90^\circ$ . Two methods were used to detect scattering  $^{28}\text{Si}$  ions; a surface barrier detector and a magnetic spectrometer and focal plane detector. The former is charge state independent whereas the latter should be capable of significantly better resolution. It should be noted that a magnetic spectrometer could be used with lighter ions to achieve the same elimination of substrate scattering by suitable location of a detector in the focal plane.

## EXPERIMENTAL DETAILS

Beams of 18 and 30 MeV  $^{28}\text{Si}$  were provided by the 14UD pelletron accelerator at ANU. The samples bombarded were masked with aluminium to prevent any scattering from heavy elements associated with the support structure.

A surface barrier detector was placed at a scattering angle of  $100^\circ$ . At smaller angles, low intensity substrate scattering was evident, due in part to scattering from  $^{29}\text{Si}$  and  $^{30}\text{Si}$  and, probably more importantly, from a halo beyond the kinematic limit arising from multiple scattering.

The magnetic spectrometer and associated detector have been described previously by Ophel et al (3). The detector was operated at a pressure of  $\sim 30$  torr with a mylar window 0.5 microns thick.

Apart from targets of thin gold, copper and a nominally blank silicon wafer, two types of implanted samples were measured. One set had been prepared such that gold or copper was trapped in voids at a depth of 1 micron. The voids were created by heat treatment at  $850^\circ$  following 80 KeV hydrogen implantation. Subsequent to a second implantation of 95 KeV gold or copper ( $\sim 10^{15}$  atoms/cm<sup>2</sup>), the sample was again heat-treated so that the gold or copper would

diffuse into the void region or of course to the surface (Weng-Leung (4)). The remaining samples were of silicon implanted with 95 KeV gold.

## RESULTS

A measurement made with the surface barrier detector using an 18 MeV  $^{28}\text{Si}$  beam is shown in Figure 1. The region of trapped gold is clearly evident, demonstrating adequate resolution ( $\sim 400$  KeV), despite the low energy of the scattered ions ( $\sim 6.5$  MeV from the gold at  $1\mu$ ). The region between the trapped layer and the surface peak is remarkably free of background.

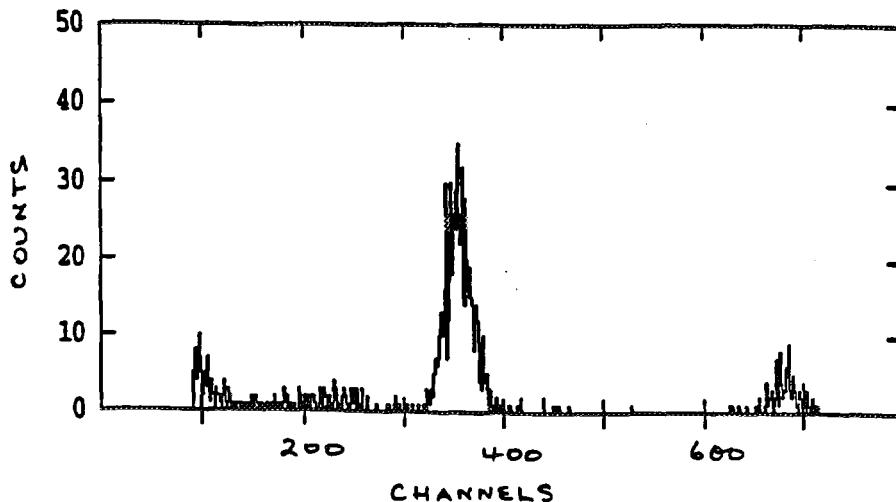


Figure 1. Spectrum of scattered  $^{28}\text{Si}$  ions obtained from a sample with Au trapped at  $1\mu$  depth.

Interestingly though, a broad distribution of events occurs at depths greater than  $1\mu$ , consistent with diffusion beyond the voids and decoration of dislocations known to exist in the region. Neither helium RBS nor SIMS is sufficiently sensitive to locate the distribution. Similar results were obtained for the copper implanted samples by increasing the beam energy to 30 MeV. For 2MeV helium RBS analysis of the latter samples, the scattered peak from the copper at  $1\mu$  depth is obscured by substrate scattering. The ability to increase the beam energy of heavy ions is therefore highly advantageous.

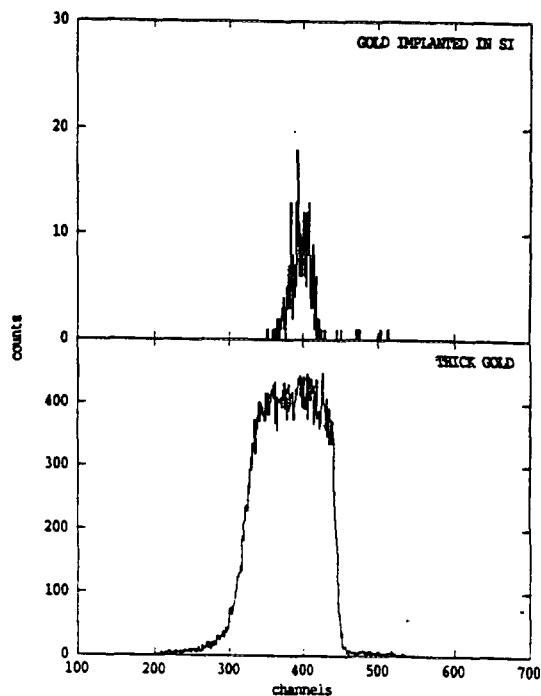


Figure 2. Spectra obtained with the focal plane detector for  $^{28}\text{Si}$  ions scattered from thick gold (lower) and from silicon implanted with 95 KeV Au (upper).

One measurement was made with the spectrometer. Back-scattered  $^{28}\text{Si}$  ions were detected with a resolution of  $\sim 100$  KeV, allowing straightforward measurement of the distribution of the implanted 95 KeV Au ions (Figure 2).

## CONCLUSIONS

Heavy ion RBS with beams of Si or heavier almost certainly is capable of providing the ultimate sensitivity presently available for detection of heavier elements in silicon (excluding AMS which provides only bulk analysis). The sensitivity can be enhanced further with hybrid gas  $\Delta E$ /surface barrier E detectors (5), which would eliminate extraneous background effects such as cosmic rays and ambient  $\alpha$ -activity. In fact, hybrid detectors would also provide the means of eliminating very effectively pile-up effects for conventional RBS using helium beams.

The magnetic spectrometer measurement demonstrates that good depth resolution can be achieved with low energy  $^{28}\text{Si}$  beams.

## ACKNOWLEDGEMENTS

One of us (IVM) would like to thank the Department of Electronic Materials Engineering, ANU for support and use of facilities.

## REFERENCES

- (1) Yang, Q., O'Connor, D.J., Fang, Z., Ophel, T.R., Hay, H.J. and Jackman, T.E., Nuclear Instruments and Methods B74 (1993) 431-438.
- (2) Fang, Z., PhD Thesis 1994, University of Newcastle (unpublished).
- (3) Ophel, T.R., Fifield, L.K., Catford, W.M., Orr, N.A., Woods, C.L., Harding A. and Clarkson, G.P., Nuclear Instruments and methods A272 (1988) 734-749.
- (4) Weng-Leung J., Department of Electronic Materials Engineering, R.S.Phys.S.E. ANU developed the procedure.
- (5) Ophel, T.R., Galster, W., Hinde, D.J. and Leigh, J.R, Nuclear Instruments and Methods 193 (1982) 507-512 and references therein.

# Focussed MeV Ion Beam Implanted Waveguides

M. L. VON BIBRA, A. ROBERTS, K. NUGENT, D. N. JAMIESON  
 School of Physics, University of Melbourne, Parkville, Victoria, 3052

Single mode buried optical waveguides have been fabricated in fused silica by MeV proton implantation using a focussed hydrogen ion beam. The technique has the potential to direct write waveguide devices and produce multi-layered structures, without the need for intermediate steps such as mask fabrication or layered depositions. A micron resolution Confocal Raman Spectrometer has been used to map the distribution of atomic vacancies that forms the waveguiding region. The results are compared with theoretical calculations. Losses of  $3 \text{ dB cm}^{-1}$  have been measured in unannealed samples, which decreases to less than  $0.5 \text{ dB cm}^{-1}$  after annealing at 500 degrees Celsius. We describe methods for determining the refractive index distribution of single mode buried waveguides from their output intensity distributions via an inversion of the scalar wave equation.

## INTRODUCTION

An optical waveguide is a region in a transparent material that has a higher refractive index than the surrounding medium. The most common type of optical waveguide is the optical fibre. Light travelling through the fibre is contained within the high index fibre core by total internal reflection from the lower index cladding interface. In Integrated Optics the term 'waveguide' is generally reserved for waveguides that are fabricated within a substrate material. One of the aims of Integrated Optics is to develop optical devices in materials that can be integrated with current silicon technology, bridging the gap between existing intercontinental fibre spans and domestic digital communications networks. The components that this technology requires include signal couplers, junctions, signal amplifiers and optical switches. The fundamental component of all these devices is the waveguide.

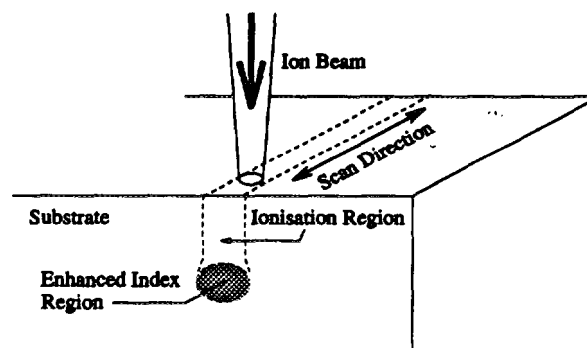


FIGURE 1. A focussed ion beam with a spot size of the order of a few microns penetrates the surface of the substrate. The ions lose their energy by nuclear interactions at the end of their range.

Whilst ion implantation has been used to make optical waveguides, it is generally used in the fabrication of planar waveguide structures [1]. Where channel waveguides have been fabricated, the use of a mask has been employed to localise the sample area penetrated by the ions [2]. We have used the Micro-Analytic Research Centre's (MARC) particle accelerator and ion beam micro-probe for the fabrication of buried channel waveguides (Figure 1). The micro-probe can focus the ion beam down to a spot size of the order of a few microns. This is comparable with the dimensions of a single mode optical waveguide. By a combination of beam and sample scanning it is possible to direct write buried waveguides and waveguide devices in the substrate material without the need for photolithographic masking. This is particularly important for buried waveguide fabrication at MeV energies for which mask production requires exact specifications.

## FABRICATION

Upon entering the substrate the hydrogen atoms ionise and split into two protons. The protons continue into the substrate losing energy mostly by ionisation at first, but then predominantly by nuclear interactions at the end of range. In the case of amorphous fused silica, the nuclear interactions produce atomic vacancies, and break up silicon-oxygen bonds in the material. The effect of this is to further amorphise and densify the material, resulting in a refractive index enhancement of  $\sim 0.1\%$  at the end of range of the protons.

The waveguides are characterised by imaging their modal output under laser illumination using the setup shown in Figure 2. A 670 nm diode laser is coupled into a 4 micron core single mode fibre, which is then butt coupled against the end of the waveguide. The output intensity is imaged with a 12-bit liquid cooled Photonics CCD camera. The output for a waveguide illuminated in this manner is shown in Figure 3. This waveguide was fabricated in a 15 mm long, polished fused silica sample by irradiation with a focussed beam of hydrogen atoms at 1.9 MeV. The proton dose applied was  $\sim 1.7 \times 10^{13}$  ions  $\text{cm}^{-2}$ .

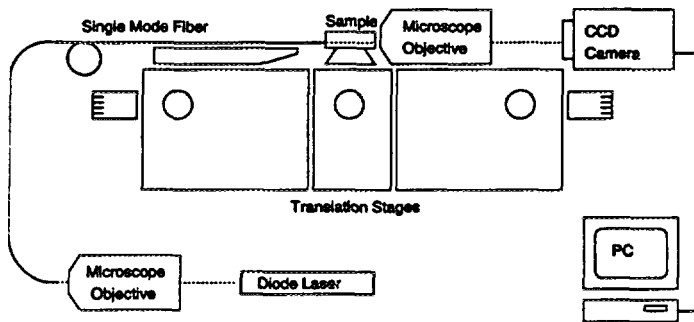


**FIGURE 2.** Laser coupling setup for waveguide imaging. A 670 nm diode laser is coupled into a single mode fibre which is butt coupled against the end of the waveguide. The output intensity is imaged with a microscope objective and CCD camera.

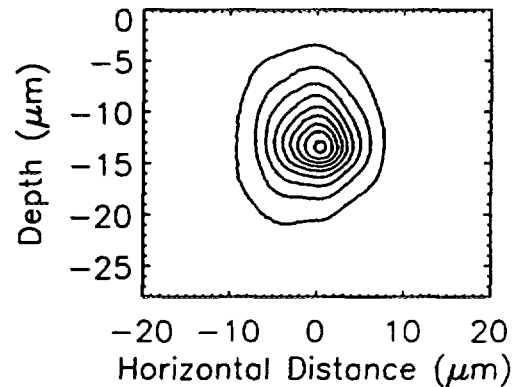


**FIGURE 3.** Output intensity image of a single mode waveguide fabricated by irradiation with a focussed ion beam.

## RAMAN SPECTRAL ANALYSIS

Previous studies [3] of neutron irradiated fused silica using Raman spectroscopy have found two peaks in the Raman spectra which increase in intensity and frequency under increasing neutron doses. These were taken to be the key indicators of densification of the material in general, and in particular, they were seen to directly reflect the amount of broken Si-O bonds within the amorphous network. We have used a Confocal Raman Spectrometer to take a series of spectra at one micron intervals in a vertical line across the end of a waveguide fabricated with 3 MeV protons at a dose of  $\sim 10^{15}$  ions  $\text{cm}^{-2}$ . The series is shown in Figure 4. The increase in intensity of the peaks at  $490 \text{ cm}^{-1}$  and  $604 \text{ cm}^{-1}$  is clearly visible. The area under the  $604 \text{ cm}^{-1}$  peak is plotted against the atomic vacancies profile calculated by the TRIM code as shown in Figure 5.

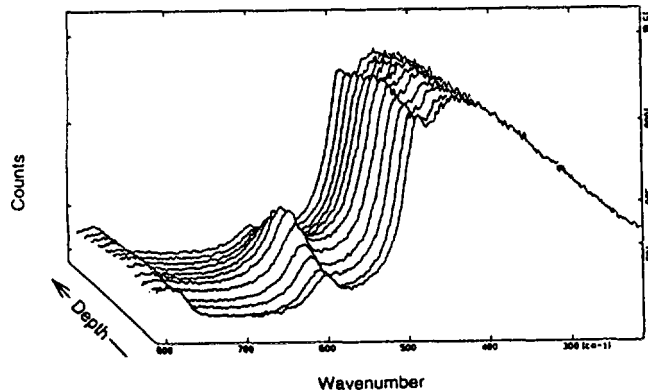


**FIGURE 4.** Series of Raman spectra taken at one micron intervals through a highly dosed waveguide. The spectral peaks at  $490 \text{ cm}^{-1}$  and  $604 \text{ cm}^{-1}$  indicate the amount of broken Si-O bonds in the substrate.

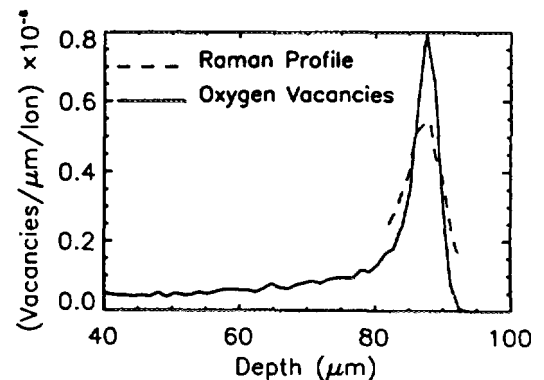


**FIGURE 5.** Raman profile (arbitrary units) plotted against the Oxygen vacancies profile as calculated by the TRIM code. The peaks of the two profiles occur at the same distance below the surface of the substrate.



# Elastic Recoil Detection Analysis of Ferroelectric Films

W.B. STANNARD, P.N. JOHNSTON, S.R. WALKER and I.F. BUBB,  
Royal Melbourne Institute of Technology, Melbourne, Australia.  
J.F. SCOTT, University of New South Wales, Sydney, Australia  
D.D. COHEN AND N. DYTLEWSKI,  
Australian Nuclear Science and Technology Organisation, Menai, Australia

## INTRODUCTION

There has been considerable progress in developing  $\text{SrBi}_2\text{Ta}_2\text{O}_9$  (SBT) and  $\text{Ba}_{0.7}\text{Sr}_{0.3}\text{TiO}_3$  (BST) ferroelectric films for use as non-volatile memory chips and for capacitors in dynamic random access memories (DRAMs). A nonvolatile memory, such as a magnetic core, retains information if the power is cut off. In DRAMs capacitors take up most of the area in the chips, the resistors and transistors being relatively small. If the dielectric constant of the material is increased, the size of the capacitor could be reduced correspondingly. This would make memories quicker and potentially cheaper to produce, as designs would be simpler and would need fewer production stages. Until recently the capacitor material in DRAMs was generally silicon dioxide (quartz) or tantalum oxide ( $\text{Ta}_2\text{O}_5$ ). The need for further reduction in capacitor area requires materials with much greater dielectric constant. Ferroelectric materials have a very large dielectric constant ( $\sim 1000$ ), approximately one hundred times greater than that of silicon dioxide.

Devices made from these materials have been known to experience breakdown after repeated voltage pulsing. It has been suggested that this is related to stoichiometric changes within the material (1,2). To accurately characterise these materials Elastic Recoil Detection Analysis (ERDA) is being developed. This technique employs a high energy heavy ion beam to eject nuclei from the target and uses a time of flight and energy dispersive (ToF-E) detector telescope to detect these nuclei. The recoil nuclei carry both energy and mass information which enables the determination of separate energy spectra for individual elements or for small groups of elements.

In this work ERDA employing  $77 \text{ MeV } ^{127}\text{I}$  ions has been used to analyse Strontium Bismuth Tantalate thin films at the heavy ion recoil facility at ANSTO, Lucas Heights. Analysis of BST films has been reported previously (3).

## EXPERIMENTAL

### Ferroelectric films

The samples analysed in this work are Strontium Bismuth Tantalate (SBT) ferroelectric wafers, produced by Symetrix Corp., Colorado Springs USA., using spin-on followed by metal organic decomposition (MOD). The wafers consist nominally of a 200 nm layer of SBT deposited a 200 nm platinum layer above a 30 nm titanium adhesion layer and a silicon substrate.

### Elastic Recoil Detection Analysis

ERDA was carried out on the ferroelectric films using the heavy ion recoil facility on the ANTARES 8 MV Tandem Accelerator at the Lucas Heights Research Laboratories of ANSTO. An analysing beam of  $77 \text{ MeV } ^{127}\text{I}$  ions was incident on the sample at an angle of  $67.5^\circ$  to the surface normal. Recoil nuclei were detected by a ToF-E detector at an angle of  $45^\circ$  to the incident beam direction.

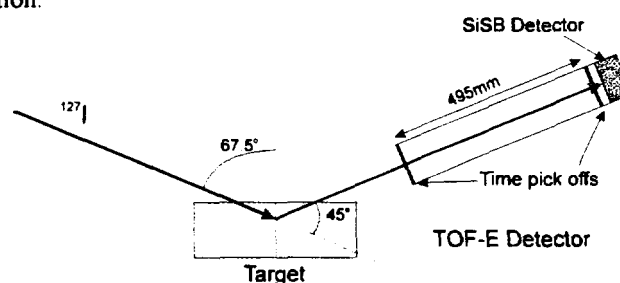


FIGURE 2 TOF-E detector setup for recoil spectrometry.

The ToF-E detector consists of a silicon surface barrier (SiSB) energy detector and two time pick-off detectors separated by a flight length of 495 mm (see figure 2). The ToF-E detector has been described in more detail in previous work (4).

### ANALYSIS

The analysis consists of (i) calibration of the data for time, energy and mass, (ii) separation of the data into one dimensional histograms for each of the elements of interest and (iii) quantitative analysis of the depth profile of the sample. The first two stages use the CERN analysis package PAW (5) and the macro package TASS (6). The third stage uses an improved and extended version of the RMIT software for nuclear reaction analysis ANALNRA (7).

#### Calibration

Calibration of time, energy and mass has been described by Stannard et al (8). The time calibration for this work is shown in figure 3.

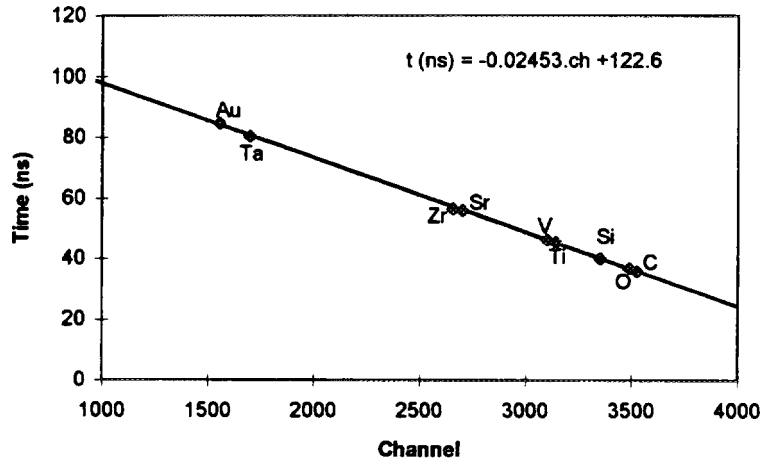


FIGURE 3 Time calibration using various elements.

Energy and mass calibration were performed using the method of El Bouanini et al (9) as described by Stannard et al (8). The mean pulse height ( $X$ ) from the SiSB detector was fitted to the function

$$E = c_0 + c_1 A + (c_2 + c_3 A) X + (c_4 + c_5 A) X^2$$

where  $A$  is the atomic mass and  $c_{0-5}$  are fitting constants. This was done using 192 time slices, each of 20 channels (0.5 ns), of the energy spectra for  $^{12}\text{C}$ ,  $^{16}\text{O}$ ,  $^{28}\text{Si}$ ,  $^{51}\text{V}$ ,  $^{58}\text{Ni}$ ,  $^{88}\text{Sr}$ ,  $^{127}\text{I}$ ,  $^{181}\text{Ta}$  and  $^{197}\text{Au}$ . Figure 4 shows calibrated mass versus SiSB detector pulse height for a thin film BST sample using 77 MeV  $^{127}\text{I}^{10+}$  ions as described by Stannard et. al. (8).

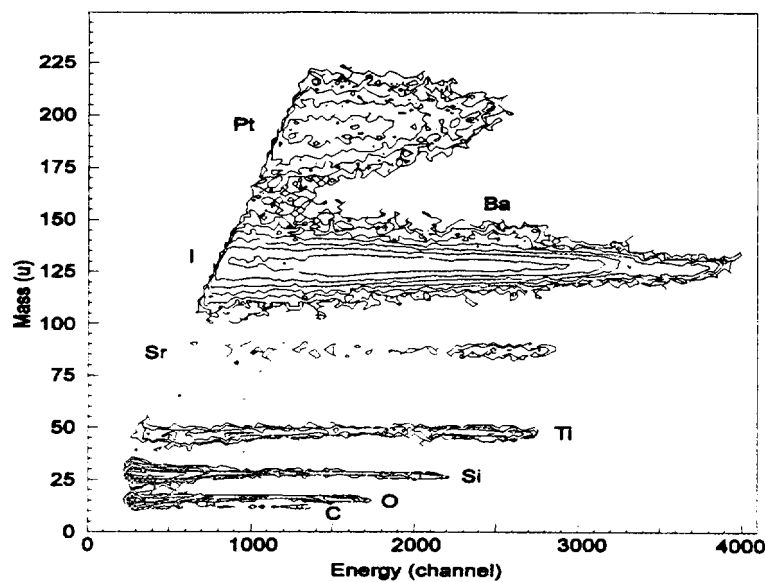


FIGURE 4 Calibrated mass versus SiSB detector pulse height for a BST sample using 77 MeV  $^{127}\text{I}^{10+}$  ions.

### Separation of Elements

One dimensional histograms of the individual elemental constituents can be derived from the mass-energy data by separating the mass data for each element and projecting onto the energy axis. The individual spectra for the previously analysed BST sample are shown in figure 5.

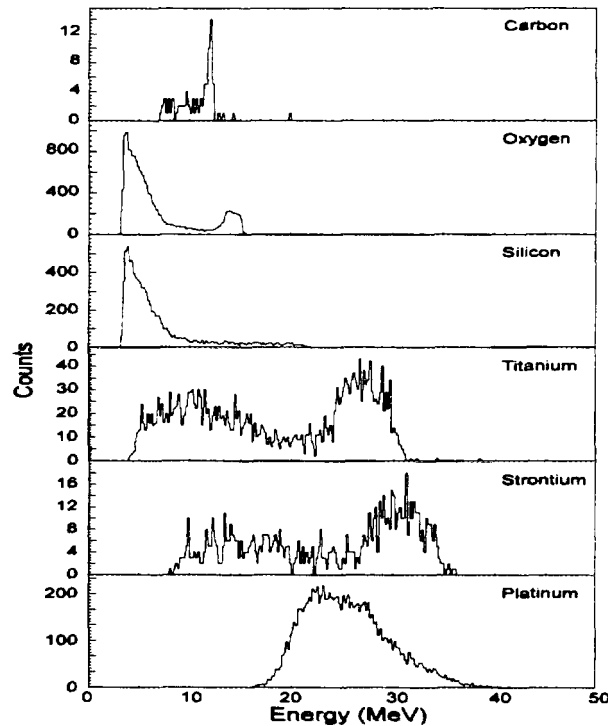


FIGURE 5 Separated individual energy spectra for carbon, oxygen, silicon, titanium, strontium and platinum.

### Quantitative Analysis

The data can be quantitatively analysed using a modified version of the software for nuclear reaction analysis, ANALNRA (8). ERDA can be considered a case of nuclear reaction analysis where the reaction is  $X(^{127}\text{I}, X)^{127}\text{I}$  and the  $Q$ -value is 0. The spectrum is simulated for each isotope and fitted to the raw data using a non-linear least squares fitting routine.

The techniques discussed above are currently being applied to the analysis of several SBT samples produced under significantly different conditions.

### ACKNOWLEDGMENTS

This work is supported by the Australian Research Council and the Australian Institute of Nuclear Science and Engineering.

### REFERENCES

1. J.F. Scott, M. Azuma, C.A. Paz de Araujo, L.D. McMillan, M.C. Scott and T. Roberts, *Integ. Ferroelectrics*, **4**, 61 (1994).
2. R. Waser and M. Klee, *Integ. Ferroelectrics*, **2**, 23 (1992).
3. W.B. Stannard, P.N. Johnston, S.R. Walker, I.F. Bubb, J.F. Scott, D.D. Cohen, N. Dytlewski and J.W. Martin, *Integ. Ferroelectrics*, **9**, 243 (1995).
4. H.J. Whitlow, G. Possnert and C.S. Petersson, *Nucl. Instr. Meth. B*, **27**, 448 (1987).
5. Application Software Group, Computing and Networks Division at CERN, the *PAW Manual Version 1.14*, (CERN, Geneva, Switzerland, 1992).
6. H.J. Whitlow, *TASS*, Internal Report, (Dept. Nuclear Physics, Lund Institute of Technology, Sölvegatan 14 S-223 62 Lund, Sweden, 1993).
7. P.N. Johnston, *Nucl. Instr. Meth. B*, **79**, 506 (1993).
8. W.B. Stannard, P.N. Johnston, S.R. Walker, I.F. Bubb, J.F. Scott, D.D. Cohen, N. Dytlewski and J.W. Martin, *Nucl. Instr. Meth. B*, (in press).
9. M. El Bouanani, M. Hult, L. Persson, E. Swietlicki, M. Andersson, M. Östling, N. Lundberg, C. Zaring, D.D. Cohen, N. Dytlewski, P.N. Johnston, S.R. Walker, I.F. Bubb and H.J. Whitlow, *Nucl. Instr. Meth. B*, **94**, 530 (1994).



# Ion Beam Induced Luminescence Characterisation of CVD Diamond Films

A. A. BETTIOL, P. GONON and D. N. JAMIESON

School of Physics, MARC  
The University of Melbourne  
Parkville, Vic., 3052

## INTRODUCTION

The characterisation of the band structure properties of materials and devices by ion microprobe techniques has been made possible at the Melbourne MeV ion microprobe facility with the development of Ion Beam Induced Luminescence (IBIL) [1]. A number of diamond films grown by Microwave Plasma Chemical Vapour Deposition (MPCVD) on silicon substrates are analysed. A preliminary study of the luminescence properties of these samples has revealed information not previously obtainable via traditional microprobe techniques. The optical effects of incorporating dopants during the deposition process is determined using IBIL. The presence of trace element impurities introduced during growth is examined by Particle Induced X-ray Emission (PIXE), and a measurement of the film thickness is made using Rutherford Backscattering Spectrometry (RBS).

## EXPERIMENT

A 3 MeV proton beam produced by a Pelletron 5U accelerator was focused down to about 20  $\mu\text{m}$  on target. IBIL, PIXE and RBS data was acquired from a range of diamond films which were grown at Melbourne by Microwave plasma CVD on (100) silicon substrates. The samples consisted of undoped and aluminium, boron and sodium doped specimens. Samples were grown at a pressure of 20-30 torr and at a temperature of about 800 – 850° C. A methane and hydrogen gas mixture of ( $\text{CH}_4/\text{H}_2 = 0.5\%$ ) was used to grow all samples with the exception of the undoped sample. The undoped sample also contained some oxygen due to the bubbling of the hydrogen gas through ethanol. Organic compounds containing boron and aluminium, and sodium chloride were used for doping.

All IBIL spectra were acquired on an Ocean Optics SD1000 spectrometer. Light collection was achieved by modifying the target chamber microscope to accommodate an optical fibre. Light collected by the microscope 4.5X objective lens was focused onto the fibre core by a collimating lens which was then attached to the spectrometer. The double spectrometer has two gratings covering the 360-850nm and 400-650nm wavelength ranges. The spectral resolution for the two ranges is 20 and 10 nm respectively when using a 400  $\mu\text{m}$  core fibre.

## RESULTS AND DISCUSSION

An understanding of the ion-solid interaction and energy loss process is important for any ion beam analytical technique, IBIL is no exception. When an ion interacts with a material it dumps energy along the whole ion track. The energy loss amongst other things goes into creating electron-hole pairs which in turn can recombine to give luminescence. For materials such as diamond which are transparent to visible wavelengths, the acquired IBIL spectrum may be a function of the beam energy. Furthermore, most of the energy deposited by an ion beam, and hence most of the damage, will be at the end of range. For this reason, an accurate measure of the film thickness is necessary in order to better understand the IBIL spectra acquired. It sometimes may be desirable to push the ion beam end of range past the epitaxial layer so as to minimise ion beam induced damage effects.

The ion beam penetration depth for 3 MeV protons in diamond was determined to be  $73 \mu\text{m}$  using a TRIM simulation [2]. The film thickness was determined by fitting a non-Rutherford RUMP RBS simulation of the carbon on silicon film to the data [3]. The approximate thickness for the boron, sodium and undoped films was 8, 17,  $20 \mu\text{m}$ . The aluminium doped sample thickness could not be determined with the 3 MeV proton beam since the beam end of range was within the diamond film. Figure 1 shows the RBS data and RUMP fit for the undoped and boron doped samples.

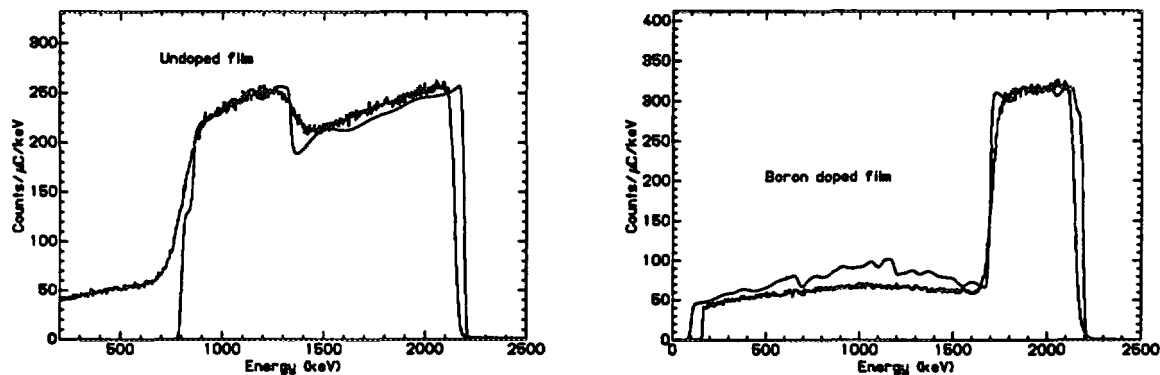


Figure 1: RBS data and RUMP simulation fit to Undoped and boron doped diamond films.

There has been much renewed discussion in recent times as to the origin of the so called "A-band" luminescence in diamond. A model which went some way into explaining the band and its properties was proposed by Dean [4] in 1965. He attributed the luminescence to the recombination of electrons and holes at donor acceptor pairs (DAP). The model predicted that the peak position of the A-band was a function of the separation of the DAP's. It was proposed that DAP's in natural diamonds were closer due to the diffusion of donors and acceptors at elevated temperatures over long time periods. In 1993 Prins [5] showed that the peak position of the A-band observed with Cathodoluminescence did not shift in samples which had been ion implanted with boron and carbon. The increased donor density should have shifted the peak position to higher energy. Ruan et al. [6] looked at boron doped diamond films and found two bands with peak positions at 2.83 eV and 2.32 eV. He attributed the 2.32 eV band to boron and the 2.83 eV band, which is the much observed A-band, to dislocations. Yacobi et al. [7] also studied the 2.83 eV band in homoepitaxial diamond films. Monochromatic CL maps of the 2.83 eV band revealed that there was a high density of dislocations on films grown on (111) substrates.

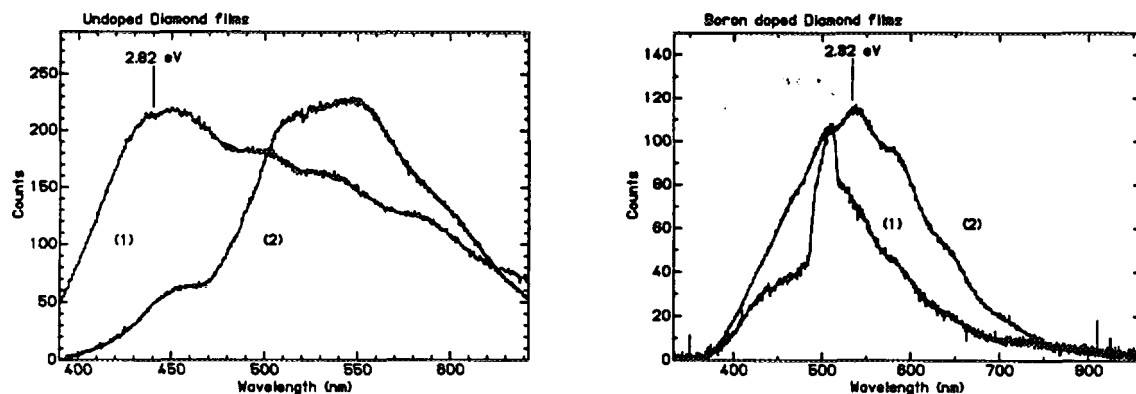


Figure 2: IBIL data comparing (a) Undoped diamond films grown with (1) and without (2) oxygen, and (b) boron doped diamond films before (2) and after (1) ion beam damage

Figure 2a shows an IBIL spectrum from two undoped diamond films. The only difference between the samples is that the first one was grown with the addition of oxygen in the gas mixture. Both samples

contain a series of possibly four broad bands centered at various wavelengths. The bands are unresolved and essentially featureless at room temperature. The band centered at about 450 nm corresponds to the luminescence observed by Ruan [6] and Yacobi [7] and is attributed to dislocations. This band is much more intense in the sample containing oxygen indicating a larger concentration of dislocations in the film.

IBIL spectra acquired from the boron doped samples is shown in figure 2b. The band observed at 2.32 eV (534 nm) corresponds to the boron related band previously observed by Ruan [6] and others. In general all of this form of luminescence is quenched by ion beam induced damage. We did however observe a band centered at 510 nm in one of the boron samples which was an exception to this rule. The origin of this luminescence is unknown at this stage. Further study is required to ascertain the nature of this band.

No evidence was found that samples doped with aluminium and sodium did in fact contain dopants. PIXE is not sensitive to these elements, only X-ray emission from elements above silicon can be observed. The IBIL data from these samples did not yield any results which would indicate the presence of these elements. It is clear that sample cooling is required to resolve the broad emission bands and identify the presence of any zero phonon lines associated with vibronic bands that might be present in the spectra. Microwave plasma CVD is a relatively clean deposition technique. Unlike samples which are grown by tungsten hot filament CVD, MPCVD samples don't contain tungsten, iron and other heavy trace element impurities. PIXE data from the samples looked at here confirmed this fact to a sensitivity of about 200 ppm.

## CONCLUSION

IBIL was used in conjunction with RBS and PIXE to characterise diamond film samples grown by MPCVD. IBIL spectra obtained at room temperature were used to show the presence of boron for doped samples, and to qualitatively compare the dislocation density in samples grown by different methods. A new band which was more resistant to ion beam induced damage was observed for one of the boron samples. Its nature still remains a mystery. This band and others will be re-examined under cooled conditions in the near future in order to better understand their nature. The presence of vibronic bands which should be resolved at 77K will further help to understand not only the growth process but also what effect the ion beam has on the samples. RBS was used to determine film thickness and impurity levels. Impurities if any were beyond the detection limit of RBS and PIXE as applied here. Ion beam damage was minimised by choosing a beam energy which had an end of range beyond the diamond film thickness. This fact must be kept in mind at all times when obtaining IBIL spectra.

## REFERENCES

- [1] Bettiol A.A., Jamieson D.N., Prawer S. and Allen M.G., Nucl. Instr. Meth B 85 (1994) 775-779
- [2] Ziegler J.F., Biersack J.P. and Littmark U., The Stopping and Range of Ions in Solids (Pergamon, New York)
- [3] RUMP, Ver. 4.0, copyright 1985 Larry Doolittle 1989 Computer Graphics service.
- [4] Dean P.J., Phys. Rev. 139 (1965) 588
- [5] Prins J. F., Diamond and Related Materials 3(4-6) (1994) 922-925
- [6] Ruan J., Kobashi K. and Choyke W.J., Appl. Phys. Lett. 60 (25) (1992) 3138-3140
- [7] Yacobi B.G., Lebens J., Vahala K.J., Badzian A.R. and Badzian T., Diamond and Related Materials, 2 (1993) 92-99



# The Compaction of Fused Silica Resulting From Ion Implantation

JOHNSON C.M.<sup>a</sup>, RIDGWAY M.C.<sup>a</sup>, LEECH P.L.<sup>b</sup>

<sup>a</sup> Department of Electronic Materials Engineering Australian National University, Canberra, 0200, ACT, Australia.

<sup>b</sup> Telstra Research Laboratories, Clayton, 3186, Victoria, Australia

**SUMMARY:** Ion implantation of fused silica results in compaction and consequently an increase in refractive index. This method of modifying the near-surface region has been shown as a potential means for fabricating single mode channel waveguides. This study has measured the compaction of the implanted regions for Si implantations as a function of dose ( $2 \times 10^{12}$ - $6 \times 10^{16}$  ions/cm<sup>2</sup>), energy (1-9 MeV) and post-implantation annealing temperature (200-900 °C). For a given energy, a dose-dependence of the step height (depth of compacted region) is observed for doses less than  $\sim 10^{15}$  ions/cm<sup>2</sup>. At higher doses the step height saturates. For a given dose, a linear trend is evident for the step height as a function of energy suggesting that the major mechanism for this compaction is electronic stopping. As the annealing temperature increases, the step height gradually decreases from  $\sim 0.1$ - $0.2$   $\mu\text{m}$  to  $\sim 10$ - $20\%$  of the original value. From the annealing data, it is possible to extract an activation energy of 0.08 eV associated with the thermal removal of the compacted region.

## 1. INTRODUCTION

Improved techniques for the fabrication of planar waveguides are of current interest to produce small-scale, integrated waveguides and devices. Ion implantation is one technique appropriate for the modification of the near-surface properties of optical materials. By varying the parameters of ion energy, dose and annealing temperature, it is possible to control the depth and extent of the modified layer. In fused silica, ion implantation has been shown to yield an increase in refractive index, thereby creating the core region for a waveguide, Townsend et al. (1). Loss values as low as 0.1 - 0.15 dB/cm have been achieved, Leech et al. (2), following post-implantation thermal annealing. Such losses are of an acceptable level for optical device fabrication.

The increase in refractive index observed in fused silica is the result of densification or compaction wherein the SiO<sub>2</sub> ring structure attains a compacted form induced by ion implantation. Such compaction has been attributed to a combination of both nuclear and electronic stopping mechanisms, EerNisse (3). The present paper provides some insight into the contributions of each process on compaction and examines the thermal behaviour of the implanted region.

## 2. EXPERIMENT

Fused silica substrates were implanted with Si ions over a range of doses ( $2 \times 10^{12}$ - $6 \times 10^{16}$  ions/cm<sup>2</sup>) and energies (1-9 MeV). The implants were performed at liquid nitrogen temperature to minimise dynamic annealing and hence, maximise implantation-induced disorder. The implanted area was defined by a  $1 \times 3$  mm<sup>2</sup> Si mask. Compaction was measured using a profilometer, wherein a needle is traced across the implanted/unimplanted boundary yielding step height measurements accurate to within  $\sim 3$  nm. Simulations were performed using a modified version of TRIM, Biersack et al. (4), (Transport and Range of Ions in Matter) to calculate the depth distribution of the implanted ions and associated energy loss. Annealing of the samples was performed for 1 hr at temperatures of 200-900 °C.

## 3. RESULTS AND DISCUSSION

### 3.1 Compaction as a function of dose

Figure 1 contains experimental results showing the compaction as a function of dose for Si ions at an implant energy of 5 MeV. Compaction evidently increases with dose, up to doses of  $\sim 10^{15}$  ions/cm<sup>2</sup>, at which point saturation is reached. Also shown in Figure 1 is the annealing behaviour of the compacted region. As expected from a thermally activated process, the reduction in step height is greater for the higher temperature anneals.

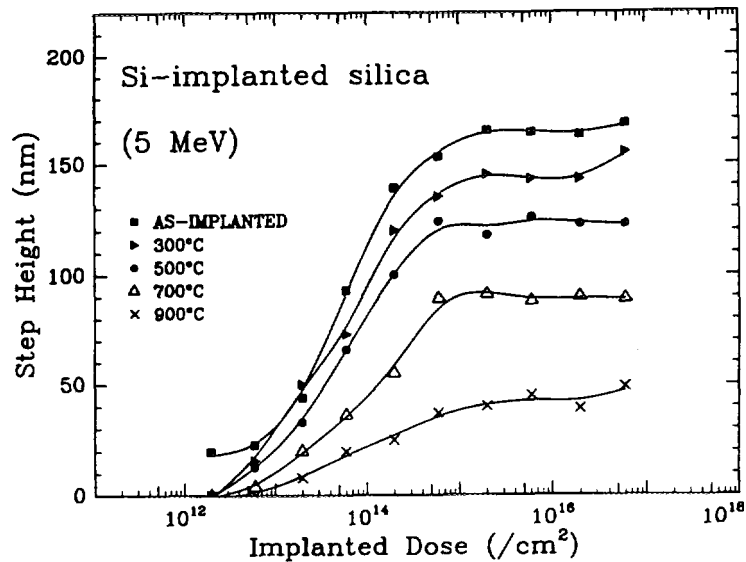


Figure 1 - Compaction as a function of dose for an energy of 5 MeV

### 3.2 Compaction as a function of energy

Compaction measured in samples implanted with Si ions from 1-9 MeV is shown in Figure 2 for a dose of  $2 \times 10^{15}$  ions/cm<sup>2</sup>. This figure demonstrates a near-linear relationship between compaction and implant energy. TRIM simulations have shown that the influence of nuclear stopping mechanisms becomes insignificant for implantation energies greater than 4 MeV. The continued increase in compaction for energies above 4 MeV suggests electronic stopping is largely responsible for compaction. As in Figure 1, the reduction of the compacted region due to annealing is apparent in Figure 2.

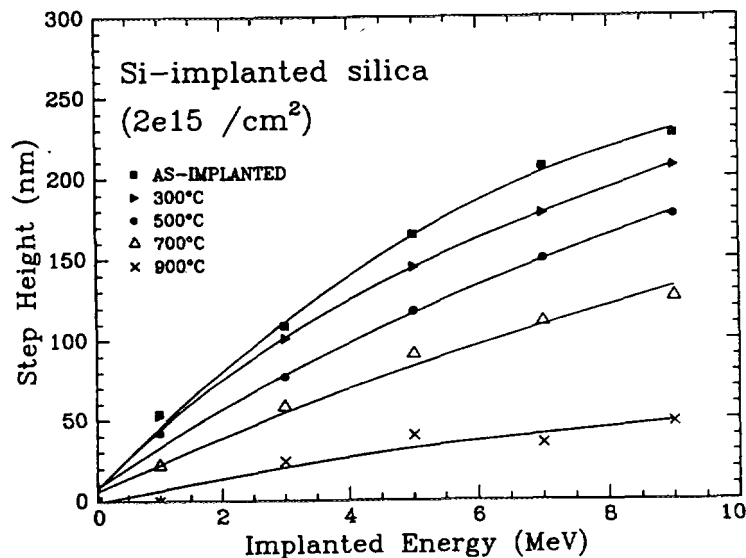


Figure 2 - Compaction as a function of energy for a dose of  $2 \times 10^{15}$  ions/cm<sup>2</sup>

### 3.3 Activation Energy for the annealing of implantation-induced compaction

Taking the change in step height within the saturated region measured for each annealing temperature, it is possible to form the Arrhenius plot shown in Figure 3 and hence extract an activation energy of  $\sim 0.08$  eV. This value is small compared to the activation energies of Si (2.7 eV) or GaAs (1.5 eV) for the epitaxial recrystallization of implantation-induced amorphous material and reflects a lesser dependence on temperature. Further study, now in progress, is necessary to deduce the significance of this activation energy. The activation energy determined herein may well be a superposition of several annealing processes.

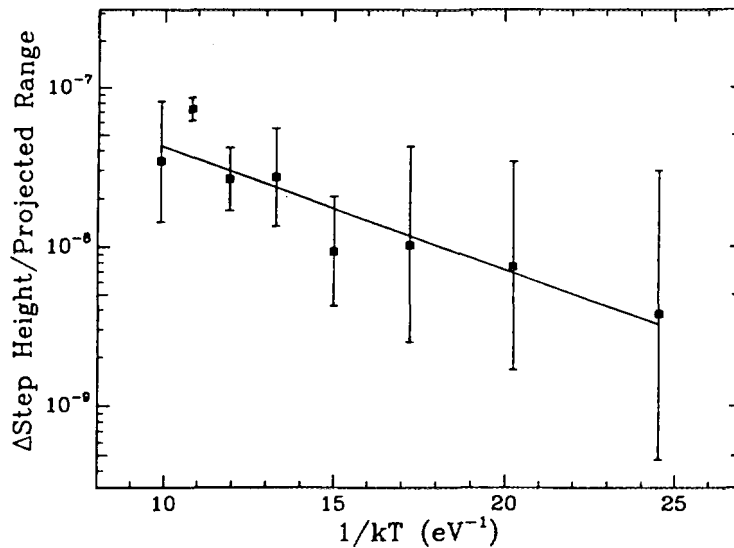


Figure 3 - Arrhenius plot for Si-implanted fused silica for an energy of 5 MeV

### 3.4 Compaction and waveguide loss

In Figure 4 the relationship between the waveguide loss and compaction is shown as a function of annealing temperature. A minimum in loss is observed at 500 °C. At lower temperatures, the presence on disorder may yield the increase in loss. At higher temperatures, the reduction in refractive index may be too great for efficient guiding and/or Si precipitation may contribute to the increase in loss. The step height shows a continual reduction as a function of annealing temperature. No direct correlation is evident between loss and step height.

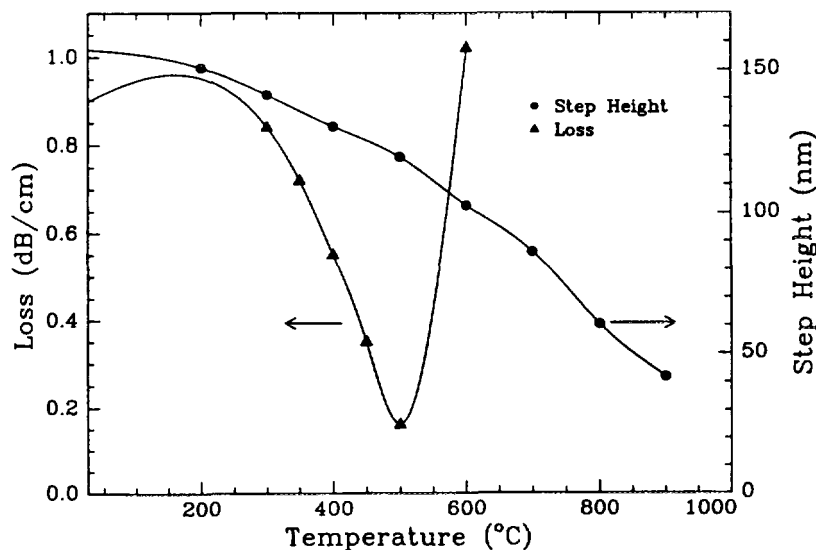


Figure 4 - Loss and step height as a function of annealing temperature for an energy of 5 MeV

## 4. CONCLUSION

For high-energy implantation, it has been observed that electronic stopping is the dominant mechanism yielding compaction. Using annealing, an activation energy of 0.08 eV has been determined for the removal of the compacted region within Si-implanted silica.

## 5. REFERENCES

- 1 Townsend P.D, Chandler P.J and Zhang L, (1994), Optical Effects of Ion Implantation, Cambridge University Press, p.52
- 2 Leech P.W, Kemeny P.C and Ridgway M.C, (1995), Low loss channel waveguides fabricated in fused silica by germanium ion implantation, *Elec. Lett.*, **31**(15), 1238-1240
- 3 EerNisse E.P, (1973) Compaction of Ion-implanted fused silica, *J.Appl.Phys.*, **45**(1), 167-174
- 4 Biersack J.P, Haggmark I.G, (1980), *Nucl. Instrum. Meth.* **174** 237

# ION BEAM ANALYSIS TECHNIQUES FOR THE ELEMENTAL FINGERPRINTING OF FINE PARTICLE SMOKE FROM VEGETATION BURNING IN NSW

David D. Cohen

Applied Nuclear Physics, ANSTO, PMB1, Menai, NSW, 2234, Australia.

## Introduction

Accelerator based ion beam analysis (IBA) techniques, including PIXE, PIGME, RBS and PESA, have been used to analyse elemental compositions of airborne particles covering a 60,000 square kilometre area of Wollongong, Sydney and Newcastle, see Fig.1 at the end, for sampling site locations. These IBA techniques provide elemental concentrations for over 20 different elements from hydrogen to lead, they include H, C, N, O, F, Na, Al, Si, P, S, Cl, K, Ca, Ti, V, Cr, Mn, Fe, Cu, Ni, Zn, Br and Pb. The four ion beam techniques are performed simultaneously on the 3MV Van de Graaff accelerator at ANSTO and have been described in detail elsewhere[1,2]. They are sufficiently sensitive to analyse for many of these elements to levels around 10ng/m<sup>3</sup> or less in about five minutes of accelerator running time per filter. This is more than adequate for aerosol analyses as most filters contain around 150 µg/cm<sup>2</sup> of material which corresponds to about 10µg/m<sup>3</sup> of fine particles in the atmosphere. For this work fine particles are those with diameters less than 2.5µm (PM2.5).

Fine particle data (PM2.5) has been collected twice a week and analysed for each of the above elements by ANSTO since 1991 at more than 25 different sites throughout NSW[3,4]. This large dataset set allows us to not only determine the composition of fine particles and to look for signature elements for particular sources but also to use multivariate statistics to define elemental source fingerprints and then to determine the percentage contributions of these fingerprints to the total fine particle mass in the atmosphere. This paper describes the application of these techniques to the study of domestic wood fires and vegetation burning in NSW over a two year period from 1992-93. It also presents, for the first time, fine particle data related to the January 1994 bushfires in NSW.

## Fine Particle Smoke Signatures

The fine particle sampling and IBA analysis techniques are able to follow the effects of both short term events (a few days) such as bushfires and control burning, and longer term events (3 months) such as domestic wood burning, on the fine particle levels in the atmosphere.

The total fine potassium concentration is an excellent signature for smoke from wood and vegetation burning, even though, at its peak, this may still be less than 1% of the total fine particle mass measured. This is well demonstrated by the data shown in Fig. 2 which shows the daily total fine potassium concentration (in ng/m<sup>3</sup>) for the months of July to September 1992 at the rural Wilton site (ASP14) south west of Sydney. Each bar represents a 24 hour sample. These were taken twice a week, every Sunday and Wednesday. On Sunday 23 August 1992 this site was affected by smoke from a bushfire 20 km west of Wilton. Wind data showed that the wind was blowing from the south west to north west quadrant for 100% of the time during this 24 hour period, and that 54% of the time it was blowing directly from the west.

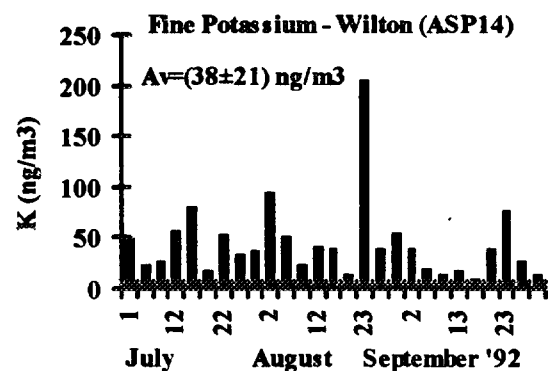


Fig. 2. Total fine potassium concentrations for Wilton (ASP14), a rural site, for July, to September 1992.

The average fine potassium level for the three month period July to September, at Wilton, was (38±21) ng/m<sup>3</sup>, but on the 23 August this daily value rose to 206 ng/m<sup>3</sup> a strong indicator of the fire to the west of this site. Experience over several years indicates that the fine potassium levels increase markedly by factors of between 3 and 10 in the presence of vegetation burning. Fig. 2 also shows that the effects of this particular local bushfire, which was extinguished quickly, were not long lived as the next 24 hour sample obtained three days later on 26 August 1995 showed levels well down on those measured during the peak of the fire. As the Aerosol Sampling Program (ASP) database covers

the years 1992 to 1993 it is possible to look at differences between the average monthly values for fine potassium for summer and winter seasons. Figures produced by the NSW EPA show that there are around half a million homes in NSW burning about 3 tonnes/ year of wood, mainly in the winter months. For smoke values, derived from fine potassium concentrations, during the summer months of 1992 and 1993, across all 25 ASP sites, a mean value of  $(18\pm 12)$  ng/m<sup>3</sup> was obtained compared with the corresponding winter value of  $(35\pm 18)$  ng/m<sup>3</sup>.

In particular, the sites at Rozelle (ASP3), Macquarie University (ASP17), Richmond (ASP18) and Cullen Bullen (ASP22) stand out as having increased winter smoke levels, showing increases of between 3 and 6 times for winter to summer values. This is shown in Table 1 where the monthly average summer and winter smoke values for these sites are compared. The monthly summer smoke values were consistent with the total network average summer value of  $(18\pm 12)$  ng/m<sup>3</sup>, however, these winter values were well above the network average winter value of  $(35\pm 18)$  ng/m<sup>3</sup>.

Site See Fig.1	Summer (ng/m <sup>3</sup> )	Winter (ng/m <sup>3</sup> )	Ratio
Rozelle	17±6	50±20	2.9
Macquarie Uni	16±2	61±14	3.9
Richmond	14±2	65±14	4.6
Cullen Bullen	8±3	53±8	6.2

Table 1. Comparison of the 1992-93 summer and winter average monthly smoke values for several sites.

Fine particle potassium was by far the best indicator for smoke, varying by orders of magnitude from non vegetation-burning days to vegetation-burning days.

### Fine Particle Smoke Fingerprint

In order to obtain a chemical fingerprint of a given fine particle source, two things must be determined: firstly which elements characterise that fingerprint and secondly the relative proportions of each of those elements which provide the signature for that fingerprint at a sampling site. These fingerprints or profiles can then be used in Chemical Mass Balance (CMB) programs[5] to determine the relative contributions of each of these fingerprints to the total ambient particle mass. The multivariate analysis method of Principal Component Analysis (PCA) followed by varimax orthogonal rotation has been employed to determine the appropriate elements for each chemical fingerprint [6].

Having determined the appropriate elements, particular events (such as favourable wind information) and sites were then selected which optimised the source receptor parameters being considered. The measured ambient relative elemental concentrations together with these parameters were then used to estimate each individual fingerprint or profile for use throughout the network. The 6 primary fine particle fingerprints thus derived were: *motor vehicles, coal combustion, industry on high sulphur days, smoke, soil, and seaspray* since their elemental make up identified them as the major contributors to these fingerprints. The relative elemental concentrations for each fingerprint are discussed in detail elsewhere [2]. In Fig. 3 we show the source fingerprint for smoke only.

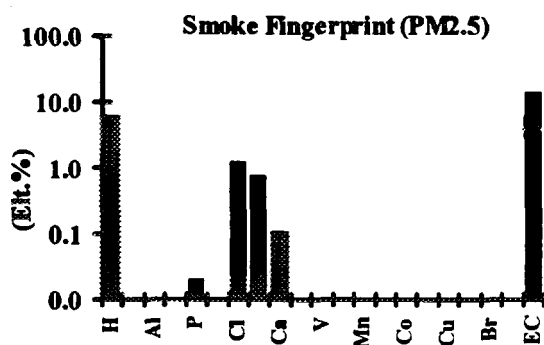


Fig. 3. The fine particle fingerprint for smoke from vegetation burning in NSW.

The principal components analysis on the data from these sites selected the following 7 key elements (factor loadings >0.81) as being strongly associated with the smoke factor H, P, Cl, K, Ca, Mn and elemental carbon (EC). Applying the smoke fingerprint of Fig. 2 together with all the other five fingerprints for fine particle sources it is possible, using Chemical Mass Balance (CMB) methods[5], to calculate the contribution of each of these individual fingerprints to the total fine particle mass. The average monthly smoke fingerprint contributions, across all network sites, for the years 1992-93 are shown in Fig. 4. This figure shows strong seasonal variations of fine particle smoke concentrations in NSW. The two year average of  $(0.92\pm 0.8)$  µg/m<sup>3</sup> for the smoke fingerprint was around 12% of the average total fine particle mass for the same period. The presence of smoke is strongly related to domestic fires and controlled burning in the winter months.

During the first two weeks of January 1994 NSW experienced some of the worst bushfires in memory. There were over 150 fires extending along 1000 km of the NSW coastline, destroying 185 homes, killing 4 people and burning more than 600,00 hectares. The location of some of these fires across the ASP network is shown in Fig. 1. During these fires the fine particle concentrations rose dramatically. This is shown in Fig. 5 where the

total mass at selected sites in Fig. 1 is plotted for the month of January 1994. Fine particle levels rose to over  $70\mu\text{g}/\text{m}^3$ , well above the yearly averages for Wollongong, Sydney and Newcastle of  $10\text{--}15\mu\text{g}/\text{m}^3$ . The peak of the smoke from these fires occurred around 9 January at these sites but levels did not return to normal till after the 16 January 1994.

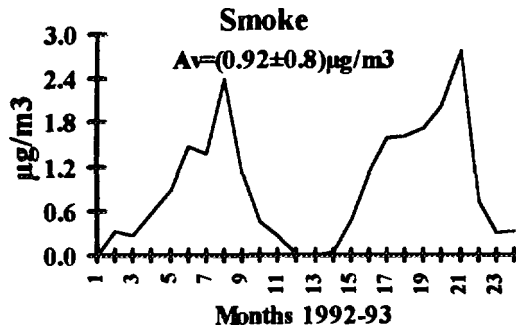


Fig. 4. Average monthly smoke contributions across the ASP network during 1992-93.

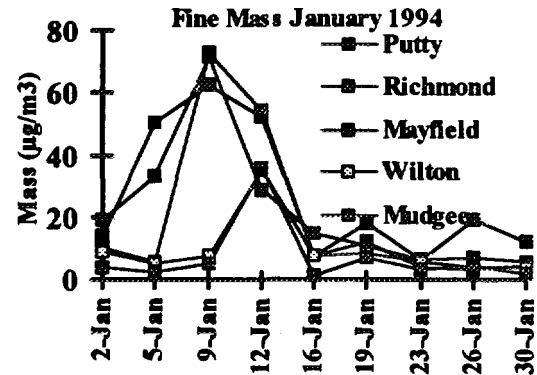


Fig. 5. Total fine particle mass at selected sites during the January 1994 bushfires in NSW.

### Conclusions

IBA methods are ideally suited to the analysis of fine particle composition. Furthermore the wealth of elemental information provided by these techniques allows statistical methods like principal components analysis to be used to obtain source fingerprints and finally to use standard Chemical Mass Balance methods to calculate the relative contributions of these fingerprints to the total fine mass concentration. This paper has demonstrated these methods for smoke from vegetation burning in and around the Sydney region and showed that smoke from domestic fires is significant during the winter months and that during major bushfires the fine particle concentrations can increase by an order of magnitude for several weeks.

### Acknowledgments

We wish to acknowledge financial support from ERDC and the NSW Environmental Trust during some phases of this work.

### References

- [1] D. D. Cohen, Nucl. Instrum. and Methods, B79(1993)385-388.
- [2] D. D. Cohen, G.M. Bailey and R. Kondepudi, Proceedings of 7th Int. Conf. on PIXE and Its Analytical Applications, 27-31 May 1995, Padua, Italy, to be published in Nucl. Instrum. and Methods 1996.
- [3] D.D. Cohen et al "Composition and distribution of fine particles in the Sydney region". Proceedings of Air Toxics Conference, NSW, Australia, 10-11 August 1994, Vol II, pages 125-140.
- [4] D.D. Cohen, J. Martin, G.M. Bailey, P. Crisp. Clean Air, 27(1993)63-71.
- [5] J.G. Watson et al Receptor model technical series, Vol III, CBM7 user's manual, USEPA Report EPA-450/4-90-004, January 1990.
- [6] P.K Hopke "Receptor Modelling for Air Quality Management", Elsevier Science, Amsterdam 1991.

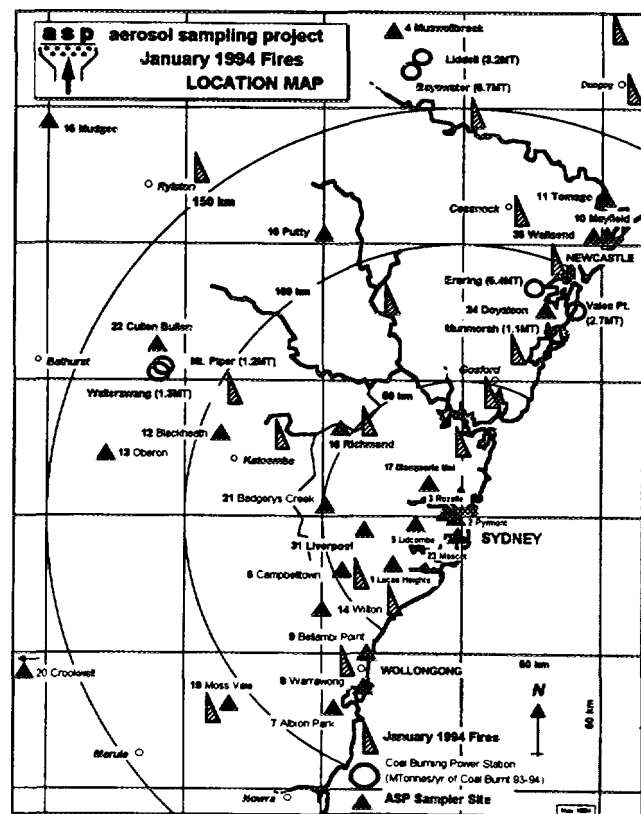


Fig. 1. ASP site location map, showing location of each of the network samplers and the bushfire locations.



# Nuclear Analysis of a Rare Earth Containing Protective Oxide on Aluminium

J.D. Gorman\*, A.E. Hughes# and P.J.K. Paterson\*

\* Department of Applied Physics R.M.I.T., Vic.

# C.S.I.R.O Div. Mat. Sci. Tech. Clayton, Vic.

## INTRODUCTION

The aim is to examine the thickness of the conversion coating as well as the elemental depth distribution of Ce and Mo using Rutherford Backscattering Spectroscopy (RBS), Scanning Electron Microscopy (SEM), Scanning Auger Electron Spectroscopy and Forward Recoil Spectroscopy (FRS). In addition, RBS has been used to examine how changes in processing conditions, particularly the treatment temperatures, influences the coating thickness and Ce distribution at each process step. SEM established that a crazed oxide structure was developed over the matrix of the alloy using the above process steps. RBS was chosen to provide elemental concentration versus depth information on these samples since it is largely insensitive to surface topography when the detector is set to high scattering angles. Another advantage of using RBS for this particular system is that the heavy elements incorporated into the coating such as Ce and Mo, because of their high atomic number compared to the aluminium oxide, are well separated from aluminium and oxygen at their higher recoil energies. Forward Recoil Spectroscopy is capable of detecting hydrogen and it has been used to confirm that the coating is hydrated and to establish the hydrogen distribution within the final oxide coating on each alloy.

## EXPERIMENTAL

RBS was performed using a 2 MeV He<sup>2+</sup> ion beam at normal incidence to the sample surface and backscattered He particles were collected at an angle of 170° degrees to the incident beam for a total charge accumulation of 100μC. The beam spot size was 1.5 x 1.5 mm<sup>2</sup>. RBS spectra were quantified using scattering cross-sections [2] and Rump simulations [3]. The oxide thicknesses were determined using simulations in Rump [3]. A "mean energy approximation" [2] was used in order to calibrate the depth scale of the oxide coatings on all depth profiles. FRS was performed using 2.5 MeV He<sup>2+</sup> ions incident at an angle of 80° to the sample surface normal and the detector was also set at 80° to the surface normal at a complimentary angle with a 10 μm aluminium filter over the detector. Scanning AES was performed on a Fisons Microlab 310F using 10 keV beam energy. A 3 kV Ar ion beam at 60° to the surface normal with a beam current of 100μA per cm<sup>2</sup> was used for ion etching of the samples.

AES sensitivity factors for this system of elements were determined by adjusting Auger sensitivities to give agreement between XPS analyses where compositions were obtained using Schofield cross-sections and the integral intensities. These Auger sensitivity factors were obtained where the Auger spectra were measured on the same sample areas as the XPS spectra.

## RESULTS

### RBS

After the 24 hour exposure to water saturated air the two alloys showed a thin native oxide at the lower limit of depth resolution for RBS hence the oxide thicknesses quoted in Table 1 were calculated from XPS results. Copper was detected within the oxide on both the 2024 and 6061 alloys with an apparent surface enrichment although these results should be treated with caution since they were taken at the limit of resolution of the instrument. The copper comes either from the alloy under treatment or from Cu left in solution by previously treated alloys and promotes oxide growth during the subsequent rinse step[4,5]. Samples put through this step without the pre-treatment process showed no such Cu enrichment. The RBS spectra of both alloys also show Cr incorporated into the surface oxide which was carried through from the chromate based de-oxidation step [5].

As a result of the 2 hour boil in Ce(NO<sub>3</sub>) the coating thicknesses increased to around 440 and 570 nm on 6061 and 2024 respectively. Both alloys had a Ce distribution which displayed a peak in concentration within the body of the oxide coating (Fig. 2(a) and 2(b)). Samples of both alloys which were put through this step without undergoing the M1 step displayed considerably thicker oxides and higher amounts of incorporated Ce. Samples put through the M2 step without the deoxidation step also showed thicker oxide growth and higher levels of Ce confirming that the combination of pretreatment and M1 steps may lead to the formation of a passivating layer which inhibited later oxide growth.

After the 2 hour boil in CeCl<sub>3</sub> the oxide thickness had increased to approximately 730 nm on the 6061 and around 1020 nm on the 2024 (Table 1). Subtraction of the Ce RBS spectra from the second and third process steps

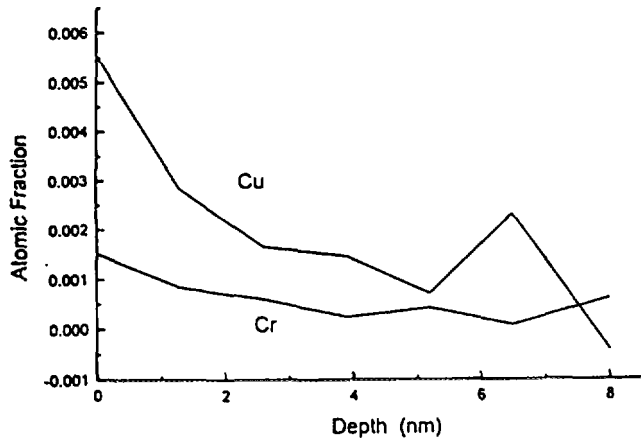


**Figure 1a.**

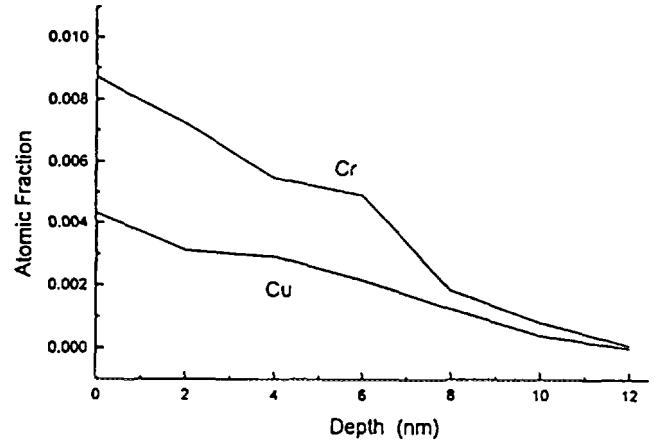


**Figure 1b.**

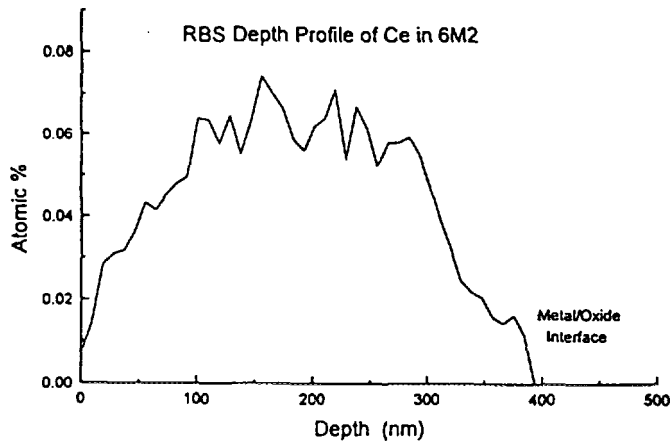


**Figure 2a.**

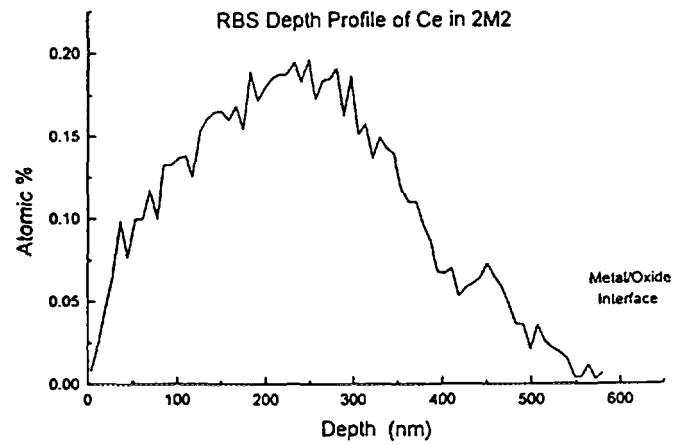


**Figure 2b.**

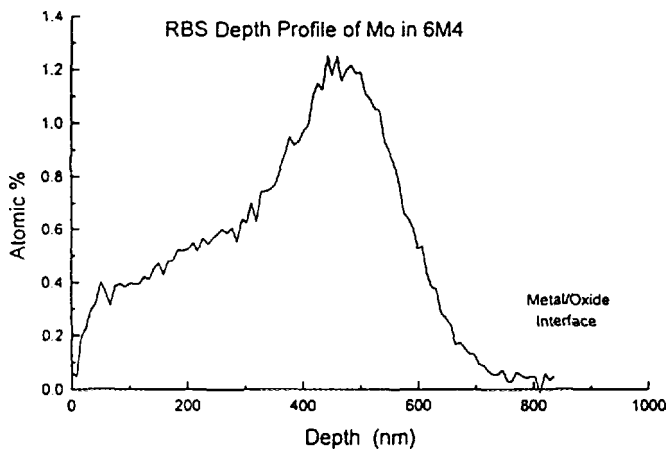


**Figure 3a.**

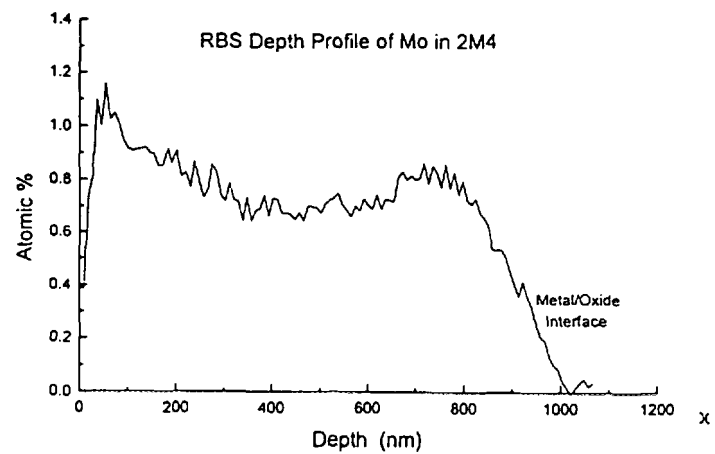


**Figure 3b.**

indicated a surface enrichment of Ce on both alloys suggesting that it deposited directly onto the surface over the existing oxide with little penetration into the oxide. This is supported by XPS and AES results.

Anodic polarisation in the  $\text{Na}_2\text{MoO}_4$  resulted in the incorporation of Mo into and onto the coatings of both alloys. On both alloys the Mo was incorporated without altering the existing distribution of Ce. On the 6061 alloy the Mo was concentrated around 300 nm above the oxide-metal interface. On 2024 Mo was also concentrated around 300 nm above the metal/oxide interface (Fig. 3(a)), however there were significant levels of Mo throughout the coating reaching a peak at the surface of the oxide. Hence the Mo spectrum for 2024 displayed a distinctive double peak structure (Fig. 3(b)). The atomic percentage of Mo present at the metal/oxide interface on the 6061 was 50% higher than that on 2024.

**Table 1. The average oxide thickness by RBS.**

Sample	Oxide Thickness	Oxide Thickness
	6061 (nm)	2024 (nm)
M1	8 #	13 #
M2	440 ± 20	570 ± 20
M3	730 ± 30	1020 ± 50
M4	790 ± 40	1050 ± 50

# Calculated by XPS .

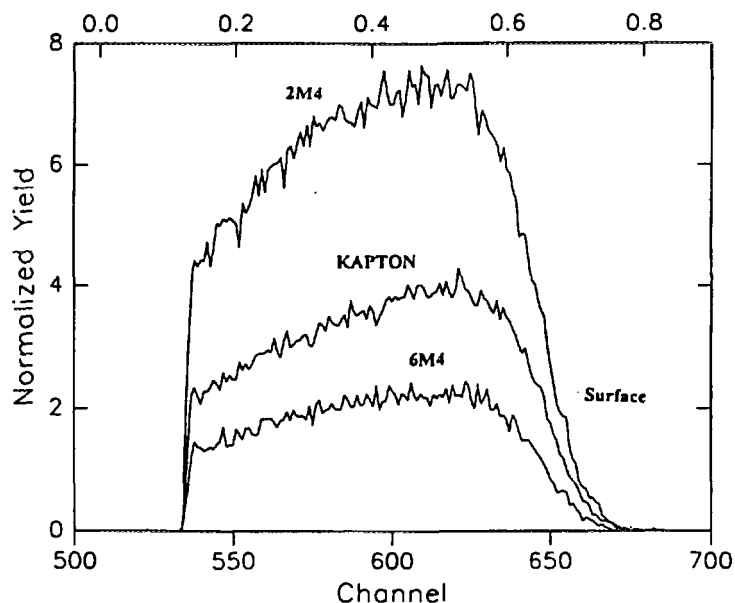


**Figure 4. Forward Recoil Spectra**

### Forward Recoil Spectroscopy

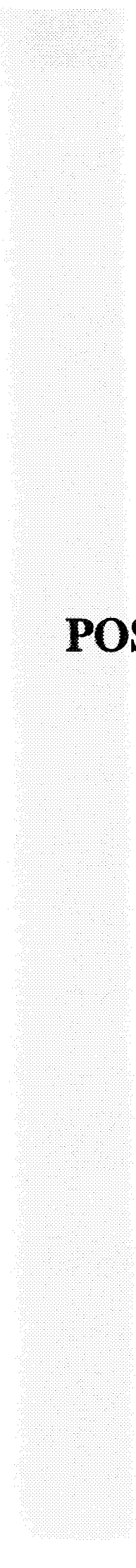
Forward Recoil Spectroscopy was performed on the M4 samples of both alloys to determine the hydrogen profile within the conversion coating. FRS showed that on both alloys hydrogen was evenly distributed throughout the oxides (Fig.4). By comparison to the Kapton standard which has approximately 2.73 mass % of hydrogen, the 2M4 coating contained  $\approx 5.1$  mass % H and the 6M4 coating  $\approx 1.7$  mass % H. These results when combined with the previously described RBS results for the Al to O ratio indicate that the 2M4 oxide had a composition of Al, O and H in the ratios [1:2:3] respectively whilst the 6M4 oxide was [1:2:1].

### CONCLUSIONS

RBS simulations indicated that for all process steps the oxide grown on both alloys had an aluminium to oxygen ratio of approximately  $1: 2.0 \pm 5\%$ . On the basis of the H/O ratio determined by FRS the oxide developed on the 2024 alloy was likely to be pseudo boehmite whilst that developed over 6061 was probably  $\text{AlOOH}$ . Regardless of the alloy type distinctly different oxides developed over the matrix and the intermetallics during the growth of the conversion coating. Ce precipitated from solution preferentially around intermetallics as small precipitates containing Ce, Al and O. During anodic polarisation in  $\text{Na}_2\text{MoO}_4$  solution some of the molybdate reacted with the surface Ce precipitates but the remainder was incorporated into the oxide.

### REFERENCES

1. F.B. Mansfeld, Hong Shih and You Wang, *Method for Creating a Corrosion Resistant Aluminium Surface*, U.S. Patent No. 5,194,138
2. W.K.Chu, J.W.Mayer and M.A.Nicolet, *Backscattering Spectroscopy*, Academic Press (1978) 34 - 35, 370 - 371
3. L.R. Doolittle, *Computer Code RUMP*, Nucl. Instr. Meth. B V15 (1986) 227.
4. A.V. Pocius, T.H. Wilson, JR., S.H. Lundquist, S. Sugii, *Mat. Sci. Mono.* 29 (1985) 71 - 81
5. A.E. Hughes, R.J.Taylor, K.J.H. Nelson, B.R.W. Hinton, L.Wilson, *Submitted to J. Mat. Sci. and Tech.*
6. I.J. Polmear, *Light Alloys*, Edward Arnold N.Y. (1989)
7. W. Vedder, D.A. Vermilyea, *Trans. Faraday Soc.* 65 (1969) 561 - 584



# **POSTER PAPERS**



# Trace Element Partitioning between Aqueous Fluids and Silicate Melts Measured with a Proton Microprobe

J. ADAM<sup>1</sup>, T.H. GREEN<sup>1</sup> and S.H. SIE<sup>2</sup>

<sup>1</sup>School of Earth Sciences, Macquarie University, NSW 2109, Australia

<sup>2</sup>CSIRO Exploration and Mining, P.O. Box 136, North Ryde, NSW 2113, Australia

## SUMMARY

A series of experiments were performed to examine the capacity of H<sub>2</sub>O-fluids to concentrate and transport incompatible elements through peridotitic mantle and metamorphosed (eclogitic) ocean crust. Two naturally occurring rock compositions, trondhjemitic and basanitic, were used in experiments. The proton microprobe was used to determine the trace element concentrations in the solutes from H<sub>2</sub>O-fluids equilibrated at 900-1100°C, 2.0 GPa with water saturated melts of trondhjemitic and basanitic compositions. Partitioning data for H<sub>2</sub>O-fluids and silicate melts show that H<sub>2</sub>O-fluids equilibrated with mantle peridotites will not be strongly enriched in trace elements relative to their wallrocks, and thus they melts do not strongly concentrate alkaline earths Th and U, relative to high-field strength elements.

## 1. INTRODUCTION

Igneous rocks from volcanic arcs and continental areas are characteristically enriched in alkalis, alkaline earths, U and Th, relative to rare earths. But they are depleted in high-field strength elements. These features, and high H<sub>2</sub>O concentrations in arc and continental magmas, are often attributed to the influence of H<sub>2</sub>O-fluids on the source regions of arc and continental magmas. To test this proposition, a series of experiments were performed to examine the capacity of H<sub>2</sub>O-fluids to concentrate and transport incompatible elements (including Rb, Ba, Sr, Y, Zr, Hf, Nb, Ta, La, Sm, Lu, Th and U) through peridotitic mantle and metamorphosed (eclogitic) ocean crust. Two naturally occurring rock compositions were used in experiments (Table 1): one is a trondhjemitic (representative of early crust-forming magmas and rich in quartz and feldspars); the other is a basanite (poor in SiO<sub>2</sub> but rich in MgO and CaO). An electron microprobe and proton microprobe were used to measure the concentrations of major and trace elements in solutes from H<sub>2</sub>O-fluids equilibrated (at 900-1100°C, 2.0 GPa) with water saturated melts of trondhjemitic and basanitic compositions.

## 2. EXPERIMENTAL AND ANALYTICAL METHODS

1:1 mixtures of trondhjemitic glass and H<sub>2</sub>O (20 mg total) were sealed in Ag<sub>70</sub>Pd<sub>30</sub> capsules and held at 900°C and 2.0 GPa for 48 hours. A 3:2 mixture of basanite glass and H<sub>2</sub>O was held at 1100°C and 2.0 GPa for 48 hours. Single capsules were used in most experiments (Fig. 1), but in one experiment on a trondhjemitic: H<sub>2</sub>O mixture, trondhjemitic glass was added to a single capsule which was then sealed within an H<sub>2</sub>O-filled outer capsule (Fig. 2).

The quenched melts (glasses) and solutes (precipitated during and after quenching) from these runs were analysed for major and minor elements with a Cameca SX50 microprobe at Macquarie University. Trace elements were analysed by a proton microprobe at the CSIRO Heavy Ion Analytical Facility (HIAF) laboratory at North Ryde, N.S.W., Australia [1,2].

## 3. RESULTS OF EXPERIMENTS

Experiments on trondhjemitic: H<sub>2</sub>O mixtures in single capsules produced finely vesicular (but otherwise coherent and uniform) glasses which occupy the lower halves of capsules (Fig. 1). These are separated by an upwardly convex meniscus from an overlying H<sub>2</sub>O-soaked mass of fine (5-30 μm diameter) glassy beads (Plate 1). A similar result was produced in the double capsule experiment (Fig. 2), with vesicular glass and glassy beads occupying the inner capsule, and glassy beads the outer capsule. The vesicular glass is interpreted as solidified melt, partially dehydrated during quenching. The glassy beads are interpreted as solute precipitated from an H<sub>2</sub>O-vapour during quenching.

In the case of the H<sub>2</sub>O-saturated basanite experiment, the low viscosity and surface tension of the melt enables turbulence and partial-intermingling of the melt and fluid phases during quenching. In spite of this, clear textural differences between quenched melts and solutes enables the two phases to be easily distinguished (Plate 2).

**Table 1**

trondhjemite:H <sub>2</sub> O = 1:1					basanite:H <sub>2</sub> O = 3:2				
run	trondhjemite starting mix	basanite starting mix	1611	1611 melt	solute	run	1611 individual beads	1627 melt (matrix)	1627 solute (individual beads)
SiO <sub>2</sub>	68.8	45.0	54.5	61.9		SiO <sub>2</sub>	62.5	36.1	55.7
TiO <sub>2</sub>	0.3	3.0	0.2	0.2		TiO <sub>2</sub>	0.2	1.5	0.6
Al <sub>2</sub> O <sub>3</sub>	16.4	13.2	16.9	13.6		Al <sub>2</sub> O <sub>3</sub>	14.5	13.6	18.6
FeO	3.0	12.3	1.7	1.8		FeO	0.7	5.7	1.0
MgO	0.5	10.1	0.6	1.1		MgO	0.2	5.7	0.03
CaO	4.1	8.6	3.7	2.9		CaO	3.9	6.7	5.1
Na <sub>2</sub> O	4.7	4.0	2.9	4.0		Na <sub>2</sub> O	5.6	2.0	3.2
K <sub>2</sub> O	0.5	2.2	0.5	0.6		K <sub>2</sub> O	0.5	0.8	1.5
total	98.4	98.4	81.0	86.2		total	86.7	72.2	85.8
Rb	147	571	99	159		Rb	110	144	753
Sr	674	734	470	472		Sr	322	417	393
Ba	1131	334	759	783		Ba	481	204	182
Y	488	191	133	1220		Y	100	130	28
Zr	506	370	166	1200		Zr	140	334	108
Hf	507	615	337	381		Hf	244	388	246
Nb	523	518	359	396		Nb	296	342	169
Ta	697	1780	148	112		Ta	110	120	440
La	700	578	220	253		La	160	363	111
Lu	825	1980	360	470		Lu	290	1240	380
Th	196	227	29	46		Th	26	172	68
U	138	188	53	96		U	45	149	30

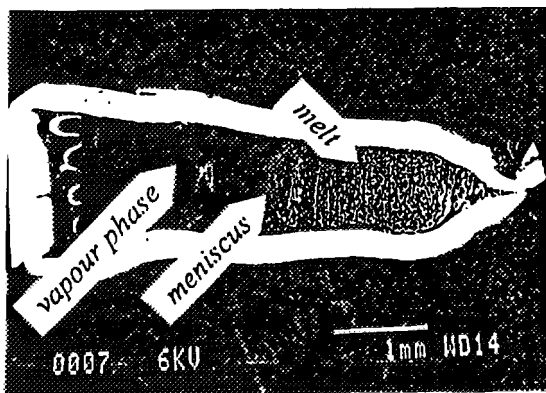


Plate 1. A section of a trondhjemite experiment single capsule showing finely vesicular glasses occupying the bottom half of the capsule, separated by an upwardly convex meniscus from an overlying H<sub>2</sub>O soaked mass of fine glassy beads.

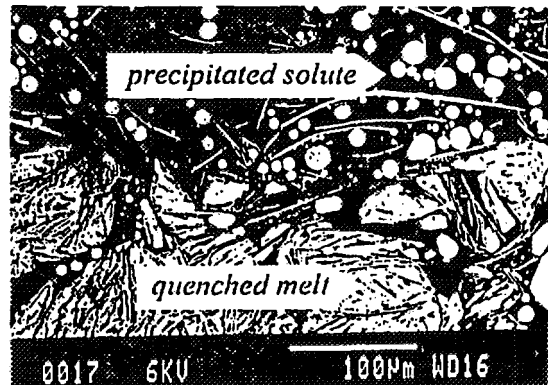


Plate 2. A section of H<sub>2</sub>O-saturated basanite experiment capsule showing clear textural differences between quenched melts and solutes.

The solutes from H<sub>2</sub>O-fluids in equilibrium with both trondhjemitic and basanitic melts are quartz- and feldspar-rich (Table 1) and of essentially granitic composition. Bulk solute concentrations vary from close to 50 wt. %, for fluids equilibrated with trondhjemitic melts, to 30 wt. %, for fluids equilibrated with basanitic melts. On a H<sub>2</sub>O-free basis, most trace elements are not strongly partitioned into either solutes or trondhjemitic melt fractions (Table 1). In particular, there is no strong enrichment of K, Rb, Sr, Ba, Th and U relative to the high-field strength elements Ti, Nb, Ta, Zr and Hf. Zr and Hf are actually enriched in bulk solutes from runs 1611 and 1640, but not in individual glassy beads (from the same experiments) or bulk solute from the outer capsule of the double-capsule experiment 1615. It is possible that the high Zr and Hf concentrations in some bulk solutes are due to crystallization of an insoluble Zr-Hf-phase.

Solutes in equilibrium with basanitic melts are moderately enriched in K and Rb, but strongly depleted in Ti, Ba, Sr, Nb, Ta, Lu, Y, Th, Zr and U (Table 1). The addition of 4% F and 4% Cl in separate experiments on trondhjemitic compositions produced only minor effects on relative trace element partitioning (Table 1). Excepting for alkalis, Cl-enriched fluids are moderately depleted in trace elements. This may reflect the dominant role of hydroxyl molecules in determining trace element solubilities; addition of Cl would have reduced the activity of hydroxyls. F partitions equally between fluid and trondhjemitic melt, and therefore has little net effect on the partitioning of other elements. Fluids in equilibrium with basanitic melts are moderately enriched in Rb and K, but strongly depleted in Ti, Ba, Nb, Ta, Lu, Y, Th, Zr and U. Except for alkalis, trace elements are also concentrated in mineral phases (amphibole and clinopyroxene) relative to fluids.

#### 4. CONCLUSIONS

The experimentally-determined partitioning data for H<sub>2</sub>O-fluids and silicate melts show that H<sub>2</sub>O-fluids equilibrated with mantle peridotites will not be strongly enriched in trace elements relative to their wallrocks, and thus they melts do not strongly concentrate alkaline earths Th and U, relative to high-field strength elements. However, data from Rapp and Shimizu [3] on the partitioning of trace elements between eclogitic minerals and trondhjemitic melts indicate that such melts (and thus also H<sub>2</sub>O-fluids) may be relatively enriched in alkaline earths and light rare-earth. H<sub>2</sub>O-fluids from subducted ocean crust (metamorphosed to eclogite) may thus be an appropriate source of incompatible elements for the source regions of volcanic arc magmas. However, the distinctive Nb and Ta depletions in arc magmas are not due to the properties of H<sub>2</sub>O-fluids.

#### REFERENCES

1. Sie, S.H., and Ryan, C.G., Nucl. Instr. Meth. B15 (1986) 664.
2. Ryan C.G., et al. Nucl. Instr. and Meth. B47 (1990) 55-71.
3. Rapp, R.P. and Shimizu, N., (1995), Trans. Am. Geophys. Union, 1995 Spring Meeting Supplement, S296.

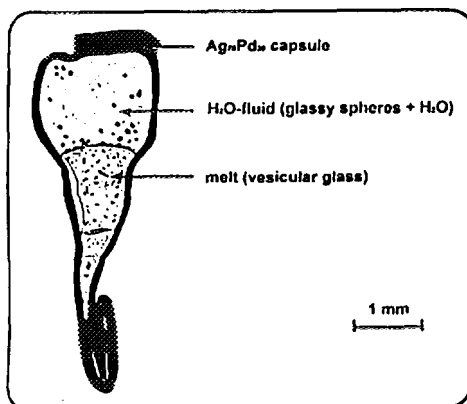


Fig.1. Longitudinal section of a single capsule on a 1:1 trondhjemite:H<sub>2</sub>O.

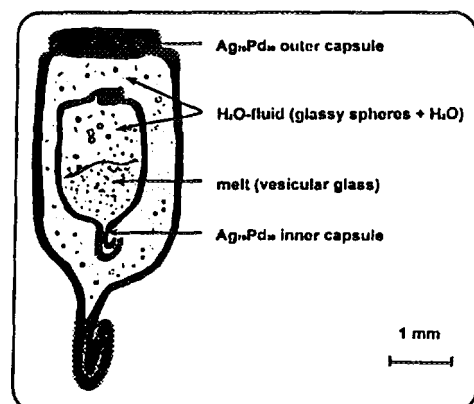


Fig.2. Longitudinal section of a double capsule experiment on a 1:1 trondhjemite:H<sub>2</sub>O.



# Laser Annealing Effects of the Raman Laser on Nitrogen Implanted Glassy Carbon

D.Barbara, S.Prawer, D.N.Jamieson

School of Physics, M.A.R.C., The University of Melbourne,  
Parkville, Vic 3052, AUSTRALIA.

## INTRODUCTION

Raman analysis is a popular method of investigating crystallite sizes, ordering and the types of bonds that exist in ion irradiated C materials, namely graphite, diamond and glassy carbon (G.C.). In particular Raman spectroscopy is used in determining the tetrahedral bonding required for the elusive and potentially important new material called carbon nitride[1]. Carbon nitride,  $\beta$ - $C_3N_4$ , is predicted to exist in several forms[1,2]. Forming the tetrahedral bond between C and N has proved troublesome bain of many experimenters. A proven method for synthesizing novel materials is ion implantation. Thus G.C. was implanted with N at low temperatures so that diffusion of the implanted N would be hindered.

G.C. is a relatively hard, chemically inert, graphitic material. The opaque property of G.C. means that Raman spectroscopy will only give information about the structures that exist at the surface and near surface layers. It was decided, after observing conflicting Raman spectra at different laser powers, that an investigation of the laser annealing effects of the Raman laser on the N implanted G.C. was warranted. The following is a preliminary investigation of the effects of increasing the Raman laser power and determining a power density threshold for high dose N implanted G.C.

## EXPERIMENT

The G.C.(V25 grade) samples were heat treated by the manufacturer to 2500°C, and prior to implantation were polished with 1 $\mu$ m diamond paste. The G.C. samples were implanted with 160 keV  $N^+$  at a temperature of -100°C, at Oak Ridge National Laboratories. The G.C. was implanted with doses of  $2.5 \times 10^{17}$ ,  $5 \times 10^{17}$ ,  $1 \times 10^{18}$  and  $2 \times 10^{18} N^+/cm^2$ . It was calculated that between 1 and  $2 \times 10^{18} N^+/cm^2$  the concentration required for the synthesis of  $\beta$ - $C_3N_4$  would be attained. Raman analysis was performed using an Argon ion laser of wavelength 513.8 nm. To observe the annealing effects of the Raman laser the following was performed on the N implanted G.C. samples. Raman spectra of powers (quoted from the laser cavity) 20, 50, 100 and 200 mW were taken. To investigate the laser annealing of the samples, the Raman spectra were acquired on the same spot in the following manner. The first spectrum was taken at a power of 20 mW, on the same spot a second spectrum at 50 mW was taken and so on with increasing laser powers of 100 and then 200 mW. Then the power of the laser was brought back down to 20 mW and the spectra were taken, again on the same spot. This was performed on the unimplanted and N implanted G.C., for all doses.

## RESULTS and DISCUSSION

Figure 1 shows the Raman spectra of unimplanted G.C. with the laser power at 20 mW. The 3 peaks observed at 1353, 1590 and 1622  $cm^{-1}$  are well known as the D, G and D' peaks. The D, G and D' peaks are due to small graphitic crystallites, the  $E_{2g}$  mode of graphite and the increase in upper  $E_{2g}$  branch for  $k \neq 0$  in the phonon dispersion curve of graphite respectively. All the fits to the unimplanted and N implanted G.C. were performed using a Breit-Wigner equation. For the unimplanted and N implanted G.C spectra a 3 and 2 peak fit was employed respectively. This was the case because the ion implantation causes the broadening of the D and G peaks as seen in Figure 4a) resulting in the G peak dominating the D' peak so for simplicity the G peak shall include both the G and D' peaks. The associated errors of the D peak were larger than those for the G peaks due to the G peak dominating the high dose ion implanted spectra.

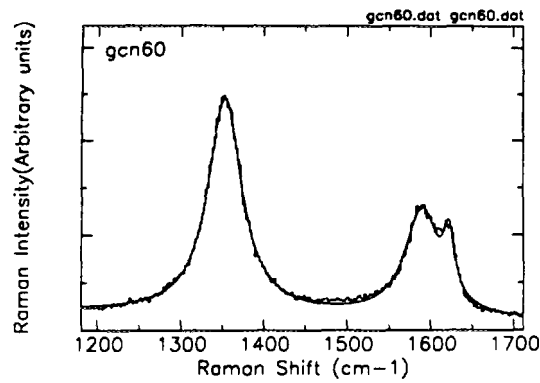


Figure 1: Raman spectra of unimplanted Glassy Carbon, with laser power of 20 mW. The solid curved line represents a B-W least squares fit to the D, G and D' peaks.

Figures 2a) and 2b) show the initial position of the G and D peaks respectively of the unimplanted G.C. as the power of the Raman laser is increased from 20 to 200 mW on the same spot as well as the final position of the G and D peaks, after the laser annealing, at 20 mW. There is a monotonic decrease in the position of both the G and D peaks. The G and D peaks were shifted down by approximately 11 and 6  $cm^{-1}$  respectively as the laser power increased from 20 to 200 mW. When the spectrum was retaken at the lowest power, it would be expected that the position of the G and D peaks would have been permanently shifted down to approximately 1578 and 1347  $cm^{-1}$ . Instead we observed that the G and D peak positions returned to the original positions. However the D peak position was shifted down slightly by approximately 0.5  $cm^{-1}$ . A similar shift, of 8  $cm^{-1}$ , and a return to its original position was also observed for the D' peak. Ordinarily, a shift down in position of both the G and D peaks is associated with an increase in the number of tetrahedral bonds forming[3]. Figure 2 shows this was not a permanent effect suggesting that thermal excitations of the unimplanted G.C. created a small and temporary increase in the number of tetrahedral bonds. Raman spectra taken at the same laser powers but on different spots of the unimplanted G.C. show very similar shifts down for both the G and D peak positions. Therefore the observed monotonic decrease of the G and D peaks was not a result of the successive laser annealing process on the same spot of the N implanted G.C.

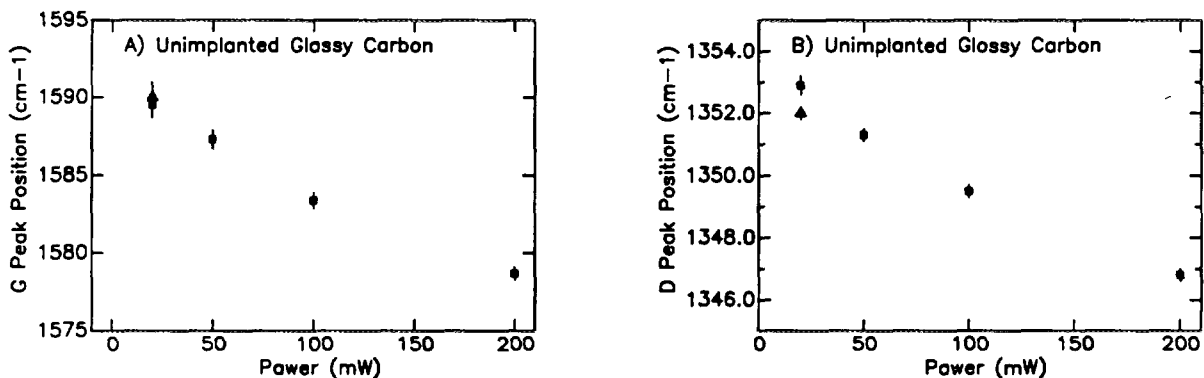


Figure 2: The squares represent the positions of the G and D peaks for a) and b) respectively as the unimplanted G.C. was successively laser annealed from 20 to 200 mW. The triangles represent the final positions of the G and D peaks after the laser annealing. All of the Raman spectra were performed on the one spot of G.C.

Figures 3a) and 3b) show the initial position of the G and D peaks respectively, for all doses of the N implanted G.C., with the laser power at 20 mW. The same spot was, as above, then laser annealed from 50 to 200 mW. Figures 3a) and 3b) also show the final position of the G and D peaks after the laser annealing, with the laser power back down at 20 mW. From Figure 3a), the initial G peak position for all doses was between 1540 and 1550  $cm^{-1}$  indicating that the high dose irradiations caused the amorphisation of the surface layers. Figure 4a) shows a typical Raman spectra of a high dose N implanted G.C. where there is a broad peak visible around the 1550  $cm^{-1}$  region which is typical of amorphous C. Figure 4b) shows the Raman spectra after the laser annealing process. Evident from just looking at Figure 4b) the return of the G and D peaks would tend to indicate a micro-polycrystalline phase away from the amorphous phase observed in Figure 4a)[4]. Interestingly the laser annealing of the N implanted G.C. caused the G peaks, for all doses, to shift up to around 1590  $cm^{-1}$ , the position for unimplanted G.C.. Figure 3b) shows a more varied response to the position of the D peak of the ion implantation and subsequent laser annealing. The initial position of the D peaks after ion implantation, for all doses, do vary considerably from 1320 to 1370  $cm^{-1}$  with large uncertainties. We observed overlap of the final and initial positions of the D peak for all the doses. There was no observation of any peaks between 1900

and  $2400\text{ cm}^{-1}$  after or before the laser annealing.

Therefore the ion irradiation caused the amorphisation of the surface layers of the implanted G.C. as evidenced by Figures 3a) and 4a). The laser annealing process transformed the amorphous C surface layers to a phase similar to that of unimplanted G.C. of a micro-polycrystalline graphite as evidenced by the return of the G peak to  $1590\text{ cm}^{-1}$  and the Raman spectra, Figure 4b). The overlap within error of the final and initial positions of the D peak indicated that the laser annealing caused little shift in the D peak position. A shift down in the G peak position with little change in the D peak was associated with bond angle disorder of graphitic materials[3]. It was demonstrated that graphite with an ideal bond angle of  $120^\circ$  would have a peak at  $1590\text{ cm}^{-1}$ . Which tends to suggest that since there is little or no C N bonds forming that the laser annealing process is causing a return to a more crystalline graphitic phase. As yet these conclusions are speculative and a more thorough analysis is required.

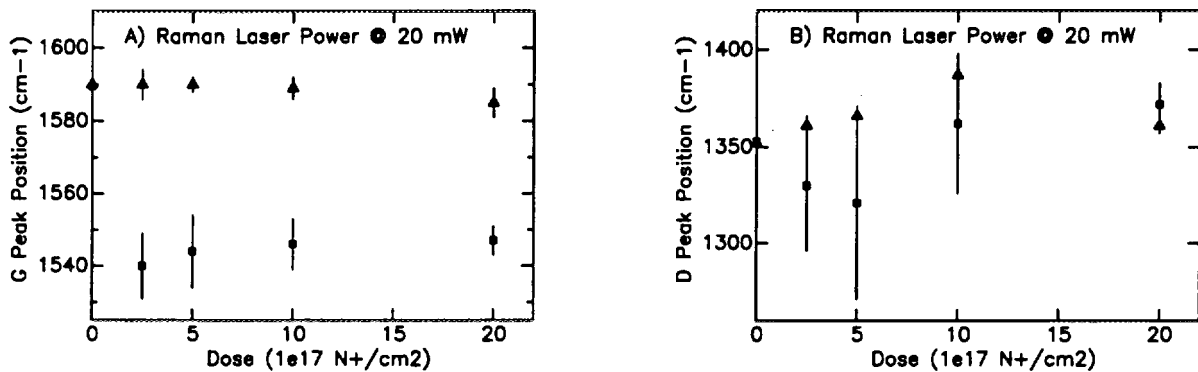


Figure 3: The squares represent the initial positions of the G and D peaks for a) and b) respectively with the Raman laser at 20 mW. The spots were successively annealed from 20 to 200 mW. The triangles point represent the final positions of the G and D peaks for a) and b) respectively with the Raman laser at 20 mW. All of the Raman spectra were performed on one spot for each dose implanted in G.C..

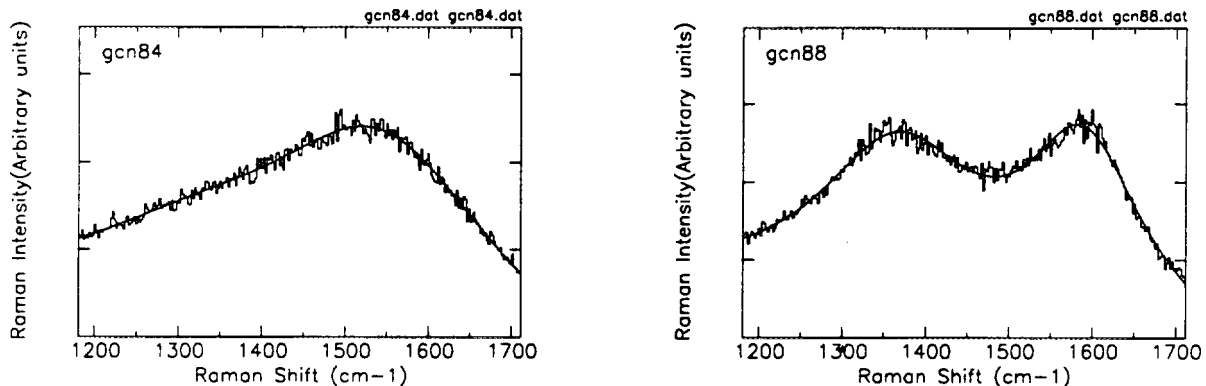


Figure 4: a): Raman spectra with the laser power at 20 mW of  $5 \times 10^{17}\text{ N}^+/\text{cm}^2$  in G.C.. b): Raman spectra with same laser power and of the same spot on the sample as above, after the spot was successively laser annealed from 20 to 200 mW.

## CONCLUSION

Laser powers less than 20 mW can be used on the above materials, with little or no laser annealing observed. An increase in laser power results in excited states of the material being studied resulting in shifts of the G, D and D' peaks for both implanted and unimplanted G.C. There is evidence that the laser annealing process causes a transformation of the implanted amorphous G.C. to a micro-polycrystalline state.

## REFERENCES

- [1] A.Y.Liu and M.L.Cohen, *Science*, **245**, 841 (1989)
- [2] A.Y.Liu and R.M.Wentzovitch, *Phys.Rev. B*, **50**, 10362 (1994)
- [3] D.Beeman,J.Silverman,R.Lynds and M.R.Anderson, *Phys.Rev. B*, **30**, 870 (1984)
- [4] R.O.Dillon,J.A.Woollam and V.Katkanant, *Phys.Rev. B*, **29**, 3482 (1984)



# THE ROLE OF OXYGEN IN QUINTERNARY SUPERCONDUCTORS

DEBORAH R BECKMAN AND DAVID N JAMIESON

MicroAnalytical Research Centre,  
School of Physics, University of Melbourne, Parkville 3052, Australia

## INTRODUCTION

The oxygen composition of the new generation of high temperature superconductors (HTSC) has been found to play a crucial role in determining the superconductivity of these materials [1]. However, measurement of the oxygen stoichiometry in such samples has proven difficult due to the small scattering cross section of oxygen, a light element, which has caused the oxygen scattering signal to be overwhelmed by the far larger signals generated off the heavier elements present in the HTSC samples. It is for this reason that previous ion beam analysis of oxide crystals has often either made no attempt to determine the oxygen content [2] or has used  $O(\alpha,\alpha)O$  resonances such as that at  $\approx 3.05$  MeV to probe the crystal [3]. This work continues tests of a new technique for probing oxygen [4] which overcomes the problem of an insignificant O BS signal by exploiting the large nuclear resonance found to occur in the  $O(p,p)O$  cross-section near an energy of 3.5 MeV [5] in order to produce a significant oxygen edge in the  $H^+$  BS spectrum obtained for the HTSC sample. The use of a  $H^+$  beam is preferable to a  $He^{2+}$  beam for such work due to its enhanced sensitivity to light elements.

## EXPERIMENT

The quinternary superconductor used for this investigation was a good quality pure  $Bi_2Sr_2CaCu_2O_{8+x}$  (BISCO, 2212) crystal. The size of this crystal was  $5 \times 5 \times 1$  mm<sup>3</sup> with the [001] face perpendicular to the surface. Measurements were performed using the University of Melbourne nuclear microprobe. The sample was mounted on an aluminium target holder using a carbon base adhesive which provided good electrical contact and it was oriented inside the target chamber by means of a four axis precision eucentric goniometer.

### Choice of beam

A series of RUMP simulations were initially performed for proton beams incident on a 2212 sample in order to find the  $H^+$  energy which would result in the optimum oxygen backscattering signal. The simulations were limited to a maximum energy of 3.6 MeV since that is the maximum energy for which the non-Rutherford scattering cross-section has been measured for oxygen [5]. The signal-to-noise ratios were compared for different beam energies and a  $H^+$  energy of 3.6 MeV was chosen due to its large and stable oxygen signal-to-noise ratio.

### Angular Scans

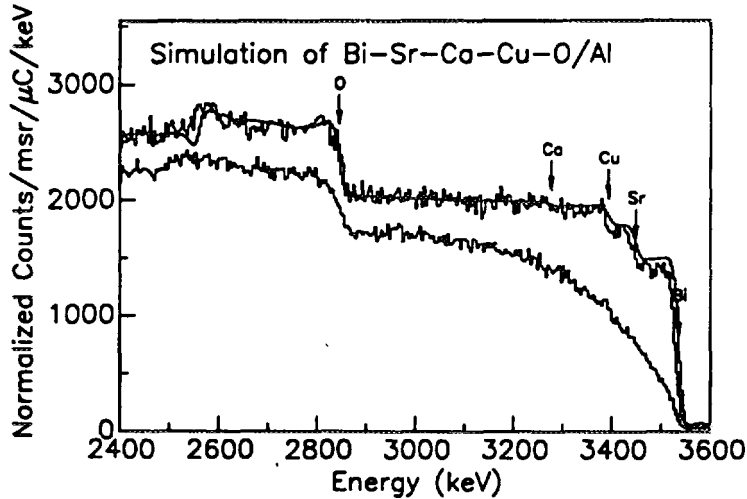
A focused 1.4 MeV  $He^{2+}$  beam was used to initially locate an axis in the 2212 sample. The beam was scanned over a large area of  $150 \times 150$   $\mu m^2$  to minimise beam induced damage in the sample [6] and the energy window was set so that the beam penetrated to a depth of roughly 100 nm into the target. Backscattered particles were detected by a large PIPS detector positioned at an angle of  $135^\circ$  to the incident beam. A 2-D angular scan was measured by collecting the backscattered particles up to  $\pm 3^\circ$  from the channelling axis in both the theta and phi directions and random and channelled backscattered  $He^{2+}$  spectra were also collected. The average beam current was 0.16 nA.

A focused 3.6 MeV  $H^+$  beam was then used to collect a series of spectra about this axis with theta varying between  $\pm 1^\circ$  from its channelling position. Backscattered protons were detected by a small PIPS detector positioned at  $145^\circ$  relative to the incident beam and the emitted X-rays were detected by a Si(Li) detector located at  $135^\circ$  to the incident beam. The scan parameters used were the same as those used previously. Channelled and random spectra were once again collected as well.

## RESULTS AND DISCUSSION

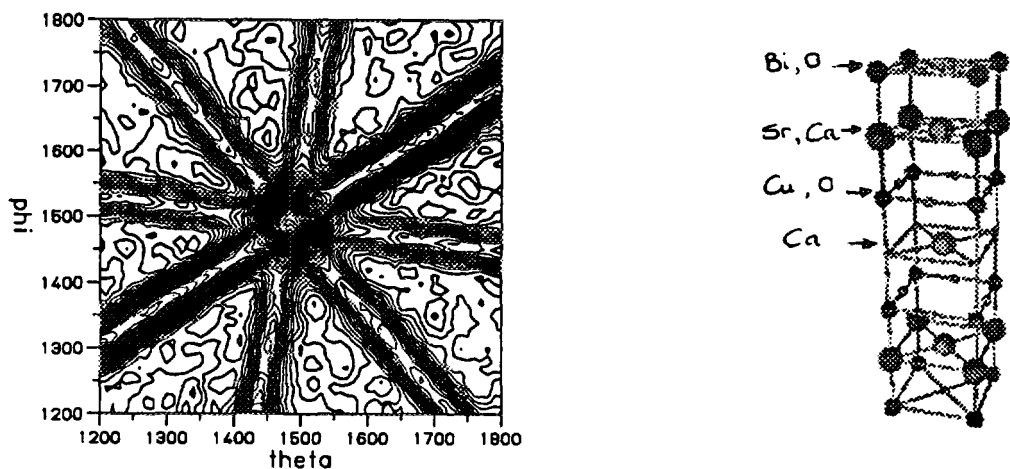
A 3.6 MeV  $H^+$  BS spectrum was fitted with a simulation in which the oxygen composition was the only free parameter and which made use of the measured non-Rutherford (p,p) cross-section for oxygen at this energy (Fig 1). This fit yielded a sample composition of  $Bi_2Sr_2CaCu_2O_{7.8}$  confirming that the crystal composition was as expected.

Figure 1: 3.6 MeV  $H^+$  RBS channelled and random spectra for 2212 with a RUMP simulation fitted to the random spectrum



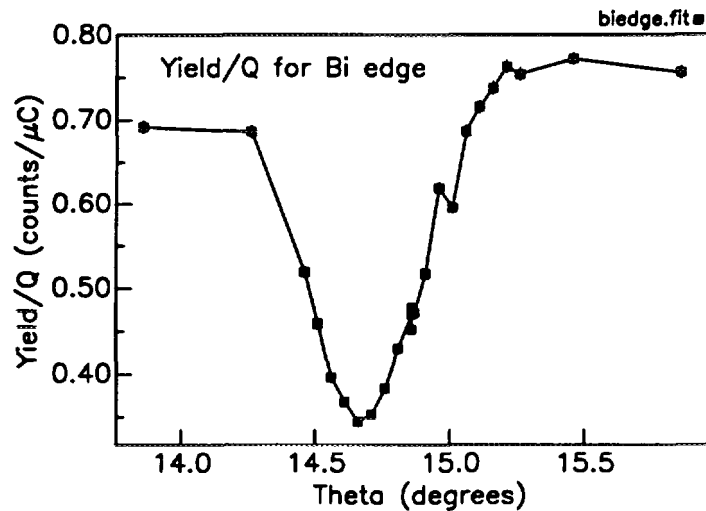
The map obtained from the 2-D angular scan can be seen in Fig 2a. This map possesses the peculiarity of having one plane through the axis appearing considerably deeper than the other planes. This is believed to be a direct consequence of the orthorhombic structure of the 2212 unit cell (Fig 2b). Further investigation is being undertaken to fully explain this phenomenon.

Figure 2: left (a) - 2-D angular scan of 2212 crystal using a 1.4 MeV  $He^{2+}$  beam. The variation in plane depths about the axis can clearly be seen. right (b) - The crystal structure of the 2212 unit cell.



The 3.6 MeV  $H^+$  angular yield about the axis obtained (Fig 3) can be seen to be consistent with the channel width measured with the 1.4 MeV  $He^{2+}$  beam in the 2-D scan above.

Figure 3: Angular Yield at the bismuth edges of the RBS spectra collected for a 3.6 MeV H<sup>+</sup> beam incident on 2212



### SUMMARY

This work shows that the use of a 3.6 MeV H<sup>+</sup> beam is effective in probing for O embedded in a matrix of heavier elements, such as 2212, since it does produce a significant O edge in the RBS spectra collected. The channelling work done indicates that the crystal structure of 2212 may be responsible for the nature of the angular scans measured, and this is an avenue we intend to pursue.

As a practical application of this nuclear elastic scattering technique, an experiment currently in progress is the measurement of the oxygen composition of a series of 2212 wires with different critical currents. By these measurements, it is hoped to establish the dependence of critical flux on oxygen stoichiometry and on crystal uniformity.

It is also planned to repeat the measurements described above at low temperatures in order to compare results and to investigate the effect of the phase transition which occurs at the critical temperature on the channel width and on the angular yield. It is hoped that these measurements may lend a clue to better understanding the superconducting mechanism in HTSC ceramics.

### ACKNOWLEDGMENTS

The assistance of P S Weiser, S P Dooley, L A Witham and A A Bettiol is gratefully acknowledged. The 2212 sample was provided by Professor G Russell of the School of Physics, University of New South Wales and was grown by Gu Genda.

### REFERENCES

- [1] R J Cava Science Vol 247, 9 February 1990, p656
- [2] L E Rehn, R P Sharma, P M Baldo, Y C Chang, P Z Jiang Phys Rev B 42 (1990) 4175
- [3] J R Tesmer and M Nastasi, NIM B45 (1990) 476
- [4] K K Lee, D N Jamieson and F Watt, paper presented at the International Conference on Nuclear Microprobe Technology and Applications, Shanghai, China, 10-14 October 1994
- [5] R Amirikas and D N Jamieson, NIM B77 (1993) 110
- [6] D N Jamieson, R A Brown, C G Ryan and J S Williams, NIM B54 (1991) 213



# THE POTENTIAL USE OF DIAMOND COATED TUNGSTEN TIPS AS A FIELD IONISATION SOURCE

A.BROWN, S.PRAWER, G.J.F.LEGGE, L.I.KOSTIDIS

School of Physics, MARC, The University of Melbourne, Parkville, VIC 3052, Australia.

## SUMMARY

Tungsten tips are convenient for use in a high brightness gaseous phase field ionisation source. However, the lifetime of these tips is not adequate for practical use. We are investigating whether coating tungsten tips with diamond using Chemical Vapor Deposition (CVD) will improve the practicality of using these tips by an improvement in longevity of the source and/or an improvement in brightness due to the effects of the property of negative electron affinity which has been observed on CVD diamond.

## INTRODUCTION

Resolution of the Melbourne University Microprobe is dependent on the beam brightness, ie. the ion current per unit area per unit solid angle. In order to achieve an order of magnitude improvement in resolution by an increase in brightness, an improvement in source brightness of at least three orders of magnitude will be necessary. This fact favors the development of a FI source, as it has sufficient intrinsic brightness to make the necessary development work worthwhile.

Field Ionisation of an atom or molecule occurs when gas atoms and molecules are attracted to the tip by polarization forces and then ionised by electrons tunneling quantum mechanically from the atom or molecule to the tip and requires electric fields greater than  $1 \times 10^{10} Vm^{-1}$ . These fields can be produced by an emitter of submicron radius biased to several kilovolts.

In previous work completed by Allan(1), it was found, for tungsten tips used as field ionisation sources and under conditions of constant voltage and gas pressure, that the ion current decreased at rates up to 1% of the initial current every 10 seconds. The decrease in FI current could only have resulted from a change in the tip structure. This change comes about from the modification of the tip endform due to reactive gas etching. This field induced etching is brought about due to the presence of nitrogen and water molecules in the vicinity of the tip.

It is hoped that by coating these tips with CVD diamond that the tips will be protected, thus increasing their endurance, and that field ionisation may be enhanced due to the property of negative electron affinity which has been observed on CVD diamond.

## EXPERIMENTAL

### Tungsten Tip Etching

A small length of  $125\mu m$  tungsten wire was immersed to a depth of a few mm into a solution of 1M NaOH which is used as the etchant. A D.C. voltage of about 12 V is then applied between the tip and a nickel electrode. Etching takes place preferentially at the surface of the solution and so the waist eventually erodes to a point where it can no longer support the weight of the wire beneath it and fractures, the fracture point quickly smoothing by the continuing etching. This event is signaled by a rapid drop in the current (from about  $3mA$

to  $1\mu A$ ), and the circuit is then broken with the use of a tapping switch.

The tips were then examined with the use of an optical microscope and ill-formed tips were rejected. Ill-formed tips are those which did not have the satisfactory sharpness required (termination radius of  $\approx 0.1\mu m$ ).

### **Chemical Vapor Deposition**

The samples were inserted into a hot filament CVD deposition system. The CVD deposition conditions were then varied to obtain a smooth diamond coating of the highest quality as determined by micro-raman spectroscopy.

### **Testing of Tips as Field Ionisation Sources**

The tips are spot welded to a support filament and positively biased using a 0-50kV power supply in a vacuum chamber which is pumped using a turbomolecular pump. For stable FI, ultra high vacuums are required prior to the introduction of the source gas (ie. the gas to be ionised). Ultra high purity hydrogen is used as the source gas at differing pressures.

The ionised beam passes through two apertures, the first being to steer the beam and the second being used for quantitative measurements. Below the second aperture there is a linear scanning arm consisting of a fine stainless steel wire  $450\mu m$  in diameter which is stepped across the beam path, and the incident beam current is recorded as a function of position, the resultant angular distribution is a convolution of the beam profile and that of the wire as it intercepted the beam. The total beam current transmitted is recorded with a Faraday Cup at the base of the beam. A negatively biased ring preceding the entrance to the cup is used to retain secondary electrons, the total brightness of the beam can then be calculated from a knowledge of the diameter of the aperture, the divergence angle of the beam and the total beam current.

Results are taken from both diamond coated and uncoated tips and compared to determine whether the CVD diamond coating gives an improvement in performance of the tips as FI sources.

### **ACKNOWLEDGEMENTS**

This work has been supported by the Australian Research Council.

### **REFERENCES**

- (1) G.L.Allan, *The SPMP as a Diagnostic Tool and Development of a High Brightness Ion Source*, PhD Thesis, University of Melbourne, 1989, pg.120 - 121.



# Trace Element Distribution In Geological Crystals

J. L. DEN BESTEN, D. N. JAMIESON and P. S. WEISER  
School of Physics, MARC, The University of Melbourne, Parkville, Vic., 3052

## INTRODUCTION

Channelling is a useful microprobe technique for determining the structure of crystals, but until now has not been performed on geological crystals. The composition has been investigated rather than the structure, which can further explain the origin of the crystal and provide useful information on the substitutionality of trace elements. This may then lead to applications of extraction of valuable metals and semiconductor electronics.

We have channelled natural crystals of pyrite,  $\text{FeS}_2$ , which contains a substantial concentration of gold. Rutherford Backscattering (RBS) and Particle Induced X-Ray Emission (PIXE) spectra using MeV ions were obtained in the experiment to provide a comparison of lattice and non-lattice trace elements.

## EXPERIMENTAL TECHNIQUE

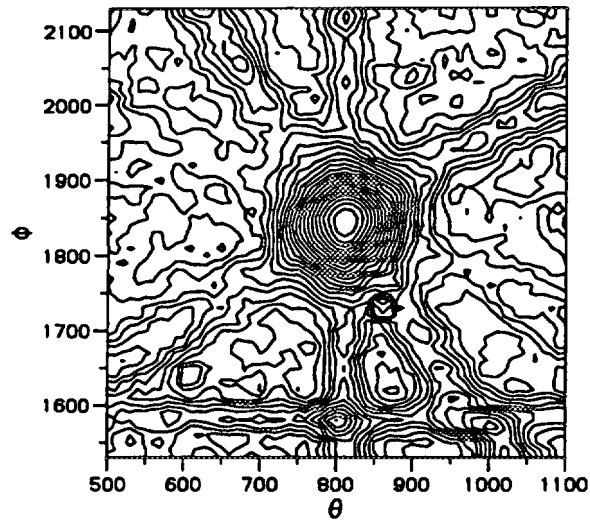
The sample consisted of two natural pyrite veins embedded in quartz and contained a significant amount of the trace element, gold. The specimen was obtained from the Emporer Gold Telluride Deposit in Fiji. The experimentation was performed on the Nuclear Microprobe with the Micro Analytical Research Centre at the University of Melbourne.

Initially 3.0MeV protons were used to determine the concentration of gold throughout the pyrite veins and the greatest amount of this trace element was used as the site for further investigation. A single crystal of hexagonal shape and diameter of approximately  $150\mu\text{m}$  was used for channelling. The sample was mounted in its natural bed of quartz and placed in the goniometer at the eucentric point. The channel axis was found using 1.4MeV Helium ions and a computer driven mechanical goniometer. A  $6^\circ \times 6^\circ$  angular scan over a  $170\mu\text{m}$  square was taken in order to identify the order of the axis by examining the orientation of the planes about the axis. Once the angular positions of the axis were obtained, RBS and PIXE spectra were obtained in the channelled region (center of the axis) and in the random region. Lastly a linear angular scan in the rotation about the x-axis was performed through the channelled axis over  $6^\circ$  using RBS and PIXE.

## RESULTS

The concentration of the trace element, gold, was found to be relatively continuous throughout the veins. Fig.1 shows the channelled axis of the single pyrite crystal in the  $6^\circ \times 6^\circ$  two dimensional angular scan. The orientation of the surrounding channel planes about the axis suggests the axis to be  $\langle 110 \rangle$  using stereographic projections of cubic crystals.

Figure 1: 2-d angular scan of pyrite crystal using 1.4MeV He<sup>+</sup> showing a low order axis



At the centre of the axis, shown in Fig.1, a channelled RBS spectra (solid line) was taken, and 2° left of the axis a random RBS spectra (triangle) was taken, the comparison seen in Fig.2. A simulation was done and was found that the gold concentration was 0.2% and can be seen above the random data points in Fig. 2. As shown, the channelled spectra is much lower in yield than that of the random spectra indicating that gold is 50% substitutional in a 38%  $\psi_{min}$  lattice crystal. The magnification of the gold spectra also shows that the trace element is present on the lattice sites and therefore can also be channelled. The PIXE spectra clearly displays the presence of gold in the pyrite. The extent of this can be seen in Fig.3 which compares the yield of each element across the axis.

Figure 2: RBS spectra of random and channelled pyrite with RUMP simulation over the spectra (left) and PIXE spectra (right) of random pyrite (3.0MeV H<sup>+</sup>)

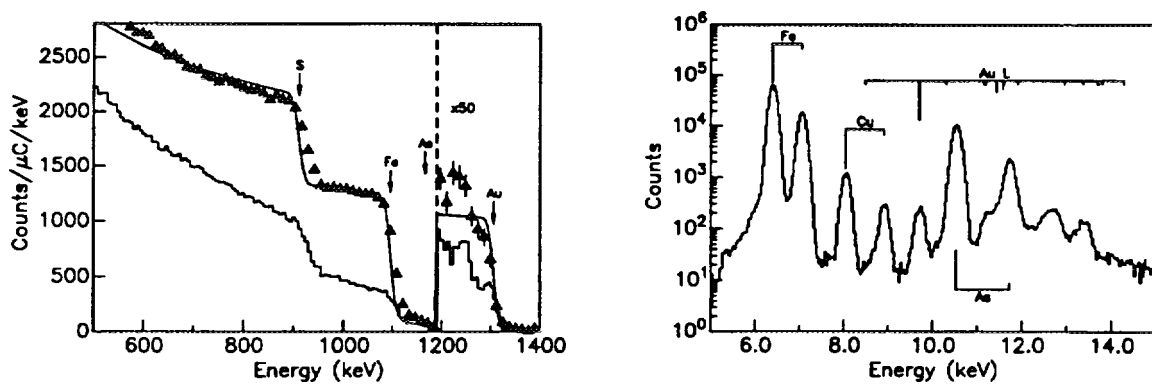
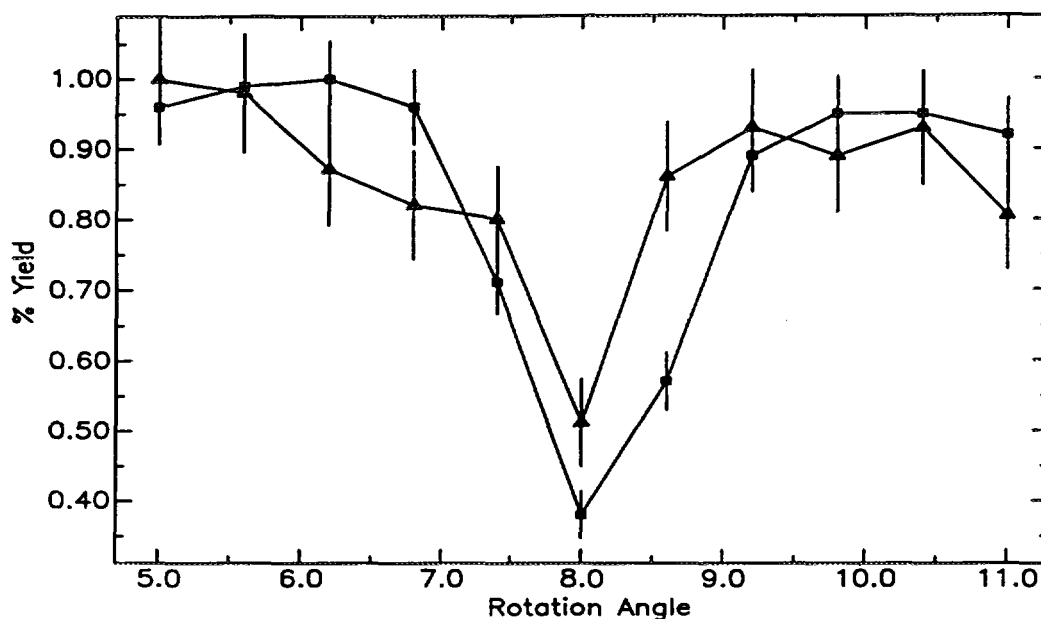


Figure 3: Yield versus angle across the axis for the single crystal pyrite (Au triangle, Fe square)



### CONCLUSION

The above results are conclusive that the gold is 50% substitutional and that geological materials may be channelled. Future work will include looking at the channels with protons which will provide more conclusive x-ray results. The technique is then to be applied to specimens of colored diamond, the color thought to be due to trace elements.



# Transverse Microanalysis of High Energy Ion Implants.

Sean P. Dooley, David N. Jamieson, Kerry W. Nugent and Steven Prawer.

Micro Analytical Research Centre, School of Physics,  
University of Melbourne, Parkville 3052, AUSTRALIA.

High energy ion implants in semiconductor materials have been analyzed by Channeling Contrast Microscopy (CCM) perpendicular to the implant direction, allowing imaging of the entire ion track. The damage produced by Channeled and Random 1.4 MeV  $H^+$  implants into the edge of a  $\langle 100 \rangle$  type IIa diamond wafer were analyzed by channeling into the face of the crystal. Our results showed negligible damage in the surface region of the implants, and swelling induced misalignment at the end of range of the implants. Channeled 1.4 MeV  $H^+$  implants in diamond had a range only 9% deeper than Random implants, which could be accounted for by dechanneling of the beam.

## INTRODUCTION.

Channeling has been extensively used to characterize ion implants in crystals to a depth of  $\sim 1.5\mu\text{m}$ . The accuracy of this technique for the analysis of deep implants is limited by the large effective straggling and dechanneling of the analysis beam. We have performed channeling analysis perpendicular to the ion implant to produce CCM images of the entire ion track (figure 1). This has been used to evaluate the damage produced in GaAs and Si by the 77 MeV Iodine beam used for Heavy Ion Recoil Spectrometry [1], by channeling into the cleaved edge of an irradiated wafer.

In this study, the damage distribution of 1.4 MeV  $H^+$  microprobe irradiations in channeling and Random orientation in  $\langle 100 \rangle$  diamond were evaluated by transverse CCM. This was to characterize the level of defects and the effects of swelling [2] on the transverse CCM analysis, and to determine the effects of channeling on implant depth. Recent Monte-Carlo simulations by a program called MABIC [3] for 0.96 MeV protons in  $\langle 110 \rangle$  Si give a Random range of  $14.6\mu\text{m}$  and a channeled range of  $16.0\mu\text{m}$ .

Diamond was chosen for this study because ion beam induced damage is clearly visible, allowing optical characterization of damage, and easy positioning of the analysis beam. In order to obtain the best possible spatial resolution,  $H_2^+$  ions were used to maximize the brightness of the RF ion source of our accelerator. This allowed a  $30\mu\text{m}$  object to be used for our measurements, giving a  $1.5\mu\text{m}$  first order beam spot size. The channeling of  $H_2^+$  ions has been found to be identical to that of protons of half the energy [3], however our measurements have shown a 1% increase in  $\chi_{min}$  for  $H_2^+$  in diamond compared to  $H^+$  at 1.2 MeV per proton. This is due to repulsion between protons within the same channel [3].

## ANALYSIS OF 1.4 MeV $H^+$ IMPLANTS IN $\langle 100 \rangle$ DIAMOND.

The implants were performed into the edge of a  $\langle 100 \rangle$  type IIa diamond wafer using a focussed 1.4 MeV  $H^+$  beam scanned over a  $100\mu\text{m}$  square (Fig 1.) in channeled and Random orientation over a dose range of  $5 - 50 \times 10^{16}/\text{cm}^2$ . Optical microscopy of the 1.4 MeV implants (Fig 2a.) gave an implant depth of  $14.0\mu\text{m}$  for Random implants and  $15.2\mu\text{m}$  for channeled implants.

The implants were then imaged with 1.2 MeV and 2.4 MeV  $H_2^+$  beams (Fig 2b.). From the 2.4 MeV  $H_2^+$  CCM images, the depth of Random implants was  $14.0\mu\text{m}$  and  $14.7\mu\text{m}$  for the channeled implants. Both Random ranges are marginally higher than calculated by TRIM ( $13.39\mu\text{m}$ ). The  $\chi_{min}$  of the end of

## Irradiation and Analysis Procedure.

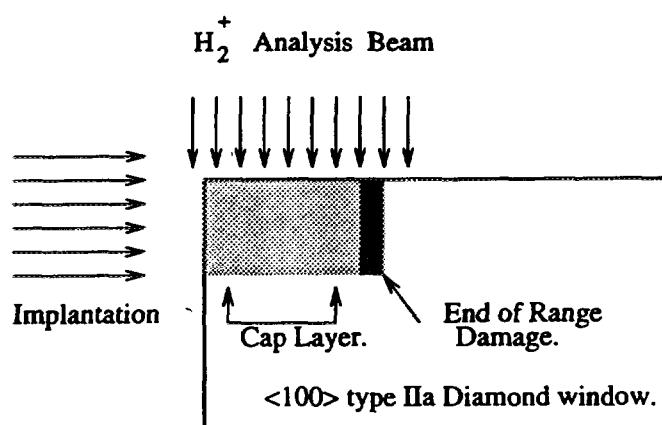


Figure 1: Experimental geometry for the transverse imaging of implants in diamond. Part of the implanting scan misses the diamond to ensure that the beam damage extends to the analysis surface.

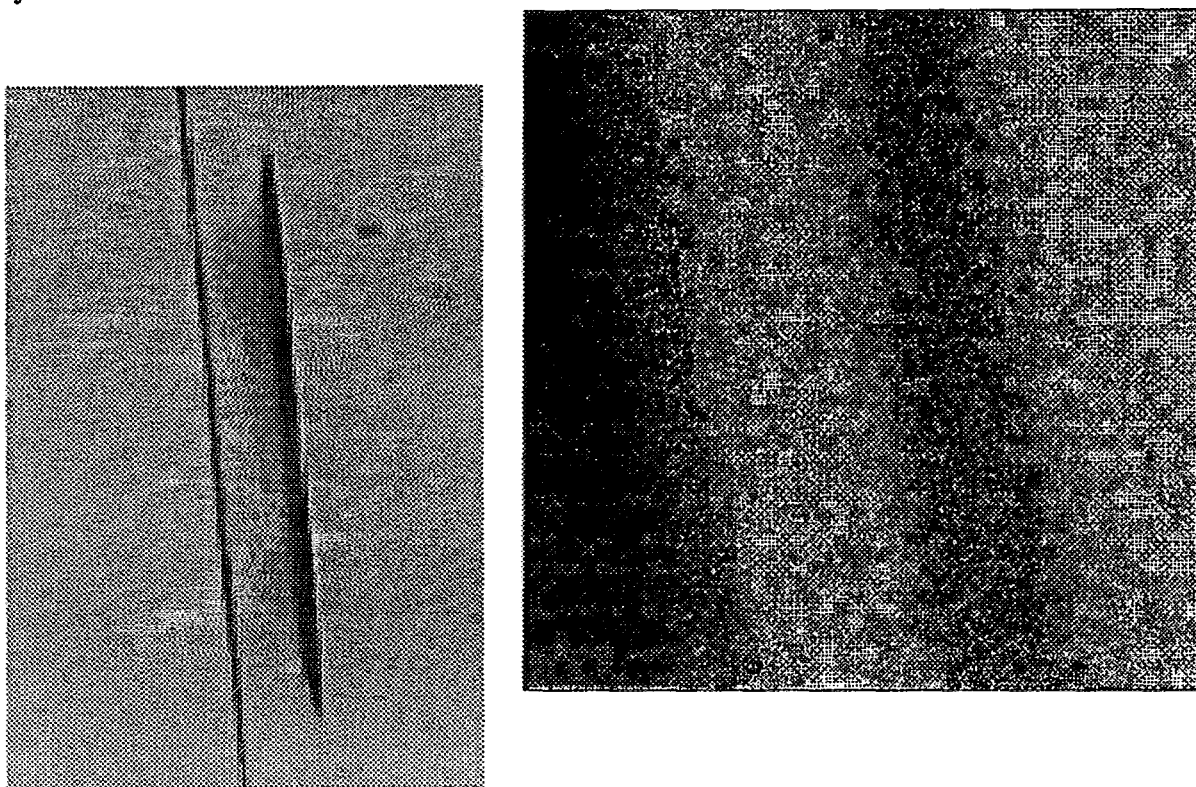


Figure 2a: Optical micrograph of a  $5 \times 10^{16}$  Random implant. The irradiated region is  $100 \mu\text{m}$  wide and the depth is  $13.4 \mu\text{m}$ . The end of range region appears black, and the crystal above it appears green.

Figure 2b: A  $2.4 \text{ MeV } H_2^+$  transverse CCM map of a  $1 \times 10^{17}/\text{cm}^2$   $1.4 \text{ MeV } H^+$  implant in diamond. The dark coloured band is poor channeling in the end of range region. The crystal above and below the end of range region shows good channeling indicating little damage in the surface region.

range region was found to be higher for Random implants than for channeled implants, but significantly lower for a 1.2 MeV  $H_2^+$  beam than a 2.4 MeV beam at the same dose. The spectra extracted from the end of range region at doses above  $10^{17}/\text{cm}^2$  were dominated by swelling induced misalignment. Spectra extracted from the near surface region showed no effects of damage.

## ANALYSIS OF CHANNELING RANGES.

Applying channeling stopping powers only to the median dechanneling depth can predict the median channeling range. The median channeling depth can be determined from the channeling spectrum of the implanted ions. Assuming the ratio  $\epsilon$  of channeling stopping power to Random is independent of energy, the range of channeled ions  $R_c$  is given by:-

$$R_c = R_R + \left( \frac{1}{\epsilon} - 1 \right) D_{med}$$

Where  $R_R$  is the range of ions in Random orientation, and  $D_{med}$  is the median depth for dechanneling. Using an  $\epsilon$  of 0.65 based on data for protons in Si [5], the range of channeled ions is estimated to be 15.1  $\mu\text{m}$ , which is comparable with our data.

## CONCLUSION.

Spectra from the end of range region of these implants show evidence of crystal misalignment due to the stress induced by the implants. The surface regions of these implants showed negligible levels of damage induced by the passage of the high energy ions. Analysis of channeled implants showed that dechanneling is a significant factor in determining the ranges of channeled high energy ions, reducing them to near Random ranges. The  $\chi_{min}$  of the end of range region of channeled implants is lower than that of Random implants of the same dose, due to a greater effective straggling in channeling orientation widening the end of range region.

With new lenses and magnetic shielding on the MP2 beam line, resolution should be improved for future measurements. In particular we hope to use transverse CCM to test the predictions of the MABIC simulation [3] for channeled protons in Si.

## REFERENCES.

- [1] S. R. Walker, P. N. Johnston, I. F. Bubb, W. B. Stannard, D. N. Jamieson, S. P. Dooley, D. D. Cohen, N. Dytlewski and J. W. Martin. Nucl. Inst. Meth. B, To be Published.
- [2] S. P. Dooley and D N. Jamieson. Nucl. Inst. Meth. B66 (1992) 369.
- [3] F. Ditrói, J. D. Meyer, R. W. Michelmann and K. Bethge, Nucl. Inst. Meth. B99 (1995) 182.
- [4] J. M. Caywood, T. A. Tombrello and T. A. Weaver, Physics Letters 37A no. 4 6/12/1971.
- [5] Channeling, D. V. Morgan (ed). John Wiley & Sons Ltd. (1973) p 143.



# Electron Stimulated Desorption of Positive and Negative Oxygen Ions from $\text{YBa}_2\text{Cu}_3\text{O}_7$ Surfaces

A. HOFFMAN<sup>1</sup>, S.D. MOSS<sup>2</sup>, P.J.K. PATERSON<sup>2</sup>, D. M<sup>C</sup>CUBBERY<sup>3</sup> AND M. PETRAVIC<sup>4</sup>.

1. Chemistry Department and The Solid State Institute, Technion, Haifa 32000, Israel.
2. Applied Physics Department, RMIT, GPO Box 2476V, Melbourne 3001 Australia.
3. Chemistry Department, LaTrobe University, Bundoora, 3083, VIC, Australia.
4. Department of Electronic Materials Engineering, Research School of Physical Science, Australian National University, GPO Box 4, Canberra, ACT, 2601, Australia.

## ABSTRACT

Electron stimulated desorption of positive and negative oxygen ions from  $\text{YBa}_2\text{Cu}_3\text{O}_7$  surfaces contaminated with  $\text{OH}^-$  chemisorbed groups and 2-3 at% Cl has been studied as function of electron kinetic energy. It has been found that the threshold electron kinetic energy to induce positive oxygen ion desorption occurs at  $300 \pm 20$  eV, whereas that associated with negative oxygen ion desorption was found to be  $110 \pm 20$  eV. These electron kinetic energies correspond to Cu, Y and Ba core level binding energies. These results suggest that negative and positive oxygen ion desorption may be initiated via a primary core level ionisation.

Electron stimulated desorption (ESD) from surfaces has been studied for many years (1). Generally speaking, ESD is initiated by a primary electronic excitation whose relaxation results in the breaking of a chemical bond and desorption of ions and neutrals. Below about 30 eV ion desorption is initiated predominantly by valence band excitations (2). Valence band excitation, which results directly in positive ion formation, has been studied in detail. Negative ions has been observed to originate from processes involving unoccupied electronic states via electron attachment (3,4). ESD at much higher bombardment electron kinetic energies has been observed and attributed in some cases to core level excitations. In this regime, and for ionic compounds, positive ion desorption has been explained in terms of core level ionisation whose de-excitation, via an interatomic Auger transition, result in a local repulsive potential leading to bond breaking and desorption (5). Only very recently have desorbing negative ions been attributed to core level ionisation (6), possibly involving the formation of excited substrate-adsorbate complexes.

The effect of 5 - 10 keV electron bombardment on  $\text{YBa}_2\text{Cu}_3\text{O}_7$  has been studied in some detail (7,8). In situ studies show that as function of 3 keV electron bombardment time a decrease in the O(KLL) Auger signal occurs suggesting that electron stimulated desorption of oxygen occurs (8). Also the superconducting transition temperature was found to decrease as function of 10 keV electron bombardment time and this was associated with oxygen loss induced by electron stimulated desorption (8).

In this work we studied ESD of positive and negative oxygen ion desorption from superconducting  $\text{YBa}_2\text{Cu}_3\text{O}_7$  surfaces as function of electron kinetic energy. Based on ion desorption yield measurements as function of electron kinetic energy, primary excitations leading to positive and negative oxygen ion desorption are suggested. To the best of the authors' knowledge this is the first study on electron energy dependent ESD from  $\text{YBa}_2\text{Cu}_3\text{O}_7$  surfaces.

The  $\text{YBa}_2\text{Cu}_3\text{O}_7$  samples were prepared from  $\text{BaCO}_3$ ,  $\text{Y}_2\text{O}_3$  and  $\text{CuO}$  using standard high temperature sintering and annealing procedures. Slices 2 mm thick were cut and further annealed at 400 C in flowing oxygen for 24 hours prior to insertion into the UHV chamber for ESD. The near surface composition and chemical state of the annealed sample after exposure to air was examined by Auger and XPS analysis. Auger measurements of the as annealed sample were performed as function of Ar ion sputtering time. It was found that the relative intensity of the various Auger lines associated with Y, Ba, Cu and O measured for the as annealed sample surface and after 20 min. Ar ion (2 keV,  $52 \mu\text{A}/\text{cm}^2$ ) sputtering were similar. Thus suggesting, that the near surface composition of the as prepared sample is similar to the bulk composition. The only detected impurity in the Auger spectrum of the annealed sample was Cl with a concentration of 2-3 at.%. The Cl impurity originates from the silica GEL used to preserve the samples from water adsorption after the annealing process. XPS examination of the annealed surface exposed to air showed a splitting in the O(1s) line suggesting the presence of  $\text{OH}^-$  adsorbed groups (9). These measurements suggest that the ESD experiments were performed on samples of similar near surface and bulk composition with some  $\text{OH}^-$  chemisorbed groups and Cl surface contaminations.

The ESD measurements were performed using a commercially available quadrupole-type ion micro probe (RIBER MIQ 256). The base pressure in the analysis chamber was  $5 \times 10^{-10}$  torr and increased to  $7 - 8 \times 10^{-10}$  torr during electron bombardment. To obtain improved sensitivity and dynamic range of the emitted ions the sample holder was biased during ion detection. The electron gun and optics used for electron bombardment (RIBER CER 306 Auger and LEED grazing angle electron gun) were not useful at electron energies below  $\sim 50$  eV as a result of low currents in the nA range. In the 100 eV range, however, typical currents of 1 - 10  $\mu$ A into a spot size of a few  $\text{mm}^2$  were obtained. The ESD experiments were performed in the 50-600 eV.

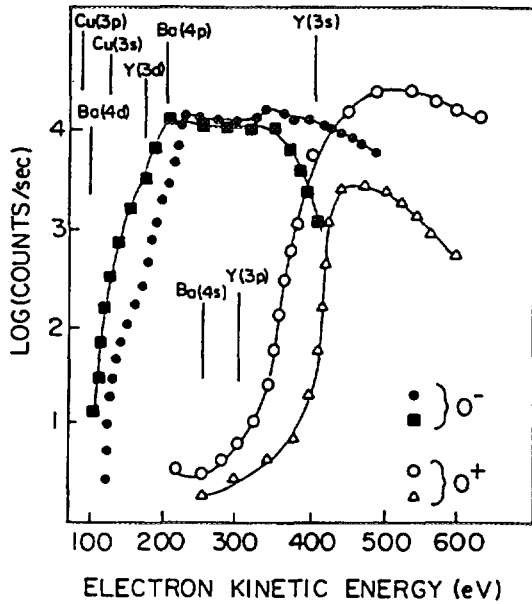


Figure 1. Normalised positive and negative oxygen ion desorption yields as function of bombarding electron kinetic energy of  $\text{YBa}_2\text{Cu}_3\text{O}_7$ .

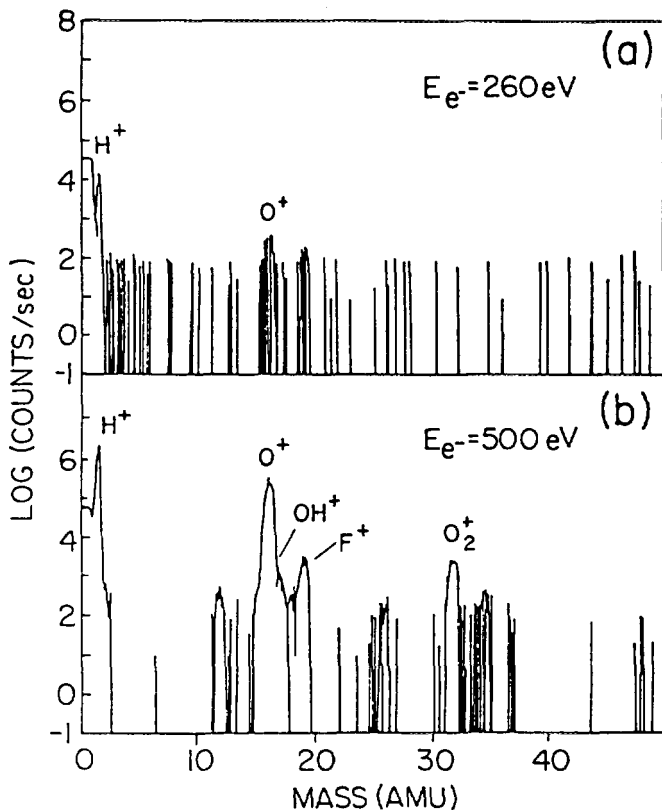


Figure 2. Positive ion spectra above (a) and below (b) the threshold electron kinetic energy for positive oxygen ion desorption.

ESD yields of  $\text{O}^+$  and  $\text{O}^-$  as a function of bombarding electron energy for two independent experiments are shown in Figure 1. The ion yields were normalized by the primary electron current, which was measured by applying a sample potential of +200 V and was found to depend on primary electron energy. The electron kinetic energy scale have been corrected for the work function of the W filament ( $\sim 5$  eV) of the electron gun and the bias potential applied to the sample to maximise ion yield. As observed from this figure there are some differences in yield as function of bombarding electron energy between the ESD experiments. These differences are associated with different biasing potentials used to optimise the ion intensities for each experiment. The results of other ESD experiments performed to verify the reproducibility of our ion yield curves were within the results presented in Figure 1.

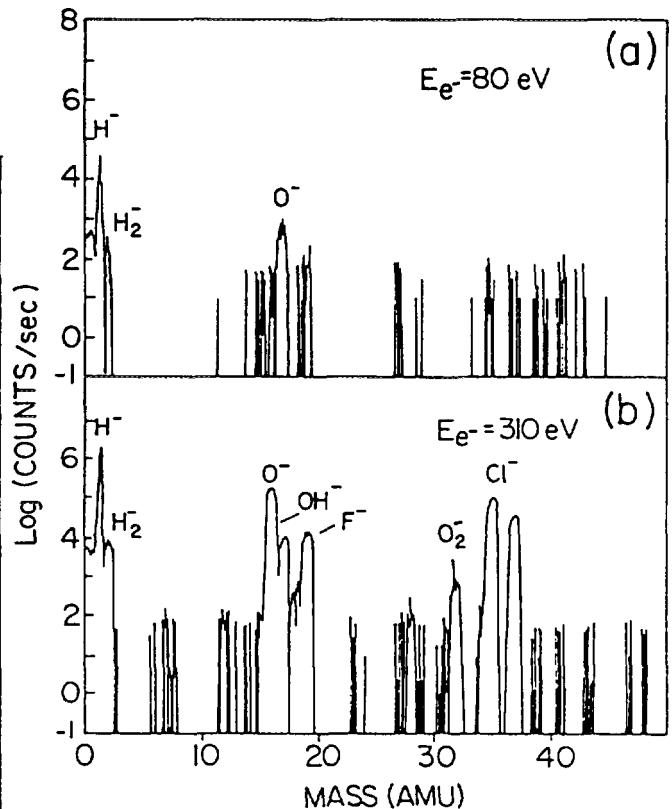


Figure 3. Negative ion spectra above (a) and below (b) the threshold electron kinetic energy for negative oxygen ion desorption.

As observed from this figure both the negative and positive ion yields display a threshold type dependence as function of electron energy. In both cases the yield is plotted in a logarithmic scale. The threshold in negative oxygen ion desorption occurs at 110 $\pm$ 20 eV followed by a step increase in yield of about four decades in the 110 - 200 eV electron energy range. At electron energies larger than about 200 eV a broad maximum is observed followed by a decrease in yield. The threshold in O<sup>+</sup> yield occurs at about 300 $\pm$ 20 eV. In this case the increase in yield is slow up to about 350 eV followed by a step increase of four decades in the energy range 350 - 400 eV. At larger energies a broad maximum and decrease in yield is observed.

In Figures 2a and 2b positive ion mass spectrum measured from the sample under electron bombardment at 260 and 500 eV are shown. As observed from this figure in addition to oxygen ions, other ions were observed in the positive ion ESD spectrum. These are most likely due to surface impurities. In Figures 3a and 3b negative ion mass spectra measured under electron bombardment at 80 and 310 eV are shown. Also in this case negative ions other than oxygen were observed in the negative ion ESD spectrum. In particular, the Cl<sup>-</sup> peak in the negative ion spectrum is associated with Cl impurities whereas the H<sup>+</sup> and H<sup>-</sup> to OH<sup>-</sup> adsorbed groups. As observed from Figures 2 and 3 the overall measured ion mass spectrum intensity below the threshold energy for oxygen ion desorption (both positive and negative) is lower than the intensity of the spectrum above threshold. These results seem to indicate that the threshold behaviour measured for oxygen ion may be similar to that of the other ionic species measured in the ESD spectrum.

From Figure 1 the negative oxygen ion desorption yield displays a very clear threshold at about 110 $\pm$ 20 eV electron kinetic bombarding energy. This electron energy correlates with Ba and Cu core levels binding energy marked in Figure 1. It is suggested that such correlations imply that negative oxygen desorption is initiated primarily by the core level ionisation of Ba and/or Cu core levels. Then the relaxation of such ionised core level through charge transfer processes, such as inter-atomic Auger transition involving a negatively charged neighbour oxygen site, may result in bond scission. If this process occurs in the near surface region, desorption of an oxygen species may occur. Similarly, the correlation between the threshold observed for positive oxygen desorption yield with electron kinetic energy and Ba and/or Y binding energy core level values suggest that these core level ionisation are prime excitation leading to desorption of positive oxygen ions.

The charge state of the desorbing oxygen is determined by the core hole relaxation processes and charge transfer processes between the escaping oxygen and its immediate surrounding. The charged state of the escaping oxygen ion (or atom) is not necessarily equal to its value just after the relaxation process. Following the core hole relaxation process the oxygen atom involved may be ejected with a specific kinetic energy that determines the probability of its escape from the surface into the vacuum and its final charge state. For example, negative oxygen formation is favoured in an environment rich in low energy secondary electrons and oxygen species as O<sup>-</sup> is energetically more stable than O<sup>+</sup> or neutral oxygen (10). However, the charge transfer probability from a surface to an escaping O<sup>+</sup> is expected to decrease as the kinetic energy of the desorbing specie increases (4).

In summary, in the present work ESD yields of negative and positive oxygen ions from YBa<sub>2</sub>Cu<sub>3</sub>O<sub>7</sub> surfaces contaminated with some adsorbed OH<sup>-</sup> and Cl have been measured as function of electron irradiation energy. It has been found that the desorption yields display very distinctive threshold as function of electron irradiation energy which correlate with different Y, Ba and Cu core levels. Based on these experimental observations it is suggested that both negative and positive oxygen electron stimulated desorption are mediated by core level ionisation of the metal atoms.

## REFERENCES

1. For review, see for example R. D. Ramsier and J. T. Yates, Jr., *Surf.Sci.Rep.* **12**, 234 (1991); T. E. Madey, D. E. Ramaker and R. Stockbauer, *Ann.Rev.Phys.Chem.* **35**, 215 (1984).
2. D. Manzel and R. Gomer, *J.Chem.Phys.* **41**, 3311 (1964); P. A. Redhead, *Can.J.Phys.* **42**, 886 (1964)
3. H. Sambe, D. E. Ramaker, L. Parenteau and L. Sanche, *Phys.Rev.Lett.* **59**, 236 (1987); **59**, 505 (1987)
4. J. J. Geerlings et. al., *Surf.Sci.* **157**, 151, (1985)
5. M. L. Knotek and P. Feibelman, *Phys.Rev.Lett.* **40**, 964 (1978)
6. A. M. Lanzilotto, T. E. Madey and R. A. Baragiola, *Phys.Rev.Lett.* **67** 232 (1991)
7. Y. Gao, T. J. Wagener, D. M. Hill, H. M. Meyer III, J. H. Weaver, A. J. Arko, B. K. Flandermeier, D. W. Capone, *Chemistry Of High Temperature Superconductors*, Chpt 21, 212 (1987)
8. S. Matsui, T. Ichihashi, T. Yoshitake, S. Muira, T. Satoh and M. Mito, *J.Vac.Sci.Tech.* **B 8**, 1771 (1990)
9. S. Lars, T. Anderson and J. C. Otamiri, *App.Surf.Sci.* **45** 1 (1990)
10. R. C. Weast and M. J. Astle, *CRC Handbook Of Chemistry And Physics*, CRC Press, 61st Edition, 1980-1981.



## Target Preparation at the ANTARES AMS Centre

G.E. JACOBSEN\*, Q. HUA, D. FINK, M.A.C. HOTCHKIS, E.M. LAWSON,  
A.M. SMITH and C.TUNIZ

Australian Nuclear Science and Technology Organisation.  
PMB 1, Menai, NSW, 2234. Australia.

### SUMMARY

The Antares AMS Centre has two chemistry labs dedicated to preparing targets for measurement. Target preparation encompasses a variety of activities ranging from the curation of incoming samples to the numerous steps involved in the purification and processing of dissimilar samples. One of the two laboratories is set up for the physical and chemical pretreatment of  $^{14}\text{C}$  samples. Treatments include cleaning by sonification, sorting, grinding and sieving, and chemical treatments such as the standard AAA treatment, and solvent extraction. Combustion and graphitisation are also carried out in this laboratory. The second laboratory is a clean room and is dedicated to the combustion, hydrolysis and graphitisation of  $^{14}\text{C}$  samples as well as the process of the targets for the other isotopes. Combustion is achieved by heating the sample to  $900^\circ\text{C}$  in the presence of  $\text{CuO}$ , the resulting gas is purified by passing over  $\text{Ag}$  and  $\text{Cu}$  wire at  $600^\circ\text{C}$ . Graphitisation is carried out by reducing the  $\text{CO}_2$  with an iron catalyst ( $600^\circ\text{C}$ ) in the presence of zinc ( $400^\circ\text{C}$ ) and a small amount of hydrogen.

Samples such as charcoal, shell, bone, wood, sediment, seawater and groundwater, containing 0.3-1 mg or more of original carbon, are processed routinely for radiocarbon analysis. The current  $^{14}\text{C}$  chemistry background for 1 mg carbon is ~ 0.3 percent of modern carbon (pMC) enabling us to date materials up to 45 000 BP. Samples of 0.5 - 3 mg carbon or more are routinely performed with a precision < 1%

At present, procedures are being tested for the treatment of samples containing a minimum of 20  $\mu\text{g}$  original carbon. Such small samples are more likely to be affected by contamination with modern carbon.

These laboratories are also being expanded to cater for the processing of a variety of samples for the measurement of other isotopes, *ie*  $^{129}\text{I}$ ,  $^{10}\text{Be}$ ,  $^{36}\text{Cl}$  and  $^{26}\text{Al}$ . Initial tests for the extraction of  $^{129}\text{I}$  from groundwater and sediment have been carried out. The chemistry background obtained for this work is encouraging.

### DILUTION OF MICROGRAM SAMPLES FOR $^{14}\text{C}$ ANALYSIS

Recently there has been a push to reduce the sample size from milligram amounts of carbon to microgram. We have attempted to process very small samples (20 - 200  $\mu\text{g}$  carbon) using the routine method of graphitisation. This has not been successful as the efficiency of the graphitisation, (ranging from 10 - 60%), is low and unreliable at these pressures. (Fig. 1). As incomplete reaction often results in fractionation, the accuracy of the final measurement can be affected.

To ensure complete reaction we are developing techniques for the dilution of small samples using  $^{14}\text{C}$  free  $\text{CO}_2$ . The size of the sample is increased to around 300 - 400  $\mu\text{g}$  and the corresponding increase in the initial pressure of the reaction results in a greater reaction efficiency. (see Fig. 1). The advantages of the dilution are also illustrated in Fig. 2. Theoretically a sample containing 40  $\mu\text{g}$  of modern carbon can be dated with a precision of 1%. This is not possible because of the limitations of the graphitisation reaction, however, if the sample is diluted 10 times, to an age of 20 000 BP, it can still be measured with a precision of 1%.

The accuracy of the measurement is reliant on the accuracy of the dilution and the degree of cryogenic fractionation which can occur during the mixing of the gasses. The degree of dilution is manometrically measured (from the pressure of the sample  $\text{CO}_2$  and blank  $\text{CO}_2$ ), the fractionation is evaluated from the  $^{13}\text{C}/^{12}\text{C}$  ratios. We are currently testing this technique by the dilution and measurement of known-age samples.

**Fig.1 - Graphitisation vs Sample Mass (ug)**

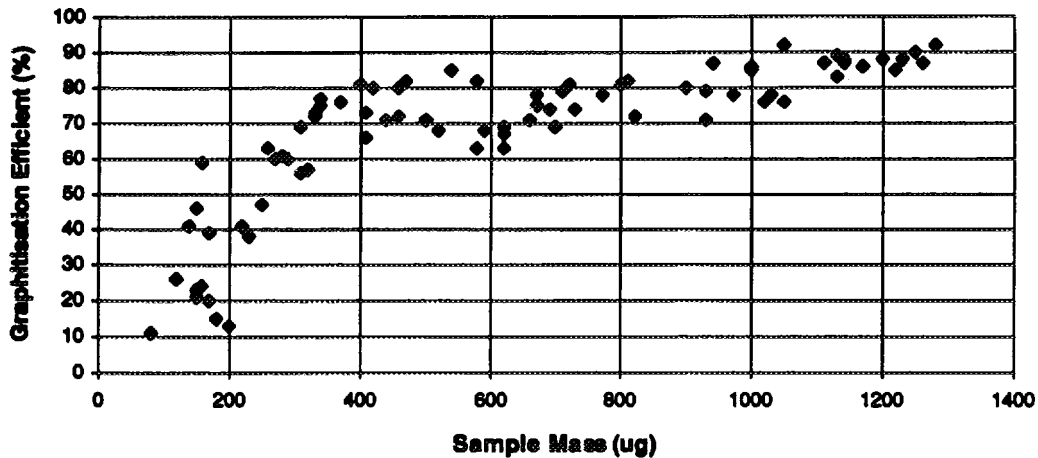
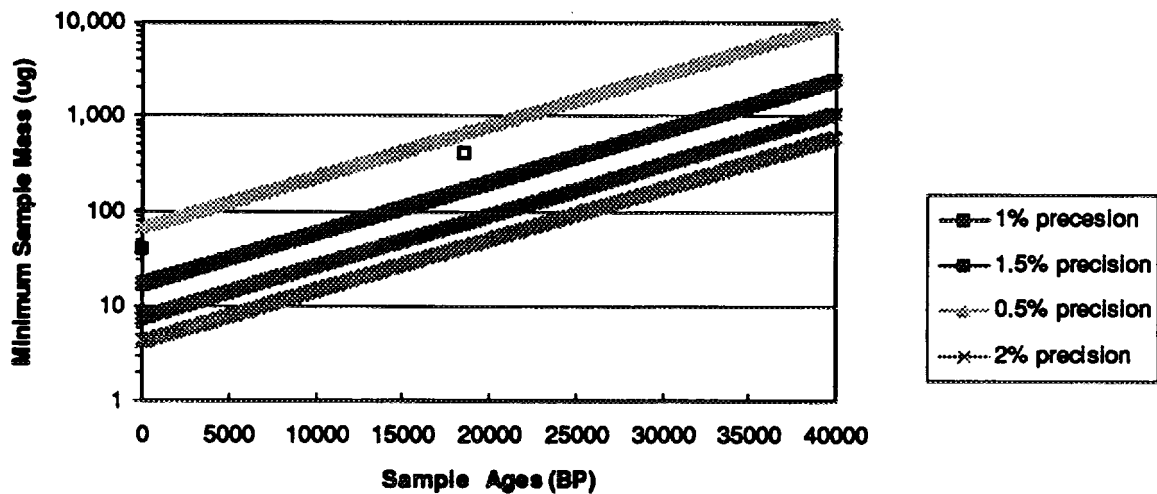


**Fig 2 - Precision vs Sample Mass at Different Ages**



**TARGET PREPARATION FOR THE MEASUREMENT OF <sup>129</sup>I**

At present this group is in the initial stages of developing procedures for the extraction of iodine from environmental samples. Care must be taken in the handling of the sample in the initial stages of drying and digestion as iodine may be lost. Foti<sup>1</sup> has shown that losses can occur in the collection and drying of the sample, to prevent this he recommends the addition of a small amount of a known volume of sodium hydroxide solution containing a small amount of iodine (which is insignificant to that of the carrier). The dry weight of the sample is determined by subtraction. There have been numerous, and conflicting, recommendations for the ashing or digestion of samples for iodine analysis. Bock<sup>2</sup> recommends alkaline ashing at as low a temperature as possible *ie* between 400 - 500°C but cautions that iodine losses have been observed at temperatures of 450°C. whereas Muramatsu<sup>3</sup> *et. al* state that ashing at 650°C was successful. Marchetti<sup>4</sup> *et. al* has also been pointed out that acid digestion has shown wide variations in the recovery of iodine. Initially, the aim of this work will be to test a variety of drying and digestion procedures to determine the most reliable and efficient method for the extraction of iodine from environmental samples.

### **Extraction from Water and Soil**

The iodine was extracted from water and soil samples using a modification of the procedures described by Wilkins and Stewart<sup>5</sup>. The method is based on solvent extraction, utilising the redox reactions of iodine/iodide. Prior to the solvent extraction the iodide is concentrated by loading onto an ion exchange resin and eluted as iodate. Following the conversion of the iodate to iodine the eluate is then extracted with chloroform and purified by back extraction using sodium metabisulphite as the reducing agent. In the case of the water samples, all iodine species in the water sample are converted to iodide prior to loading on the resin.

### **References**

1. Foti, S.C., *Health Phys.*, 33 (1979) 387
2. Bock, R., *A Handbook of Decomposition Methods in Analytical Chemistry*, Wiley, New York, 1979.
3. Muramatsu, Y., Ohmomo, Y. and Christoffers, D., *J. Radioanal. Nucl. Chem.*, 83 (1984) 353
4. Marchetti, A.A., Rose, L. and Strume, T., *Analytica Chimica Acta* 296 (1994) 243
5. B.T. Wilkins and S.P. Stewart, *J. Appl. Radiat. Isot.* 33 (1982) 1385.



# LASER TWEEZERS: SPECTROSCOPY OF OPTICALLY TRAPPED MICRON-SIZED PARTICLES

KRISTIE M. KERR\*, MICHELLE K. LIVETT and KERRY W. NUGENT

School of Physics, MARC, The University of Melbourne, Parkville, Victoria, 3052, AUSTRALIA

## INTRODUCTION

Information is often obtained about biological systems by analysis of single cells in the system. The optimum conditions for this analysis are when the cells are living and in their natural surroundings as they will be performing their normal functions and interactions. Analysis of cells can be difficult due to their mobility. Laser tweezing is a non contact method that can be employed to overcome this problem.

Laser tweezing is the term used to describe the trapping of micron-sized particles using laser beams. Ashkin *et al* [1] first demonstrated the trapping capabilities of a single laser beam in 1986. A tightly convergent laser beam exerts forces on micron-sized particles such that the resultant force is always towards the maximum intensity region of the beam. Therefore the particle is effectively trapped close to the waist of the convergent beam. For trapping to occur the particle must have a higher refractive index than the surrounding medium. Figure 1 illustrates the forces acting on a trapped particle.

The optimal application of laser tweezers to the study of biological samples requires that the above condition is satisfied and that the wavelength used for trapping is not absorbed by the cells as absorption will result in damage to the cells. Absorption of radiation by biological specimens is limited in the infrared region. Infrared radiation can therefore be used for trapping without damage to the specimen.

Raman spectroscopy is useful in the analysis of biological systems. It involves inelastic scattering of the incident beam and is used to obtain information about vibrational excitations of the molecules present. It can be resonance enhanced by choosing an excitation wavelength in the absorption band of the molecule.

Kiefer *et al* [2] reported on Raman and fluorescence spectra of single microdroplets in emulsions trapped using the laser tweezing technique. These particles were trapped using the same wavelength as that used to obtain Raman and fluorescence spectra. This paper reports on the use of a high intensity beam of one wavelength (IR) for trapping while using a low intensity beam of a different wavelength (VIS) for analysis of the trapped particle. The sample used was  $\beta$ -carotene dissolved in a microemulsion of oil in water.  $\beta$ -carotene was chosen because of its resonance enhanced Raman properties and because it does not significantly absorb infrared radiation.

## EXPERIMENT

### Preparation of Sample

$\beta$ -carotene is photo- and oxygen-sensitive and therefore care was taken in the preparation and storage of the sample. We dissolved  $\beta$ -carotene in paraffin under anaerobic conditions with the paraffin degassed before adding the  $\beta$ -carotene. The solution was frozen for storage, away from light. A microemulsion of the  $\beta$ -carotene solution in water was prepared also under anaerobic conditions.

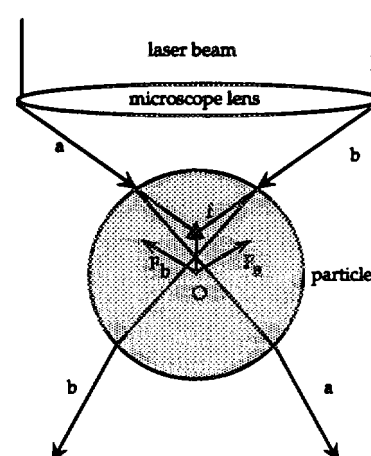


Figure 1. Rays a and b, directed towards the laser focus, f, exert forces  $F_a$  and  $F_b$  on a particle located below the focus. The resultant force is towards f. The resultant force is also towards f for particles displaced laterally or vertically from f.

### Raman Spectroscopic Investigation

Raman spectroscopy was used to examine both the solution of  $\beta$ -carotene in paraffin and its microemulsion in water. A DILOR XY confocal micro-Raman spectrometer was used, employing the 514.5 nm line from an Argon ion ( $\text{Ar}^+$ ) laser. To examine trapped particles a Nd-YAG laser beam was introduced into the system for trapping, coaxially with the  $\text{Ar}^+$  beam as illustrated in Figure 2. A 100 fold oil immersion objective with high numerical aperture (NA 1.25) was used and the sample was observed using a CCD camera. Particles ranging from 3-7 microns were trapped using the infrared radiation and their Raman spectra measured using the  $\text{Ar}^+$  laser at low power.

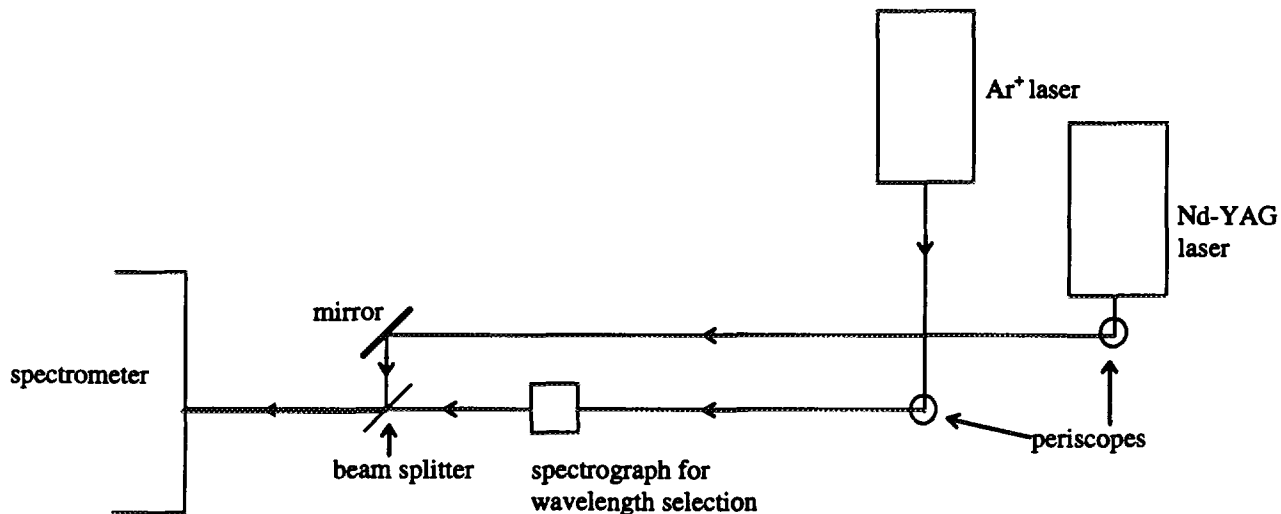


Figure 2. Schematic diagram of the experimental set-up.

### RESULTS AND DISCUSSION

A  $\beta$ -carotene in oil droplet, approximately seven microns in diameter, was trapped and dragged below the surface using the Nd-YAG laser. The spectrum of this droplet was measured using the  $\text{Ar}^+$  laser. The power of the Nd-YAG laser was approximately 42 mW at the sample and the  $\text{Ar}^+$  laser was approximately 1 mW. At this power the  $\text{Ar}^+$  laser beam was unable to maintain the trap once the Nd-YAG laser beam was removed. The spectrum measured of the droplet trapped below the surface contained the same features as that of a droplet trapped at the surface and of the  $\beta$ -carotene dissolved in paraffin solution. Figures 3 and 4 illustrate the comparison between a spectrum obtained of  $\beta$ -carotene dissolved in paraffin and a  $\beta$ -carotene in oil droplet trapped at the surface using the Nd-YAG laser.

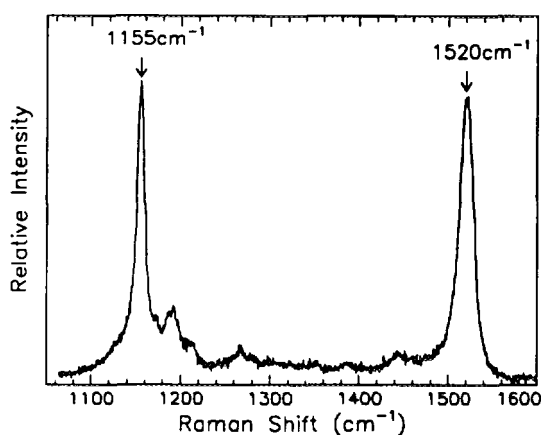


Figure 3. Raman spectrum of  $\beta$ -carotene dissolved in paraffin.

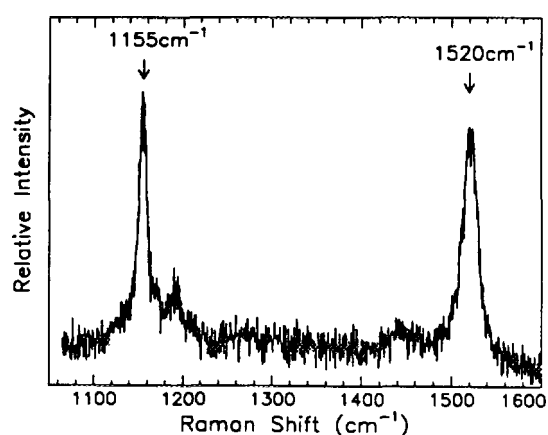


Figure 4. Raman spectrum of  $\beta$ -carotene oil droplet trapped at the surface.

An attempt was made to measure Raman spectra of droplets approximately three microns in diameter using the Nd-YAG laser for trapping and the Ar<sup>+</sup> laser at low power for spectroscopy but no spectrum was recorded. This suggested that when the Nd-YAG laser was employed for trapping it held the droplets vertically displaced from the focus of the Ar<sup>+</sup> laser so that the spectrum obtained was of the surrounding medium. The surrounding medium was predominantly water and this corresponds to the null spectrum observed. We believe that there was a vertical displacement of the order of microns between the two foci, a result of the beams having different wavelengths and therefore being refracted by different amounts in their paths through the objective lens.

The Ar<sup>+</sup> laser was also employed at high powers to trap droplets as well as obtain Raman spectra. The Raman spectra showed that high Ar<sup>+</sup> laser powers result in reaction of the  $\beta$ -carotene. This is due to the photo-sensitivity of  $\beta$ -carotene. The relative intensities of the  $\beta$ -carotene spectrum and the spectrum of its products depends on the size of the trapped droplet, the power of the laser and the length of time the droplet is exposed to radiation. Figure 5 shows the spectrum of a droplet, approximately six microns in diameter, held only by the Ar<sup>+</sup> laser at a power of approximately 5 mW at the sample for 5-10 minutes. The  $\beta$ -carotene spectrum is not observed indicating that it has reacted and its products are now present. There is a peak at approximately 1155 cm<sup>-1</sup> that could possibly coincide with the 1155 cm<sup>-1</sup> peak present in the  $\beta$ -carotene dissolved in paraffin spectrum however the  $\beta$ -carotene peak of similar intensity observed at 1520 cm<sup>-1</sup> is not observed in the spectrum of the droplet therefore no  $\beta$ -carotene is present.

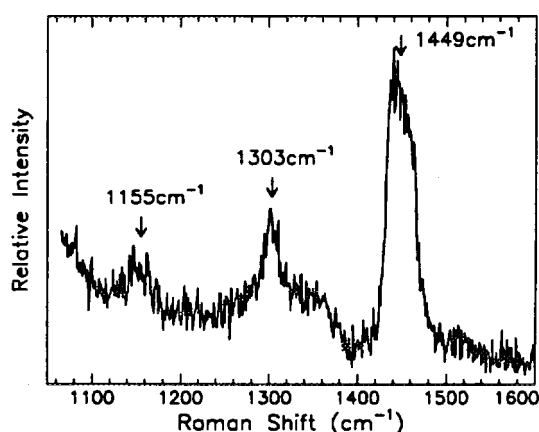


Figure 5. Raman spectrum of products present in droplet after  $\beta$ -carotene has reacted.

## CONCLUSION

The application of laser tweezing to biological samples provides a powerful tool in the analysis of functions and interactions at single cell level. In this investigation we have successfully obtained Raman spectra of a molecule of biological interest, dissolved in microdroplets of oil. The droplets were trapped using a Nd-YAG beam with the Raman spectra obtained using an Ar<sup>+</sup> beam at low powers. Further investigation is required into the feasibility of trapping smaller particles approximately three microns in diameter. For this to be possible the problem of the different beams focussing in different planes will have to be addressed.

## REFERENCES

1. A. ASHKIN, J. M. BJORKHOLM and S. CHU, *Opt. Lett.* , **11**, 288 (1986)
2. W. KIEFER, M. LANKER and J. POPP, *Appl. Spectrosc.* , **48**, 1166 (1994)



# STUDIES OF DEFECTS ON ION IRRADIATED DIAMOND

**\*PELAI, \*S.PRAWER, A.E.C.SPARGO, L.A.BURSILL**

*\*MARC, School of Physics, University of Melbourne, Parkville, Vic 3052, Australia  
School of Physics, University of Melbourne, Parkville, Vic 3052, Australia*

## 1. INTRODUCTION

It has recently been shown that successful doping of diamond may be achieved by implantation at low temperatures followed by rapid thermal annealing and that the degree of activation depends on a competition between C interstitial-vacancy recombination and implanted dopant-vacancy combination. Studies on ion bombarded diamond have primarily involved methods such as electrical measurements, Raman Spectroscopy and Rutherford Back Scattering Spectroscopy [1-3]. Although electron microscopy is widely used to analyze the microstructural properties of many materials, the microstructural nature of the ion beam induced defects in diamond has not been studied extensively. An extensive microstructural investigation of the ion irradiated diamond would be most desirable for the understanding of the defect structures and their behavior. This is crucial for optimizing the doping of diamond by ion irradiation and for understanding the final characteristics of the annealed layer.

It is known that diamond is amorphized or graphitized when irradiated above a critical dose [4]. Above this critical dose,  $D_c$ , the resistance  $R$  is found to drop very rapidly due to the formation of graphite regions which overlap at  $D_c$  to form a semi-continuous electrically conducting pathway through the sample [4]. One particularly interesting method of studying this transformation is electron energy-loss spectroscopy (EELS). Using EELS, the different phases of carbon can be identified and distinguished from each other using the extended energy-loss fine structure (EXELFS) of the core-loss part of the spectrum [5-7]. EELS is a sensitive method for determining the electronic structure of small areas of a sample. In this paper, transmission electron microscopy (TEM) and EELS measurements of the ion irradiated diamond were combined in an attempt to correlate the microstructural nature of the ion-beam induced damage to the changes in the electrical and other properties.

## 2. EXPERIMENT

Type IIa diamond windows  $2 \times 2 \times 0.1 \text{ mm}^3$  of [110] orientation were irradiated with 320keV Xenon ions at room temperature at the Technion, Israel. The doses selected were  $3 \times 10^{13}$  ( $D < D_c$ ),  $1 \times 10^{14}$  ( $D = D_c$ ) and  $3 \times 10^{14}$  ( $D > D_c$ ) Xe/cm<sup>2</sup>. Raman spectroscopy was performed on the samples using the 514nm line of an Ar ion laser. The samples were prepared for TEM analysis using ion beam thinning (IBT) (plan view, from the back). A Jeol TEM 4000 high resolution transmission electron microscope (HRTEM) interfaced to a Gatan PEELS spectrometer for parallel-detection energy loss spectroscopy analysis was used to study the microstructure and EELS of the unirradiated and irradiated samples.

## 3. RESULTS AND DISCUSSION

### A. Raman Spectroscopy

Raman spectroscopy was used to indicate the degree of irradiation damage in the diamond crystal after ion irradiation. Spectra from all samples show a strong diamond phonon peak at  $\sim 1330 \text{ cm}^{-1}$ , attributed mostly to the underlying undamaged diamond substrate of the irradiated samples. A very weak peak at  $\sim 1630 \text{ cm}^{-1}$ , most likely due to point defects, can be observed in the  $3 \times 10^{13}$  Xe/cm<sup>2</sup> sample which diminishes with increasing ion dose. Also, a small non-diamond disorder-induced peak at  $1200\text{-}1300 \text{ cm}^{-1}$  can be observed in the spectra of the implanted samples. Only the sample irradiated with  $3 \times 10^{14}$  Xe/cm<sup>2</sup> showed a broad peak at  $\sim 1530 \text{ cm}^{-1}$ , which is indicative of the presence of either disordered graphite or amorphous carbon.

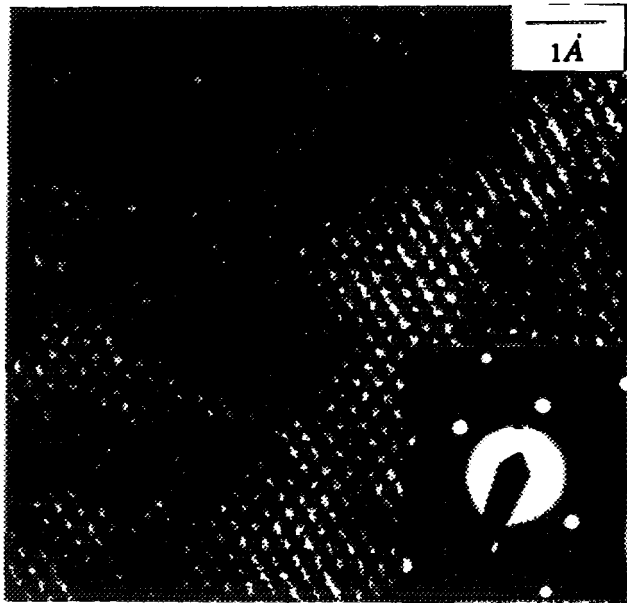


**Figure 1.** Lattice image and diffraction pattern in the {111} direction of the sample irradiated with  $1 \times 10^{14}$  Xe/cm<sup>2</sup>. The lattice spacing is  $\sim 2.1 \text{ \AA}$ . Note the diffuse background in the diffraction pattern. The unimplanted sample also show similar high resolution lattice images, without the diffuse background in the diffraction pattern. Amorphous regions were also observed in the implanted samples.

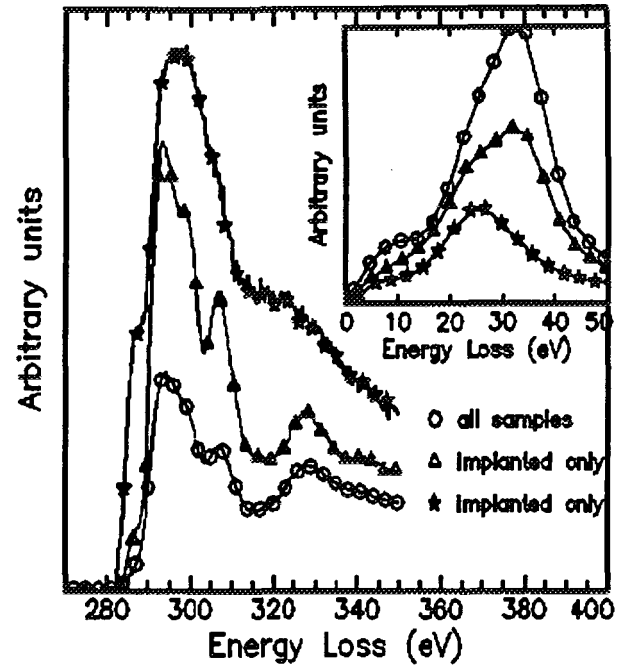


**Figure 2.** Electron energy loss spectra in the K-edge region with the corresponding processed low loss spectra inset for the unimplanted and implanted samples. Both spectra  $\Delta$  and  $\star$  were observed only in the damaged areas of the implanted samples while spectrum  $o$  is typical for both unirradiated and the undamaged regions of the irradiated samples.

Spectrum	Material	$\pi-\pi^*$ peak	$E_p/\sqrt{2}$	$E_p$	$1s-\pi^*$ peak	$1s-\sigma^*$ edge
	graphite	$7^L$	$20^L$	$26^L$	$286^B$	$292^B$
	a:C	$5^B$	-	$24^B$	$285^B$	$291^B$
	diamond	-	$23^E$	$33^E$	-	$290^E$
	a:D	$5^B$	-	$30^B$	$287^B$	$290^B$
spectrum $o$	diamond	-	23	33	-	291
spectrum $\Delta$	a:D	-	23	33	286	291
spectrum $\star$	graphite	$6(?)$	-	26	286	291

**Table 1.** A list of the peak positions (eV) of the major features for graphite, amorphous carbon (a:C), diamond and amorphous diamond (a:D), together with those from Figure 2. The references are B : Berger et al. [6], E : Egerton et al. [5] and L : Lurie et al. [7].

## B. TEM

Figure 1 show a HRTEM lattice image of the sample implanted with  $1 \times 10^{14}$  Xe/cm<sup>2</sup>, with its diffraction pattern inset. Whilst the TEM image shows that much of the crystallinity of the irradiated samples is retained, large amorphous regions are observed in other areas of the samples as well. This indicates that ion beam induced damage is rather inhomogeneous. The unimplanted sample show similar lattice images as Figure 1, but with no amorphous rings visible

in the diffraction patterns. Large amorphous regions are also not observed in the unimplanted sample.

The density of dislocations, being the predominant defects in all the samples, was not found to increase significantly with increasing dose. However, the density of the amorphous regions were observed to increase with irradiation dose. As the implanted dosage increases, the crystalline areas were also found to be more susceptible to electron beam damage during TEM analysis due to the presence of already damaged bonds. The inhomogeneity of the distribution of amorphous areas in the implanted samples could be due to the inhomogeneously scattered dislocation defects. The diffraction patterns showed an increase in diffuse scattering with increasing dose, with amorphous diamond rings also being observed. Although the amorphous zones could be an artifact of the IBT process during sample preparation, it must be noted that they were observed in the implanted samples only.

### C. EELS

Figure 2 shows the K-edge spectra for the irradiated and unirradiated samples, with the low-loss energy spectra inset. The major features of the spectra are listed in Table 1, together with various forms of carbon from other references. The low-loss spectra for all samples also show a shoulder at ~9 eV, which has been associated with the onset of the conduction-band edge in diamond [5]. The 23 eV peak may be associated with the 33 eV peak through the  $\hbar\omega_p/2\pi\sqrt{2}$  surface plasmon relation. Alternatively, it could be due to the presence of an amorphous carbon layer, produced during IBT or from the electron beam.

The 26 eV s-p plasmon peak and ~286 eV p-peak are attributed to ion implantation as they were not observed in the unimplanted sample. There appears to be a small peak at ~6 eV, which could only be discerned in the processed data; attributed to the  $\pi-\pi^*$  peak, although it may also be due to an artifact arising from the zero-loss peak removal. The electron diffraction patterns from such areas also show faint amorphous diamond rings.

### 4. SUMMARY

Surprisingly, destruction of the diamond structure due to ion irradiation occurs only to a small extent even when the dose exceeds that above which large increases in the electrical conductivity are observed. Amorphous diamond and graphitic zones are observed in the TEM and EELS spectra following irradiation, but are inhomogeneously distributed throughout the implanted volume. The non-diamond spectra observed here are broad, unlike the expected sharp K-edge spectra of graphite. Evidence of crystalline diamond is not surprising, as, even at high doses ( $>10^{15}$  Xe/cm<sup>2</sup>) the resistance of diamond saturates at a value of  $\sim 10^5 \Omega$ , which is much higher than that expected from a fully graphitized layer. This makes it difficult at this stage to compare quantitatively between the EELS, TEM and the electrical conductivity measurements. Further analysis using convergent beam electron diffraction to study very small areas of the samples may provide the quantitative comparison.

### ACKNOWLEDGEMENTS

We would like to thank Prof. R.Kalish for his help in implanting the diamond, and Dr. K.W.Nugent for his help on the Raman spectroscopy.

### REFERENCES

- [1] E.H.Lee, D.M.Hembree, G.R.Rao and L.K.Mansur, Phys. Rev. B48 (1993) 15440
- [2] T.E.Derry, R.A.Spits and J.P.F.Sellschop, Mat. Sc. Eng. B11 (1992) 249
- [3] S.Prawer, A.Hoffman and R.Kalish, Appl. Phys. Lett. 57 (1990) 2187
- [4] S.Dresselhaus and R.Kalish, in : Ion Implantation in Diamond, Graphite and Related Materials (Springer-Verlag, Berlin Heidelberg, 1992)
- [5] R.F.Egerton and M.J.Whelan, Phil. Mag., 30 (1974) 739
- [6] S.D.Berger, D.R.McKenzie and P.J.Martin, Phil. Mag. Lett., 57 (1988) 285
- [7] P.G.Lurie and J.M.Wilson, Surf. Sci. 65 (1977), 476



# ACCURACY of RADIOCARBON ANALYSES at ANTARES

EM Lawson, D Fink, MAC Hotchkis, Q Hua, G Jacobsen, AM Smith, C Tuniz  
ANTARES AMS Centre, Applications of Nuclear Physics, ANSTO,  
Private Mailbag 1 MENAI, NSW 2234

## SUMMARY

Accuracy in AMS measurements, as distinct from precision, requires the application of a number of corrections. Most of these are well known except in extreme circumstances and AMS can deliver radiocarbon results which are both precise and accurate in the 0.5 to 1.0% range. The corrections involved in obtaining final radiocarbon ages are discussed here.

## INTRODUCTION

In  $^{14}\text{C}$  analyses by AMS the isotopic ratio  $^{14}\text{C}/^{12}\text{C}$  (or  $^{14}\text{C}/^{13}\text{C}$ ) is measured for both the unknown and a standard sample. Presently at ANTARES we measure the  $^{14}\text{C}/^{13}\text{C}$  (14/13) ratio. From these two measurements a fraction of modern F (or a percent modern) carbon, and subsequently, a radiocarbon age T are reported via the equations:-

$$F = K \cdot R_{\text{sam}} / R_{\text{std}}$$

and

$$T = - 8033 \cdot \ln F$$

Where  $R_{\text{sam}}$  is the 14/13 ratio from the sample,  $R_{\text{std}}$  the 14/13 ratio from the standard, and K a constant which depends on the particular standard being used.

The efficiencies and transmission factors which determine the 14/13 ratio of sample and standard are subject to both short-term fluctuations, and long-term drifts. For this reason the measurement time, and the time between measurement on sample and measurement on standard, are important. At ANTARES, as at many other AMS laboratories, we employ fast cycling, which allows quasi-simultaneous measurements of  $^{14}\text{C}$  and  $^{13}\text{C}$ . Details of our fast cycling system can be found in the paper by Smith et al. (1994). To counter the precision-reducing effects of the time between sample and standard measurements we normalise our sample using a average value obtained from a bracketting pair of standards. Furthermore, as is pointed out by Hotchkis et al., this procedure is repeated so that the fraction of modern (or percent modern, pMC) is obtained at least three times. The final pMC can therefore be obtained with the required counting statistics and (hopefully) with identical, or at least similar, standard error.

The precision of AMS radiocarbon measurements is usually dominated by counting statistics. At ANTARES it is quite possible to measure samples with a precision of between 0.5 and 1.0 % provided the samples have ages of < 5000 yr and masses of at least one mg carbon.

There are a number of fixed systematic errors, or biases, which must be allowed in order to make the result, not only precise, but also accurate. These errors are removed by making an appropriate correction - which of course needs to be well known. As a rule of thumb it should be noted that a correction of 1% means a change of 80 yrs. The remainder of this paper is devoted to a consideration of the following corrections; dead-time, natural mass fractionation, other mass fractionation effects, accelerator induced background, and chemistry contamination. It is not intended to discuss here corrections which may arise due to natural reservoir effects.

## DEAD-TIME

In our measurements this is estimated by feeding into the detector preamplifier the signal from a pulser operating at 10 Hz. The pulser signal is also fed directly into a scaler. A comparison with the count rates - direct and indirect - allows the deadtime to be estimated. In normal circumstances with a  $^{14}\text{C}$  count rate of 100 to 200 cps the dead time is typically about 0.5 % and a small, but significant, correction. However, because of our selection of the  $^{14}\text{C}^{4+}$  charge state after the stripper-foil we find that lithium in the target can occasionally lead to unacceptably high dead times. A singly

charged di-molecule of  ${}^7\text{Li}$  is indistinguishable from  ${}^{14}\text{C}^-$  as far as the stripper-foil. After the foil we find a high probability that at least one of the component  ${}^7\text{Li}^{2+}$  will reach the detector and a significant probability that a pair will enter the detector at the same time. These events can be easily discriminated from the  ${}^{14}\text{C}$  events. However, the dead-time in exceptional circumstances can become greater than 10 %. The Li is considered to come from the silica-ware used in the graphitisation process. In the ANTARES chemistry laboratories we use Vycor glassware which does not introduce any Li. However, we find that samples prepared at other laboratories may sometimes contain lithium. The dead-time correction is not reliable above 5% (400 yrs) and no good estimate of age can be given.

#### NATURAL MASS FRACTIONATION EFFECTS

In nature, mass fractionation can occur in chemical reactions and mass-dependent physical processes (such as evaporation, condensation and diffusion). Corrections for mass fractionation are expressed in terms of the parameter  $\delta^{13}\text{C}$ . Corrections are normalised to a reference value of  $\delta^{13}\text{C} = -25$  o/oo. In the situation where the 14/13 ratio is being measured the natural mass fractionation correction involves multiplication of the fraction of modern by the factor

$$(1 - 25/1000)/(1 + \delta^{13}\text{C})$$

Measurements of  $\delta^{13}\text{C}$  are made on conventional mass spectrometers on a second portion of the sample. Usually a small fraction of the  $\text{CO}_2$  produced on combustion is used for this measurement. The value of the natural, or environmental,  $\delta^{13}\text{C}$  for a sample is generally found to lie in the range +1 to -27 o/oo and different materials have typical values. For example, charcoal typically has a  $\delta^{13}\text{C}$  value of  $-25 \pm 2$ , bone collagen  $-20 \pm 2$ , and bone apatite  $-10 \pm 2$  (all in o/oo). So if measured values are not available, a literature will usually provide an age which is a good approximation to the correct value. For most samples the correction amounts to about 2.5 % (200 yrs) at most. The table below shows the effect of the natural  $\delta^{13}\text{C}$  correction. The percent modern carbon is denoted by pMC.

OZ No	Collaborator	Sample Type	pMC (uncorr)	Age (uncorr) yrs BP	$\delta^{13}\text{C}$ per mil	pMC (corr)	Age (corr) yrs BP
OZB098	Sedwick	marine sed.	74.46	2369	-24.20	74.40	2376
OZB527	De Deckker	ostracod	3.83	26206	0.76	3.73	26418
OZB653	Pessina	apatite	37.52	7875	-10.0	36.95	7998
OZA848	Grave	collagen	72.09	2629	-20.0	71.72	2670

#### OTHER MASS FRACTIONATION EFFECTS

Mass fractionation may occur at the source, and in the stripping process. At the source the fractionation can be a function of ion-current, cratering in the cathode, and space-charge. These effects can be minimised but in any case tend to cancel out on normalisation provided the standard and sample are run under similar conditions. A measurement of  $\delta^{13}\text{C}$  at the accelerator will allow a better control of these fractionation effects. We are presently setting up to make this measurement.

Mass fractionation can also occur during the chemistry stages - in particular during graphitisation.. Although the conditions for complete graphitisation are fairly well established these do not readily apply to very small (< 500  $\mu\text{g}$ ) samples. Fractionation occurs when graphitisation is incomplete and the degree of fractionation increases as the mass decreases.

#### ACCELERATOR INDUCED BACKGROUND

Due to cross-talk or accumulated carbon deposits close to the sample position background may originate at the the ion source even when there is no graphite loaded into the cathode. Even with a  ${}^{14}\text{C}$ -free sample events may be detected. These are usually due to  ${}^{13}\text{C}$  (or  ${}^{12}\text{C}$ ) being scattered into the detector and misidentified as  ${}^{14}\text{C}$ . Scattering will be a function of vacuum, terminal stability, beam line alignment, etc. The sum of these two components is the effective residual accelerator-related background which dermines the limiting sensitivity of the system. At ANTARES we find a best sensitivity of 0.013 pMC (72,000 yrs) and the associated correction is negligible. However, this best sensitivity can only be maintained by constant attention to detail. This background always needs to be assessed and the correction applied if necessary.

#### CHEMISTRY BACKGROUND

When the sample is subject to combustion, hydrolysis and graphitisation, it acquires an amount of contamination typical of the particular process(es). This contamination can be determined by measurement of blank ( ${}^{14}\text{C}$ -free) materials such as mineral graphite, marble and old  $\text{CO}_2$ . The assumption of constant contamination mass has been confirmed by experiment. We typically find between 2 and 5  $\mu\text{g}$  of modern carbon (between 43 and 50 kyrs BP for a 1 mg blank). We correct for the background in the manner described by Donahue et al. (1990). This correction has little

effect for young, near-modern samples, but for old samples can be very significant. In certain conditions the age after correction can be older than the blank. For example, for a shell sample, we have found 0.27 pMC (after correction for natural fractionation) and a blank of 0.17 pMC. The background corrected value is 0.10 pMC (or 55,000 yrs BP). Sample masses are determined from measurements of pressure. For old and very small (< 0.2 mg, say) samples the fractional mass error may become very significant, and carry through into, and even dominate, the final result.

## **CONCLUSIONS**

Most corrections are well known except in extreme circumstances and AMS can deliver dates which are both precise and accurate in the 0.5 to 1.0% range. However, it should be noted that as AMS has developed over the years there have been efforts to date materials where less than 100  $\mu\text{g}$  of carbon is available. As noted previously there are often additional, less well known corrections in this extreme region. As samples get smaller the determination of their mass becomes increasingly more difficult and uncertain, with the result that the correction for background is less well known. Furthermore, the efficiency of the graphitisation process can drop below 100% with a related change in fractionation. This fractionation change is not well known but can be as large as a few percent in extreme circumstances. Measurements of  $\delta^{13}\text{C}$  with the AMS system should determine this correction accurately.

## **BIBLIOGRAPHY**

Smith, AM, Fink, D, Hotchkis, MAC, Jacobsen, GE, Lawson, EM, Shying, M, Tuniz, C, Watt, GC, Fallon, J, and Ellis, PJ, (1994) *Nuclear Instrum. and Methods B92*, 122-128.

Hotchkis, MAC, Fink, D, Hua, Q, Jacobsen, G, Lawson, EM, Smith, AM, and Tuniz, C, presented at the 4th European Conference on Accelerators in Applied Research and Technology, Zurich, Sept 1995; to be published in *Nuclear Instrum. and Methods B*.

Donahue, DJ, Linick, TW, and Jull, AJT, (1990) *Radiocarbon Vol 32 No 2*, 135-142.



# The ANTARES Recoil Time-of-Flight Spectrometer

J. W. MARTIN <sup>a</sup>, D. D. COHEN <sup>b</sup>, N. DYTLEWSKI <sup>b</sup> and G. J. RUSSELL <sup>a</sup>

<sup>a</sup> School of Physics, University of NSW, Sydney 2052.

<sup>b</sup> Australian Nuclear Science and Technology Organisation, PMB 1 Menai NSW 2234.

## ABSTRACT

The Australian National Tandem for Applied Research (ANTARES), is a 8MV FN tandem particle accelerator at the Australian Nuclear Science and Technology Organisation. Research on the accelerator is divided between two groups, Accelerator Mass Spectrometry (AMS) and Ion Beam Analysis (IBA). The IBA group carries out a range of research projects from nuclear physics to materials characterisation. The major IBA project on the accelerator is a recoil time-of-flight spectrometer which consists of two electrostatic time pulse generators and an ion-implanted surface barrier detector. The spectrometer is ideally suited to the profiling of layered multi-element materials, and has been used to characterise materials such as metal-germanides, optoelectronics, superconductors and catalytic converters. This paper will describe the time-of-flight system as well as some recent materials characterisation results.

## 1. INTRODUCTION

Accelerator-based ion beam analytical techniques have progressed rapidly in the last 20 years or so. The range of techniques available through these dedicated laboratories is ever increasing, such that now there is usually a specialised technique for a particular materials characterisation problem. These include particle induced x-ray emission (PIXE) for bulk ( $< 50 \mu\text{m}$ ) compositional determination, Rutherford backscattering spectroscopy (RBS) for elemental depth profiling of heavy elements, and nuclear reaction analysis (NRA) for isotope studies. A relatively new technique is that of recoil time-of-flight spectroscopy (TOF-RS), which has the ability to profile a layered multi-elemental materials. In comparison with RBS, TOF-RS has the unique ability to profile light elements in heavy substrates which has been unavailable through other accelerator based materials characterisation techniques. This is achieved through the simultaneous determination of a recoiled particles time-of-flight and energy. Such a spectrometer has been constructed on the 8 MV tandem accelerator at the Australian Nuclear Science and Technology Organisation.

## 2. RECOIL SPECTROMETRY

The recoil spectrometer is attached to the ion beam analysis chamber on the 8 MV tandem particle accelerator. The analysis chamber is multi-purpose with a  $360^\circ$  rotatable surface barrier detector, ports positioned at every  $22.5^\circ$ , and a 10 position sample holder attached to multi-parameter goniometer. Beam definition is by way of a 4-way slit system in which beam spot sizes down to  $2 \text{ mm}^2$  are possible. Ion beams from the accelerator vary from 4 MeV H to  $100+$  MeV  $^{127}\text{I}$ . The recoil time-of-flight spectrometer is positioned at  $45^\circ$  to the straight through and houses two time pulse generators and an ion implanted surface barrier detector subtending a solid angle of  $0.1 \text{ msr}$ . The flight length is nominally 495 mm. From previous resolution studies on TOF-RS [1], it has been shown that heavy high energy ion beams give the best resolution. For this reason  $70+$  MeV  $^{127}\text{I}$  is used for most experimental runs. Sample run times are usually between 15-30 mins.

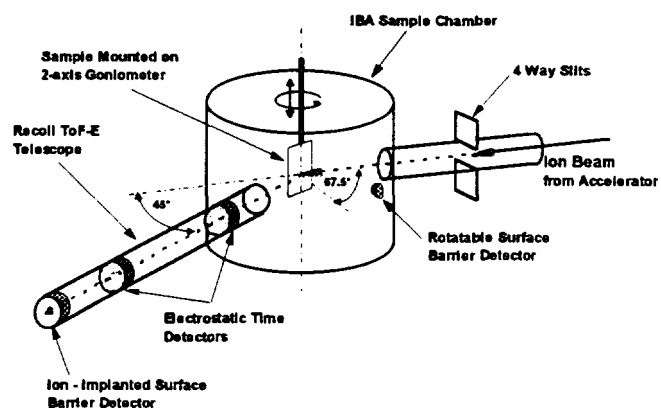


Figure 1. Time-of-Flight Beamline

The two electrostatic time pulse generators produce a fast timing pulse after the passage of a recoil. The operation of the time pulse generators is schematically represented in Fig. 2, such that when a recoil passes through a thin carbon foil ( $25 \mu\text{g}/\text{cm}^2$ ), the resulting secondary electrons are directed towards a set of micro-channel plates. The positioning of the accelerating electrodes ensure that the secondary electrons follow an isochronous parabolic path.

Upon determining the time-of-flight and energy of a recoil the simple non-relativistic transformation in equation 1 is used for the mass determination.

$$M = 2E\left(\frac{t}{l}\right)^2 \quad (1)$$

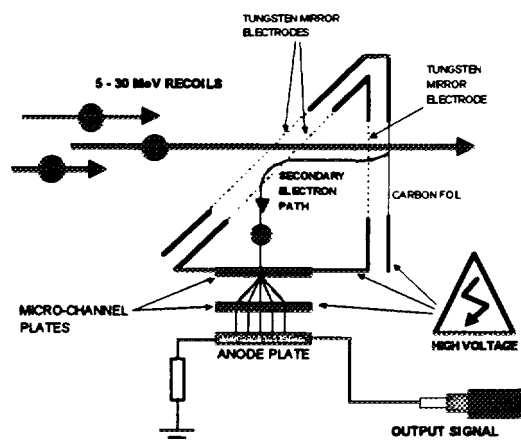


Figure 2  
Electron Mirror Time Detector

### 3. EXPERIMENTAL APPLICATION

In essence, the recoil spectrometer provides two simultaneous signals that are recorded, time and energy. To illustrate the operation of the spectrometer, a sample of a thin Cu film on teflon ( $\text{CF}_2$ ), which is used in the study of metallised polymers, is shown in Fig. 3. In the top left of the figure the spectrum from the energy detector is shown. The main features of this are the front edge at channel 2500 corresponding to the surface of the sample, and an edge at channel 500. One would speculate from this that there were two elements in this material. Similarly if we look at the signal from the time-of-flight, we get the spectrum shown in the top right of the figure. This shows a peak centred on channel 3000 and then a long tail. Again one might suggest that there was only one element present. Both these spectra are hard to unambiguously analyse due to the convolution of the signals from the different elements within the material. If we plot time-of-flight versus energy the resulting 2-dimensional spectrum is that shown in the centre of Fig. 3. There is clearly three distinct structures (curves), with each of these corresponding to a different element. They are curved due to the relation between energy and time being quadratic. The intensity of the curve is directly related to the atomic abundance within the material. In this case the lower curve is the Cu film, whereas the upper two curves correspond to C and F respectively, from the teflon substrate.

We can go further by using software to appropriately remove each curve and look at it separately. This is achieved using the software, Physics Analysis Workstation (PAW) written by the CERN group. Each curve is removed by placing a polygonal box around it. We can then project this onto the energy axis and as such will have an energy profile for that element. This is shown in the three lower spectra of Fig. 3 where the individual profiles for C, F and Cu are shown respectively. The thickness of the film can be estimated from the Cu profile, as well as diffusion across the polymer interface. The composition of the teflon and interfacial region can also be calculated. This simple example illustrates the power of the TOF-RS technique to individually profile multi-elemental layered materials.

### 4. CONCLUSION

A recoil time-of-flight spectrometer has been constructed on the tandem accelerator at the Australian Nuclear Science and Technology Organisation. The spectrometer consists of two time pulse generators and a surface barrier detector. The spectrometer is ideally suited to characterisation layered multi-elemental materials. Its experimental application has been shown by way of the analysis of a thin Cu film on teflon ( $\text{CF}_2$ ) in which the three elemental profiles (C, F and Cu) can be individually obtained for unambiguous sample characterisation.

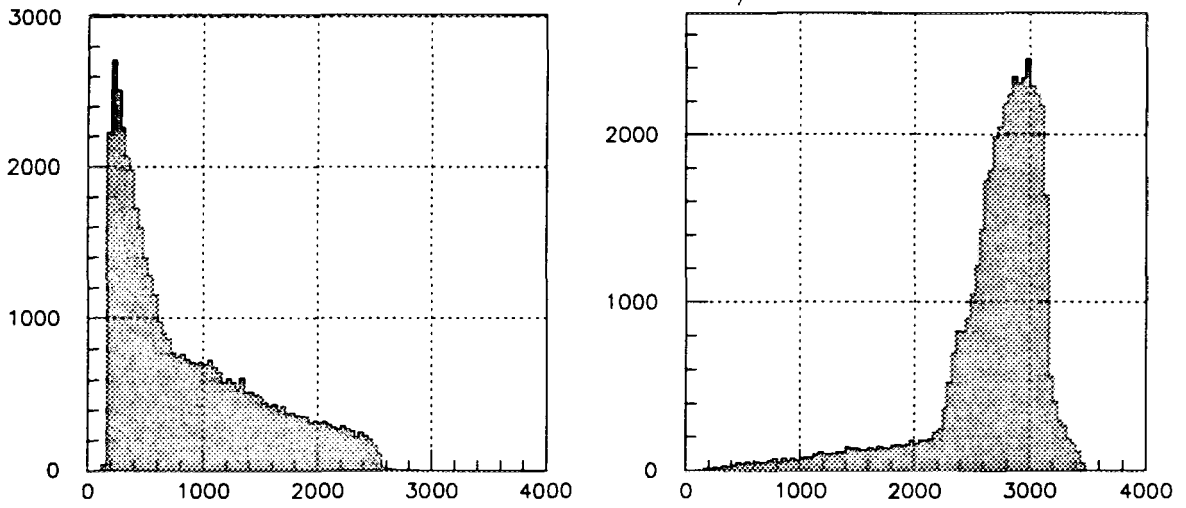
### ACKNOWLEDGMENTS

The support from the Australian Institute of Nuclear Science and Engineering for the entirety of this project is gratefully acknowledged.

### REFERENCES

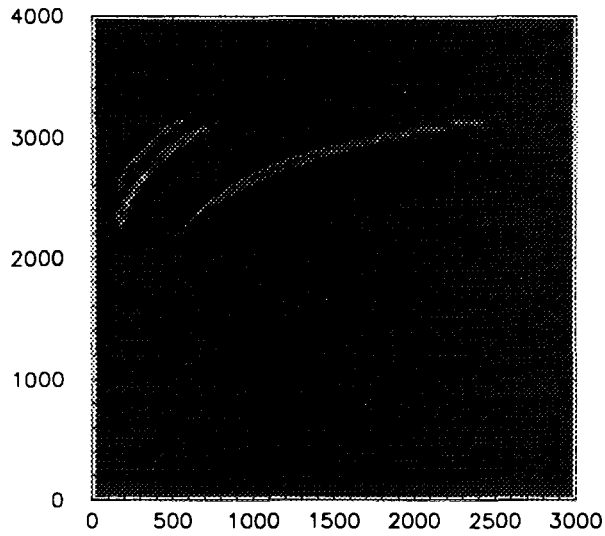
- [1] J. W. Martin, D. D. Cohen, N. Dytlewski, D. B. Garton, H. J. Whiltow and G. J. Russell, Nucl. Instr. and Meth. B 94 (1994) 277-290.

Figure 3. Recoil Time-of-Flight Spectra for a Cu thin film on teflon (CF<sub>2</sub>).

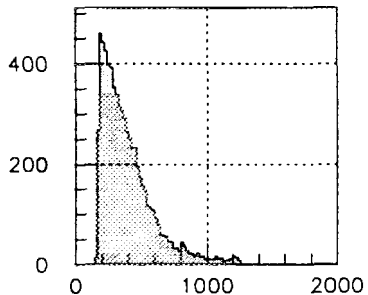


Energy

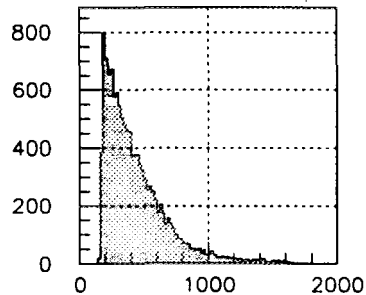
Time



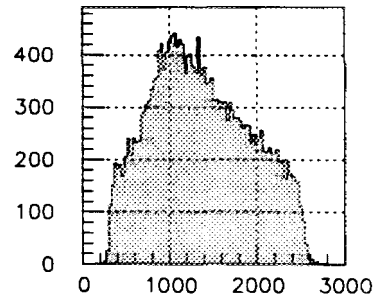
Time vs Energy



C



F



Cu



# Structural investigation of two carbon nitride solids produced by cathodic arc deposition and nitrogen implantation.

A.R.MERCHANT<sup>†</sup> (1), D.G.McCULLOCH (1),  
D.R.McKENZIE (2), Y.YIN (2) and E.G.GERSTNER (2).

(1) Electron Microscope Unit, University of Sydney, NSW, 2006, Australia

(2) School of Physics, University of Sydney, NSW, 2006, Australia.

## SUMMARY

Carbon nitride materials have been the focus of research efforts worldwide. Most materials studied have been amorphous, with only a few groups claiming to have found a crystalline material. In this paper, carbon nitride materials prepared by two different techniques are analysed, and found to be remarkably similar in bonding and structure. The materials appear to have a primarily  $sp^2$  bonded carbon structure with a lower bond length than found in an amorphous carbon. This is explained by nitrogen substituting into 'rings' to a saturation level of about one nitrogen per three carbon atoms. We found no evidence for a crystalline structure of formula  $C_3N_4$ , or any amorphous derivative of it.

## I. INTRODUCTION

Carbon nitride materials containing varying nitrogen concentrations have been reported using various deposition techniques [1-4]. *Ab initio* theoretical calculations by Liu *et al.* [5] proposed a crystalline material  $\beta$ - $C_3N_4$  with a structure similar to  $\beta$ - $Si_3N_4$ , but having a bulk modulus predicted to be greater than that of diamond. Subsequent refinements of this structure have predicted other possible crystalline forms [6,7]. To our knowledge only two reports have been made claiming to observe small crystallites of  $\beta$ - $C_3N_4$  [8,9].

In this paper we present analysis of carbon nitride materials produced by two separate techniques: unfiltered cathodic arc deposition and implantation of glassy carbon with 50keV nitrogen ions. Ion implantation provides a means of studying the solubility limit of nitrogen in carbon under non-equilibrium conditions. Transmission Electron Microscopy (TEM), Electron Energy Loss Spectroscopy (EELS), energy filtered electron diffraction and Infra-Red (IR) Spectroscopy are all used to derive structural information. The results from these experiments and the validity of various structural models is discussed. A new structural model for carbon nitride alloys is proposed.

## II. EXPERIMENTAL

### Carbon Nitride Deposition

Carbon nitride films were deposited using an unfiltered cathodic arc onto clean glass substrates using carbon targets in a nitrogen ambient atmosphere. Chamber pressures of 20mTorr and 50mTorr were used to deposit two different CN films named CN-20mTorr and CN-50mTorr respectively. At these pressures, the arc behaves as a low energy ion assisted deposition system. In all cases graphite targets of 99.9% (or better) purity were used. For comparative purposes a carbon film (henceforth referred to as a-C) was also deposited using argon as the ambient inert gas. Specimens for TEM were prepared by floating glass substrates in de-ionised water.

### Nitrogen implantation into carbon

Glassy carbon substrates in the form of plates were obtained from Atomergic Chemetals Corp. (New York). According to the manufacturers specifications, these have been heat treated to a temperature of 2500°C. The subsequent material has a density of 1.5 g/cm<sup>3</sup>. Prior to

implantation, these glassy carbon substrates were polished to a mirror finish. The polished substrates were then implanted with 50keV  $N^+$  ions to doses up to  $1 \times 10^{18}$  N/cm<sup>2</sup>. The implanted glassy carbon samples were prepared is cross section for TEM using ultramicrotomy.

## III. ANALYSIS TECHNIQUES.

### Electron Energy Loss Spectroscopy

EELS spectra were acquired using a Phillips EM430 transmission electron microscope fitted with a GATAN 666 parallel electron energy-loss spectrometer. Using an operating voltage of 200keV, an energy resolution in the energy loss spectra of 1.6eV was achieved. The plasmon energy which is related to the electron density [10], was determined by analysing the low-loss region (0-100eV). Measurements of the [N]/[C] ratios were made using the k-edge features at 285eV and 400eV for carbon and nitrogen respectively.

### Spectroscopy

The cathodic arc deposited samples were prepared for IR spectroscopy by mixing the material into KCl and compressing. The IR spectrum was collected used a Shimadzu IR-470 Spectrometer.

### Energy Filtered Electron Diffraction

A useful technique for determining the structure of amorphous or polycrystalline materials is the calculation of the reduced density function (RDF) from energy filtered diffraction patterns [11]. The RDF, denoted  $G(r)$ , gives information on nearest neighbour (NN) distances and average bond angles.

## IV. RESULTS & DISCUSSION.

### Cathodic Arc Deposited Films

Except for the presence of graphite macroparticles, the CN films deposited in the cathodic arc were featureless in the TEM. The diffraction patterns were typical of amorphous materials and no crystallinity was found.

Figures 1 and 2 show the carbon and nitrogen EELS K-edges for CN-20mTorr, CN-50mTorr and a-C after background subtraction. The interesting features of the nitrogen and carbon EELS K-edges shown in Fig. 1 and 2 are: (1) the strong  $\pi^*$  feature on both, indicative of  $sp^2$  type bonding and (2) the similarity between N and C K-edges.

<sup>†</sup> Corresponding author: merchant@physics.usyd.edu.au

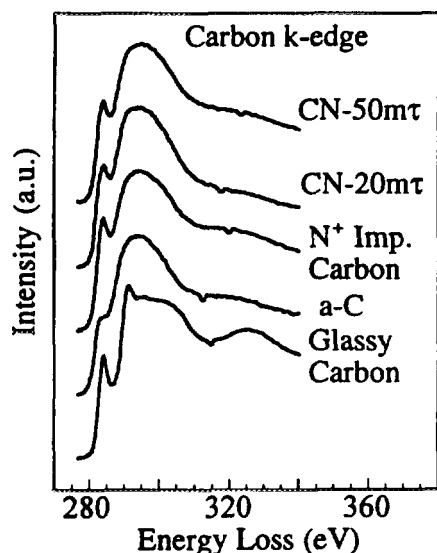


**Figure 1.** The carbon EELS K-edges for (i) glassy carbon, (ii) cathodic arc system deposited a-C with argon ambient, (iii) nitrogen implanted glassy carbon to dose of  $1 \times 10^{18} \text{ N}^+/\text{cm}^2$ , (iv) cathodic arc deposited carbon nitride materials at 20mTorr (CN-20mt) and 50mTorr (CN-50mt).

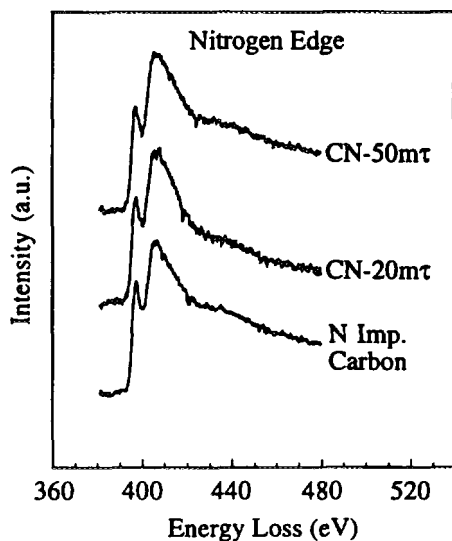


**Figure 2.** The nitrogen EELS K-edges (i) nitrogen implanted glassy carbon to dose of  $1 \times 10^{18} \text{ N}^+/\text{cm}^2$  and (ii) cathodic arc deposited carbon nitride materials at 20mTorr (CN-20mt) and 50mTorr (CN-50mt).

These two facts indicate that the CN material is predominantly  $sp^2$  bonded, and that nitrogen and carbon are in a similar bonding state. Quantitation of the EELS K-edges (listed in Table 1) shows that the nitrogen content increases with nitrogen gas pressure: CN-50mTorr had a  $[N]/[C]$  atomic ratio of  $0.35 \pm 0.05$  whereas the CN-20mTorr was  $(0.25 \pm 0.05)$ .

The IR spectra for the a-C sample (see Figure 2) shows a featureless spectrum except for an absorption peak at  $2325 \text{ cm}^{-1}$  assigned to  $C \equiv C$  stretching. The CN-50mTorr sample shows significant absorption in the  $1200\text{-}1600 \text{ cm}^{-1}$  region and an additional peak at  $2200 \text{ cm}^{-1}$ . It has been pointed out [13] that substituting a N atom in place of a C atom in an  $sp^2$  bonded carbon network will induce strong IR activity in the  $1200\text{-}1600$

$\text{cm}^{-1}$  region. The weak absorption peak at  $2200 \text{ cm}^{-1}$  is attributed to  $C \equiv N$  stretching in nitrile groups [12-14].

Exp Data	$[N]/[C]$ atm. rat.	Plasmon (eV)	1 <sup>st</sup> NN (Å)	Bond Angle
GC	0	24	1.42	$118.4^\circ$
CN-50mt	0.35	23	1.40	$119.6^\circ$
CN-20mt	0.25	24	1.42	$118.4^\circ$
Imp. GC*	0.25	24	-	-
a-C	0	24	1.48	$116.7^\circ$

**Table 1.** Lists the experimentally measured plasmon energy,  $[N]/[C]$  ratio and nearest neighbour for a-C, a  $50 \text{ keV}$  nitrogen ion implanted glassy carbon of dose  $1 \times 10^{18} \text{ N}^+/\text{cm}^2$ , CN-20mTorr, CN-50mTorr and glassy carbon.

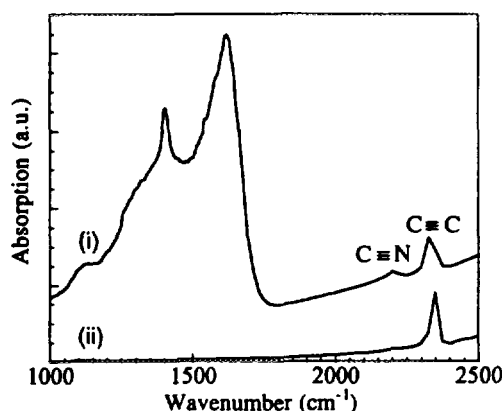


**Figure 3.** Infrared Absorption Spectra of (i) CN-50mTorr and (ii) a-C materials.  $C \equiv C$  and  $C \equiv N$  absorption peaks identified from Han and Feldman [13].

The  $G(r)$  from the a-C sample (Figure 3) shows an increase in the first NN distance ( $1.48 \text{ \AA}$ ) relative to glassy carbon ( $1.42 \text{ \AA}$ ), due to a small proportion of diamond like bonds (bond length  $1.55 \text{ \AA}$ ) and bond angle disorder caused by five and seven membered rings [15]. Compared to a-C, the nitrogen containing materials have a shorter bond length. The bond angle of approximately  $120^\circ$  is very close to the angle expected for  $sp^2$  bonded hexagonal layers.

#### Nitrogen Implanted glassy carbon

Figures 1 and 2 show the carbon and nitrogen EELS K-edges from the glassy carbon sample implanted to a dose of  $1 \times 10^{18} \text{ N}^+/\text{cm}^2$ . The shapes of both C and N edges in the implanted glassy carbon sample and arc deposited materials are almost identical, strongly suggesting a similar bonding configuration. The  $[N]/[C]$  ratio for the implanted glassy carbon sample was calculated from the EELS spectra to be  $0.25 \pm 0.05$ .

#### Structural Model:

We have found that the material from the two different deposition methods is remarkably similar: both in bonding and nitrogen content. We propose that the two materials share a common structure in which the nitrogen primarily enters as an in-plane substitution into aromatic rings. Occasional C-N (nitrile) groups are attached as side groups. Evidence from the carbon and nitrogen energy loss shows that the local bonding in both materials is mostly  $sp^2$ .

Additional evidence for  $sp^2$  bonding is provided by the nearest neighbour distances and bond angles determined from  $G(r)$ . The NN distance and IR spectra also indicate that nitrogen substitutes into the  $sp^2$  rings.

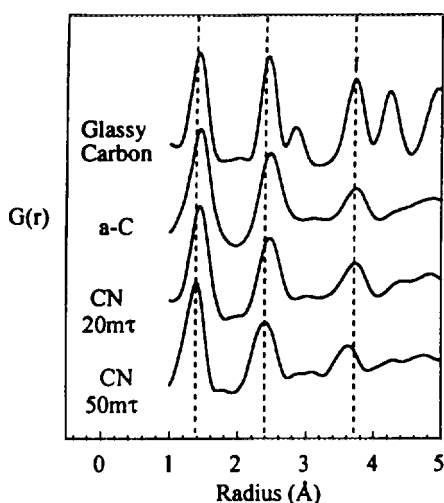


**Figure 4.** Experimentally measured reduced density functions for three cathodic arc deposited materials and glassy carbon.

Figure 5 shows the energy filtered electron diffraction pattern for the a-C and CN-50mτ materials. It can be seen that there is an enhancement of the {002} carbon peak in the carbon nitride material. This is caused by an increased planarity of the carbon nitride material. The presence of nitrogen therefore improves the in-plane ordering as well as reducing the the number of sp<sup>3</sup> bonded carbons.

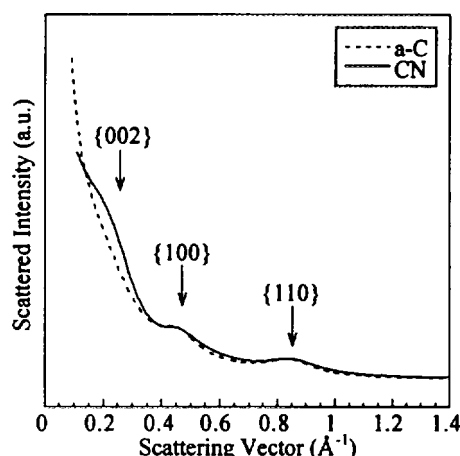


**Figure 5.** Electron scattering intensity of a cathodic arc deposited carbon nitride and amorphous carbon.

These results parallel the findings for CN<sub>x</sub> films deposited by d.c. magnetron sputtering where the CN<sub>x</sub> structure was also found to be mainly sp<sup>2</sup> bonded, with the nitrogen is substituting into carbon lattice sites [16].

The observed atomic ratio of nitrogen of about 0.3 is expected for the above structural model of nitrogen substituting into rings, as sp<sup>2</sup> bonded carbon rings with greater than two nitrogen atoms per ring will then be rare. In any case, each nitrogen atom substituting into an sp<sup>2</sup> ring removes one bond between that ring and the local environment by the formation of a lone pair. Rings containing excess nitrogen atoms are likely to be volatile and therefore readily lost from the network.

#### V. CONCLUSIONS:

The above structural model views the carbon nitride network as being closer in structure to glassy carbon than a-C because it has a lower density and a greater amount of planarity.

The CN material is predominantly an sp<sup>2</sup> network, but with variable ring size and a smaller sp<sup>3</sup> residual than a-C. We have found no evidence for a crystalline structure of C<sub>3</sub>N<sub>4</sub>, nor an amorphous derivative of it.

#### ACKNOWLEDGEMENTS:

This work was supported by a Commonwealth Grant through the Australian Research Council. We would also like to thank Mike Lenny and Ron Cissold from CSIRO Division of Applied Physics for implanting the glassy carbon samples used in this study.

#### REFERENCES:

1. T.Sekine, H.Kanda, Y.Bando, M.Yokoyama and K.Hojou, (1990) "A graphitic carbon nitride", *J. of Mat.Sci.Lett.* Vol.9, 1376-1378.
2. J.F.D. Chubaci, T.Sakai, T.Yamamoto, K.Ogata, A.Ebe and F.Fujimoto,(1993), "Properties of carbon nitride thin films prepared by ion and vapour deposition", *NIM B* **80/81** 463-466.
3. D.Marton, K.J.Boyd, A.H.Al-Bayati, S.S.Todorov and J.W.Rabalais, (1994) , "Carbon Nitride Deposited Using Energetic Species: A Two Phase System", *Phys. Review Letters* **73**, 118-121.
4. C.A.Davis, D.R.McKenzie, Y.Yin, E.Kravtchinskaia, G.A.J. Amaratunga and V.S.Veerasingam,(1994) "Substitutional nitrogen doping of tetrahedral amorphous carbon", *Phil.Mag.B* **69**, 1133-1140.
5. A.Y.Liu and M.L.Cohen, (1990) "Structural properties and electronic structure of low-compressibility materials: β-Si<sub>3</sub>N<sub>4</sub> and β-C<sub>3</sub>N<sub>4</sub>", *Physical Review B* **41**, 10727-10734.
6. A.Y.Liu and R.M.Wentzcovitch, (1994) "Stability of carbon nitride solids", *Physical Review B* **50**, 10362-10365
7. Y.Guo and W.A.Goddard, (1995) "Is carbon nitride harder than diamond? No, but its girth increases when stretched (negative poisson ratio)", *Chemical Physics Letters* **237**, 72-76.
8. C.Niu, Y.Z.Lu and C.M.Leiber, (1993) "Experimental Realization of the Covalent Solid Carbon Nitride", *Science* **261**, 334-337.
9. K.M.Yu, M.L.Cohen, E.E.Haller, W.L.Hansen, A.Y.Liu and I.C.Wu. (1994) "Observation of crystalline C<sub>3</sub>N<sub>4</sub>", *Physical Review B* **49**, 5034-5037.
10. R.F.Egerton '*Electron Energy Loss Spectroscopy in the Electron Microscope*' 1986 (Plenum Press New York).
11. D.Cockayne and D.R.McKenzie (1988) "Electron Diffraction of Polycrystalline and Amorphous Thin Films", *Acta. Crystallographica*, **A44**, 870-878.
12. S.D.Berger, D.R.McKenzie and P.J.Martin, (1988) "EELS analysis of vacuum arc-deposited diamond-like films", *Philosophical Magazine Letters* **57**, 285.
13. H.X.Han and B.J.Feldman. (1988) "Structural and optical properties of amorphous carbon nitride", *Solid State Communications* **65**, 921-923.
14. J.H.Kaufman,S.Metin and D.D.Saperstein. (1989) "Symetry breaking in nitrogen doped amorphous carbon: Infrared observation of the Raman-active G and D bands", *Physical Review B* **39**, 13053-13060.
15. K.Ogata, J.F.D.Chubaci and F.Fujimoto, (1994) "Properties of carbon nitride films with composition ratios C/N=0.5 -3.0 prepared by ion and vapour deposition method", *J.App.Physics* **76**, 3791-3796.
16. D.G.McCulloch, E.G.Gerstner, D.R.McKenzie, S.Prawer and R.Kalish, (1995) "Ion implantation into tetrahedral amorphous carbon", *Physical Review B* **52**, 850-857.



# A Study of the Distribution of Rare-Metals in Kuroko-Type Ore.

S.MURAO<sup>1,2</sup>, S.H. SIE<sup>1</sup> and G.F. SUTER<sup>1</sup>

<sup>1</sup>CSIRO Exploration and Mining, P.O. Box 136, North Ryde, NSW 2113, Australia

<sup>2</sup>Geological Survey of Japan, 1-1-3 Higashi, Tsukuba 305, Japan

## SUMMARY

We have performed PIXE analysis of kuroko-type ore from the JADE hydrothermal site of the Okinawa Trough, Japan using the proton microprobe (PIXEPROBE). We analysed five kinds of ores dredged from the sea floor: (1) barite ore with small sulfide dissemination; (2) sphalerite-pyrite chimney; (3) pyrite ore; (4) sulfide veinlets in strongly altered rock; and (5) pyrite megacrystals in strongly altered rock. The analyses revealed that the trace element distribution is regulated by the occurrence mode of the ore, and within each ore, by the crystal structure. The distribution suggests that the hydrothermal system for kuroko ore formation is quite heterogeneous and its chemistry is controlled by local factors such as difference in temperature, and that in-situ PIXE analyses are essential for effective beneficiation strategy for the rare-metals from kuroko-type ore.

## 1. INTRODUCTION

The Japanese word "kuroko (black ore)" is used to describe massive sulfide deposits which are associated with calc-alkaline acid volcanism. The type locality is the Hokuroku district, northern part of Japan, where intense Miocene volcanism is accompanied by kuroko and vein type deposits. The kuroko ore, mainly composed of lead, zinc, copper and barium minerals, carries trace elements (e.g., Au, Ag, In, Bi, Ga, Ge and Tl) useful for high-technology and medical industry applications [1,2]. Many of these trace elements occur at low levels not amenable to electron microprobe analysis. The lack of information on trace elements which exist at the order of ppm to ppb has prevented the mining industry from establishing a beneficiation strategy for rare metals. We have thus performed a proton microprobe study of the modern analogue of kuroko ore to determine the distribution of these useful elements in this type of ore.

A specimen from an active hydrothermal site in the Okinawa Trough was used for this research because Miocene kuroko proper preserves neither the original structure and texture, nor the initial distribution of elements due to the alteration and metamorphism.

## 2. OKINAWA TROUGH

The Okinawa Trough is a tectonically active intercontinental back-arc basin generated by the subduction of the Philippine plate under the Eurasian continent [3,4]. It lies between the Ryukyu islands and trench to the southeast, and the East China Sea to the northwest and it is the only back-arc basin along a continental margin in the world that shows rifting. Hemipelagic unconsolidated silty clays of Holocene age cover the sea floor and have a maximum thickness of some 20 to 30m [5].

Rifting and volcanism in the Okinawa Trough back-arc basin gave rise to the formation of holes of hydrothermal fields. One of these, named the Izena cauldron, lies 110km northwest of the Okinawa Island, with NNW-SSE axis of 6km and ENE-WSW axis of 3km. The ENE-WSW is the direction of normal faults in this area. The JADE hydrothermal site at ca. 27°15'N and 127°04.5'E is one of a number of sites found in 1988 along the northeastern slope of the Izena cauldron and Iheya deep of the Middle Okinawa Trough. The specimens for the present study were recovered from this site. The temperature of a black smoker fluid was measured to be 320 °C [8] and pH = 4.7 [5]. In addition to the black smoker, chimneys and mounds that are emitting clear solution up to 220 °C are also present [5]. The maximum depth of the Izena cauldron is 1665m and the bottom is covered with muddy sediments and white clay, comprised of magnesian chlorite, aluminian chlorite, halloysite and kaolinite [6]. The walls of the cauldron are composed of tuff, tuff breccia, tuff rich woody pumice and mudstone consistent with a volcanic activity, which is considered to have occurred after middle Pleistocene [7].

## 3. ORE SAMPLES

The ore samples dredged from the trough for this research are barite ore, barite-bearing massive sulfide (mainly sphalerite and pyrite), pyrite ore, sulfide stringer in strongly altered rock, and pyrite megacrystals in strongly altered rock. They are rich in Ag [8], As [5] and Tl [2]. The gold content reaches 24.4µg/g in the "replacement ore"

where pyrrhotite, chalcopyrite, marcasite and pyrite replace previous ores such as sphalerite and galena [5].

The barite ores were recovered as fragments of irregular shapes. They do not seem to create chimney. Sometimes they exhibit zonality from the rim inward: barite zone and barite-sulfide zones. The barite zone contains olive green clay, barite, orpiment, realgar, amorphous silica and rarely opal. Barite is predominant and makes rosette or prismatic single shape up to 30 x 400 $\mu$ m. The rosette is much more common than prismatic habit.

The sulfide chimney contains mainly pyrite and sphalerite-pyrite ores. In the pyrite ore, the pyrite exhibits pseudomorph of barite or subhedral to euhedral character. Barite is replaced along cleavages or replaced completely. Small amount of sphalerite coexists with anhedral pyrite. Sphalerite contains isocubanite/chalcopyrite dusts. In the sphalerite-pyrite ore, sphalerite and pyrite are common while galena, orpiment and anglesite are noticed rarely. Pyrite exhibits framboid, incomplete sphere, colloform, subhedral to euhedral habits and partial replacement of barite.

The sulfide network is the stringer veins in strongly altered gray host rock which contains quartz, cristobalite, and mica/montmorillonite mixed layer minerals [2,5]. The original rock type cannot be identified. Sphalerite is common, having colourless, pale brown or pale orange character. Neither isocubanite nor chalcopyrite are included in the sphalerite. Tennantite, pyrite, chalcopyrite and galena are also found. Pyrite is sub to euhedral and no framboids are seen. Pyrite euhedral crystals are developed up to megacrystals of a few millimeters size in strongly altered gray rock. It is different from the sulfide network in occurrence mode and mineral assemblage: this ore does not carry any sphalerite or galena and does not develop veinlets.

#### 4. PIXEPROBE ANALYSES

The samples were analysed by PIXE using the CSIRO proton microprobe [9]. The 3 MeV microbeam of protons was focused to between 5 and 15  $\mu$ m, depending on the size of the grains analysed. X-rays were detected in a Si(Li) detector at 135° angle with respect to the beam direction, at 25 mm distance from the target, through a filter. For barite analysis, a 200  $\mu$ m thick Al filter was used in most runs. For some, a 125  $\mu$ m Be filter was used to reveal lighter elements. For pyrite and orpiment analyses a 300  $\mu$ m Al filter was used, and for sphalerite 400  $\mu$ m Al. Beam currents between 1 nA to 15 nA were used, and data were collected for 3  $\mu$ C integrated charge per spot analysis. The X-ray spectra were processed with the Geo\_PIXE software [10]. The orpiment grains are typically less than 20  $\mu$ m in dimension and less than 10  $\mu$ m thick, and the data must be corrected for the underlying matrix- usually barite.

A total of 140 spot analyses were carried out on barite (20 analyses), pyrite (30), sphalerite (20), orpiment (20) and an assortment of other minerals (tennantite, veinite, silicates, and realgar). In this paper we only summarise the results for the relatively more abundant sphalerite minerals, the host barite and orpiment. The results for pyrite is given in more detail in tables 1. The minimum detection limit (MDL) values defined at 99% confidence limit are given for the typical spot analysis.

**Barite (BaSO<sub>4</sub>):** Two kinds of barite, a frondescent variety found in the center of rosettes and a transparent clear variety, were analysed. The former exhibits higher concentration of Zn (160-24000 ppm, average 24000) and Pb (620-5000 ppm, avg. 1950), vs. 126 ppm and 296 ppm average respectively in the latter. The latter has higher Cu (0-1470 ppm, avg. 566), As (0-6.4%, avg. 2.08%) and Sb (130-1980 ppm, avg. 1100) vs. 236, 5000 and 1270 ppm average respectively in the rosette samples. Indium is below detection limit (48 ppm) in the frondescent barite, while the rosette carries 0-180 ppm, avg. 89 ppm. Bi content in both samples are similar at 10 ppm average (range 0-27 ppm) close to the detection limit of 12 ppm.

**Sphalerite (ZnS):** Sphalerite shows clear difference in trace element composition depending on the occurrence mode. Sphalerite from barite ore is more rich in As (1910 ppm avg.), Sb (2.79%), Pb (4.2%), Ag (9710 ppm), Hg (3270 ppm), Tl (13 ppm) and Bi (148 ppm) than other ores. Sphalerite from the sulfide chimney is enriched in Cd (4010 ppm) and Sn (744 ppm). Sphalerite from sulfide stringers in strongly altered rock is rich in Ga (91 ppm) and Ge (187 ppm). For all types of sphalerite, Cd and Cu are commonly detected at levels > 1000 ppm. The In and Bi content in the barite ore are 42 ppm and 148 ppm avg. respectively, while in the sphalerite-pyrite ore they are 15 and 11 ppm respectively. The stringer carries In at 47 ppm avg. and Bi is below detection limit.

**Orpiment (As<sub>2</sub>S<sub>3</sub>):** Small inclusions (10-30  $\mu$ m) of orpiment in host barite were analysed with smaller beam (5-10  $\mu$ m) and corrected for contribution from the host matrix. These samples are important because their occurrence mode suggest that their chemical composition can represent the initial conditions of mineralizing fluid for barite ore. The result indicated that orpiment carries Fe (1600-3090 ppm, avg. 2900), Cu (187-555 ppm, avg. 402), Sb (0-4500 ppm, avg. 181), Pb (0.2%-8.6%, avg. 1.58%), Ga (01210 ppm, avg. 254) and Ag (40-8100 ppm, avg. 926) as trace elements.

**Pyrite (FeS<sub>2</sub>):** Four kinds of pyrite show different trace element contents. Pyrite of barite ore (sphere or framboids) has high amount of Ag, Cu, Zn, Pb, Cd, As, and Tl (table 1). Pyrite in sulfide chimney is enriched in Cu, Zn, Pb, and As. Pyrite from pyrite ore (mainly barite pseudomorph) show concentration of Se and Cu. Pyrite of the stringer in altered rock is rich in Cu, Zn, Se, and As. Pyrite megacrystals in altered rock show concentration of Zr and Cu.

## 5. DISCUSSION

From this study we conclude that there are three kinds of mineralizing fluid: one for major orebodies (barite, sphalerite-pyrite and pyrite ores), one for stringer and one for pyrite megacrystals. Such heterogeneity in a hydrothermal system is one of the important controlling factors for the trace element distribution in kuroko-type ore. According to the textural evidence, major ores (barite ore, sphalerite-pyrite ore and pyrite ore) seem to be the products from a common fluid. The fluid was rich in Pb, Zn, Cu, Fe, As, Sb, Ag, Ba, Sr, and slightly enhanced in Hg, Bi, Sn, and Tl. Within this fluid system, elements are partitioned by physical, chemical, biological and mineralogical (crystallographic) factors. The fluid precipitates orpiment in the initial stage of the mineralization with the decrease in temperature. During this process, elements with ionic radii close to that of As are partitioned into orpiment leaving larger ions such as Rb, Sr, Ag and Tl in the fluid. The rest of the elements are partitioned into barite and spongy/framboidal pyrite. Barite incorporates larger ions such as Sr and Ag of which ionic radii are close to that of Ba, while pyrite with ragged surface may absorb Ag and Tl. Stringer and pyrite megacrystals have no relation with the major ores and they are probably the precipitate from independent local solutions. The solution which was responsible for the stringer was enriched in Zn, Cu, Fe, Se, As, Ga and Ge. The occurrence mode of this ore type suggests that water/rock interaction was intense at the site of mineral precipitation and Ga and Ge were derived from the host rock. This idea should be tested in more detail because Ga and Ge are exclusively detected in kuroko-type ore [1] in Japan. In the fluid responsible for pyrite megacrystals, Zr and Co were present in addition to Fe, which implies that sea water was predominant in the fluid.

This study revealed that proton probe microanalysis is an effective method for detection of trace elements in massive sulfide ore like kuroko and that the trace element distribution is very heterogenous even within one orebody. Bulk analysis thus could not provide a reliable and decisive guideline for the beneficiation and exploration of rare metals. The proton probe can clarify the precise "heterogenous distribution" of trace elements (including important rare metals) in each ore type and texture, and hence will contribute to improvement of the exploration and exploitation strategies for kuroko-type mineral deposits.

## ACKNOWLEDGEMENTS

This study was conducted whilst S. M. was on leave at CSIRO from the Geological Survey of Japan under the auspices of the Japan-Australia Science and Technology Exchange Scheme. S. M. thanks Science and Technology Agency, Embassy of Japan at Canberra, and Metal Mining Agency of Japan for their support and advice on the research. He also thanks the crew and Captain Mueller of RV Sonne for their assistance during the cruise SO71.

## REFERENCES

1. Murao, S., and Itoh, S. (1990). Minor elements in ores and concentrates from various types of ore deposits in Japan. In: Koshogaku Pro Memoria, Hiroshima Univ., Hiroshima, pp 106-110 (in Japanese with English abstract)
2. Murao, S., and Itoh, S. (1992), *J. Geochemical Explor.* 43, 223.
3. Halbach, P., et al. (1989) *Nature*, 338, 496.
4. Sibuet, J.C., et al. (1987) *J. Geophys. Res.* 92, 14041.
5. Halbach, P., Pracejus, B., and Marten, A., (1993) *Econ. Geol.*, 88, 2210.
6. Marumo, K., JAMSTEC Deepsea Research, September (1989) 211-221 (in Japanese with English abstract).
7. Kato, Y., et al., *ibid* p.p.163-182.
8. Tanaka, T., et al. JAMSTEC Deepsea Research, September, 1990, 11-26.
9. Sie, S.H., and Ryan, C.G., *Nucl. Instr. Meth.* B15 (1986) 664.
10. Ryan C.G., et al. *Nucl. Instr. and Meth.* B47 (1990) 55-71.

**Table 1. Pyrite (FeS<sub>2</sub>) analyses.**

Element (MDL)	Barite ore	Barite ore average	pyrite ore	pyrite ore average	sphalerite-pyrite ore	sph-py average	stringer	stringer average	pyrite megacrystals
Ag (12)	61-1240	464	0-13	5.7	4-117	38	7-45	17	0-9
Sn (18)	0-86	32	0-18	11.8	0-272	46	0-18	9.7	0-26
Pb (33)	28-2530	925	32-183	89	71-5950	2060	22-665	259	49-269
Zn (37)	151-4.7%	1.57%	15-64	38	49-5000	1280	184-1170	682	3-15
As (15)	0-1006	428	6-58	21	15-4400	154700	6-1.6%	3570	3-7
Sb (21)	0-131	66	0-27	10.4	4.6-304	70	6-66	23	0-14
Cu (66)	17-6150	2230	480-811	648	91-6040	1430	59-5.4%	1.43%	40-62
Cd (14)	0-2770	926	0-15	5.7	0-100	20	0-17	5.9	1-9
Bi (30)	0-203	68	7-14	9.7	0-112	43	2-15	(10.5)	15-23
Se (12)	3-48	22	213-444	321	4.2-130	45	9-310	114	5-8.8
Tl (35)	0-3670	1220	8-12	11	0-17	6.3	0-20	(7.2)	13-20
Zr (7)	0-11	5	9-13	11	0-9	3.9	0-10	(3.9)	33-51

concentrations and MDL in ppm unless noted otherwise



## Oxide Growth on Aluminium Alloys in the Presence of Ammonium Fluoborate

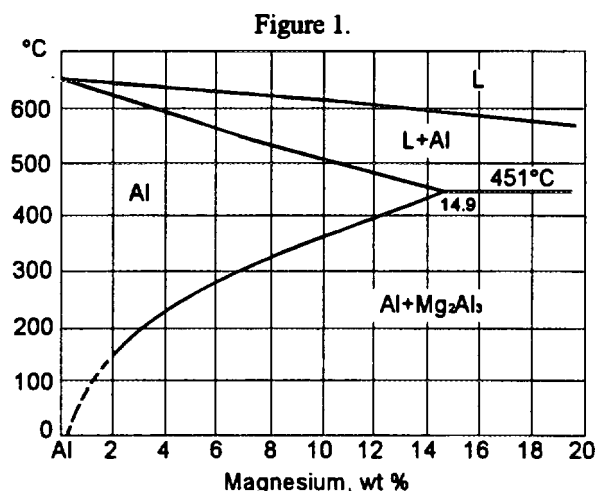
JAMES OLIVER & PETER PATERSON, Applied Physics Dept. RMIT  
TERRY FLAVELL, Metallurgical Engineering Dept., RMIT  
GERRY BIDDLE, Alcoa Rolled Products, Aust.

### 1. INTRODUCTION

The issues of oxide growth on rolled aluminium alloys, are a problem prior to rolling. Rolling requires that an ingot be heated to temperatures above 500°C, and held for periods greater than four hours, which allows substantial oxide growth, as well as chemically and mechanically driven diffusion of some elements to the surface.

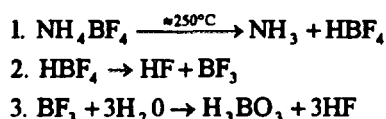
In the ammonium fluoborate has been used to control oxide growth during preheating. Their current published literature suggests however that the mechanisms involved with the usage of this chemical are unknown for AA5182. It was the aim of this study to determine the mechanisms involved in using ammonium fluoborate as a reducing atmosphere when preheating a high magnesium content aluminium alloy. The preheated alloy was compared for both air and ammonium fluoborate atmospheres.

A cast 5182 alloy comprises of approximately 4.5 wt% magnesium, lesser amounts of manganese, iron, silicon, copper and chrome (>1.5 wt%), as well as trace amounts of a number of other elements including gallium, zinc, titanium and vanadium. These elements, along with the industrial processing operation, are cause for a multitude of compounds to form, such as salts and intermetallics. It is known that the inclusion of compounds in an alloy will affect its cast structure and melting point.. This is also evident as being chemically driven, by the readiness of magnesium and oxygen bonding to form Mg<sub>2</sub>O. Saied and Sullivan (1) established that Mg is chemically driven to the surface of aluminium to react with excess oxygen. The Al-Mg phase diagram (2), figure 1, clearly shows the solidus line below 600°C at 4.5% magnesium, and allowing consideration for other impurities reducing the solidus line further, this feature could lower the melting point dangerously close to the typical homogenising temperatures.



Such temperatures as used, can enter the mushy zone of the material, and the consequential diffusion of magnesium occurs rapidly.

In 1989 Strohmeier (3) proposed the following equations as reactions involved with the use of ammonium fluoborate;



These equations focus on removing water vapour from the atmosphere inhibiting oxide growth. This project compares the change in oxide layer thickness, composition and structural characteristics, for both the air and  $\text{NH}_4\text{BF}_4$  atmospheres through the techniques of Rutherford Back Scattering (RBS), X-ray Photoelectron Spectroscopy (XPS), and Auger Electron Spectroscopy (AES). RBS has also been used to determine composition and verify sensitivity factors of XPS and AES.

## 2. EXPERIMENTAL

Specimens for the experimentation were prepared from hot rolled aluminium sheet of thickness 2.7 mm. Each sample of approximate  $11 \times 11 \text{ mm}^2$  dimension was ground to 600 SiC wet paper, to replicate an ingot surface prior to preheating. The samples were ultrasonically cleaned in acetone, and ethanol, and dried with nitrogen. Preheat treatments were conducted in a Tetflow furnace, heating to the maximum temperature over 10 minutes, and then holding constant ( $\pm 5^\circ\text{C}$ ). The experiment investigated preheat treatments at temperatures 480, 500, 520, 540 and  $550^\circ\text{C}$ , with samples at each stage being heated for 1, 2, 3, 4, & 5 hours. Ammonium fluoborate was used at a 5 g/m<sup>2</sup> ratio.

RBS was performed using a 2 MeV  $\text{He}^{2+}$  ion beam at normal incidence to the sample surface and backscattered He particles were collected at an angle of  $170^\circ$  degrees to the incident beam for a total charge accumulation of  $100 \mu\text{C}$ . The beam spot size was  $1.5 \times 1.5 \text{ mm}^2$ . RBS spectra were quantified using scattering cross-sections (4) and Rump simulations (5). The oxide thicknesses were determined using simulations in Rump (5). A "mean energy approximation" (4) was used in order to calibrate the depth scale of the oxide coatings on all depth profiles. Scanning AES and XPS were performed on a Fisons Microlab 310F. AES using 10 keV beam energy and XPS using a 300W Mg anode at  $60^\circ$  to the sample surface normal with escaping electrons being collected normal to the sample surface. A 3 keV Ar ion beam at  $60^\circ$  to the surface normal with a current of  $100 \mu\text{A}$  per  $\text{cm}^2$  was used for ion etching of the samples.

## 3. RESULTS

RBS has been the major technique used in the analysis of samples, it revealed significant reduction in both the diffusion of magnesium to the surface and the calculated oxide thickness in the presence of  $\text{NH}_4\text{BF}_4$ . At temperatures above  $500^\circ\text{C}$  in air, SEM images revealed depressions and voids due to incipient melting at various stages, around the grain boundaries. Grain boundaries effectively acted as pipes, aiding the diffusion of magnesium to the surface. These results have been verified through compositional analysis with both RBS and AES. Results from  $\text{NH}_4\text{BF}_4$  atmosphere preheat conditions showed significant improvements.

It was verified experimentally that above  $500^\circ\text{C}$  AA5182 alloys undergo incipient melting at the grain boundaries, with magnesium diffusing through to the surface

1. Saied S.O., Sullivan J.L., (1993), *A Study of Thermally Induced Segregation of Magnesium in Aluminium-Magnesium Alloys by means of AES*, J.Phys Condens. Matter, V5 A165-A166
2. *Aluminum, Properties, Physical Metallurgy, and Phase Diagrams*, (1967), American Society of Metals, V1 375
3. Strohmeier B.R., (1989), *Surface Characterization of Aluminum Foil Annealed in the Presence of Ammonium Fluoborate*, Applied Surface Science, V40 249-263
4. Chu W.K., Mayer J.W. and Nicolet M.A., (1978), *Backscattering Spectroscopy*, Academic Press
5. Doolittle L.R., (1986), *Computer Code RUMP*, Nucl. Instr. Meth. B V15 227.



# Radiation-Enhanced Thermal Processes During Implantation of Gold into Copper

N. E. PERRET, B. V. KING, P. C. DASTOOR,  
Physics Department, University of Newcastle

## ABSTRACT

A copper (100) single crystal has been implanted with gold ions at temperatures ranging from 133 K to 673 K. Rutherford Backscattering Spectroscopy (RBS) has been used to observe the changes in the gold implant distribution that occur as a function of the sample temperature during implantation. Two distinct effects have been observed. Firstly the gold implant distribution, as a function of depth, broadens with sample temperature. This broadening of the gold depth profile is most marked at temperatures above 473 K. Secondly, the gold is implanted deeper into the copper crystal as the sample temperature is increased. These results are discussed in terms of radiation-enhanced diffusion and radiation-induced segregation processes.

## INTRODUCTION

Diffusion mechanisms are of great interest in advanced materials development; for example in nuclear reactor applications, where material properties can be significantly altered under irradiation. Mechanical properties of materials such as hardening and ductility loss may be critically modified, as described by Holmes et al. (1). In addition, Myers et al. (2) have shown that the irradiation may also lead to precipitation in alloys and redistribution of dopants in semiconductors.

The copper-gold system has been widely investigated both theoretically: Hoffmann (3) and experimentally: Graham (4) and Hoffmann (5). However, although many low energy studies have been carried out to investigate surface composition, little work has been performed in regard to diffusion and segregation effects in sublayers.

The purpose of the present study was to determine the influence of substrate temperature upon the distribution of gold atoms when implanted into a single crystalline copper (100) substrate. The variation of the gold atom profile provides an insight into the diffusion processes that are activated during implantation and thus allows an investigation of the phenomena of radiation enhanced diffusion (RED) and radiation induced segregation (RIS).

## EXPERIMENTAL

The sample surfaces were carefully prepared by first mechanically polishing each surface to 1  $\mu\text{m}$  and then electropolishing to remove any subsequent surface damage. The roughness, cleanliness and orientation of the surface (100) structure were checked by alphascan measurements and X-ray diffraction.

The ion implantation was performed at the Australian National University using the 1.7 MV tandem accelerator NEC model 5 SDH-4. Implants were carried out at the following surface temperatures: 140 K, 300 K, 473 K, 573 K, 673 K. The system pressure during implantation was better than  $10^{-6}$  Torr. Gold ions, accelerated to 2.0 MeV, were implanted to a dose of  $10^{16}$  ions. $\text{cm}^{-2}$  for about 20 minutes. The gold ion current was 1.5  $\mu\text{A}$  and varied by less than 10 % during the experiment. After irradiation, the samples were cooled down to room temperature at a rate of 10 K. $\text{min}^{-1}$ .

The implant profiles were obtained by Rutherford Backscattering Spectroscopy analysis performed at the Australian National University. The experiment was carried out with a 2.0 MeV He beam, the charge collected was 40  $\mu\text{C}$ , and the current  $20 \pm 5$  nA. To avoid channelling, which generates oscillations at the edge of the substrate spectrum, the spectra were randomized by allowing the samples to move by  $4^\circ$  in all directions about the initial orientation. The calibration of the energy scale was carried out by testing a standard sample (Au-Cu-Si alloy).

## RESULTS AND DISCUSSION

Figure 1 shows the gold profiles for implantation at 133 K and 673 K. The experimental RBS profiles (scatter points) have been fitted to Gaussian profiles (solid lines) using the RUMP computer program. From the fitted profiles the ion range (depth of the gold implant) and the full-width-half-maximum of the profiles have been calculated in order to determine quantitatively the effects of diffusion.

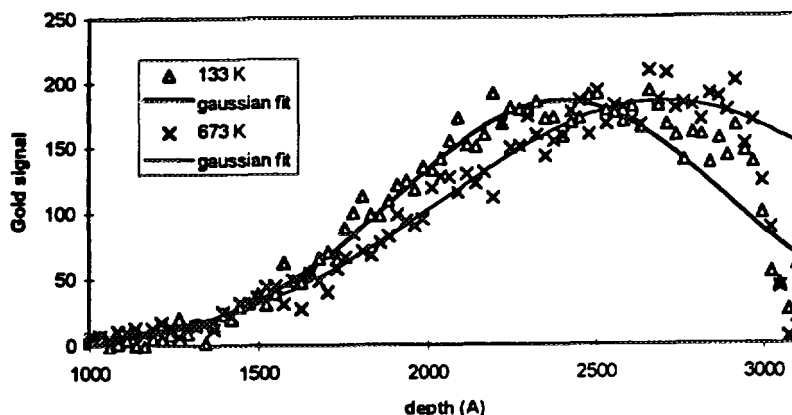


Figure 1: RBS analysis of the temperature effect on the gold implant distribution

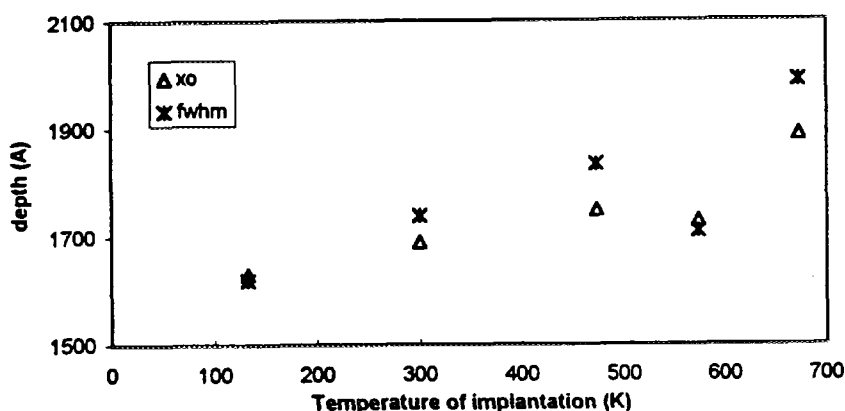


Figure 2: Results obtained from the RBS data for the full width half maximum and ion range of the gold implant as a function of the temperature. The error in both  $x_0$  and fwhm has been estimated to be approximately  $\pm 100 \text{ \AA}$ .

As the implantation temperature increases, it is necessary to consider the influence that irradiation has upon the diffusion of dilute solute atoms. It is well known that high energy particles can modify solid state transport in two ways, through radiation enhanced diffusion (RED) and radiation induced segregation (RIS). These two mechanisms are thermally activated processes, which significantly enhance the diffusion of atoms in the range 0.2 to 0.6 times the crystal melting temperature. These mechanisms occur by the inverse Kirkendall effect (a defect concentration gradient induces a flux of atoms) or by defect-atom or atom-atom cluster migration.

RED describes the increasing migration of atoms and defects with temperature and as a consequence is probably responsible for the broadening of the gold implant distribution with increasing temperature.

RIS allows the diffusion of some species in a preferential direction with respect to others. This mechanism can arise from differences in the coupling between atoms and defects and/or differences in the speed of diffusion of some component with respect to the others and thus probably describes the migration of the gold implant distribution towards the bulk as the temperature increases.

Other common atom displacement mechanisms are not considered in this study. Displacement mixing is ignored at sufficiently high temperatures. The effects of sputtering (ejection of atoms from the first layer), preferential sputtering (preferential removal of gold rather than copper), and Gibbsian segregation (thermally activated segregation which reduces the free energy of the system) are ignored since they affect only the outermost layers (Lam et al. (6)).

A simulation of the implantation of gold into copper has been performed using the TRIM code with Kinchin-Pease estimates, in order to compare a theoretical prediction for the gold implant distribution and damage peak with the experimental profiles. The gold ion range is estimated to be of the order of  $1800 \text{ \AA}$ , with a straggling range of  $420 \text{ \AA}$ . The maximum gold concentration was calculated to be 1.1 %, therefore no precipitation is expected to occur. The damage peak appears shallower than the implant distribution (figure 3).

Although for clarity figure 1 only shows the results of the RBS spectra collected for implants at the two extremes of the temperature range, all of the RBS spectra have in fact been fitted and the results of ion range and spread of the profile are shown in figure 2.

It is clear from the results shown in figure 2 that the gold implant distribution broadens and moves towards the bulk as the temperature of implantation increases. The diffusion coefficient associated with the migration of the gold atoms can be calculated from the fwhm values of the implant profiles. Using the experimental values shown in figure 2, a diffusion constant  $D_0 = 2.4 \times 10^{-14} \text{ cm}^2 \cdot \text{s}^{-1}$  has been calculated which compares favourably with the value of  $D_0 = 9.2 \times 10^{-14} \text{ cm}^2 \cdot \text{s}^{-1}$  reported by Li & Koshikawa (7). The activation energy  $E_a = 0.06 \text{ eV}$  quoted by Li & Koshikawa (7) is somewhat larger than the value of  $0.003 \text{ eV}$  calculated from the results of the present study.

In order to explain the observation that the gold implant profile broadens and moves to greater depths as the

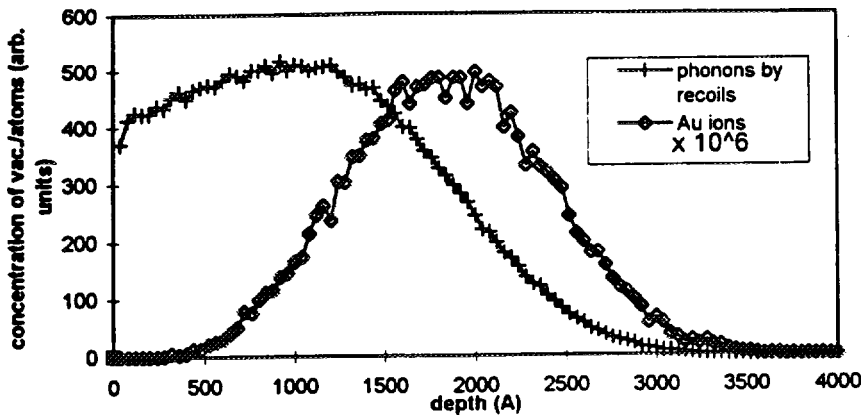


Figure 3 TRIM simulation results showing the damage layer due to the bombardment and the gold implant distribution. Note: the concentration of Au ions has been scaled by a factor of  $10^6$ .

It is interesting to compare the experimental results outlined here with the diffusion model developed by Lam et al. (8) describing the migration of oversized solute atoms in an alloy during irradiation. In this model the diffusion occurs by the inverse Kirkendall effect, along the vacancy gradient, towards the damage layer as the temperature increases. Gold is oversized in copper (volume size misfit parameter: +48 % from (9)) and if vacancies are located in the damage peak calculated by TRIM, the gold implant distribution should move towards the surface as

temperature increases. However the figure 2 shows the gold to move further into the bulk with increasing temperature, and thus away from the damage peak. Assuming the damage peak position is always on the surface side of the implant peak at all temperatures, the experimental results of the present study appear to contradict Lam's vacancy model.

Thus it appears that an alternative mechanism to that proposed by Lam is required to explain the RBS data. One possibility involves the formation of gold-vacancy complexes; vacancies diffusing away from the damage peaks towards the bulk would tend to drag gold atoms with them. However such a mechanism seems unlikely for two reasons. Firstly, the calculated binding energy of such a gold-vacancy complex is less than 0.07 eV (10) and as such it seems unlikely that such complexes would form since the thermal energy of vibration is of the order of the binding energy. Secondly, the low activation energy for the diffusion process suggests an interstitial rather than a vacancy based mechanism because whilst interstitial diffusion can be activated at temperatures as low as 133 K most vacancy diffusion is believed to occur only at higher temperatures (with activation energy about 8-10 times higher than that for interstitials).

A more likely possibility therefore, may involve the diffusion of gold-copper interstitial complexes; interstitials diffusing away, from the damage peak would tend to draw gold atoms into the bulk. Indeed, the binding energy of such a complex (0.21 eV from (9)) appears to move in line with the temperatures used in the present study. In addition the inverse Kirkendall effect induced by interstitials would provide an explanation for the observed broadening of the peak with increasing implantation temperature.

## CONCLUSION

The implantation of 2 MeV gold atoms on a copper single-crystal at different temperatures shows the diffusion and segregation of the solute atoms within the bulk. These mechanisms are believed to be due to the diffusion of the point defects and complexes created during the implantation. Mechanisms involving interstitials seem to be most probable for the system studied, in the temperature range of the experiment (133 K - 673 K); however further work is underway to investigate this hypothesis.

## REFERENCES

- (1) Holmes J. J., J. L. Straalsund, 1977, Radiation effects in breeder reactor structural materials, Met. Soc. AIME, p 53
- (2) Myers S. M., D. E. Amos, D. K. Brice, 1976, *J. Appl. Phys.*, **47**, 1812-1819
- (3) Hoffmann M. A., P. Wynblatt, 1990, *Surf. Sci.*, **236**, 369-376
- (4) Graham G. W., 1987, *Surf. Sci.*, **184**, 137-162
- (5) Hoffmann M. A., S. W. Bronner, P. Wynblatt, 1988, *J. Vac. Sci. Technol.*, **A6**, 2253-2259
- (6) Lam N. Q., S. Tang, A. M. Yacout, L. E. Rehn, 1991, *Nucl. Inst. Meth. Phys. Res.*, **B59/60**, 889-892
- (7) Li R. S., T. Koshikawa, 1985, *Surf. Sci.*, **151**, 459-476
- (8) Lam N. Q., P. R. Okamoto, R. A. Johnson, 1978, *J. Nucl. Mat.*, **78**, 408-417
- (9) Nolfi F. V., 1983, Phase transformations during irradiation, Applied Science Publishers, p 124
- (10) Doyama M., 1978, *J. Nucl. Mat.*, **69&70**, 350-361



# The Non-Destructive Analysis of Fluid Inclusions in Minerals Using the Proton Microprobe

C.G. RYAN<sup>1</sup>, C.A. HEINRICH<sup>2</sup>, E. VAN ACHTERBERGH<sup>1</sup>, T.P. MERNAGH<sup>3</sup>,  
C. BALLHAUS<sup>4</sup> and KHIN ZAW<sup>5</sup>

- 1 CSIRO Exploration and Mining, PO Box 136, North Ryde NSW 2113, Australia.
- 2 Department Erdwissenschaften, ETH Zentrum, Zürich CH-8092, Switzerland.
- 3 Australian Geological Survey Organization, GPO Box 378, , Australia.
- 4 Max Planck Institut für Chemie (Abt. Kosmochemie), PO Box 3060, 55020 Mainz, Germany.
- 5 CODES, Geology Department, University of Tasmania, Hobart, TAS 7001, Australia.

The study of ore forming fluids trapped as fluid inclusions in minerals is the key to understanding fluid flow paths at the time of ore formation and to predicting the location of ore bodies within large-scale magmatic hydrothermal systems. The large penetration depths and the predictable nature of MeV proton trajectories and X-ray absorption enables reliable modelling of PIXE yields and the development of standardless quantitative analytical methods. This permits quantitative microanalysis of minerals at ppm levels, and more recently has enabled the development of methods for quantitative trace-element imaging and the quantitative, non-destructive analysis of individual fluid inclusions. This paper reports on recent developments in Proton Microprobe techniques with special emphasis on ore systems and fluid inclusion analysis.

## FLUID INCLUSION MICROANALYSIS

Recent advances in fluid inclusion analysis technique at the CSIRO have come from improvements in modelling of PIXE yields from the complex 3D geometry of the inclusion in its host mineral (Ryan *et al.* [1]), and from the installation of beam-scanning to control the proton dose distribution across an individual inclusion (~20 µm) to better obtain the overall composition of the enclosed fluid (Ryan *et al.* [2]). The method has been tested by the direct analysis of synthetic fluid inclusions in quartz, produced from undersaturated aqueous solutions of NaCl and various metal chlorides. Inclusions, 5-20 µm in diameter and at depths of 2-17 µm, were probed using 3 MeV protons, and the geometry of each inclusion was determined by optical microscopy, and the depth was inferred from the

fit to the Cl  $K_{\alpha}/K_{\beta}$  ratio. Using these geometry parameters, expected X-ray yields per ppm were calculated with the GeoPIXE package [1,2]. The results of the PIXE microanalysis of the synthetic inclusions demonstrated an accuracy of ~10-15% (Ryan *et al.* [2]; Fig. 1). Note that natural inclusions with daughter crystals show increased scatter due to the positioning of the crystals within the inclusion cavity (up to ~30% for Cl).

## APPLICATIONS

Collaborative research at the CSIRO has focused on the analysis of ore elements in fluids, experiments to study chalcophile element partitioning between crystalline material and magmatic fluids (Ballhaus *et al.* [3]), and the study of elements in fluids that provide an indication of their source(s). Much of this work is centred on the analysis of hydrothermal fluids associated with copper-gold deposits. A good example is the analysis of inclusions from the Kidston granite-related breccia gold-copper deposit in North Queensland, Australia. Brine and vapour inclusions from Kidston showed strong partitioning of Cu into the vapour phase and the presence of S in the vapour (Heinrich *et al.* [4]; Fig. 2). A similar effect was observed in brine/vapour inclusions from the Yankee Lode Sn deposit within the Mole Granite of Northern NSW (Heinrich *et al.* [5]) where it was concluded that brine-vapour segregation of trace metals, and transport in the vapour phase, plays an important role in the formation of Cu deposits in these systems. Heinrich *et al.* argued that if a S complex is responsible for

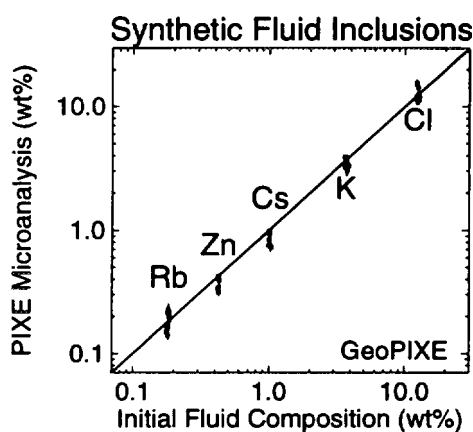
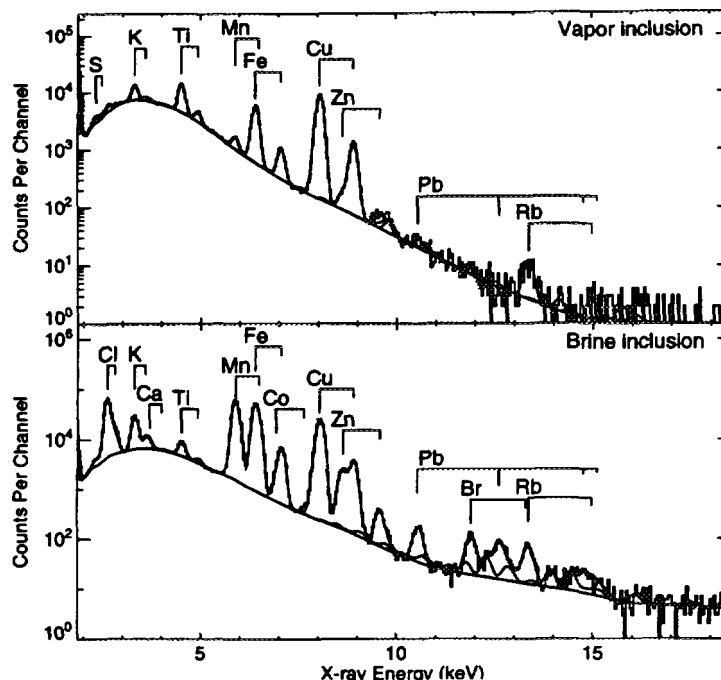


Fig. 1 Results of standardless microanalysis of synthetic fluid inclusions in quartz.

Fig. 2 PIXE spectra from vapour (top) and brine (bottom) fluid inclusions in quartz from the Kidston copper-gold deposit, Queensland, analyzed using a 0.5 nA 3 MeV proton beam.



preferential partitioning of Cu into the vapour, then Au is predicted to show a similar, but probably more extreme behaviour. This helps to understand the formation of deposits such as Kidston in terms of vapour transport of Cu and Au.

The detailed PIXE analyses of the more primitive brines, which are closely related to the fluid exsolved from the granite, also provide starting compositions for modelling the formation of ore deposits. Modelling of progressive cooling of the brine composition, given by PIXE analysis of brine fluid inclusions in the Yankee Lode quartz, with addition of meteoric water was used by Heinrich and Ryan [6] to explain the detailed zonation of ore deposits in the Mole Granite. The model predicted the sequence of ore deposition from cassiterite, through arsenopyrite, chalcopyrite, galena and sphalerite, to pyrite in the country rock. This is in general agreement with the regional distribution of Sn, Ag and base metal deposits away from the Mole Granite [6], and illustrates the usefulness of PIXE analysis as a basic research tool for the study of hydrothermal processes.

## CONCLUSIONS

PIXE analysis using the Proton Microprobe provides a means of exciting and detecting characteristic X-rays from ore-forming elements trapped within fluid inclusions in minerals. By modelling PIXE yields from the complex 3D structure which characterizes a fluid inclusion, and its multiphase components, a method has been developed which is non-destructive, quantitative and standardless, and with sensitivities down to ~50 ppm in the fluid. The method is currently in use to study ore-forming fluids in magmatic hydrothermal systems.

## References

- [1] Ryan, C.G., C.A. Heinrich and T.P. Mernagh (1993), *Nucl. Instr. Meth. B* 77, 463-471.
- [2] Ryan, C.G., Heinrich, C.A., Van Achterbergh, E., Ballhaus, C., and Mernagh, T.P., (1995), "Microanalysis of ore-forming fluids using the scanning proton microprobe", *proc. 4th Int. conf. on Nuclear Microprobe Technology and Applications*, Shanghai, China, October 1994, *Nucl. Instr. Meth. B*, in press.
- [3] Ballhaus, C., C.G. Ryan, T.P. Mernagh and D.H. Green (1994), "The partitioning of Fe, Ni, Cu, Pt and Au between sulfide, metal, and fluid phases - a pilot study", *Geochim. et Cosmochim. Acta* 58, 811-826.
- [4] Heinrich, C.A., C.G. Ryan and T.P. Mernagh (1993a), "Ore Metals in Magmatic Brine and Vapour: New Evidence from PIXE Microanalysis of Fluid Inclusions", Abstract, 'Specialist Group in Economic Geology' meeting, Armidale, 2-6 February 1993.
- [5] Heinrich, C.A., C.G. Ryan, T.P. Mernaugh and P.J. Eadington (1993b), "Segregation of Ore Metals between Magmatic Brine and Vapor: a Fluid Inclusion Study using PIXE Microanalysis", *Economic Geology* 87, 1566-1583.
- [6] Heinrich, C.A., and C.G. Ryan (1992), in *Proc. 7th Int. Symp. on Water - Rock Interaction*, eds. Y.K. Kharaka and A.S. Maest, (Balkema, Rotterdam, 1992) p. 1583-1587.



# An Update in Proton Probe Tomography.

A. SAKELLARIOU, J. HOWARD <sup>1</sup>, M. CHOLEWA, A. SAINT, G.J.F. LEGGE

School of Physics, MARC, The University of Melbourne,  
Parkville, Vic. 3052, AUSTRALIA

<sup>1</sup> Plasma Research Laboratory, Research School of Physical Sciences  
and Engineering, ANU, Canberra, AUSTRALIA

## ABSTRACT

The analysis of STIM tomography data is improved. The volumetric density information is obtained directly from an iterative convolution and back-projection (BFP) reconstruction method. The iterative method allows the effects of stopping-power to be incorporated easily. One draw back is that *a priori* constituency information is required for the iterative method to work. However, this is of no concern because the iterative method was designed with PIXE tomography in mind. In this light, the *a priori* information will be obtained as the zeroth iteration of a PIXE tomography iterative reconstruction method.

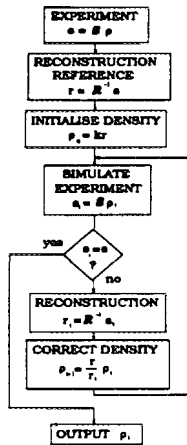
## INTRODUCTION

Ever since three-dimensional STIM tomography was first performed, A.E. Pontau, *et al.* (1), there has been doubt on how to properly extract density information from the reconstruction. Structure is accurately reconstructed but numeric values are usually inaccurate. This is the result of using the two-dimensional Radon transformation (2,3) to model the STIM experiment. This transform is defined as line integrals through a function that has a constant value at each point. In a STIM experiment, the trajectories of the ions through the sample represent the line integrals of the Radon transform. Since the energy loss rate of the ions is energy dependent, the amount of energy lost at each point varies with the direction the ion approaches this point. This means the quantity  $\rho(\vec{x}) \frac{dE}{d\vec{x}}$ , where  $\rho(\vec{x})$  is the local density and  $\frac{dE}{d\vec{x}}$  is the local stopping power, is not constant at each point. Therefore, applying a simple linear reconstruction based on the two-dimensional inverse Radon transformation (2,3) can not possibly reconstruct accurate sample densities. The inability to isolate unique values at each point of the reconstruction has, until now, prevented the extraction of accurate density information from STIM data. A new iterative method for extracting density information from STIM data has been devised. In the sections that follow, the method is described and reconstructions of a simulation and experimental data are given to show the effectiveness of the technique for compensating stopping power non-linearities.

## ITERATIVE TECHNIQUE

The fact that a STIM experiment can not be represented by the Radon transformation does not mean we can not use the inverse Radon transformation. The information obtained from the inverse Radon transformation is used to calculate correction factors for the current approximation of the density on a pixel by pixel basis. The iterative technique that has been devised is shown in flowchart form in Figure 1. The inverse Radon transformation is implemented by using the backprojection of filtered projections (BFP) method, and is represented as the operator  $\mathcal{R}^{-1}$ . The term sinogram refers to the projection data set. The initial application of the BFP algorithm to the sinogram creates a reference reconstruction  $r$  which also serves as a first approximation to the density  $\rho_0 = kr$  within a proportionality constant  $k$ . It is imperative to define what parts of the reconstruction  $r$  is a vacuum, as stopping power calculations should only be performed at points where material is present. The algorithm now proceeds into the loop. With the approximated density  $\rho_i$ , a simulated STIM experiment is performed and a new simulated sinogram  $s_i$  is generated. The simulated experiment includes stopping power effects calculated using Ziegler's model(4), this calculation being designated by the operator  $\mathcal{S}$ . In fact, it may be possible that any physical phenomena can be modelled at this point. Anyway, the sinogram  $s_i$  is reconstructed to give  $r_i$  and is compared to the initial reconstruction  $r$ . Correction factors  $[\frac{r_i}{r}](\vec{x})$  are applied to the density at each pixel to give a better approximation for the sample density. The process is repeated until the experimental  $s$  and simulated sinograms  $s_i$  are sufficiently similar. One problem with using an iterative technique is the BFP method produces noisy reconstructions. Propogating such noise through an iterative technique results in

unusable information after only a few iterations. To reduce the amount of noise at each iteration some alterations to the BFP method were necessary.



The measured sinogram data is modelled by the operator  $S$  and is given by,

$$s(\theta, k) = [S\rho](\theta, k) = \int \rho(\vec{x}(l))S(E(l))dl, \text{ where}$$

$$\vec{x}(l) = (k \cos \theta + l \sin \theta)\vec{i} + (-k \sin \theta + l \cos \theta)\vec{j}.$$

The BFP method is expressed by the operator  $\mathcal{R}^{-1}$  and is given by

$$r(x, y) = \mathcal{R}^{-1}s(\theta, k) = \mathcal{B}[\mathcal{F}_1^{-1}[|k|\mathcal{F}_1(s(\theta, k))]],$$

where  $\mathcal{B}$  is the Backprojection operator and  $\mathcal{F}_1$  and  $\mathcal{F}_1^{-1}$  are the one-dimensional Fourier and inverse Fourier transform.

Figure 1: Flowchart of Algorithm

### MODIFICATIONS TO BFP METHOD

The normal procedure to reduce noise in the BFP method is to decrease the bandwidth of the filter. However this has major drawbacks. The frequency response of the image is decreased, and consequently the reconstruction is infested with long wavelength sinusoids with the resolution of sharp structures diminishing. These problems were reduced by maintaining the maximum bandwidth and to alternatively smooth each projection of the sinogram in the following manner. The smoothing consisted of locating points of discontinuity, followed by mean averaging of the data between successive points of discontinuities. The new smoothing procedure has given excellent results for both the simulated and experimental data. It remains to minimise possible aliasing artifacts due to insufficient angular sampling. The ideal number of projections to be used in the BFP method is  $N_\theta = \frac{\pi}{2}N_m$ , where  $N_m$  is the number of equi-spaced samples in a projection. To ensure this requirement is satisfied, the sinogram is expanded by interpolation to have  $N_\theta$  projections. This has reduced many of the streaking artifacts that are caused by undersampling.

### RECONSTRUCTION OF SIMULATED SINOGRAMS

To illustrate the method we present reconstructions of a difficult test object containing a number of sharp boundaries. The phantom and its reconstruction are shown in Figure 2. To assess the accuracy of the reconstruction, two representative profiles are displayed in Figure 3. The phantom composition is taken to be pure carbon and has dimensions of 256x256 resels with a resel size of  $0.1\mu m$ . The simulated sinogram data has 180 projections with 256 samples per projection. The initial proton energy is 3MeV. Since noise is increased with each application of the BFP code it is found that about 5 iterations gives a good compromise between reconstruction accuracy of the density values and noise content.

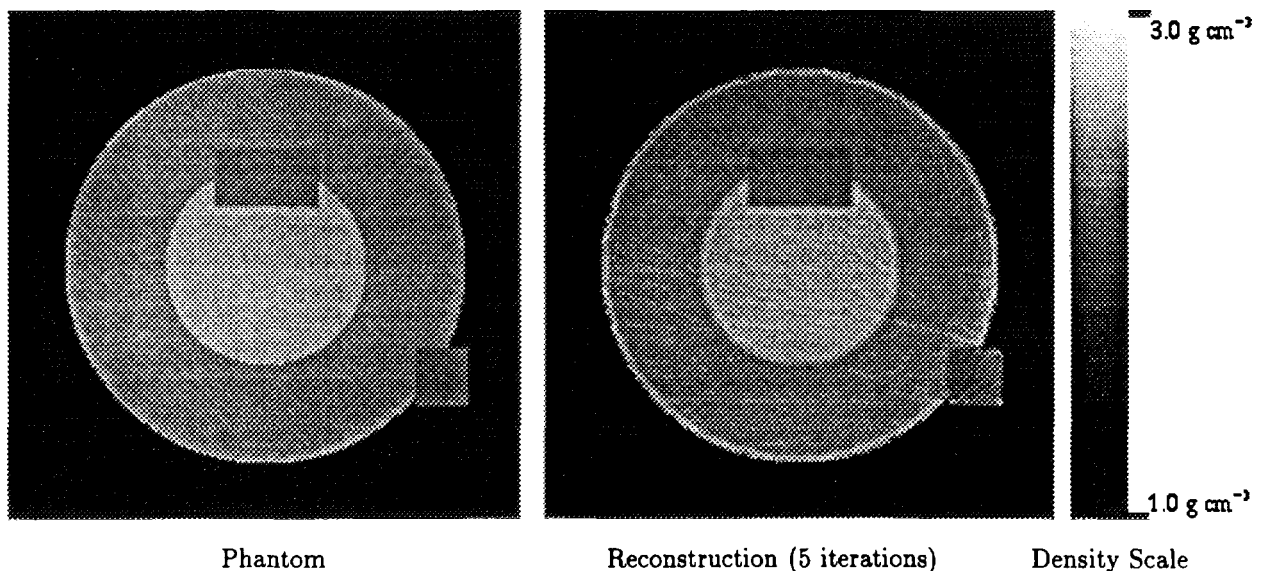


Figure 2: Phantom and its Reconstruction

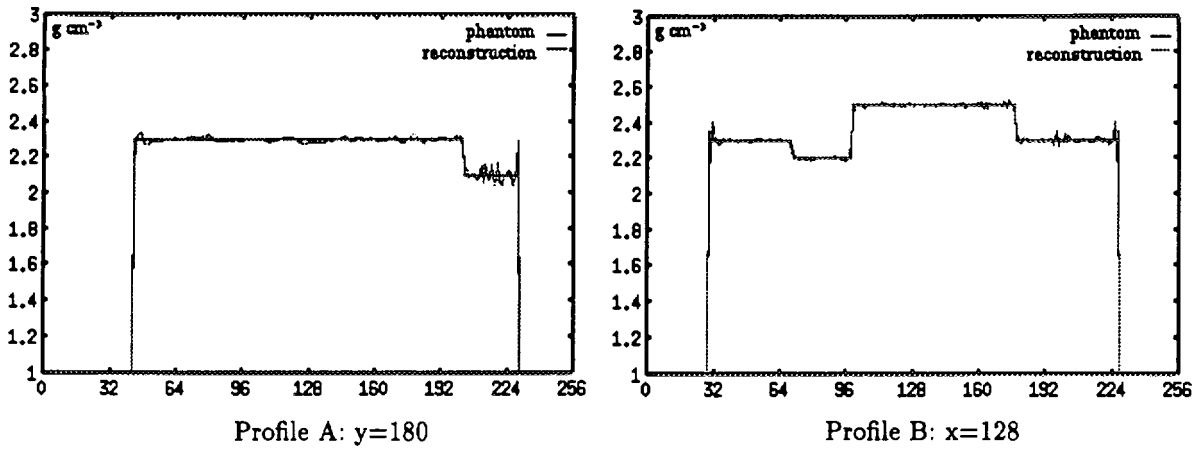


Figure 3: Some interesting profiles of Figure 2.

### RECONSTRUCTION OF EXPERIMENTAL SINOGRAMS

A sample of accurately known composition and density was used to test the reconstruction method. The sinogram data was acquired on the Melbourne microprobe using an incident 3MeV proton beam. The resel size was  $0.23\mu\text{m}$  and the focussed beam spot size was of a comparable diameter. The scan size is 400 resels and 360 projections were taken. A randomly chosen sinogram has been reconstructed and the solution after 5 iterations is shown in Figure 4. The accompanying tables compares the standard densities (specified by the manufacturer) with the reconstructed densities which are the statistical mean of density values over the corresponding regions of the reconstruction. The stated errors are the fluctuations of the density at each pixel. The errors of the means are much smaller. As can be seen, the agreement is very good.

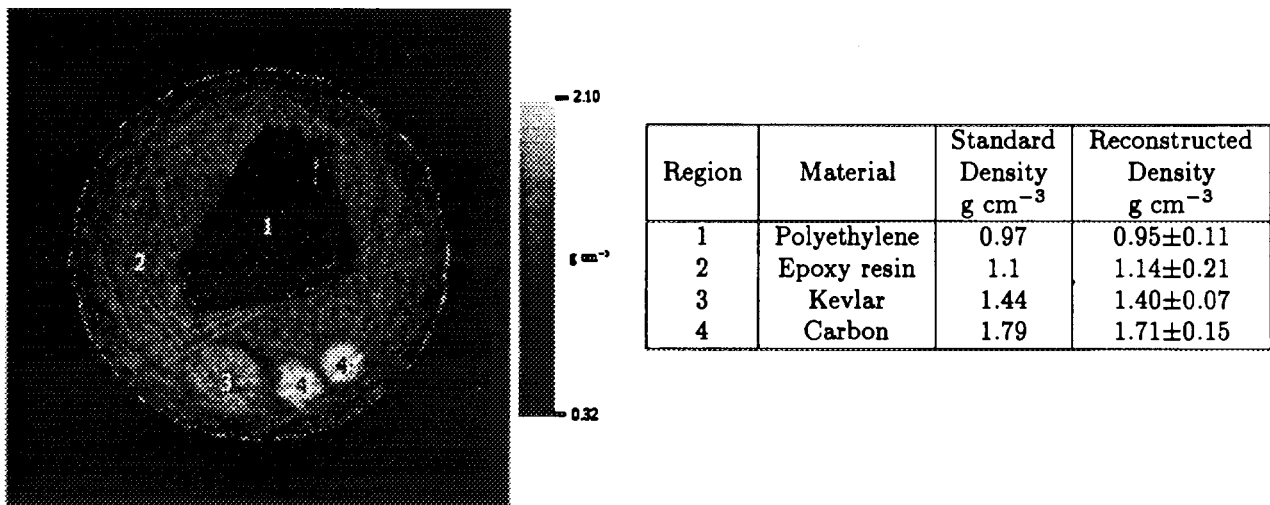


Figure 4: A reconstructed slice of the test sample, with a table of results.

### CONCLUSION

It is now possible to extract accurate density information from STIM data. It has been accomplished by incorporating the effects of stopping power into an iterative reconstruction technique. At present it is necessary to enter the elemental composition of the sample as *a priori* information. In the future, we could implement other effects such as beam broadening. Most importantly, having made substantial progress on this problem, we can continue to tackle the more difficult problem of three-dimensional PIXE tomography.

### ACKNOWLEDGMENTS

I gratefully thank Dr. Sue-Anne Stuart of the CSIRO, Division of Forest Products, for painstakingly making the test sample. The sample's characteristics have been very useful for testing the reconstruction technique.

### REFERENCES

- (1) A.E. Pontau *et al*, Nucl. Instrum. & Meth., **B40/41** (1989) 646.
- (2) S.R. Deans, The Radon Transformation and Some of its Applications, Krieger 1993.
- (3) F. Natterer, The Mathematics of Computerised Tomography, John Wiley 1986.
- (4) J.F. Zeigler *et al*, The Stopping and Ranges of Ions in Matter, Pergamon Press 1985.



# **AMS of heavy radionuclides at ANTARES: status and plans**

A.M. SMITH, D. FINK, M.A.C. HOTCHKIS, E.M. LAWSON AND C. TUNIZ

Australian Nuclear Science and Technology Organisation

Private Mail Bag 1, Menai NSW 2234, Australia

Long-lived radioisotopes are produced in the environment by cosmic ray interactions, natural radioactivity and through the use of nuclear technologies. Detection of trace amounts of anthropogenic isotopes by accelerator mass spectrometry (AMS) is a means of monitoring the safe operation of nuclear facilities and the presence of nuclear activities, however for heavy isotopes such measurements are difficult.

This paper discusses the approach taken at ANTARES in developing AMS measurement capability for the actinides and summarises the current status of the project.

## **INTRODUCTION**

There is considerable scientific effort underway to analyse rare nuclides of heavy mass, such as the long-lived actinides. These radioisotopes are ideal tracers to identify, on long time scales, nuclear activities for verification of arms control agreements and to monitor environmental responsibility related to the use of nuclear technologies, Tuniz [1]. AMS is the ultrasensitive analytical method of choice, as milligram sized samples taken from environmental media provide a sufficient signal. AMS also improves detection limits by 2 to 3 orders of magnitude over alternative methods such as alpha and gamma spectrometry, neutron activation analysis and thermal ionisation mass spectrometry.

## **ACTINIDES BEAM LINE**

The ANTARES AMS facility has been fully described elsewhere [2-5]. Features of the facility include an isotope cycling system for rapid sequential injection of isotopes into the tandem accelerator, image chambers with off-axis Faraday cups for both the injection and analyzing magnets, and two AMS beam lines, one optimised for radiocarbon measurements and the other for general AMS measurements including  $^{26}\text{Al}$ ,  $^{36}\text{Cl}$  and  $^{129}\text{I}$  to date. The limited bending power of the existing analysing and switching magnets (nom. 72 amu-MeV) restricts the use of these beam lines for larger masses and so we are

developing a beam line from the 0° port of the analysing magnet, designed specifically for these AMS measurements. The preliminary layout of the 'actinides beam line' is shown below.

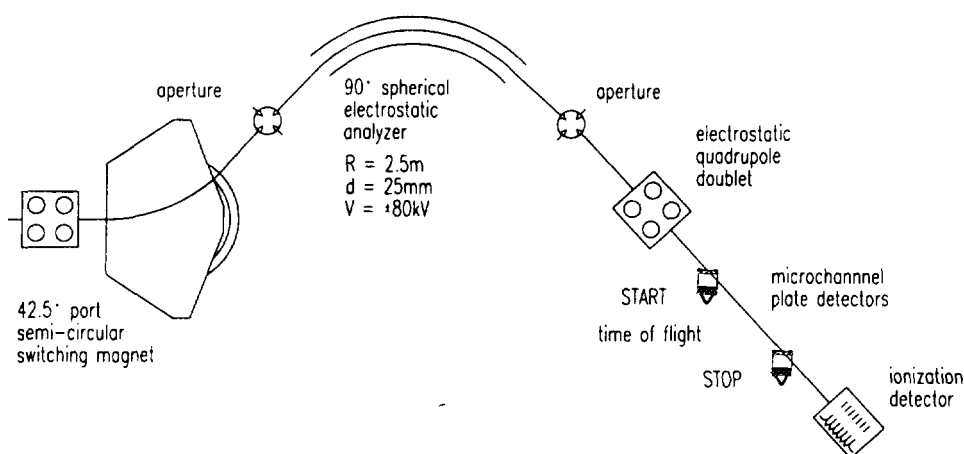


**Figure 1. Preliminary version of the actinides beam line.**

AMS measurement of high Z elements poses technical challenges in addition to those normally encountered with established isotopic systems, Zhao et al. [6]. The negative ion yield is low from cesium sputter sources, with a characteristic high energy 'sputter tail'. With small relative mass difference at high masses and greater possibility of interference from molecular masses, the limited mass resolution of the injection magnet results in the acceleration of unwanted molecules and sputter tails, which contribute directly to the ultimate sensitivity of the system and to overall detector deadtime. Furthermore, backgrounds will generally be higher due to the larger cross sections of elastic scattering and of charge changing events for low energy heavy ions.

Later this year, we plan to test the yield of  $^{238}\text{U}$  from the high intensity 846B ion source using  $\text{U}_3\text{O}_8$  as a source material, and to assess the mass resolution of the injection magnet for high masses. It will not be possible to determine whether this will result in acceptable sensitivity until the beam line and detectors are in place. If inadequate, consideration will have to be given to adding an electrostatic analyser [ESA] to the injection line to provide energy resolution and eliminate the sputter tails.

Measurement sensitivity is improved by eliminating ME ambiguities through the use of high charge states, but often at the price of decreasing measurement efficiency as the available terminal voltage may prevent operation at the maximum in the stripping yield. The overall measurement efficiency is also lowered by the poor negative ion source yield for the actinides. An FN tandem accelerator has an advantage over smaller machines, since the attainable terminal voltages of up to 10 MV will permit operation with higher charge states. We plan to assess the yields from both gas and carbon foil strippers using Pb beams in the near future. The effectiveness of the turbomolecular pumping system installed in the terminal with the new gas stripper will be critical, since leakage of stripping gas into the high energy acceleration tubes may introduce significant and undesirable charge changing events.

With the significant injection of molecular and sputter tail background, both the magnetic rigidity and the electric rigidity must be analysed in order to achieve adequate isotopic resolution for these high masses. In the first stage of development, the 42.5° port of a spare 55° switching magnet will be trialed. This magnet has a small air gap and a large focal length and is not expected to perform well, but it should at least reduce the background rate and allow us to assess the need for a replacement magnet. Specifications for a spherical ESA and two electrostatic quadrupole doublets [EQD] were completed in June and delivery is expected towards the end of October. The ESA has a radius of 2.5 m, plate separation of 25 mm, +/-80 kV voltage rating, and will provide an energy dispersion of 5000 for ions of up to 7.6 MeV. The EQDs will be used for mass independent beam transport, and should also benefit the existing high energy beam lines by decreasing the beam envelope size. Beam optics calculations aimed at establishing a layout for a prototype experimental beam line have commenced.

Final identification of the ions will be made using a time of flight [TOF] telescope and ionization detector to provide velocity and energy loss signals for the multiparameter data acquisition system. The need for an intermediate lens between the TOF detectors is under investigation.

## REFERENCES

- [1] C. Tuniz and J. Boldeman, Environmental monitoring in support of international safeguards arms agreements, Proc. 9th Pacific Basin Nuclear Conference, Sydney Australia, 1-6 May 1994, National Conference Publication No. 9416, p.841
- [2] A.M. Smith, D. Fink, M.A.C. Hotchkis, G.E. Jacobsen, E.M. Lawson and C. Tuniz, Recent developments at the ANTARES AMS centre, Proc. 7th Int. Conf. on Heavy Ion Accelerator Technology, 18-22 Sep. 1995, Canberra Australia, to be published in Nucl. Instr. and Meth.
- [3] M.A.C. Hotchkis, D. Fink, Q. Hua, G.E. Jacobsen, E.M. Lawson, A.M. Smith and C. Tuniz [1995], High Precision Radiocarbon Measurements at the ANTARES AMS Centre, proceedings ECAART, 29th Aug - 2nd Sept. 1995, Zürich
- [4] C. Tuniz, D. Fink, M.A.C. Hotchkis, G.E. Jacobsen, E.M. Lawson, A.M. Smith, Q. Hua, P. Drewer, P. Lee, V. Levchenko, J.R. Bird, J.W. Boldeman, M. Barbetti, G. Taylor and J. Head, The ANTARES AMS Centre: a status report, Proc. 15th International Radiocarbon Conference, Glasgow, 15-19th Aug. 1994, to be published in Radiocarbon.
- [5] A.M. Smith, D. Fink, M.A.C. Hotchkis, G.E. Jacobsen, E.M. Lawson, M. Shying, C. Tuniz, G.C. Watt, J. Fallon and P.J. Ellis [1994], Equipment and Methodology for high precision, high throughput AMS analyses at ANTARES, , Nucl. Instr. and Meth. B92, p.122-128.
- [6] X-L. Zhao, M-J. Nadeau, L.R. Kilius and A.E. Litherland [1994], The first detection of naturally - occurring <sup>236</sup>U with accelerator mass spectrometry, , Nucl. Instr. and Meth. B92, p.249-253.

# NANOCRYSTALLINE DIAMOND IN CARBON IMPLANTED SiO<sub>2</sub>.

KELLY A. TSOI\*, STEVEN PRAWER, KERRY W. NUGENT, RUSSELL J. WALKER  
and PAUL S. WEISER.

School of Physics, MARC, The University of Melbourne, Parkville, Victoria, 3052, AUSTRALIA

## INTRODUCTION

It has been found that diamond surfaces have the unusual property of negative electron affinity at low applied voltages [1]. These surfaces can be used as cold cathode devices, emitting electrons at room temperature with a moderate applied field. These devices are currently under investigation for use in high luminosity, flat bed displays. It has been shown that nanocrystalline diamond also displays these properties.

Recently, Walker *et al* [2] observed that nanocrystalline diamond can be produced via laser annealing of a high dose C implanted fused quartz (SiO<sub>2</sub>) substrate. The implanted amorphous carbon exists in a high pressure insulating matrix environment. This environment and the laser heating produces conditions suitable for the annealing of the carbon from a disordered, amorphous state to an ordered state of graphite and, if the temperature and power are high enough, nanocrystalline diamond. It is envisaged that cold cathode surfaces will be easier to produce if this synthesis of nanophase diamond proves to be successful. Since the initial findings of Walker *et al* [2] remain unpublished they will be discussed herein.

The aim of this investigation is to reproduce this result on higher C<sup>+</sup> dose samples and the original sample, as well as optimise the power range and annealing time for the production of these nanocrystals of diamond.

In order to provide a wide range of laser powers the samples were annealed using an Ar ion Raman laser. The resulting annealed spots were analysed using scanning electron microscopy (SEM) and Raman analysis. These techniques are employed to determine the type of bonding produced after laser annealing has occurred.

## EXPERIMENTAL

The samples used in these experiments were carbon implanted fused SiO<sub>2</sub> substrates, one with a dose of  $5 \times 10^{17}$  C<sup>+</sup>/cm<sup>2</sup> implanted with an energy of 100 keV, at a temperature of 400°C and the other with  $5 \times 10^{18}$  C<sup>+</sup>/cm<sup>2</sup> with an energy of 300 keV and at a temperature of 500°C.

Spot sizes ranging from 1 - 3 μm were annealed using an Ar ion Raman laser of wavelength 514 nm, at a variety of laser powers. The range of spot sizes was achieved by using a 100× objective with different powers and annealing times.

A DILOR XY confocal micro-Raman spectrometer was used to analyse the annealed spots, with an Ar ion laser using a 100× objective. The depth of the scan was restricted to 2 μm since the implanted region is close to the surface (~2 μm). The depth of the implanted region was obtained using the TRIM90[3] program and found to be 277.1 nm for the  $5 \times 10^{17}$  C<sup>+</sup>/cm<sup>2</sup>.

The sample of Walker *et al* [2] consisted of an optical grade polished fused silica substrate which was implanted with 100 keV C<sup>+</sup> ions to a dose of  $1 \times 10^{17}$  C<sup>+</sup>/cm<sup>2</sup> at a temperature of 400°C. The estimated projected range (Rp), determined by TRIM90[3], was 282 nm. The ion beam currents were kept  $\leq 1$  μA/cm<sup>2</sup> to reduce additional effects due to ion beam heating. The sample was then thermally annealed at 1100°C over an hour and then laser annealed using the same experimental set up as stated previously. The annealing parameters consisted of a laser power of 50 mW for 10 minutes duration.

SEM micrographs of the annealed spots were taken using a scanning Auger nanoprobe (5 keV) due to the fact that the insulating nature of the sample causes it to charge when using a conventional SEM (25 keV).

## RESULTS AND DISCUSSION

Figure 1(a) shows a Raman spectra of the laser annealed spot of Walker *et al* [2] for a thermally and laser annealed spot and figure 1(b) shows a spot which has only been laser annealed. The peak at 1130 cm<sup>-1</sup> has previously been attributed to nanophase diamond [4].

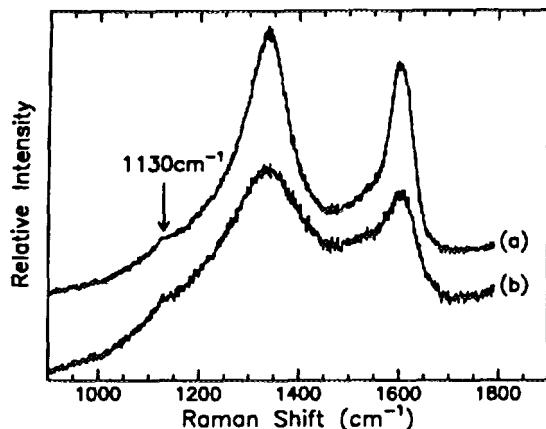


Figure 1. Raman spectra for  $1 \times 10^{17} \text{ C}^+ / \text{cm}^2$  sample, (a) post implantation thermal annealing followed by laser annealing, (b) laser annealed region

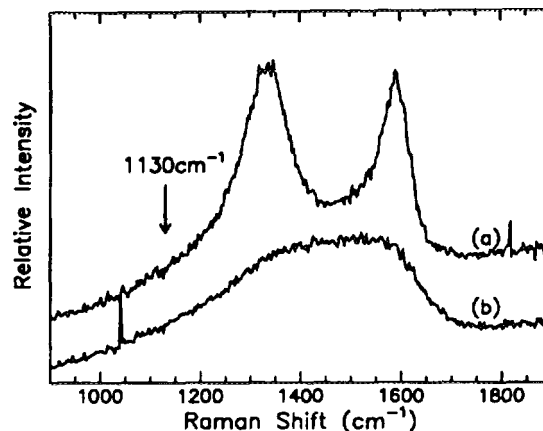


Figure 2. Raman spectra for  $5 \times 10^{17} \text{ C}^+ / \text{cm}^2$  sample, (a) laser annealed region, (b) unannealed region.

Raman spectroscopy of the  $5 \times 10^{17} \text{ C}^+ / \text{cm}^2$  sample was taken *in situ* with the annealing, using a focused beam spot of  $\sim 1 \mu\text{m}$  at a power of 60 mW at the sample over 30 seconds. Figure 2(a) shows two very distinguishable peaks at  $1580 \text{ cm}^{-1}$  and  $1330 \text{ cm}^{-1}$ , these correspond to the graphite (G) peak due to ordering of the amorphous carbon into  $\text{sp}^2$  bonded carbon planes, and the disorder (D) peak, respectively.

A Raman spectrum was also obtained of an unannealed region of the same sample, using a power of 1 mW at the sample over a period of 5 minutes. Figure 2(b) shows that the sample is made up of amorphous carbon, with no ordering of any bond type.

These results indicate that for this sample, nanocrystalline diamond won't be formed. This occurs because once graphite has been formed, no amount of further annealing will change the bonds formed within the amorphous carbon since graphite is the most energetically stable form of carbon. The reasons for this could be that the pressure within the  $\text{SiO}_2$  matrix has decreased due to the laser annealing, suggesting laser ablation has occurred. This reasoning is supported by the SEM micrograph shown in figure 3. This figure shows that the annealing of the sample has created a crater,  $\sim 4 \mu\text{m}$  in diameter. The centre of the craters appears to have graphite being pushed out which, in doing so, relieves the pressure of the surrounding area, thus removing any possibility of producing nanophase diamond.



Figure 3. SEM micrograph of laser annealed regions of  $5 \times 10^{17} \text{ C}^+ / \text{cm}^2$  sample.

Similar analysis of the  $5 \times 10^{18} \text{ C}^+ / \text{cm}^2$  sample was completed and the resulting Raman spectra can be seen in figure 4. It also shows the graphite D and G peaks of the annealed spot and amorphous carbon spectra of the unannealed region.

A Raman spectra of the annealed spots which produced the spectrum observed in figure 1 was repeated. The results were found to differ from those found originally (see figure 5(a) and 5(b)).

The differences in the Raman spectra of the originally annealed spots and the more recent annealing of the same sample could be due to a deterioration of the sample over time. When the sample was first implanted, the pressure obtained within the matrix could have been caused by not only the implanted  $C^+$  ions but also by the existence of co-implanted gases, which over time have leaked out, thus relieving the pressure.

Atomic force microscopy (AFM) studies were also completed by Walker *et al* [2], and it was found that a smooth crater of depth 15 nm was produced at the annealed region. This was accounted for as being due to the differences in density between the amorphous carbon ( $\rho \approx 2.0 \text{ gcm}^{-3}$ ), graphite ( $\rho \approx 2.24 \text{ gcm}^{-3}$ ) and diamond ( $\rho \approx 3.51 \text{ gcm}^{-3}$ ).

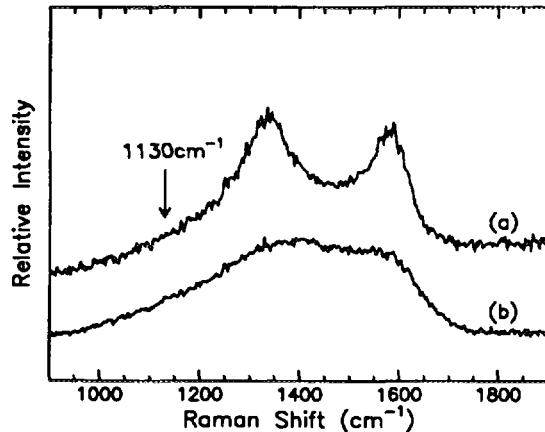


Figure 4. Raman spectra for  $5 \times 10^{18} \text{ C}^+/\text{cm}^2$  sample, (a) laser annealed region, (b) unannealed region.

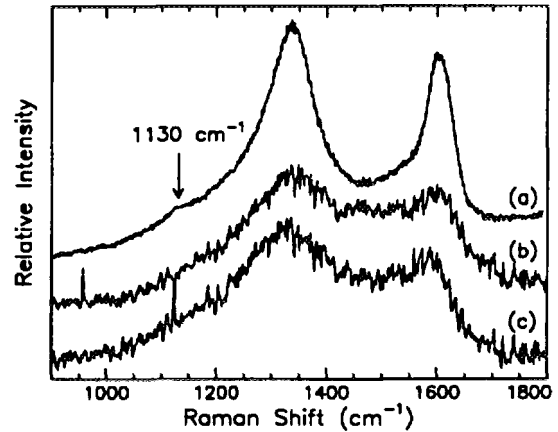


Figure 5. Raman spectra for  $1 \times 10^{17} \text{ C}^+/\text{cm}^2$  sample, with post implantation thermal annealing. (a) original annealed spot, (b) spectrum of annealed spot, 18 months later, (c) spectrum of newly annealed spot.

The  $1 \times 10^{17} \text{ C}^+/\text{cm}^2$  sample was then annealed with a power of 40 mW over a time of 10 minutes and a Raman spectrum was taken at the same power for 30 sec. The results are shown in figure 5(c).

It appears that the higher dose samples more readily revert to a graphite form. When the laser anneals a region of these high pressure implants, the  $\text{SiO}_2$  cap ablates and there is a rapid decrease in the pressure, resulting in the production of graphite only.

## CONCLUSION

From the analysis carried out to date, it can be seen that high dose samples readily produce graphite instead of nanocrystalline diamond. Further work is required in exploring the possibility of ablation occurring, resulting in a decrease of the pressure which exists within the quartz substrate. Analysis using AFM, as well as optical transmission experiments will enable the change in the surface to be mapped.

There is also the possibility that the structure of the quartz substrate results in the production of different types of carbon bonding after laser annealing.

## ACKNOWLEDGMENTS

The authors would like to gratefully acknowledge Dr Steve Johnston for his assistance with the scanning Auger nanoprobe, and Deborah Beckman for her previous work in this area.

## REFERENCES

- [1] J. van der Weide, Z. Zhang, P.K. Baumann, M.G. Wensell, J. Bernholc, and R.J. Nemanich, *Phys Rev B* **50**, 5803, (1994)
- [2] R.J. Walker, S. Prawer and D.R. Beckman, Private communication
- [3] J.F. Ziegler, J.P. Biersack and U. Littmak, *The Stopping and Ranges of Ions in Matter*, Pergamon Press (1985)
- [4] W.A. Yarbrough and R. Roy, Extended Abstracts. *Diamond and Diamond-like Material Synthesis*, Materials Research Society, Pittsburgh, PA, 33, (1988)



# Multivariate techniques of analysis for ToF-E Recoil Spectrometry Data

H.J. WHITLOW<sup>1</sup>, M. EL BOUANANI<sup>1</sup>, L. PERSSON<sup>1</sup>, M. HULT<sup>1</sup>, P. JÖNSSON<sup>1</sup>, M. ANDERSSON<sup>2</sup>, M. ÖSTLING<sup>3</sup>, C. ZARING<sup>3</sup>, P.N. JOHNSTON<sup>1,4</sup>, I.F. BUBB<sup>4</sup>, S.R. WALKER<sup>4</sup>, W.B. STANNARD<sup>4</sup>, D.D. COHEN<sup>5</sup> AND N. DYTLEWSKI<sup>5</sup>

<sup>1</sup>Department of Nuclear Physics, Lund Institute of Technology, Sölvegatan 14, Lund, Sweden.

<sup>2</sup>Department of Inorganic Chemistry, Uppsala University, Box 531, S-751 21 Uppsala, Sweden.

<sup>3</sup>Department of Electronics, Solid State Electronics, Royal Institute of Technology, P O Box Electrum, S-164 40 Kista, Sweden.

<sup>4</sup>Department of Applied Physics, Royal Melbourne Institute of Technology, GPO Box 2476V, Melbourne 3001, Australia

<sup>5</sup>Australian Science and Technology Organisation, PMB 1 Menai 2234, Lucas Heights, Australia

## ABSTRACT

Multivariate statistical methods are being developed by the Australian-Swedish Recoil Spectrometry Collaboration for quantitative analysis of the wealth of information in Time of Flight (ToF) and energy dispersive Recoil Spectrometry. Here we present an overview of our progress in the use of multivariate techniques for energy calibration, separation of mass-overlapped signals and simulation of ToF-E data.

## INTRODUCTION

The multivariate nature of the data obtained in Recoil Spectrometry (RS) measurements using Time of Flight - Energy (ToF-E) or  $\Delta E$ -E detector telescopes is very information rich. We have been investigating multivariate methods for energy detector calibration and separation of mass overlapped signals in ToF-E RS. Here the objective is to present an overview of our research in this field.

## ENERGY CALIBRATION

A critical step in the analysis of ToF-E RS data is the energy calibration as this is used in establishing the depth and concentration scales. In contrast to the case for ion backscattering, where a single ion species is detected, RS involves the detection of a wide range of energetic recoils with widely varying masses. Provided the foils in the time detector are thin ( $\sim 5 \mu\text{g cm}^{-2}$ ), the time calibration is independent of the recoil mass and consequently the time vs. channel-number relationship is a straight line. (Fig. 1). On the other hand the relationship between pulse height and energy for the Si detector is not a linear, but governed by the recoil energy and mass number. A consequence of this non-linearity is that if the recoil mass  $M$  is assigned using,

$$M = KX(T - T_0)^2, \quad (1)$$

then the data points in plots of  $M$  vs.  $X$ . will not lie along straight lines corresponding to the different mass recoils. In eqn. 1  $X$  is the energy channel,  $T$  the time

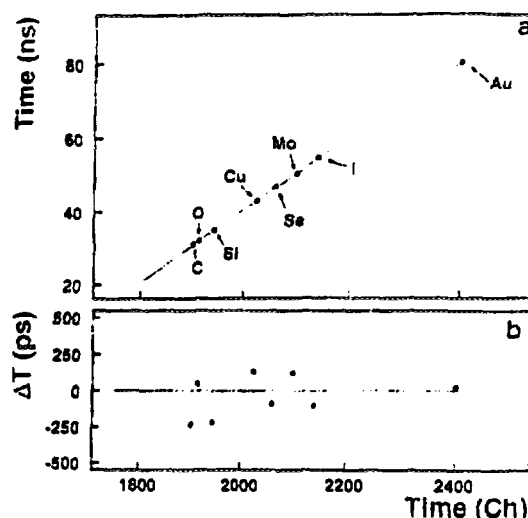


Fig. 1 (a) Time calibration determined from the positions of the surface edges. (b) Deviation of the data from the straight line fit. From [1].

channel,  $T_0$  an adjustable constant for electronic delays etc. and  $K$  an arbitrary constant assigned to give a suitable mass range. The departure from straight lines implies it is difficult to select gates so as to minimise interference from near-lying isotopes.

We have used the calibrated ToF to tag recoils from reference samples with known mass  $A$  with their energy. By trial and error it was found that the energy detector calibration was quite well described by a polynomial. The energy  $E_i$  of the  $i$ th recoil is then given in terms of its mass  $A_i$  and channel number  $X_i$  by:

$$E_i(X_i, A_i) = c_0 X_{i0} + c_1 X_{i1} + c_2 X_{i2} + c_3 X_{i3} + c_4 X_{i4} + c_5 X_{i5} \quad (2)$$

where  $X_{i0} = 1$ ,  $X_{i1} = A_i$ ,  $X_{i2} = X_i$ ,  $X_{i3} = A_i X_i$ ,  $X_{i4} = X_i^2$ ,  $X_{i5} = A_i X_i^2$  and  $c_0, \dots, c_5$  are constants. For the ensemble of  $n$  recoils eqn. 2 can be written in matrix form:

$$E = XC + e, \quad (3)$$

where  $E$ ,  $C$  and  $e$  are column matrices of the  $n$   $E_i$  values from the ToF, the calibration constants  $c_1, \dots, c_5$  and the  $n$  element error matrix, respectively.  $X$  is a  $n \times 6$  matrix of the  $X_{i0}, \dots, X_{i5}$  values. Then  $C$  is given by [3]:

$$C = (X^T X)^{-1} X^T E. \quad (4)$$

Rather than manipulate  $n \times 6$  matrixes where  $n \sim 10^6$  we instead choose some 53 representative values of  $E_i$ ,  $A_i$  and  $X_i$  by averaging. Fig. 2 shows a plot of  $M$  vs.  $E$  where the energy has been assigned according to eqn. 2. The data for the recoils clearly lie along straight lines corresponding to the different recoil masses. Our experience with this technique suggests that it is important that the range of  $E$  and  $A$  space for which the calibration is carried out must span the recoil masses of interest. It was also found that the technique works with quite thick foils in the time detectors, however extra terms have to be included in eqn. 2 to compensate for the larger energy losses in the carbon foils.

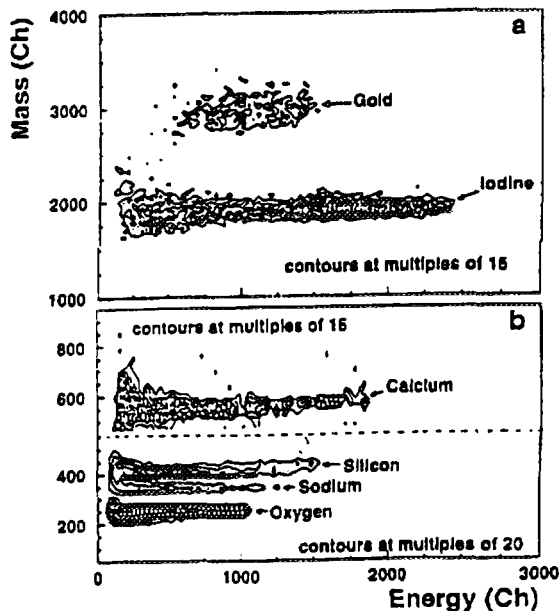


Fig. 2 Contour plot of 2-dimensional mass vs. energy spectra for 64 MeV  $^{127}\text{I}^{10+}$  ions at  $\phi = 45^\circ$  with mass assignment using energy from eqn. 2 (a) Au/soda-lime glass (b) soda-lime glass only. From [1]

### SEPARATION OF SIGNALS FROM RECOILS OF CLOSELY LYING MASSES

The mass resolution of a ToF-E RS system is generally limited by the the resolution of the energy detector. Many important materials systems involve elements with closely lying masses e.g. steels, (Fe, Cr, Ni Co) and III-V semiconductors (AlP, GaAs, InSb). Typically the mass

resolution of a ToF system is sufficient to separate isotopes spaced by 1u at  $A \leq \sim 28$  [4]. The resolution decreases as  $A$  increases and is  $\sim 4u$  and  $\sim 8u$  fwhm at  $A = 75$  and 127, respectively. Our interest in the Pd/InP system has led us to study how overlapped signals can be separated. In this case the signals from  $^{102}\text{Pd}$ ,  $^{104}\text{Pd}$ ,  $^{105}\text{Pd}$ ,  $^{106}\text{Pd}$ ,  $^{108}\text{Pd}$ ,  $^{110}\text{Pd}$ ,  $^{113}\text{In}$ ,  $^{115}\text{In}$  and scattered  $^{127}\text{I}$  projectiles lie so closely as to be superimposed.

Investigations revealed that over the energy and mass range of interest in ToF-E RS, the mass instrument function for a particular isotope was well described by a Gaussian function where  $\sigma$  is governed by the energy  $E$  and mass  $A$  of the recoil. We have measured  $\sigma$  over the range of interest for ToF-E RS using the ANTARES accelerator (Fig. 3). Using the multivariate least-squares fitting procedure above we found the data was well described by the empirical relation:

$$\sigma = b_1 + b_2 A^{3/2} E^{-1} + b_3 A^2 E^{-2/3} + b_4 A E^{1/2}. \quad (5)$$

$b_1, \dots, b_4$  are constants determined by fitting. Fig. 3 shows the measured  $\sigma$  vs.  $E$  data and the fit obtained using eqn. 5.

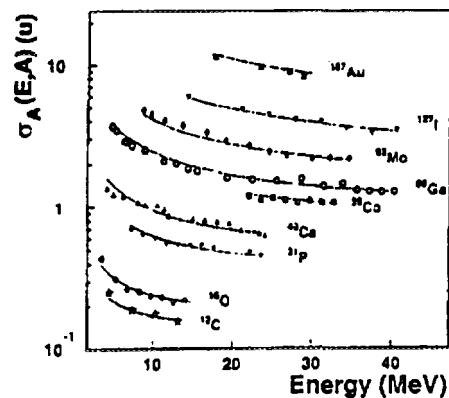


Fig. 3  $\sigma$  vs. recoil energy  $E$  for Gaussian isotopic line-shapes. The lines indicate the best fit for eqn. 5. From [2].

We have used two different strategies for separation of near-lying masses such as In and Pd. Both strategies divide the two dimensional histogram data into slices in energy channel number  $X$ . These slices must be sufficiently wide so that the statistics are sufficient for a reliable fit. In the first approach, the resulting one-dimensional mass spectra are decomposed by non-linear fitting of elemental line-shapes made up of Gaussian isotope line-shapes, with centroids and intensity corresponding to mass number and natural abundance. The second strategy used Ryan and Jamieson's Dynamic Analysis (DA) approach [5,6]. In this technique a *linear* combination of previously established line-shapes are fitted with a linear-least squares method. It should be remembered that both these methods rely heavily on the reliability of the energy (and thus mass) assignment based on eqn. 2. We found that this calibration is quite adequate where gates in the mass energy plane can be selected to obtain elemental energy distributions with minimal cross talk from neighbouring

elements. However the small, but persistent, non-linearities are troublesome when the signals have so much overlap that spectral decomposition by fitting has to be applied.

The non-linear fitting procedure has the advantage that it can be made rather insensitive to the non-linearities in the mass assignment. This can be achieved by fitting with the relative spacing and isotope abundance as fixed parameters and the mass calibration, elemental signal amplitudes and  $\sigma$  as free parameters. The disadvantage with the non-linear fitting procedure is that it is iterative which renders it slow, limiting its practical application to small regions of the  $M$  vs.  $E$  histograms. The DA method on the other hand, is very rapid, which makes it attractive for on-line extraction of energy distributions from overlapping elements. In DA the experimental energy slice is fitted with a linear combination of the previously defined line shapes. In our case the mass was assigned according to eqn. 2 and the width from eqn 5. Experiments with simulated test data using  $\sigma$  from eqn. 5, revealed that in the absence of statistical scatter the relative intensities of  $^{102}\text{Pd}$ ,  $^{103}\text{Pd}$  and  $^{104}\text{Pd}$  with 100:1:10 ratio could be reliably resolved. Inclusion of counting statistical scatter leads to significant disturbance of the measured distributions.

In the case of both methods the most reliable fitting was when the fitted functions were composite elemental line shapes obtained by summing the Gaussians, weighted according to the natural isotopic abundance rather than the individual isotope line shapes. This has the disadvantage that the energy resolution is degraded because the different isotopes give rise to an associated isotopic broadening that can no longer be resolved. However, the fitting is more precise and faster because of the fewer free parameters in the fit. Ryan and Jamieson[5,6] have pointed out the DA method is critically dependent on the position and shape of the elemental line shapes. Fig. 4 shows the Pd, In and I elemental energy distributions associated obtained using

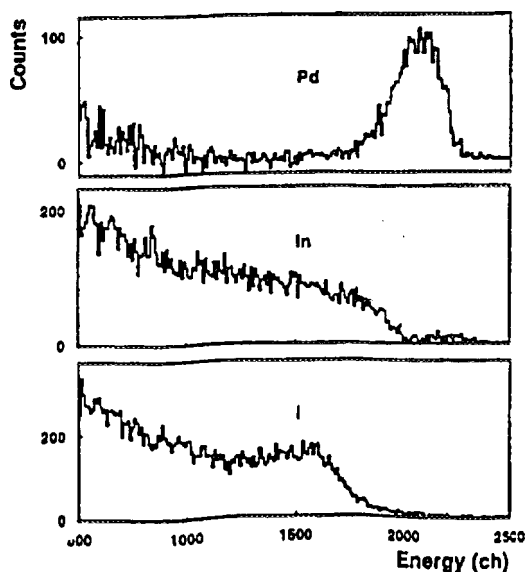


Fig. 4 Signals for Pd, In and scattered  $^{127}\text{I}$  from a 50 nm Pd film on InP separated using the DA method.

the DA method from an as-deposited 50 nm Pd/(100)InP structure. The low energy tail in the Pd signal around ch. 500 is a consequence of cross talk arising from a non-linearity in the mass calibration. This sensitivity to the non-linearities in the energy, and hence mass calibration, is a principle limitation. This could be overcome by determining the line shapes directly from reference samples of the elements to be measured.

All the methods that assign a mass from the ToF and E signals have the disadvantage that the uncertainties in mass are correlated with both the uncertainties in ToF and energy measurements. Thus separation directly in the ToF-E plane are preferable because the uncertainties will be uncorrelated. For this purpose we are extending the ANALNRA simulation code to produce data directly in the ToF-E plane. Figure 5 shows experimental simulated ToF-E data for a  $\text{Si}/\text{Si}_x\text{Ge}_{(1-x)}(\text{O})/\text{Si}$  sample. Note that because the isotope signals are treated separately in the simulations, the effect on resolution from isotopic broadening is taken account of in a natural way.

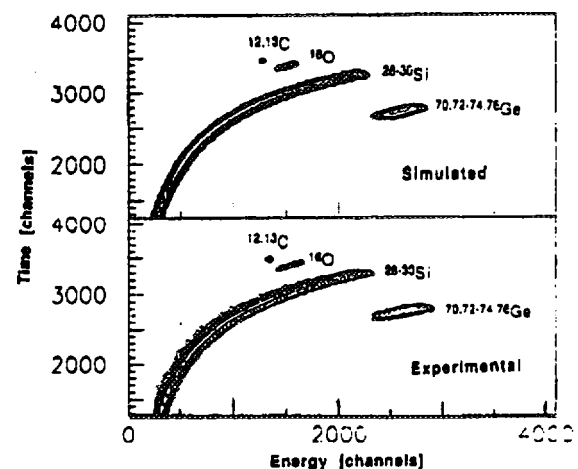


Fig. 5 Simulated and experimental ToF vs. E histograms for a 10 nmSi/100nmSi $_x$ Ge $_{(1-x)}$ (O)/structure. The time scale is inverted.

## ACKNOWLEDGEMENTS

We are grateful for financial support from the Australian Department of Trade Industry and Commerce (DITAC), the Australian Institute for Nuclear Science and Engineering (AINSE), Carl Tryggers Foundation, Kungl. Fysiografiska Sällskapet and Wenner-Gren Foundation.

## REFERENCES

1. M. El Bouanani, M. Hult, L. Persson, E. Swietlicki, M. Andersson, M. Östling, N. Lundberg, C. Zaring, D.D. Cohen, N. Dylewski, P.N. Johnston, S.R. Walker, I.F. Bubb and H.J. Whitlow, Nucl. Instrum. Methods B94(1994)530.
2. M. Hult, M. El Bouanani, L. Persson, H.J. Whitlow, M. Andersson, C. Zaring, M. Östling, D.D. Cohen, N. Dylewski, I.F. Bubb, P.N. Johnston and S.R. Walker, Nucl. Instrum. and Methods, B101(1995)263.
3. N.R. Draper and H. Smith, Applied Regression Analysis, Wiley 1966.
4. H.J. Whitlow, G. Possnert and C.S. Petersson, Nucl. Instrum. and Methods B27(1987)448. See also: H.J. Whitlow, B. Jakobsson and L. Westerberg, Nucl. Instrum and Methods, A310(1991)636.
5. C.G. Ryan and D.N. Jamieson, Nucl. Instrum. and Methods B77(1993)203.
6. C.G. Ryan, D.N. Jamieson, C.L. Churns and J.V. Pilcher. Nucl. Instrum and Methods. B. (Submitted.)



# Application of $^{14}\text{N}(^3\text{He},^4\text{He})^{13}\text{N}$ Nuclear Reaction to Nitrogen Profiling.

L. S. Wielunski, Division of Applied Physics, CSIRO, Lindfield, NSW 2070, Australia.

## Abstract

In this paper the  $^{14}\text{N}(^3\text{He},^4\text{He})^{13}\text{N}$  reaction is proposed for nitrogen profiling in metals and other materials. The beam energy is chosen to be 4.65 MeV in order to use the high cross section. Two types of particle filtering are used: a 25  $\mu\text{m}$  thick mylar in front of the detector to avoid backscattered particle pileup and reduced detector bias voltage to avoid full energy detection of high energy protons produced by competing reactions. The depth resolution is about 150-200 nm and the sensitivity is better than for the  $^{14}\text{N}(d,^4\text{He})^{12}\text{C}$  reaction. The low level of neutron radiation background allows use of this reaction in accelerator laboratories without radiation shielding.

## 1. Introduction

Tribological properties of steels are modified substantially by nitriding processes. Nitrogen can be introduced by different techniques, from traditional chemical nitriding to plasma immersion ion implantation (PI<sup>2</sup>) or ion implantation using high energy ion implanters or low energy ion guns. The concentration depth profile of nitrogen in steel is strongly dependent on physical and chemical parameters of the nitriding process: temperature, time, nitrogen pressure, nitrogen ion current density, ion energy and of course steel composition. Nuclear reaction analysis can measure nitrogen concentration and nitrogen depth profiles as a function of physical and chemical parameters used [1-2]. The results can be compared with results of hardness and other tribological tests.

Usually nitrogen is detected and profiled using the  $^{14}\text{N}(d,^4\text{He})^{12}\text{C}$  nuclear reaction [2-3]. This reaction can be used in laboratories with small accelerators (~1.2 MV), however laboratory neutron radiation background is high when using this reaction and in practice this limits its use to laboratories with adequate neutron radiation shielding [4].

An alternate method for nitrogen profiling is the use of  $^{14}\text{N}(^2\text{He},p)^{16}\text{O}$ , however the low cross section and low depth resolution limit its use [5].

In this work the use of the nuclear reaction  $^{14}\text{N}(^3\text{He},^4\text{He})^{13}\text{N}$  in the broad resonance region ( $^3\text{He}$  energy about 4.65 MeV) is proposed. The high cross section of about 2.5 mb/str provides good sensitivity [6]. This reaction can be used to profile nitrogen in steels up to a depth of 2200 nm with depth resolution about 150-200 nm and can be used in laboratories without neutron shielding.

## 2. Experimental

Nitrogen was detected using the  $^{14}\text{N}(^3\text{He},^4\text{He})^{13}\text{N}$  nuclear reaction with a 4.65 MeV  $^3\text{He}^{++}$  ion beam from a tandem accelerator and a standard silicon surface barrier detector placed at about 160° scattering angle. A 25  $\mu\text{m}$  thick mylar foil was used in front of the detector to stop backscattered  $^3\text{He}$  ions. The Q-value of the  $^{14}\text{N}(^3\text{He},^4\text{He})^{13}\text{N}$  reaction is 10.024 MeV and the energy of the emitted  $^4\text{He}$  ions is about 8.1 MeV. The mylar absorber reduces this  $^4\text{He}$  energy to about 5.6 MeV. In order to use this  $^4\text{He}$  line for nitrogen profiling other nuclear reaction products with comparable energy must be eliminated or filtered out. There are many proton lines from  $^{14}\text{N}(^3\text{He},p)^{16}\text{O}$  and  $^{12}\text{C}(^3\text{He},p)^{14}\text{N}$  nuclear reactions in this energy region [5]. The detector bias was lowered to 70 V in order to reduce the energy deposited by these high energy protons in the active layer of the detector. In this way the interference of high energy protons has been removed and  $^4\text{He}$  particles are detected without significant background.

The  $^3\text{He}$  beam diameter was about 1 mm and current about 50 nA. The samples were mounted on a sample manipulator inside the vacuum chamber with vacuum about  $3 \times 10^{-7}$  torr. Nuclear reaction spectra were collected using a typical RBS data collection system (HYPRA) in 512 channels mode with channel width about 17.6 keV.

Fig 1 shows spectra obtained from the same thin AlN on GaAs sample at three different detector bias voltage: 50V, 60V and 80V. The  $^4\text{He}$  line (nitrogen signal) in about channel 320 is almost identical in all three spectra, however the suppressed proton background high energy edge visible in the low energy part of this figure is clearly sensitive to detector bias voltage.

In order to calibrate the concentration scale of nitrogen a high purity (99.5%) bulk AlN standard was used [7]. Fig 2 shows spectra obtained from bulk AlN standard and a pure Al sample. The pure Al sample spectrum shows a

low level background in the region of the nitrogen signal (channels 240-320). The correction for this Al background has been taken into account in the calibration. In order to obtain nitrogen concentration in the new sample, the nitrogen signal height from this sample was compared with the corrected height of an AlN standard spectrum. It was assumed that introduction of nitrogen into the sample does not change the relative concentrations of other elements and  $^3\text{He}$  and  $^4\text{He}$  stopping powers in the elements involved [8] were used in concentration calculations.

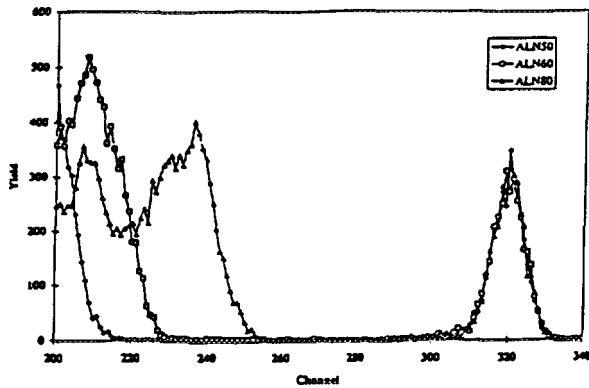


Fig 1. Nuclear reaction spectra from thin AlN film on a GaAs substrate measured with detector bias voltages 50, 60 and 80 V respectively.  $^3\text{He}$  energy is 4.65 MeV, beam charge  $50 \times 10^{-6}\text{C}$  and a 25 micrometre mylar absorber is placed in front of the detector.

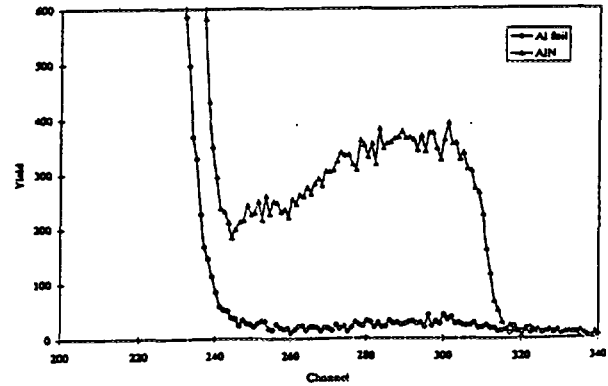


Fig 2. Nuclear reaction spectra from pure aluminium and bulk AlN standard sample. The detector bias is 70V and other parameters are the same as on Fig 1.

### 3. Results and discussion

Fig 3 shows typical spectra from a TiN thin film (900 nm) on a silicon substrate produced by ion-assisted arc deposition (IAAD) [9] and a bulk tool steel sample treated with nitrogen plasma in a plasma immersion ion implantation ( $\text{PI}^3$ ) system [10]. From the height of the TiN nitrogen peak, the nitrogen concentration has been estimated to be about  $\text{TiN}_{0.93}$ . The nitrogen signal from the treated tool steel sample is much lower and corresponds to about 7.6 atomic % nitrogen in this material. The tool steel depth scale is about 32 channels per micrometre.

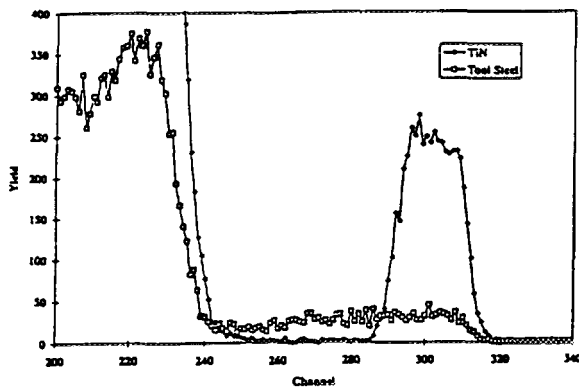


Fig 3. Nuclear reaction spectra from 900 nm thick TiN film deposited by IAAD method on silicon substrate and bulk tool steel sample treated in nitrogen plasma in  $\text{PI}^3$  system.

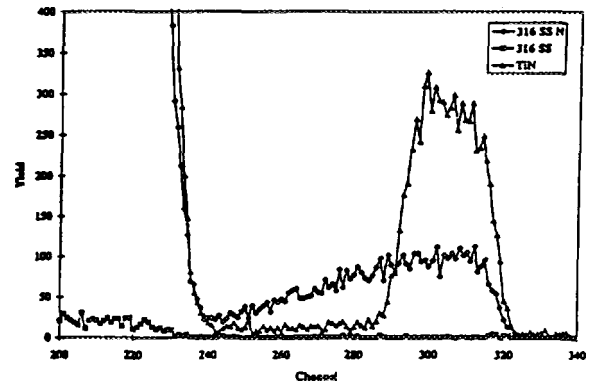


Fig 4. Nuclear reaction spectra from two 316 stainless steel bulk samples one nitrided in  $\text{PI}^3$  system and the other an untreated sample. For comparison the spectrum from 1100 nm thick TiN film deposited by IAAD method on  $\text{Al}_2\text{O}_3$  substrate is shown.

Fig 4 shows two spectra from 316 stainless steel bulk samples: one treated with nitrogen plasma in a  $\text{PI}^3$  system (316 SS N) and an untreated sample (316 SS). It is clear from these two spectra that in the second sample (untreated) there is no nitrogen present in the near surface region and there is very low background, however in the first sample ( $\text{PI}^3$  treated) the nitrogen concentration is about 21.8 atomic % near the sample surface and the nitrogen concentration is decreasing with increasing depth. The depth scale is similar to the tool steel case about 32 channels per micrometre, and at a depth of about 2000 nm, the nitrogen concentration is only 10.9 atomic %. On the same figure, the spectrum from TiN thin film (1100 nm) deposited on  $\text{Al}_2\text{O}_3$  substrate is shown. The estimated film composition is about  $\text{TiN}_{1.02}$ . In this spectrum background similar to the background from pure aluminium (see Fig. 2) is observed in the region below the nitrogen peak (channels 240-280). This background is

most likely due to aluminium being present in the sample substrate ( $\text{Al}_2\text{O}_3$ ).

The spectra from TiAlV alloy (Ti90/Al6/V4) treated with DC nitrogen plasma [11] for different times and at different temperatures are shown on Fig. 5. In this case the nitrogen enriched layer thickness is about 900 nm for 4 hours treatment at 800°C, 1400 nm for 8 hours at 800°C and 2400 nm in the case of 8 hours at 900°C. The near surface nitrogen enriched layer composition is similar in each case and is about Ti90/Al6/V4/N61.

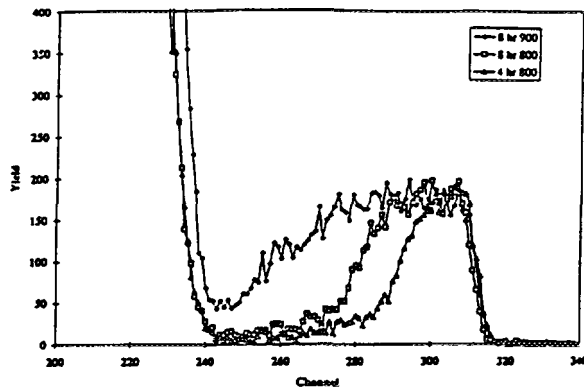


Fig 5. Nuclear reaction spectra from TiAlV alloy (Ti90/Al6/V5) samples treated in DC nitrogen plasma for 8 hours in 900°C, 8 hours in 800°C and 4 hours in 800°C respectively.

#### 4. Summary

In this paper we demonstrate the use of the  $^{14}\text{N}(^3\text{He},^4\text{He})^{13}\text{N}$  nuclear reaction in nitrogen profiling in metals. This reaction provides very good sensitivity due to its high cross section ( about 2.5 mb/str at 4.65 MeV  $^3\text{He}$  energy ) and low background when using a silicon surface barrier detector with reduced sensitive layer thickness. The nitrogen depth profile can be measured up to a depth of 2.2 micrometers in steels and similar depths in other materials. In the case of materials containing aluminium, the aluminium related background is present and limits sensitivity.

This reaction can be used in laboratories without radiation shielding due to its low radiation background. The only case of substantial, but acceptable for laboratories, radiation background was observed when the sample was bulk carbon. This reaction is a good alternative to the  $^{14}\text{N}(d,^4\text{He})^{12}\text{C}$  reaction usually used in nitrogen profiling.

An aluminium nitride bulk standard is used for calibration in order to reduce uncertainty of results.

#### Acknowledgments

The author would like to thank P. Martin, A. Bendavid, S. Butcher, M. Samandi, M. Doroudian, J. Tendys, G. Collins and K. Short for stimulative valuable discussions and samples. I am also very grateful to M. Kenny for his help in the final manuscript preparation.

#### References

- [1] G. Amsel, J. P. Nadai, E. D'Artemare, D. David, E. Girard and J. Moulin, Nucl. Instr. and Meth. 92 (1971) 481.
- [2] A. Barcz, A. Turos, L. Wielunski, J. Radioanal. Chem. 31 (1976) 227.
- [3] H. Abeyta, G. Amsel, J. W. Butler, L. C. Feldman, H. Mayer and S. T. Picraux in "Ion Beam Handbook for Materials Analysis", eds J. W. Mayer and E. Rimini ( Academic Press, Inc. New York 1977 ) p. 151.
- [4] M. J. Kenny in " Ion Beams for Materials Analysis " eds. J. R. Bird and J. S. Williams ( Academic Press, Sydney 1989 ) p. 72.
- [5] G. Terwagne, D. D. Cohen and G. A. Collins, Nucl. Instr. and Meth. in Phys. Res. B 84 (1994) 415.
- [6] A. R. Knudson and F. C. Young, Nuclear Physics A149 (1970) 323.
- [7] AL643064 ceramic sheet, Goodfellow Metals Limited, Cambridge Science Park, Cambridge CB4 4DL, England.
- [8] J. F. Ziegler, H. H. Andersen and U. Littmark, Stopping Powers and Ranges in All Elements ( Pergamon Press, NY, 1977 ).
- [9] A. Bendavid, P. J. Martin, X. Wang, M. Wittling and T. J. Kinder, J. Vac. Sci. Technol. 13 (3), (1995) 1658.
- [10] M. Samandi, B. A. Shedden, D. I. Smith, G. A. Collins, R Hutchings and J. Tendys, Surf. Coat. Technol. 59 (1993) 261.
- [11] H. G. Brading, P. H. Morton and T. Bell, Surface Engineering 8 no.3 (1992) 206.



# Elastic Recoil Detection Analysis of Hydrogen in Polymers

<sup>a</sup>THOMAS R.H. WINZELL, <sup>b</sup>I.F. BUBB, <sup>b</sup>R. SHORT, <sup>c</sup>H.J. WHITLOW and <sup>b</sup>P.N. JOHNSTON.  
<sup>a,c</sup>University of Lund, Sweden and <sup>a,b</sup>Royal Melbourne Institute of Technology, Australia.

## INTRODUCTION

Elastic recoil detection analysis (ERDA) allows low-energy accelerators to be used for hydrogen depth profiling of thin films using a few MeV He ions. The technique enables the use of the same equipment as in Rutherford backscattering (RBS) analysis, but instead of detecting the incident backscattered ion, the lighter recoiled ion is detected at a small forward angle.

Hydrogen profiling is a very powerful technique for investigation of the hydrogen content of thin films. If the excitation function is known at the alpha energy used, the hydrogen profile of the material can be easily calculated. If the excitation function is not available, hydrogen profiles can still be determined by direct comparison with the measured proton recoil spectra from an infinitely thick standard of known hydrogen concentration, and assuming that it is not damage sensitive to particle irradiation. Polymeric films have a well-known stoichiometry and have also been shown to be fairly stable against bombardment of helium ions in the few MeV region. These properties make it appropriate to use them as reference standards. Furthermore, the polymers are readily available, not very expensive and do not demand much preparations.

ERDA of hydrogen in thick polymeric films has been performed using 2.5 MeV He<sup>2+</sup> ions from the tandem accelerator at the Royal Melbourne Institute of Technology. The purpose of this work is to investigate how selected polymers react when irradiated by helium ions. The polymers are to be evaluated for their suitability as reference standards for hydrogen depth profiling. Films investigated were Du Pont's Kapton and Mylar, and polystyrene.

## EXPERIMENTAL

Two silicon surface barrier (SiSB) detectors were placed at a forward angle of 15° and at a backscattering angle of 170°, respectively. The latter was used to simultaneously obtain the RBS[1] spectra for the heavier elements in the films. An aluminium filter of 10 μm was placed in front of the forward angle detector to shield off scattered helium ions. A conducting glue to avoid charge build up and consequent discharges in the polymers. A Faraday cage, at -300V, surrounded the target holder to repel sputtered electrons. The Faraday cage was also cooled with liquid nitrogen to decrease surface contamination.

The geometry of the experimental setup is shown in figure 1. The actual geometry was developed to get the best depth

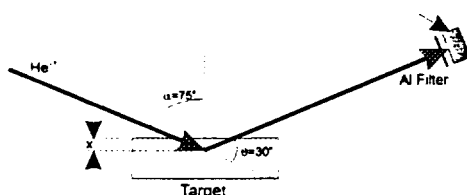


Figure 1. Geometry.

resolution at the energy used. Turos et. al. [3] carried out a depth profiling technique for hydrogen using 2.5 MeV He<sup>+</sup> ions, which improved the depth resolution [3, 7]. In that work it is shown how the incident and outgoing angle to the target can optimise the depth resolution. The results shows that  $\alpha = 75^\circ$  and  $\theta = 30^\circ$  gives the best depth resolution at this energy. This geometry, as given in figure 1, was used throughout all the measurements.

The experimental runs were made by collecting charge in steps of 30 μC at two different energies as well as at two different currents. The experiments done by J.E.E Baglin et. al [4] and R. Pretorius et. al [5], showed that the hydrogen loss is not very dependent on beam energy nor on beam current when irradiating polystyrene. These facts pointed at a more thorough investigation of the hydrogen loss as a function of collected charge. The hydrogen loss measured by Baglin [4] was about 0.8% / 10 μC on an area of 1 cm<sup>2</sup> up to 60 μC using a rastered beam and in Pretorius [5] the hydrogen loss rate was about 6% per 5 μC not using a rastered beam. The latter work by R. Pretorius does not reveal how large an area over which this charge was collected, which could be a key factor of the large differences in hydrogen loss received in these two papers. In this work a non rastered beam was used, irradiating an area of about 20 mm<sup>2</sup>.

## RESULTS

The first measurements carried out were to observe the reproducibility of Kapton and Mylar results. A sample, 2cm by 3cm, was used in both cases to collect three, and two spots of about 20mm<sup>2</sup> for kapton and mylar, respectively. Charge spots of 30μC were collected at a current of 50nA for both materials. The ratios between the three first 30μC spots for Kapton were within 3.5% and for Mylar within 1%. After 60μC the ratios for Kapton were within 3% and for Mylar within 1%. The large difference between the 30μC and 60μC ratios for Kapton was due to the differences in beam spot areas. Beam spots were satisfactorily uniform.

Large charge build up in mylar was observed which forced the use of a well polished fine copperwire placed across the beam spot. This reduced the charge build up to zero and the beam spot area could still be accurately measured. The charge build up was due to the fact that the sample used was large(about 6cm<sup>2</sup>). When a smaller(about 2cm<sup>2</sup>) sample of Mylar was used no charge build up was observed. Both Kapton and polystyrene showed no charge build up.

The Kapton data showed a hydrogen loss of 2.8% (all within 1%) between 30μC and 60μC. The Mylar runs showed an increase in counts by 3%(within 0.5%). A possible explanation is that Mylar contains H<sub>2</sub>O. Most polymers can contain appreciable amounts of water. H<sub>2</sub>O may also be absorbed on the surface of the polymer, but there was no hydrogen peak observed in the proton recoil spectra at the surface. This will be discussed further down.

The beam current and total charge dependence of the hydrogen loss were then measured. First a 2.5MeV/30μC steps/20nA-run was done on both polymers, taken over four steps up to 120μC. Secondly the same procedure was carried out at a higher current of 50nA. In Kapton the hydrogen loss was nearly linear(see figure 2.) with 2.5% per 30μC and a total of 7.4%(within 10%) for both currents. This suggests that a larger current is more effective than a smaller

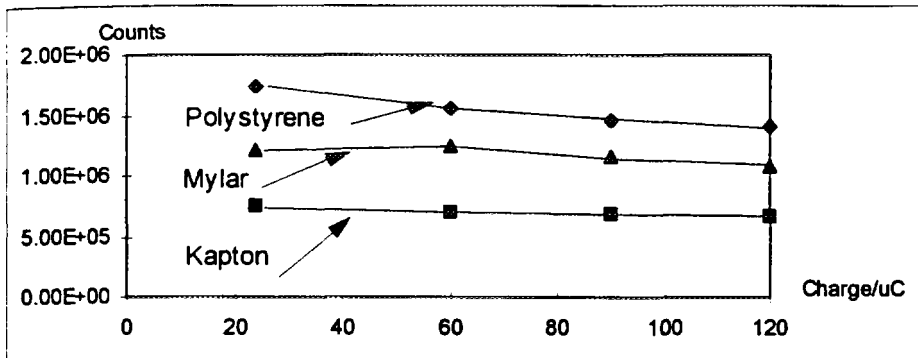


Figure 2. Hydrogen loss.

one when large amounts of charge are collected. For Mylar the variation was much larger. This may be due to different amounts of water in the film and the time under vacuum, but as in Kapton a larger current is more effective than a smaller one. The hydrogen count as a function of collected charge at 50nA is plotted in figure 2 for all three polymers. The hydrogen loss in polystyrene and Mylar was fitted by an exponential curve, while in Kapton a linear curve was fitted to the data, all three by using least square fitting. Polystyrene showed a hydrogen loss of 19% in the charge interval [30μC,120μC].

The hydrogen loss dependence on beam energy was investigated only in Kapton. A run with 2.0MeV(50nA) in 30μC steps was carried out. Very weak hydrogen loss energy dependence was observed.

The large differences in the results between Baglin[4](0.8%/10μC(1cm<sup>2</sup>)) and Pretorius[5](6%/5μC) may be due to differences in area. Another factor is that with a rastered beam a uniform beam spot is obtained. Without a rastered beam this is possible, but much more difficult, which also can have effected the results. This was observed in this work.

## ANALYSIS

The hydrogen recoil spectra are shown in figure 3. The front edge is the surface of the material and the back edge the aluminium filter cut off. Notable is the very much larger proton energy for polystyrene than for the other materials. All three spectra show no hydrogen peak at the surface and by comparison with much larger amounts of charge collected, the shape of the spectra does not change. This indicates that no surface hydrogen contamination was in the materials. The large increase in counts for Mylar between 30μC and 60μC is then likely due to water contained within the bulk. For all three polymers the RBS spectra showed no loss of other components, by comparing these spectras after 30μC and 120μC. However all materials showed a strong coloration, which indicates that a rearrangement of components has occurred. This is consistent with the paper of A. Chapiro[9], in which it is shown that irradiated polymers can undergo chemical changes without losing large amounts of their components. The hydrogen loss rate is greatest in polystyrene, which increases the errors in a hydrogen depth profile application. Kapton shows a low hydrogen loss. The errors in a hydrogen profile of a sample using Kapton as a standard would then

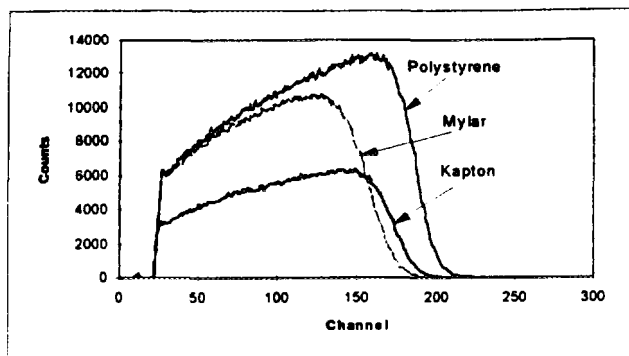


Figure 3. Hydrogen recoil spectra.

be small. Mylar needs more investigation of the water content inside, but a run to investigate the hydrogen loss as a function of time under vacuum would reveal the amount of water in Mylar.

The rather large hydrogen loss in all three films is due to the large amount of charge that is collected on the targets. In a hydrogen profiling application[3,4,6] the usual amount of collected charge is typically about  $5\mu\text{C}$ . In this charge region Kapton will have the lowest hydrogen loss, and polystyrene the largest. The hydrogen loss was not investigated thoroughly in this small charge region and ought to be closely examined before a standard application is carried out with these polymers. However polystyrene has been used for calculating the differential cross-section

for elastic recoiling of hydrogen from helium in the few MeV region and has showed good irradiating properties[3,5,7,8] in the few  $\mu\text{C}$  region. Furthermore this cross-section application has also been carried out by J. Tirira et. al[10], using Mylar with satisfactory results and seen from the results above. Kapton is the least radiation sensitive material of the polymers.

## CONCLUSIONS

- (1) Kapton shows a nearly linear hydrogen loss dependent mainly on collected charge. The loss is about 2.5% per  $30\mu\text{C}(20\text{mm}^2)$ . Mylar showed possible water contamination within the bulk. The hydrogen loss is weakly exponential, but larger than in kapton. Polysterene showed a clear exponential hydrogen loss as a function of collected charge with about 19% in the interval  $[30\mu\text{C}, 120\mu\text{C}](20\text{mm}^2)$ .
- (2) Generally the hydrogen loss as a function of energy and current was weak.
- (3) Polystyrene had the largest hydrogen loss of the three films, which decreases the accuracy of a depth profile using polystyrene.
- (4) Mylar showed large charge build up, but this could be avoided.
- (5) All three can be used for hydrogen profiling. If possible a rastered beam should be used to uniformly distribute the incident beam over large areas. However by moving the beam to a fresh spot in between runs and sum up the recoil spectra, it would be possible to use a non-rastered beam and still obtain good statistics and precision, using a few  $\mu\text{C}$  in every run. The energy of the beam should be worked out with the shielding filter thickness to optimise depth resolution and the current should be kept small, maybe  $20\text{nA}$ , but most important it should be kept stable(to collect the charges consistently).
- (6) No other losses than hydrogen was found to occur, only a rearrangement of material components.

## CURRENT INVESTIGATIONS

- (1) Investigation of the hydrogen loss for the polymers in the lower charge regions.
- (2) Investigation of the probable water contamination in Mylar.
- (3) Completion of energy dependence measurements for all the materials.
- (4) A hydrogen profiling application of the polymers, using samples of known and unknown hydrogen profiles, for concluding the precision of hydrogen profiling using these polymers as reference standards.

## REFERENCES

- [1] Chu, Wei Kan et. al., Backscattering spectrometry(Academic Press, New York, 1978).
- [2] The version 92.02 of TRIM(Transport of Ions in Matter) computer code written by J.F. Ziegler and J.P. Biersack.
- [3] R. Pretorius and M. Peisach, Nucl. Instr. and Meth. B35(1988)478.
- [4] A. Turos and O. Meyer, Nucl. Instr. and Meth. B4(1984)92.
- [5] J.E.E. Baglin, A.J. Kellock, M.A. Crockett and A.H. Shih, Nucl. Instr. and Meth. B64(1992)469.
- [6] J. Tirira and F. Bodart, Nucl. Instr. and Meth. B74(1993)496.
- [7] J. Genzer, J.B. Rothman and R.J. Composto, Nucl. Instr. and Meth. B86(1994)345.
- [8] V. Quillet, F. Abel and M. Schott, Nucl. Inst. and Meth. B83(1993)47.
- [9] Adolphe Chapiro, Nucl. Instr. and Meth. B32(1988)111.
- [10] J. Tirira, P. Trocellier, J.P. Frontier and P. Trouslard, Nucl. Instr. and Meth. B45(1990)203.
- [11] B.L. Doyle and P.S. Peercy, Appl. Phys. Lett. 34(11), 1 June 1979.

# **INDEX OF AUTHORS**

## INDEX OF AUTHORS

Adam, J	100
Andersson, M	158
Ashley, P M	11
Ballhaus, C	147
Barbara, D	104
Beckman, D R	107
Belay, K B	44
Bettioli, A	22, 77, 88
Biddle, G	142
Boldeman, J	59
Bonani, G	25
Breese, M B H	68
Brown, A	110
Bubb, I F	85, 158, 164
Bunder, J	47
Bursill, L A	127
Cholewa, M	17, 149
Clacher, A	28
Cohen, D	59, 65, 94, 133, 158
Cresswell, R G	28
Dastoor, P C	144
Day, J P	28
Den Besten, J L	112
Di Tada, M	28
Dooley, S	22, 50, 115
Dymnikov, A	65
Dytlewski, N	47, 133, 158
El Bouanani, M	2, 158
Elliman, R G	41
Ellis, P	59
Evans, P J	47
Fallon, J	59
Fang, Z	38
Fifield, L K	28
Fink, D	29, 62, 121, 130, 152
Flavell, T	142
Gerstner, E G	136
Gonon, P	22, 88
Gorman, J D	97
Green, T H	100
Griffin, W L	19
Habermehl, M A	32
Heinrich, C A	147
Hoffman, A	118
Hotchkis, M A C	29, 62, 121, 130, 152
Howard, J	149

Hua, Q	29, 121, 130
Hughes, A E	97
Hult, M	158
Hutton, J T	32
Jacobsen, G E	29, 62, 121, 130
Jakobsson, B	2
Jamieson, D N	22, 50, 77, 83, 88, 104, 107, 112, 115
Jaworowski, J	2
Jiang, H	41
Johnson, C M	91
Johnston, P N	85, 158, 164
Jönsson, P	158
Kenny, M J	71
Kerr, K M	124
King, B V	144
Kostidis, L I	77, 110
Kringhoj, P	41
Lai, P F	127
Lawie, D C	11
Lawson, E M	29, 62, 121, 130, 152
Leandersson, M	2
Leech, P L	91
Legge, G J F	17, 65, 68, 110, 149
Leistner, A	71
Livett, M K	124
Llewellyn, D J	44
Lottermoser, B G	11
Martin, J S	133
Martin, P J	71
McCubbery, D	118
McCulloch, D G	136
McKenzie, D R	136
McOrist, G D	5
Merchant, A R	136
Mernagh, T P	147
Mitchell, I V	80
Moloney, G	65
Moss, S D	118
Murao, S	8, 139
Netterfield, R P	71
Niklaus, Th R	25
Noorman, J T	47
Nugent, K W	50, 77, 83, 115, 124, 155
O'Connor, D J	38
Oliver, J	142
Ophel, T R	28, 80
Östling, M	158
Paterson, P J K	97, 118, 142
Pearce, J	22

Perry, A J	74
Persson, L	158
Petravic, M	118
Plimer, I R	11, 14
Prauer, S	22, 50, 77, 104, 110, 115, 127, 155
Prescott, J R	32
Priest, N D	28
Prinoth-Fornwagner, R	25
Reeves, S J	14
Ridgway, M C	44, 91
Roberts, M L	83
Romanski, J	2
Russell, G J	133
Ryan, C G	19, 147
Saint, A	17, 65, 68, 149
Sakellariou, A	149
Short, R	164
Sie, S H	8, 56, 100, 139
Smallwood, A	5
Smith, A M	29, 62, 121, 130, 152
Spargo, A E C	127
Stannard, W B	85, 158
Suter, G F	8, 56, 139
Swain, M V	74
Treglio, J R	74
Tsoi, K A	155
Tuniz, C	29, 53, 62, 121, 130, 152
Van Achterbergh, E	147
Van Moort, J	32
Van Veldhuizen, E J	2
Von Bibra, M L	83
Walker, R J	22, 155
Walker, S R	85, 158
Watts, R O	1
Weiser, P S	77, 112, 115
Westerberg, L	2
Whitlow, H J	2, 158, 164
Wielunski, L S	35, 47, 71, 161
Win, T T	19
Winzell, T R H	164
Wong, W C	41
Yin, Y	136
Zaring, C	158
Zaw, K	147

# **LIST OF PARTICIPANTS**

## LIST OF PARTICIPANTS

(as at time of printing)

---

Askraba, S	Victoria University of Technology
Barbara, D	The University of Melbourne
Baxter, G	CSIRO Division of Applied Physics
Beck, D R	The University of Melbourne
Beckman, D R	The University of Melbourne
Belay, K	Australian National University
Bendavid, A	CSIRO Division of Applied Physics
Bettioli, A A	The University of Melbourne
Bieske, E J	The University of Melbourne
Biggs, S	The University of Newcastle
Bhansali, S	Royal Melbourne Institute of Technology
Boldeman, J W	Australian Nuclear Science and Technology Organisation
Brongersma, H H	Eindhoven University of Technology
Brown, A	The University of Melbourne
Bubb, I F	Royal Melbourne Institute of Technology
Chakrabarthy, C K	The Flinders University of South Australia
Cholewa, M	The University of Melbourne
Clark, R G	University of New South Wales
Clissold, R A	CSIRO Division of Applied Physics
Cohen, D	Australian Nuclear Science and Technology Organisation
Collins, G A	Australian Nuclear Science and Technology Organisation
Collins, J	John Morris Scientific Pty Limited
Cotterill, G F	The University of Newcastle
Dastoor, P C	The University of Newcastle
Den Besten, J L	The University of Melbourne
Dinte, B	Griffith University
Dobbie, E W	Javac Pty Ltd
Dooley, S P	The University of Melbourne
Drage, D G	CSIRO Division of Applied Physics
Durandet, A	Australian National University
Dyson, A J	The University of Newcastle
Dytlewski, N	Australian Nuclear Science and Technology Organisation
Elliman, R	Royal Melbourne Institute of Technology
Evans, P	Australian Nuclear Science and Technology Organisation
Fallon, J P	Australian Nuclear Science and Technology Organisation
Fang, Z	The University of Newcastle
Fifield, L K	Australian National University
Fink, D	Australian Nuclear Science and Technology Organisation

# LIST OF PARTICIPANTS

(as at time of printing)

---

Freund, C	CSIRO Division of Applied Physics
Furst, J	The University of Newcastle
Gammon, R	Australian Institute of Nuclear Science and Engineering
Gibson, C T	Griffith University
Glasko, J M	Australian National University
Gonon, P	University of Melbourne
Gorman, J D	Royal Melbourne Institute of Technology
Guan, P	The University of Sydney
Halfpenny, D R	Macquarie University
Hickman, S	Fisons
Holt, S A	Australian Defence Force Academy
Hotchkis, M A C	Australian Nuclear Science and Technology Organisation
Hsu, Y T	The University of Newcastle
Hughes, J M	The University of Newcastle
Jacobsen, G E	Australian Nuclear Science and Technology Organisation
Jackson, P	University of New South Wales
Jamie , I M	University of Wollongong
Jamieson, D N	The University of Melbourne
Johnson, C M	Australian National University
Kaalund, C J	University of New South Wales
Kenny, M J	CSIRO Division of Applied Physics
Kerr, K M	The University of Melbourne
Kinder, T J	CSIRO Division of Applied Physics
King, B V	The University of Newcastle
LLewellyn, D J	Australian National University
Lachlan, C	The University of Melbourne
Lai, P F	The University of Melbourne
Lanigan, M	Conference Overload
Lawson, E M	Australian Nuclear Science and Technology Organisation
Legge, G J H	The University of Melbourne
Livett, M	The University of Melbourne
Lu, Q B	The University of Newcastle
Lund, C P	Murdoch University
MacDonald, R J	The University of Newcastle
Manory, R R	Royal Melbourne Institute of Technology
Marks, N	The University of Sydney
Marshall, C	Balzars
Martin, J W	University of New South Wales

# LIST OF PARTICIPANTS

(as at time of printing)

---

<b>Martin, P J</b>	<b>CSIRO Division of Applied Physics</b>
<b>McCulloch, D</b>	<b>The University of Sydney</b>
<b>McDonough, A</b>	<b>Royal Melbourne Institute of Technology</b>
<b>McKay, T J</b>	<b>The University of Adelaide</b>
<b>McKenzie, D R</b>	<b>The University of Sydney</b>
<b>McOrist, G D</b>	<b>Australian Nuclear Science and Technology Organisation</b>
<b>Merchant, A</b>	<b>The University of Sydney</b>
<b>Morris, G</b>	<b>The University of Queensland</b>
<b>Moss, S D</b>	<b>Royal Melbourne Institute of Technology</b>
<b>Muralidhar, G K</b>	<b>Royal Melbourne Institute of Technology</b>
<b>Murao, S</b>	<b>Geological Survey of Japan</b>
<b>Myhra, S</b>	<b>Griffith University</b>
<b>Netterfield, R P</b>	<b>CSIRO Division of Applied Physics</b>
<b>Nguyen, H</b>	<b>The University of Sydney</b>
<b>Niklaus, TH R</b>	<b>CSIRO Exploration and Mining</b>
<b>Nowak, R</b>	<b>Nagoya Institute of Technology</b>
<b>Nugent, K W</b>	<b>The University of Melbourne</b>
<b>O'Connor, D J</b>	<b>The University of Newcastle</b>
<b>O'Malley, B</b>	<b>Royal Melbourne Institute of Technology</b>
<b>Oliver, J A</b>	<b>Royal Melbourne Institute of Technology</b>
<b>Ophel, T R</b>	<b>Australian National University</b>
<b>Pailthorpe, B</b>	<b>The University of Sydney</b>
<b>Paterson, P J K</b>	<b>Royal Melbourne Institute of Technology</b>
<b>Payling, R</b>	<b>BHP Research</b>
<b>Petravic, M</b>	<b>Australian National University</b>
<b>Perry, A</b>	<b>Australian National University</b>
<b>Perret, N</b>	<b>The University of Newcastle</b>
<b>Pickering, S</b>	<b>Royal Melbourne Institute of Technology</b>
<b>Plimer, I</b>	<b>The University of Melbourne</b>
<b>Prescott, J R</b>	<b>University of Adelaide</b>
<b>Prince, K E</b>	<b>Australian Nuclear Science and Technology Organisation</b>
<b>Radny, M W</b>	<b>The University of Newcastle</b>
<b>Reeves, S</b>	<b>The University of Melbourne</b>
<b>Russo, S P</b>	<b>Royal Melbourne Institute of Technology</b>
<b>Ryan, C</b>	<b>CSIRO Exploration and Mining</b>
<b>Saint, A</b>	<b>The University of Melbourne</b>
<b>Sainty, W G</b>	<b>CSIRO Division of Applied Physics</b>
<b>Sakellariou, A</b>	<b>The University of Melbourne.</b>

# LIST OF PARTICIPANTS

(as at time of printing)

---

Shen, Y S	The University of Newcastle
Shorrocks, H	Varium
Sie, S H	CSIRO Exploration and Mining
Siegele, R	Australian Nuclear Science and Technology Organisation
Singh, J	Royal Melbourne Institute of Technology
Singh, N K	University of New South Wales
Smith, A M	Australian Nuclear Science and Technology Organisation
Smith, P V	The University of Newcastle
Snook, I K	Royal Melbourne Institute of Technology
Stannard, W B	Royal Melbourne Institute of Technology
Stanton, W B	Stanton Scientific
Stevenson, K P	The University of Melbourne
Swain, M V	CSIRO Division of Applied Physics
Swingler, D L	Victoria University of Technology
Trost, A	Vacuum Society of Australia
Tsoi, K A	The University of Melbourne
Tuniz, C	Australian Nuclear Science and Technology Organisation
Von Bibra, M	The University of Melbourne
Von Nagy-Felsobuki, E I	The University of Newcastle
Walker, E	Murdoch University
Watson, G S	Griffith University
Watts, R	The University of Melbourne
Weiser, P S	The University of Melbourne
Whitlow, H J	Lund Institute of Technology
Wielunski, L	CSIRO Division of Applied Physics
Williams, G J	The University of Newcastle
Wilson, J	Flinders University
Winzell, T	Royal Melbourne Institute of Technology
Witham, L	The University of Melbourne
Wong-leung, J	Australian National University
Yao, J	The University of Newcastle
Young, A	Fisons
Zhang, F	The University of Newcastle
Zubonov, D	Royal Melbourne Institute of Technology